Universidade de São Paulo

Faculdade de Filosofia, Ciências e Letras de Ribeirão Preto

Departamento de Química

Programa de Pós-Graduação em Química

“YAG:Ln^{3+} obtidos via pirólise de aerossol - partículas e compostos à base de fibroína e suas aplicações fotônicas”

“Ln^{3+}:YAG obtained via spray pyrolysis - particles and fibroin-based compounds, and its photonic applications”

Roberta Silva Pugina

Tese apresentada à Faculdade de Filosofia, Ciências e Letras de Ribeirão Preto da Universidade de São Paulo, como parte das exigências para a obtenção do título de Doutor em Ciências. Área: **Química.**

RIBEIRÃO PRETO-SP
2022

Universidade de São Paulo

Faculdade de Filosofia, Ciências e Letras de Ribeirão Preto

Departamento de Química

Programa de Pós-Graduação em Química

Versão Corrigida

“YAG:Ln^{3+} obtidos via pirólise de aerossol - partículas e compostos à base de fibroína e suas aplicações fotônicas”

“Ln^{3+}:YAG obtained via spray pyrolysis - particles and fibroin-based compounds, and its photonic applications”

Roberta Silva Pugina

Orientador: Prof. Dr. José Maurício Almeida Caiut

Tese apresentada à Faculdade de Filosofia, Ciências e Letras de Ribeirão Preto da Universidade de São Paulo, como parte das exigências para a obtenção do título de Doutor em Ciências. Área: **Química.**

RIBEIRÃO PRETO-SP
2022

FICHA CATALOGRÁFICA

Pugina, Roberta Silva.

YAG:Ln^{3+} obtidos via pirólise de aerossol - partículas e compostos à base de fibroína e suas aplicações fotônicas

Ribeirão Preto, 2022.

170 p. : il. ; 30 cm

Tese de Doutorado apresentada à Faculdade de Filosofia, Ciências e Letras de Ribeirão Preto da Universidade de São Paulo, como parte das exigências para a obtenção do título de Doutor em Ciências.

Área: Química.

Orientador: Caiut, José Maurício Almeida.

1. Espectroscopia de Luminescência 2. LASER Aleatório 3. Termometria

“Quando os ventos de mudança sopram, umas pessoas levantam barreiras, outras constroem moinhos de vento.”

Erico Verissimo

Dedicatória

Ao meu pai, Ricardo, um dos maiores incentivadores dos meus sonhos, e cuja presença é cada vez mais forte em minha vida!

Agradecimentos

A Deus, pela serenidade nos momentos difíceis.

Ao Prof. Dr. José Maurício Caiut, pelo apoio em cada passo dado nesta trajetória, por ter me ensinado grande parte do que sei sobre química e, principalmente, pela relação de amizade e respeito construída durante estes 11 anos de trabalho. Agradeço também pelo apoio, compreensão e paciência nos momentos difíceis, e por ter me dado a certeza de que o NanoLum era o meu lugar. Estendo meus agradecimentos à Silvana, pelo carinho, educação e respeito com que trata a todos nós. Obrigada também, Sil, pela paciência durante os encontros do nosso grupo.

À minha mãe, Helena, que desde muito cedo me ensinou a importância da educação, principalmente para nós mulheres, e que nunca mediu esforços para que tivéssemos acesso a tudo que precisássemos, para chegar onde quiséssemos. Por mais clichê que posso parecer, sem você, sua força e resiliência, esta trajetória não estaria chegando ao fim. Obrigada, mais uma vez, por fazer das nossas vidas a sua vida, e dos nossos sonhos os seus sonhos.

Ao Ricardo, meu irmão, amigo e a base mais sólida da minha vida. Obrigada por segurar sozinho as “barras” que seriam nossas, e desviar o seu caminho para que eu pudesse seguir no meu. Jamais serei capaz de expressar a minha gratidão, pois, sem você e seu apoio, eu não estaria aqui escrevendo esta tese.

Ao Fer, que compartilha comigo todas as alegrias e tristezas da vida. Obrigada pelas nossas infinitas conversas, por me apoiar em absolutamente tudo, vibrar com minhas conquistas como se fossem tuas e, por muitas vezes, trazer a calma que falta em mim. Estendo minha gratidão à sua família, Maria, Du, Tha, Tami e Thi, obrigada por me acolherem e por se tornarem minha segunda família desde o início.

Aos meus tios, Sônia e Zé, pelo apoio e presença durante toda minha vida. Agradeço também pelo acolhimento nos momentos difíceis, e por tudo que fizeram por nós. Neste sentido, agradeço também a Tati e a Tia Marlene por se fazerem presentes, cada uma a sua maneira, quando mais foi necessário.

Às minhas primas e, não por coincidência, melhores amigas, Carol, Mari e Vivi, por tudo que compartilhamos durante toda a vida. Vocês são as irmãs que, de fato, eu não tive.

Aos meus amigos, Camila, Cláudio, João Pedro, Karmel, Larissa Tomazela, Lucas Bahia, Lucas Urbano, Luiz Fernando, Luiz Henrique, Marcos e Tamires, agradeço pelo apoio, incentivo, discussões acadêmicas ou não, e pelas infinitas risadas. Cá, te ter em minha vida e compartilhar com você sorrisos e lágrimas durante todos estes anos, com certeza faz de mim uma pessoa melhor, obrigada por tudo, sua força me inspira! Lu Bahia, você é um presente na vida dos que te cercam, obrigada por essa longa e tão importante amizade. Mel, sou muito grata por ter compartilhado, tão de perto, parte desses anos de doutorado com você; sua leveza e seu apoio foram fundamentais. Mar, obrigada pelos conselhos e por sempre compartilhar o que sabe de forma tão genuína. Luiz Fernando, obrigada por compartilhar comigo tantos momentos bons e outros nem tanto. Tami, obrigada por se fazer sempre tão presente em minha vida. Claudinho, obrigada pela sua gentileza, educação e por todos os momentos agradáveis que compartilhamos. Luizinho, obrigada por estar sempre disposto para ajudar ou compartilhar um café.

Aos colegas que fizeram parte do NanoLum, e que de alguma forma contribuíram para que eu chegasse até aqui. De forma especial ao Douglas, à Eloísa, ao Francisco, à Tatiana e ao Pedro. Elô, obrigada por, literalmente, estar ao meu lado durante grande parte do desenvolvimento deste trabalho, e por toda ajuda dentro do laboratório, sem você está tese não chegaria na página 100. Agradeço também por sua amizade que torna meus dias mais leves. Chico, obrigada pela amizade, pela sua alegria e disponibilidade em ajudar a todos e, principalmente, por ter sido um grande apoio quando mais precisei. Doug, obrigada pela sua calma e paciência em nos ajudar. Tatiana, Pedro, Elô e Chico, obrigada por gentilmente terem me auxiliado na revisão deste texto. Agradeço também aos “agregados”, Luan e Cintya, pelos momentos compartilhados.

Ao Felipe, à Carol e à Lari Justino, pela amizade que se mantem apesar da distância. Saibam que, apesar de não estarmos perto tanto quanto eu gostaria, a amizade e apoio de vocês são essenciais na minha vida.

À Lari Flávia, por tudo que compartilhamos durante a graduação, e pelo carinho e amizade que se mantêm apesar do tempo e da distância.

Ao Prof. Dr. Anderson Gomes, pela colaboração nas análises de emissão laser randômico e termometria, que ocorreram no âmbito do projeto INCT-INFO e foram fundamentais para o desenvolvimento deste trabalho. Agradeço pela forma tão gentil e solicita que me recebeu no Laboratório de Fotônica e Óptica Não Linear, do Departamento de Física da Universidade Federal do Pernambuco (DF-UFPE). Obrigada pelos ensinamentos, conselhos, cafés e risadas, foi uma honra poder trabalhar com você, "prof"! Ainda na UFPE, agradeço imensamente a colaboração do Dr. Manoel Leonardo, sua paciência e disponibilidade em me auxiliar em tudo que permeia o universo da óptica não-linear. Meu muito obrigada também ao Dr. Avishek Das e à Dra. Cecília Vegas pelo auxílio durante minhas passagens pelo Recife e, por assim como o Manoel, se tornarem bons amigos apesar do pouco tempo de convívio.

Ao Prof. Dr. Lauro Maia, pelos dias que passei em seu laboratório, no Instituto de Física da Universidade Federal do Goiás (IF-UFG), onde foram realizados os testes iniciais de emissão laser, e emergiram discussões de extrema importância para este trabalho. Obrigada também, Lauro e Gisane, por nos apresentar Goiânia.

Ao Prof. Dr. Sidney José Lima Ribeiro, pelas contribuições, disponibilidade e uso de seu laboratório e equipamentos, situados no Instituto de Química da UNESP, Campus de Araraquara (IQ-UNESP).

À Profa. Dra. Rogéria Rocha Gonçalves, por toda a contribuição durante a minha formação. Agradeço às oportunidades, ensinamentos, conselhos, e por ser uma grande inspiração! Estendo meus agradecimentos aos colegas do MaterLumen, pela disponibilidade e parceira, que são de extrema importância para o desenvolvimento de nossos trabalhos.

À Profa. Dra. Ana Paula Ramos, pela amizade, incentivo e por sempre ter deixado as portas de seu laboratório abertas a mim, para qualquer coisa que fosse preciso.

Ao Prof. Dr. Pietro Ciancaglini, pelo uso de equipamentos e reagentes, e pelos cafés e conversas no corredor.

Ao Prof. Dr. Antônio Cláudio Tedesco, pela colaboração no âmbito do projeto PRONON (Programa Nacional de Apoio à Atenção Oncológica) do Ministério da Saúde, 2016–2021, que foi essencial para o desenvolvimento deste projeto.

Aos demais docentes e funcionários do Departamento de Química da Faculdade de Filosofia Ciência e Letras da USP de Ribeirão Preto que, em algum momento, fizeram parte da minha formação. De forma especial, agradeço ao Dr. Lourivaldo dos Santos pela disponibilidade e auxílio, principalmente durante o período mais crítico da pandemia da COVID-19, que foram de fundamental importância para o desenvolvimento deste projeto.

À CAPES (Finance Code 001) e à FAPESP (2016/11670-5 e 2019/18828-1) pelo fomento dos projetos, e ao CNPq (141954/2018-3) pela bolsa concedida.

Resumo

PUGINA, R. S. **YAG:Ln^{3+} obtidos via pirólise de aerossol - partículas e compostos à base de fibroína e suas aplicações fotônicas.** 2022. Tese (Doutorado em Ciências – Faculdade de Filosofia Ciências e Letras de Ribeirão Preto, Universidade de São Paulo, Ribeirão Preto, 2022.

Os avanços na área da fotônica estão intimamente relacionados à obtenção de novos materiais e sistemas nanoestruturados, bem como ao estudo de efeitos ópticos não-lineares. Neste sentido, a emissão laser em ambiente aleatório é um promissor campo de pesquisa, assim como o desenvolvimento de termômetros óticos e de materiais possíveis de serem aplicados como dispositivos anti-falsificação, entre outros. Visto isto, neste trabalho, esferas de YAG (Ítrio Alumínio Garnet, $Y_3Al_5O_{12}$) dopadas com diferentes íons lantanídeos foram obtidas via pirólise de aerossol, uma metodologia que proporciona alto rendimento e pode ser empregada para produção em larga escala, não gerando subprodutos, e oferecendo a vantagem de não introduzir impurezas no produto final, uma vez que não há contato externo com os precursores, e cada gota constitui um mini reator homogêneo que possui a mesma composição química da solução inicial. Durante a síntese e, mesmo após tratamento térmico a 1100 °C, as partículas não coalesceram. Todas as caracterizações confirmaram que a fase YAG foi obtida na presença dos íons lantanídeos (Nd^{3+}, Yb^{3+}/Er^{3+} ou Yb^{3+}/Tm^{3+}), que tiveram suas propriedades espectroscópicas analisadas e exploradas visando aplicações fotônicas. As partículas de YAG:Nd^{3+} foram estudadas quanto à suas emissões em ambientes desordenadas, já as partículas de YAG:Yb^{3+}/Er^{3+} foram destinadas à estudos em diferentes temperaturas, enquanto nos sistemas YAG:Yb^{3+}/Tm^{3+} foi observado a emissão caraterística no azul, o que torna este material um possível candidato à dispositivo anti-falsificação. Além disto, visando aplicações biológicas, estas partículas foram adicionadas à fibroína da seda, uma matriz biocompatível que permite a inserção de diferentes íons, moléculas ou nanopartículas; apresenta boa adequação em sistemas ópticos, devido, principalmente, a elevada transparência (> 95%) em toda a região visível do espectro; é mecanicamente robusta e modelável na forma de filmes, fios ou partículas. No caso dos compósitos SF-YAG:Yb^{3+}/Er^{3+} e SF-YAG:Yb^{3+}/Tm^{3+}, os mesmos comportamentos observados nas partículas foram constatados também na forma de filme.

Palavras-chaves: Espectroscopia de Luminescência. LASER Aleatório. Termometria.

Abstract

PUGINA, R. S. **Ln^{3+}:YAG obtained via spray pyrolysis - particles and fibroin-based compounds, and its photonic applications.** 2022. Tese (Doutorado em Ciências – Faculdade de Filosofia Ciências e Letras de Ribeirão Preto, Universidade de São Paulo, Ribeirão Preto, 2022.

Advances in photonics are related to obtaining new materials and nanostructured systems, as well as studying non-linear effects. In this sense, laser emission resulting from the confinement of light in a disordered structure is a promising field of research, as well as the development of optical thermometers and materials that can be applied as anti-counterfeiting devices, among others. In this work, YAG (Yttrium Aluminum Garnet, $Y_3A_{l5}O_{12}$) spheres doped with different lanthanide ions were obtained via spray pyrolysis, a methodology that provides high yield and can be used for large-scale production, without generating byproducts, and offering the advantage of not introducing impurities into the final product, since there is no external contact with the precursors, and each drop constitutes a homogeneous mini reactor that has the same chemical composition as the initial solution. During the synthesis and even after heat treatment at 1100 °C, the particles did not coalesce. All characterizations confirmed that the YAG phase was obtained in the presence of lanthanide ions (Nd^{3+}, Yb^{3+}/Er^{3+} or Yb^{3+}/Tm^{3+}), which had their spectroscopic properties analyzed and explored for photonic applications. The Nd^{3+}:YAG particles were studied for their emissions in disordered environments, Yb^{3+}/Er^{3+}:YAG were intended for studies at different temperatures, while in the Yb^{3+}/Tm^{3+}:YAG systems the characteristic blue-emission was observed, which makes this material a possible candidate for an anti-counterfeiting device. Furthermore, aiming for biological applications, these particles were added to silk fibroin which is a biocompatible matrix that allows the insertion of different ions, molecules or nanoparticles; that shows good suitability in optical systems, mainly due to high transparency (> 95%) throughout the visible region of the spectrum; that is mechanically robust and moldable in the form of films, wires and particles. In the case of SF-Yb^{3+}/Er^{3+}:YAG and SF-Yb^{3+}/Tm^{3+}:YAG composites, the same behavior observed in the particles was also observed in the film form.

Keywords: Luminescence Spectroscopy. Random LASER. Thermometry.

List of Figures

List of Tables

LIST OF CONTENT

Introduction

This thesis is a result from the studies carried out during the PhD project titled "Structural and spectroscopic study of luminescent composites based on fibroin and rare earth ions for photonic applications" funded by CNPq (process 141954/2018-3) and developed from March/2018 to January/2022 in the Nanomaterials and Luminescent Systems Group (NanoLum). During this period, particles of Ln^{3+}:YAG (Ln^{3+}: Nd^{3+}, Yb^{3+}/Er^{3+} and Yb^{3+}/Tm^{3+}) were prepared via Spray Pyrolysis (SP), a methodology that provides high yield and could be employed also for large-scale production. This methodology generates few byproducts that are associated with the production of micro- and submicrometric spherical particles that do not coalesce, and it can provide dense or hollow materials. In addition, offers the advantage of not introducing impurities in the final product because there is no external contact with the precursors, and each drop constitutes a homogeneous mini reactor that has the same chemical composition as the initial solution. This system involves three main steps: aerosol generation, pyrolysis, and final product collection [1–4]. The precursor used was a boehmite suspension obtained by sol-gel methodology, since, in previous works of the group, the effectiveness in the preparation of these aluminates from this suspension was demonstrated [5]. Crystalline YAG (Yttrium Aluminum Garnet) presents a cubic structure and, when doped with lanthanide ions (Ln^{3+}), the resulting materials have important applications in the optical and photonic fields [6,7].

Aiming for photonic and biological applications, compounds based on Silk Fibroin (SF) were also obtained. Fibroin is a fibrous protein extracted from *Bombyx mori* cocoons. A natural, resistant, and biocompatible polymer that has been studied for several applications over the last 70 years [8,9], which reuses the waste from the textile industry and has several interesting characteristics that have been widely explored by the field of research. The silkworm cocoons used for fibroin extraction were kindly donated by the silk spinning company BRATAC, located in Londrina in Paraná state, Brazil.

The Nd^{3+}:YAG laser has over 50 years of history. It has been the most commonly used material in commercial solid-state lasers because it combines the advantageous properties of the YAG matrix and the inserted Nd^{3+} ion. The YAG matrix presents good transparency, high melting point, high thermal conductivity, low thermal expansion coefficient, chemical stability, and hardness. Whereas the Nd^{3+} ion has four energy levels associated with absorption bands in the near infrared region and high efficiency for stimulated emission in laser studies [10–12]. The materials herein produced in the presence of Nd^{3+} ions were intended for application as Random

Laser (RL) devices. The laser emission tests of these materials were carried out at the Physics Department of the Universidade Federal do Pernambuco (DF-UFPE) in collaboration with Prof. Dr. Anderson S. L. Gomes and Dr. Manoel L. da Silva-Neto, within the INCT-INFO project. In addition, the YAG matrix was also doped with the Yb^{3+}/Er^{3+} pair, and its thermometry properties were studied, since Er^{3+} ions are particularly interesting because their excited levels $^2H_{11/2}$ and $^4S_{3/2}$ are energetically close, so they can be classified as thermally coupled levels; that is, under 980-nm laser excitation, Up-Conversion (UC) emissions sensitive to temperature changes can be achieved [13]. The initial tests of these materials were also carried out at UFPE, in collaboration with Professor Anderson's group. Finally, the results obtained with the systems doped with Yb^{3+}/Tm^{3+} ions demonstrated that they can be explored in the future as anti-counterfeiting systems, due to the interesting blue emission observed. The data presented in this thesis are published in scientific journals[*] [†] [‡] [§], which are attached, along with the authorizations for reproduction, and a summary of the author's curriculum (see appendix).

This document has a general introduction to the main subjects that permeate the work, Aluminum and its Compounds, Rare Earth Elements, Principles of Photonics, and Silk, as well as their objectives, experimental methods, and results, which will be presented by section: firstly, the structural, morphology and spectroscopic characterization of the materials and, subsequently, their possible applications such as laser systems, thermometers and anti-counterfeiting devices.

---

[*] Pugina, Roberta S.; Caiut, José Maurício A. Silk: History, Obtaining, Structure and Properties of an Old Material in the Development of New Technologies. International Journal of Advances in Medical Biotechnology, v. 4, p. 27-45, 2021.

[†] Pugina, Roberta S.; Hilário, Eloísa G.; da Rocha, Euzane G.; da Silva-Neto, Manoel L.; Das, Avishek; Caiut, José Maurício A.; Gomes, Anderson S.L. Nd^{3+}:YAG Microspheres Powders Prepared by Spray Pyrolysis: Synthesis, Characterization and Random Laser Application. Materials Chemistry and Physics, v. 269, p. 124764, 2021.

[‡] Pugina, Roberta S.; Silva, Douglas L.; Riul, André; da Silva-Neto, Manoel L.; Gomes, Anderson S.L.; Caiut, José Maurício A. Silk Fibroin-Yb^{3+}/Er^{3+}:YAG Composite Films and their Thermometric Applications based on Up-conversion Luminescence. Polymer, v. 241, p. 124541, 2022.

[§] Pugina, Roberta S.; Caiut, José Maurício A. Blue emission from silk fibroin-Yb^{3+}/Tm^{3+}:YAG films by up-conversion. Materials Letters, v. 314, p. 131866, 2022.

1. State-of-the-Art

1.1. Aluminum and its Compounds

The element aluminum is represented by Al, with a molar mass equal 27 g/mol and atomic number of 13. This metal is the most abundant metallic element and the third most abundant element in the earth's crust, and the non-ferrous metal most used by man. The first reports of the use of this element date back to 6000 b.c. when the Persians made clay pots and containers that contained aluminum oxide. Three thousand years later, clays with alumina were used by ancient peoples in Egypt and Babylon to make cosmetics, medicines and fabric dyes. In the 19th century of the common era, many events mark the history of this metal, as Humphrey Davy's first obtainment of what so far came closest to aluminum from the smelting of iron in the presence of alumina (1809); discovery of a reddish ore containing 52% aluminum oxide near the village of Les Baux in southern France by Frenchman P. Berthier. This is the discovery of bauxite, the most common aluminum ore (1821) [14]. As early as 1825 Danish physicist Hans Christian Oersted manages to isolate aluminum in another way, from aluminum chloride as it is known today, and in 1855, Deville shows, at the Paris exhibition, the first ingot made of a metal much lighter than iron. The process of obtaining aluminum through the electrolytic reduction of alumina dissolved in a melted cryolite bath is made public. This procedure was developed separately by the Charles Martin Hall and the Paul Louis Toussaint Héroult, who discovered and patented it almost simultaneously, becoming a process known as Hall-Heróult and allowing the establishment of the global aluminum industry. Almost a century later, in the city of Ouro Preto (Minas Gerais, Brazil) the first aluminum ingot in the Southern Hemisphere is produced at the Elquisa factory [15].

The name aluminum comes from the Latin *alumen* which means alum, name given to aluminum sulfate today. This element presents several applications – in the automobile industry, it is present in several components used in the manufacture of vehicles; as packaging, in addition to being light and practical, it helps to conserve food, as it protects it from the action of light, moisture and air; in the production of consumer goods such as electronics, furniture, decoration, and sporting goods bringing modernity and durability to the products; and in civil construction, where the search for sustainable construction makes the material ideal for this application, being present in products such as aluminum frames, cladding panels, glazed façades, box and construction tools [16]. It is used a lot because of its physical and chemical properties, as showed in the Table 1.

Table 1. Chemical and physical properties of metallic aluminum [17]

Density	2.7 g/cm³, this density is approximately 1/3 that of steel. With this, the automobile industry is increasingly using this metal to replace steel.
Melting point	660 °C
Boiling point	2467 °C
Thermal conductivity at 25 °C	0.53 cal/cm/°C, 4.5 times bigger than steel, that allows its use in the manufacture of kitchen utensils.
Corrosion resistance	High due to the fact to form a thin and transparent layer of aluminum oxide on its surface, protecting the metal from further oxidation.
Antimagnetic property	It is not magnetic and does not produce sparks, it can be used as protection in electronic equipment, and to store flammable products.

In addition to its interesting properties that allow its use in various applications, aluminum unlike other materials, can be recycled infinitely without losing its characteristics in the reuse process, both from scrap generated by products with an exhausted useful life, as well as from leftovers from the production process. In Brazil, aluminum recycling begins with the establishment of the metal industry in the country. The first records of production of aluminum utensils in the national territory date back to 1920, when the sector used scrap imported from several countries as raw material. Seventy years later, with the beginning of the production of cans in Brazil, metal recycling was intensified, recording increasing volumes. Currently, aluminum recycling in Brazil takes place with high efficiency, above the world average, recycling practically all available scrap. The ratio between recycled and consumed material indicates a percentage of 38.5%, which is higher than the 2014 world average that was 27.1%. In the following year, 602 thousand tons of aluminum were recycled in national territory. Of this total, 292.5 thousand tons refer to scrap aluminum cans for beverages, which corresponds to 97.9% of the total packaging consumed that year, an index that has kept Brazil among the leading countries in the recycling of cans since 200l [18].

This element is found in igneous rocks, in minerals such as micas, feldspar, beryl ($Be_3Al_2[Si_6O_{18}]$), spinel ($MgAl_2O_4$), cryolite ($Na_3[AlF_6]$), garnet ($[Ca_3Al_2(SiO_4)_3]$), and in the corundum (Al_2O_3) which is the mineral with the highest Al content. Ruby and sapphire, gemstones, are impure forms of corundum containing Cr^{3+} and Fe^{3+} ions, which give the gems their red and blue colors, respectively. However, the main source of metallic aluminum is bauxite. This mineral is mainly composited by gibbsite (γ-$Al(OH)_3$), boehmite (γ-$AlO(OH)$), and diasporium (α-$AlO(OH)$). The proportion of the three forms varies depending on the geographic location of the ore. Bauxites containing more boehmite are found in European deposits, while those rich in diasporium in China, Hungary, and Romania. Geologically younger bauxites, on the other hand, have a high gibbsite content, and occur in large deposits in tropical climate areas such as Jamaica, Brazil, Australia, Guinea, Guyana, Suriname, and India. The most important trade route for the purification of bauxite is the Bayer process [15,19], and currently, global bauxite reserves with a total of around 30 billion tons, including Guinea, Australia, Vietnam, Brazil, and Jamaica which are the five largest bauxite producers [20].

By the thermal treatment of the aluminum hydroxides that constitute bauxite, the aluminum oxide, Al_2O_3, is obtained and called alumina. The alpha phase (α-Al_2O_3) is the most thermodynamically stable, called corundum and which occurs in the monocrystalline form. It is also possible to obtain other transitional alumina phases, known as gamma (γ), theta (θ), eta (η), chi (χ), kappa (κ), beta (β), and delta (δ) [15].

After this brief report on the history and properties of the aluminum element, and its main compounds, we will talk about the structures known as yttrium aluminates, focusing on the garnet-shaped structure (YAG), as well as the precursor suspension and the method used to obtain it in this work.

1.1.1. Yttrium Aluminates – YAG in focus

The element yttrium is represented by the letter Y, it has an atomic number of 39 and molar mass of 89 g/mol. This element is located in the ‘d-block’ of the periodic table, and is part of the group known as ‘rare earths’, which is discussed in more details below. Yttrium is commonly found in the oxide form, Y_2O_3, so it is known as yttria. This compound is a white substance, stable to air, used as a precursor in the synthesis of several inorganic compounds, and was first used for commercially application in red phosphors.

Together with yttrium oxide (Y_2O_3, yttria), the aluminum oxide (Al_2O_3, alumina) constitutes a pseudo-binary system, Al_2O_3-Y_2O_3, that contains components that are of great importance in the development of electronic and optical devices, this will also be discussed in more details in the following sections. In addition to the presence of both oxides, the Al_2O_3-Y_2O_3 system contains three stable crystalline phases at room pressure: YAP ($YAlO_3$), YAM ($Y_4Al_2O_9$), and YAG ($Y_3Al_5O_{12}$). Moreover, the metastable phase YAH ($YAlO_3$) may arise. YAM (Yttrium Aluminum Monoclinic) has monoclinic structure, while YAP (Yttrium Aluminum Perovskite) and YAH (Yttrium Aluminum Hexagonal) have distorted orthorhombic perovskite structure and hexagonal structure, respectively [21], as showed in Figure 1. The information of all the intermediate phases are summarized in Table 2.

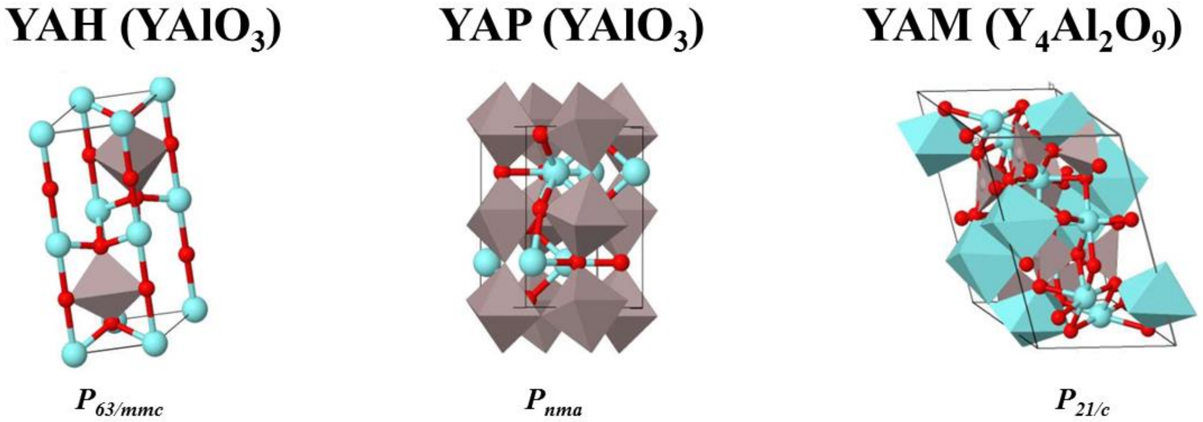

Figure 1. Unit cell of YAH, YAP and YAM, and their point groups [22].

Table 2. Chemical formula, abbreviation, name, structure, and point group of the intermediate compounds of the Al_2O_3-Y_2O_3 system [21]

Chemical Formula	Abbreviation	Name	Structure	Point group
$Y_3Al_5O_{12}$	YAG	yttrium aluminum garnet	cubic	I_a3_d
$Y_4Al_2O_9$	YAM	yttrium aluminum monoclinic	monoclinic	$P_{21/c}$
$YAlO_3$	YAP	yttrium aluminum perovskite	orthorhombic form with distorted perovskite	P_{nma}
	YAH	yttrium aluminum hexagonal	hexagonal	$P_{63/mmc}$

The intermediate compounds of the Al_2O_3-Y_2O_3 system have many optical and photonic applications, but can also be used as a promising material candidate for the ceramic layer in the thermal barrier coating system (YAM) and as scintillators and acousto-optics (YAP), for example [23,24]. They can be obtained by different methodologies. Polycrystalline powders of YAM and nano-crystalline YAP perovskites were produced by a modified sol-gel synthesis (Pechini) [25,26], and by a polymer complex method [27]. By conventional sol-gel method using yttrium and aluminum citrate complexes as precursors, YAM can be obtained also [28], as well as YAP via hydrothermal synthesis [29]. Twenty years ago, Lo and Tseng [30] demonstrated that the YAG and YAM phases can be obtained in a pure form via sol-gel methodology, and that the YAP phase occurs through the reaction between the YAM and YAG.

Medraj and his collaborators [24] observed that obtaining the intermediate phases from the ends compounds (Al_2O_3 and Y_2O_3 oxides) by solid-state reaction is not so simple, since these cases portions of the oxides may not react. They studied the development of these phases that constitute the Al_2O_3-Y_2O_3 binary system using neutron diffraction, which provides real-time information about the solid-state reaction that occurs at its temperature ranges. In this study, they demonstrated the possibility of obtaining the intermediate phases via melt extraction or solid-state reaction. Table 3 shows the chemical composition and the constituent phases of the samples studied.

Table 3. Chemical composition and the expected phases of the studied samples in Medraj work [24]

Sample no.	Al_2O_3 mol%	Composition
1	79	Y_2O_3/YAG
2	62.5	YAG
3	57.5	YAG/YAP
4	50	YAP
5	33.33	YAM

Besides, the stability of the YAP, YAG and YAM phases were observed at temperatures below 25 °C, clarifying any doubts about their decomposition. In this study, it was observed that the formation of the YAG compound started at around 1200 °C and finished at 1600 °C, while YAP and YAM finished at 1800 °C. The melting temperature of samples number 1 to 5 were 1820, 1942, 1908, 1915, and 1978 °C, respectively. In Figure 2, these samples are located in the phase diagram of the Al_2O_3-Y_2O_3 binary system [24].

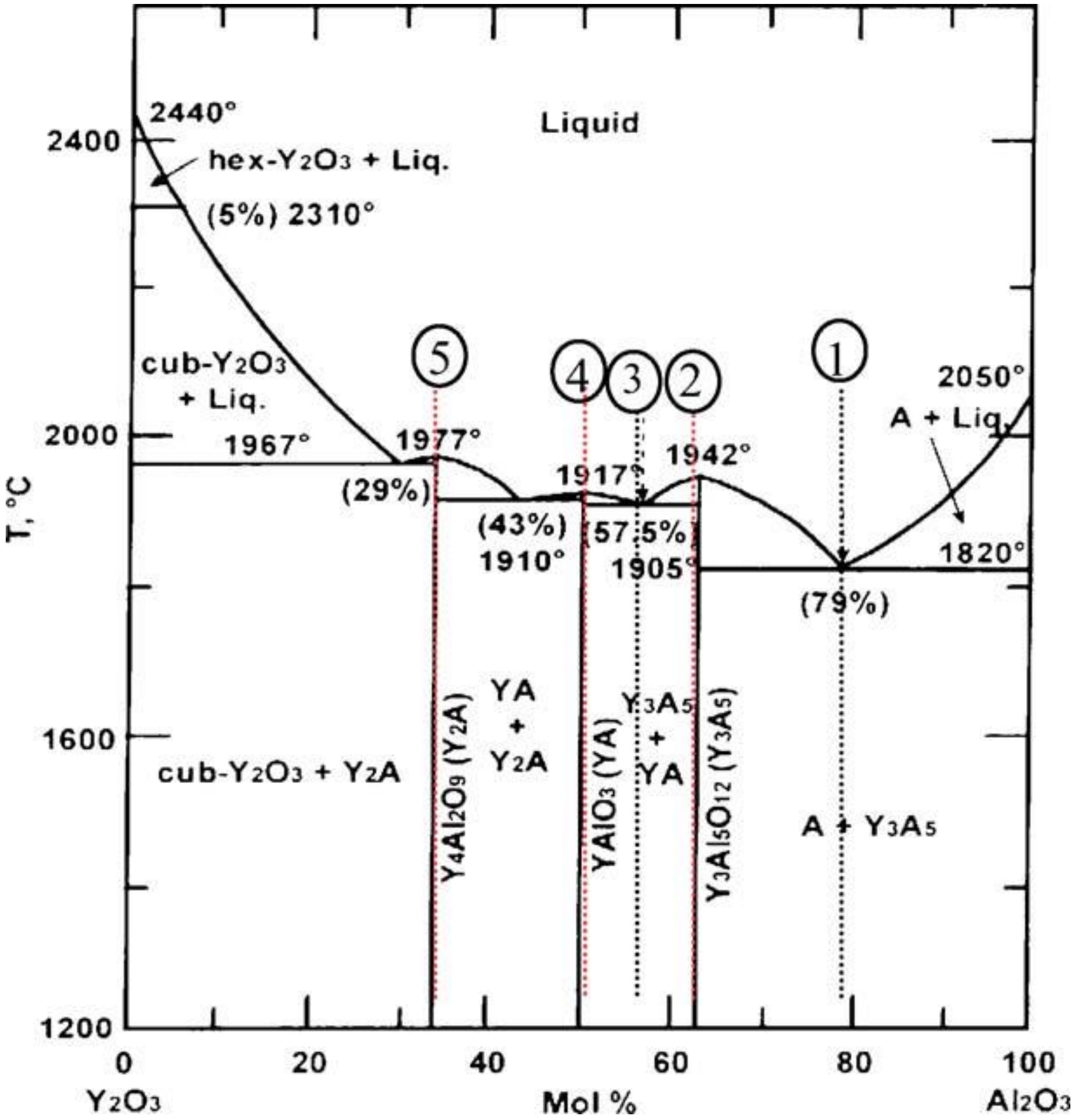

Figure 2. Experimental Al_2O_3–Y_2O_3 phase diagram with the investigated compositions [24].

Since the 1960s, luminescent Ln (which will have their spectroscopic properties discussed below) doped materials based on this binary aluminum and yttrium oxide system have been one of the most important materials for the development of opto-electronic devices [31], as luminescent temperature sensor based on $Y_3Al_5O_{12}$ doped V^{3+}/V^{4+} and Ln^{3+} (Eu^{3+}, Dy^{3+} and Nd^{3+}) [32], Ce^{3+}-doped $Y_3Al_5O_{12}$ as nanophosphors in LED lighting technology [33], warm-light and cyan emitting garnet [34], and nanoprobes (Ce^{3+} and Nd^{3+}-doped) for biological application [35].

Crystalline YAG (Yttrium Aluminum Garnet) presents a cubic structure and contains three different types of polyhedron where Y^{3+} occupies dodecahedral sites and Al^{3+} occupies both octahedral and tetrahedral sites [36], as shown below in Figure 3.

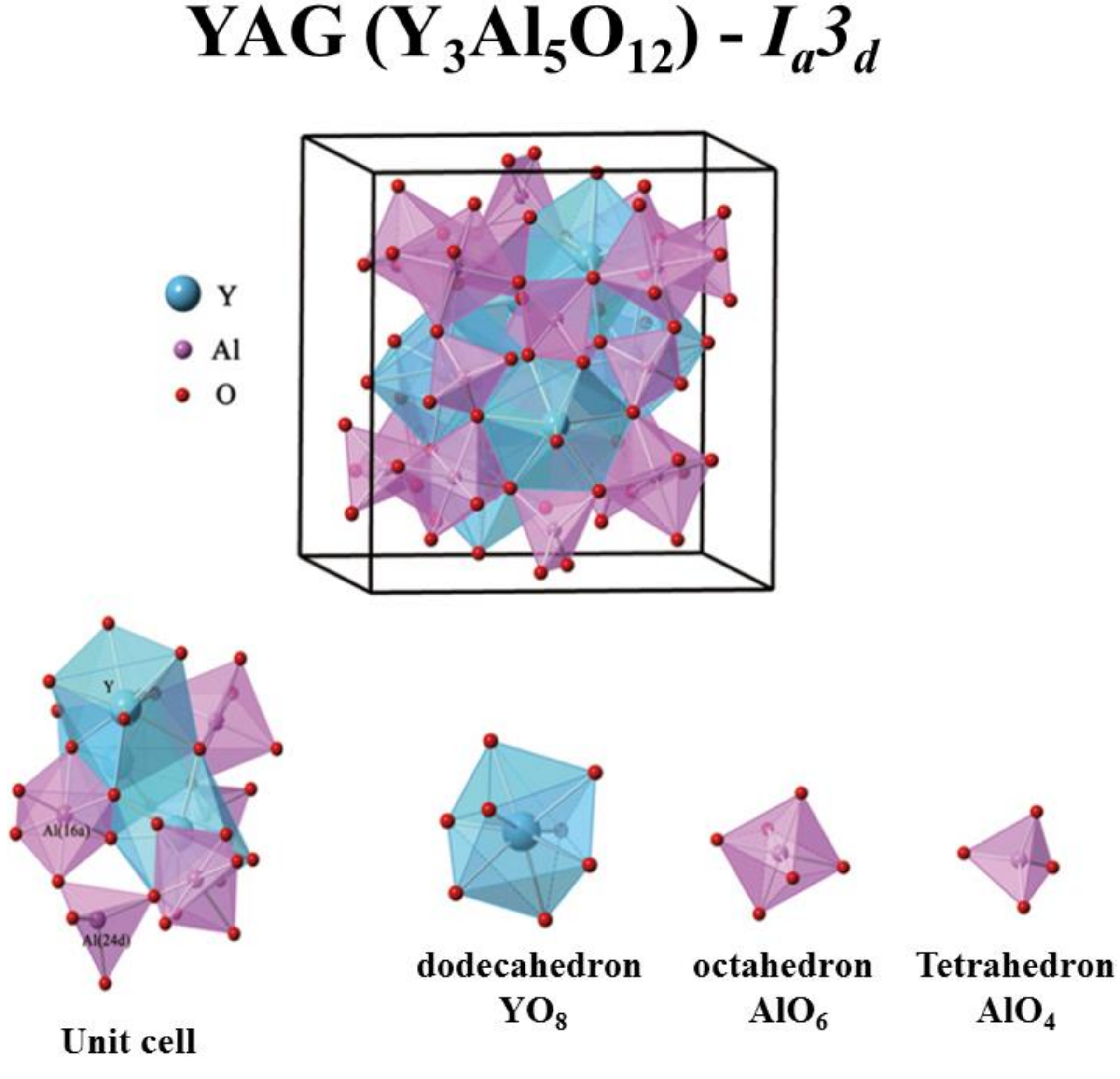

Figure 3. Crystal structure, unit cells and point group of YAG [6].

The general formula of the complex structure formed by the crystallization of the YAG is $\{\mathbf{A}\}_3[\mathbf{B}]_2(\mathbf{C})_3O_{12}$, where the cations are represented by **A**, **B** and **C** (Y, Al and Al) present oxygen coordination number equal to 8, 6 and 4, as can also be seen in the Figure 3 (YO_8, AlO_6 and AlO_4) [6]. As already shown, YAG has a space group I_a3_d (Oh) where ions with higher radius values (**A**) occupy distorted dodecahedron sites, while the smaller ions (**B**) occupy octahedral sites [37].

As already mentioned, when YAG is doped with Ln ions, the resulting materials have important applications in the optical and photonic fields; for example, Ce^{3+}:YAG [7] and Eu^{3+}:YAG phosphors have been widely studied and employed in efficient devices that generate white light [38]. Furthermore, YAG stands out as host matrix for Er^{3+} and Nd^{3+}, which are usually applied as active media for solid-state lasers [37]. The Nd^{3+}:YAG laser has over 50 years of history [10]. It has been the most commonly used material in commercial solid-state lasers because it combines the advantageous properties of the inserted Nd^{3+} ion and YAG matrix, that presents good transparency, high melting point, high thermal conductivity, low thermal expansion coefficient, chemical stability, and hardness [39]. There are numerous studies about this material, which can be obtained by various synthesis routes such as solid-state synthesis [37], sol-gel process [40], co-precipitation [6], and flame pyrolysis [41], among other methods. In the specific case of RL applications, high Ln ion content is required to improve the emission gain [37], but some synthesis methodologies could form clusters, leading to the luminescent properties being quenched. Herein, we prepared YAG (Ln^{3+}-doped according to the application of interest) in spherical particles by SP, a methodology that provides high yield and could be employed for large-scale production. For this, we prepared by sol-gel methodology boehmite suspension doped with rare earth ions (Y^{3+} and Nd^{3+} or Yb^{3+}/Er^{3+} or Yb^{3+}/Tm^{3+}), and this suspension was used as a precursor in SP synthesis. The precursor and the method employed are discussed in more detail in the next topics.

1.1.1.1. Boehmite – the precursor

The mineral boehmite, as already mentioned, is one of the three economically important mineral components of bauxite, and presented form γ-AlO(OH). This mineral, as well as the others that make up bauxite, contain hydroxyls within its structure and are transformed into aluminum oxide in different metastable polymorphic phases, after thermal treatment or dehydration. In the laboratory, this compound can be prepared by hydrothermal treatment of $Al(OH)_3$, or through sol-gel methodology from hydrolysis and condensation reactions of aluminum salts or alkoxides obtaining stable and transparent colloidal suspensions [4,42]. This methodology was used in this work to obtained rare earth doped boehmite, which was applied as a precursor in the synthesis of the particles. Its structure (Figure 4) presents an orthorhombic unit cell with 4 AlOOH units (space group D_{2h}^{17}). Each aluminum atom is surrounded by oxygen atoms in a distorted octahedron, the layers represented in the image are joined by hydrogen bonds involving hydroxyl groups from a close layer [43].

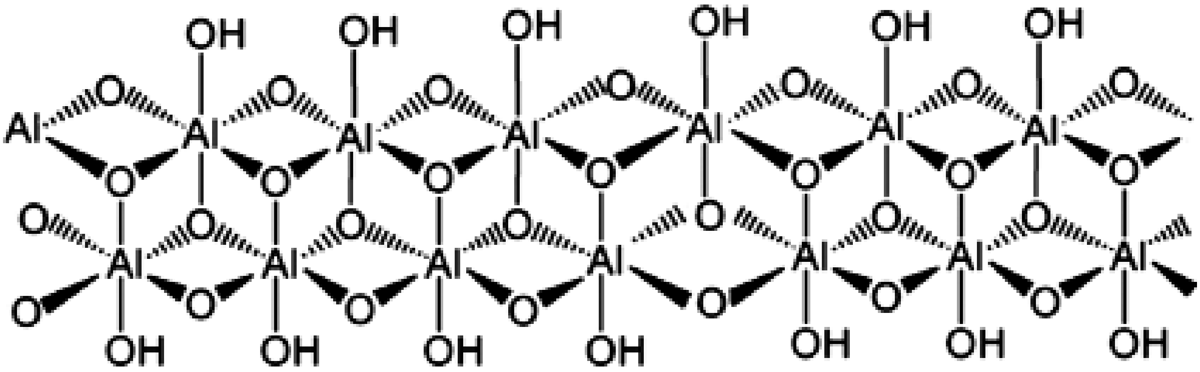

Figure 4. Drawing of the boehmite structure consisting double sheets of octahedral with Al ions at their center [43].

It is also possible to find the term pseudo-boehmite, which refers to aluminum monohydroxide of low crystallinity, named by Calvet in 1952. The X-ray diffractogram of this structure differs from that of crystalline boehmite by the relative intensities of the peaks [44]. In addition to the application already mentioned, this mineral is also used, in powder form, as a catalyst in the petrochemical industry as well as an adsorbent, optical and coating material [43].

1.1.1.2. Spray Pyrolysis – the method employed

A wide variety of powdered materials including metals, metal oxides, ceramics, phosphors, superconducting materials, fullerenes, and others can be obtained by aerosol pyrolysis technique [45], or **Spray Pyrolysis (SP)**. In addition, films can be prepared also, by deposition over a wide variety of substrates that can be easily adapted for industrial production processes [46]. This methodology provides high yield and could be employed for large-scale production. Additionally, SP generates few byproducts that are associated with the production of micro- and submicrometric spherical particles that do not coalesce, and can provide dense or hollow materials [1]. SP offers the advantage of not introducing impurities in the final product because there is no external contact with the precursors, and each drop constitutes a homogeneous mini reactor that has the same chemical composition as the initial solution. The system used for this methodology involves three main steps: aerosol generation, pyrolysis, and final product collection [4], and can be represented by the scheme in Figure 5.

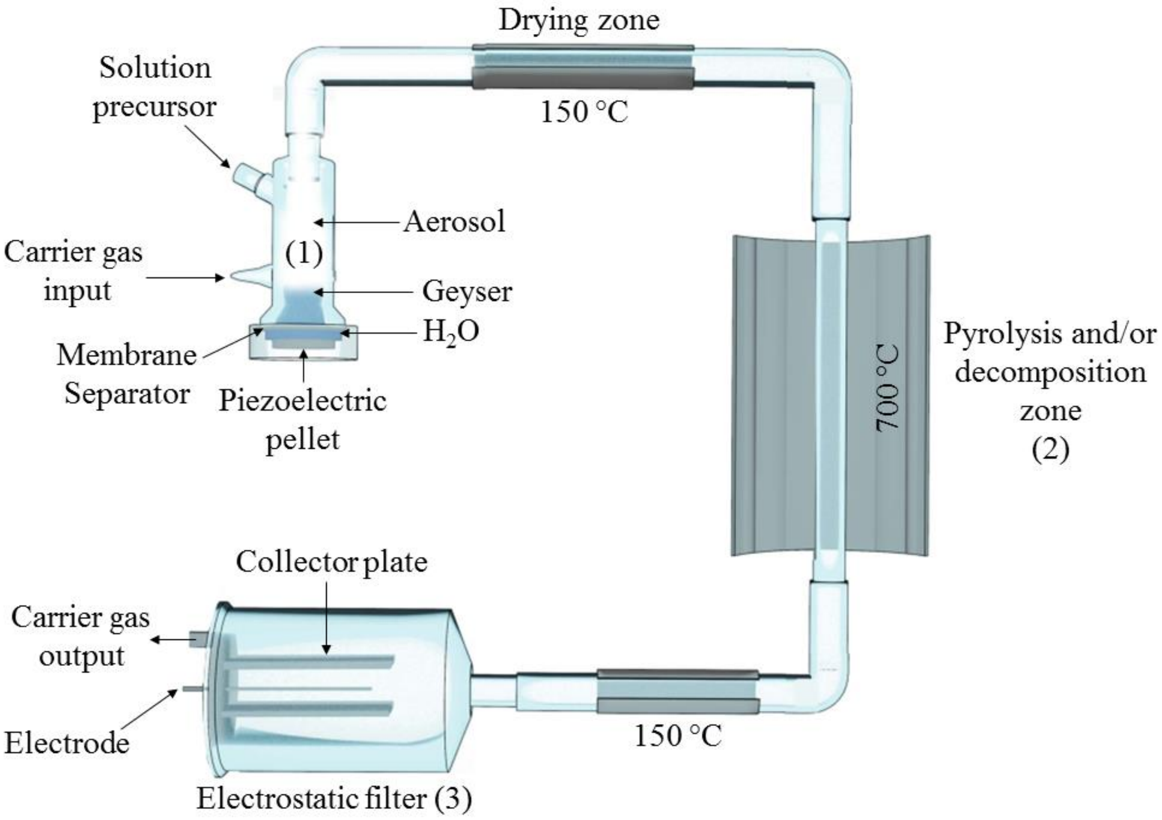

Figure 5. SP experimental setup.

The aerosol can be generated by different methods. In the system in Figure 5, the aerosol is originated in the ultrasound chamber. In this first step **(1)** a 2.4-MHz frequency piezoelectric pellet is used to generate an ultrasound field in the precursor solution (boehmite suspension, in this work specifically), and the propagation of these waves causes a succession of comprehension and dilation waves to appear inside the liquid, leading to the phenomenon of cavitation. So, micro drops are ejected from the surface of this liquid, forming a geyser due to the applied ultrasound. The cavitation, during this aerosol production step, depends on different factors such as: ultrasonic frequency, liquid surface tension, viscosity and solution temperature. A solvent suitable for ultrasonic nebulization needs to have low surface tension and viscosity. In addition, the particle size distribution of the aerosol, which will be an important parameter in defining the size and shape of the grain of the dry material, depends directly on the aerosol generation mode and the concentration of the precursor; when the aerosol is generated by ultrasound, the droplet size depends on the frequency of the tablet used, and the particle diameter (**PD**) can be calculated by [47]:

$$\mathbf{PD} = \sqrt[3]{\frac{\mathbf{C.M}}{\mathbf{d}}}.\mathbf{DD}$$ **Equation 1**

C: molar concentration of the final product in the solution, **M**: mass molar of the final product, **d**: apparent density of the final product, and **DD** diameter of the drop.

Next, the aerosol formed is carried through the two heat-treatment zones, the drying zone (with milder temperature, 150 °C in the represented case) and the pyrolysis zone **(2)** (higher temperature - 700 °C, in this case), by gas flow. In the drying zone, the solvent is evaporated and initial precipitation occurred; and in the decomposition or pyrolysis zone, the desired material is obtained by fast thermal treatment. In the third and last step **(3)**, the product formed is collected in an electrostatic filter operating at 11 kV and 150 ºC to avoid water condensation. The carrier atmosphere may present reactive interactions with the droplet, so the nature of the gas can generate or not a specific reactive interaction on the nebulized precursor [1,2,4,46]. Herein, the atmospheric air was not a trouble when used as a carrier gas because the precursor was obtained by hydrolysis in a water medium on atmospheric air and the desired crystalline phases were attained by dehydration process and structure organization.

As mentioned, the morphology of the particles depends on the composition of the starting solution, which can then be controlled, since each drop of aerosol can be seen as a mini reactor. In Figure 6, we can see two possibilities of particles formation: one, where the drying of the drop occurs with consequent precipitation of material on the surface of this drop, which can lead to the formation of hollow spheres or broken particles; and another, where drying is accompanied by polymerization of the precursor, leading to the formation of dense spherical particles [45].

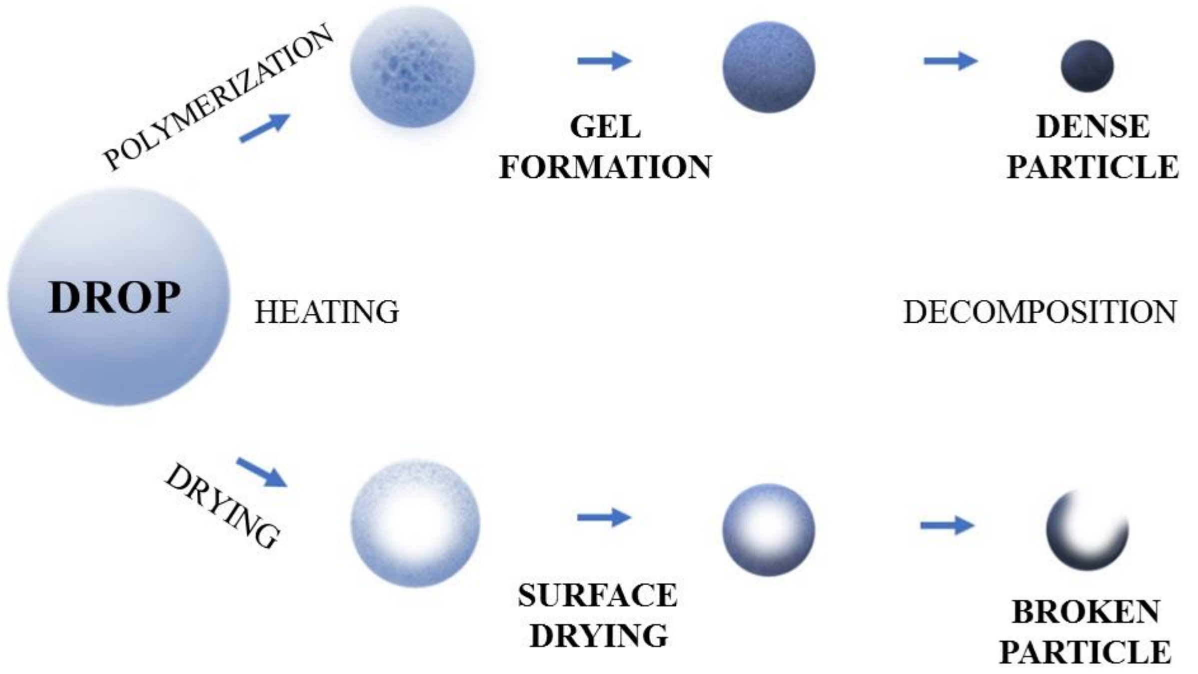

Figure 6. Particle formation process by SP [45].

The formation of solid particles is favored by the use of soluble, low concentrated and low volatile precursor solution, which pass through the furnace for a long time. The hollow particles will be formed as a result of the creation of a concentration gradient of the solute during the evaporation of the solvent in the drop. If there is not enough time for the solute to diffuse into the drop, it will precipitate on its surface. After this, two hypotheses are possible: the solid layer formed on the surface is impermeable to the solvent, resulting in particle fragmentation due to the internal pressure of the drop; or formation of hollow solid particles, if this pressure is not very high and the gases are trapped inside the particle [4,45].

1.2. The Rare Earth

The group of 17 chemical elements known as **‘Rare Earths’ (RE)** is composed of the metals scandium (Sc, Z=21) and yttrium (Y, Z=39), in addition to the group of **Lanthanides (Ln)**, located in period 6 of the periodic table and that includes all the elements from lanthanum (La, Z=57) to lutetium (Lu, Z=71) [12,48], as can be seen in the table represented in Figure 7.

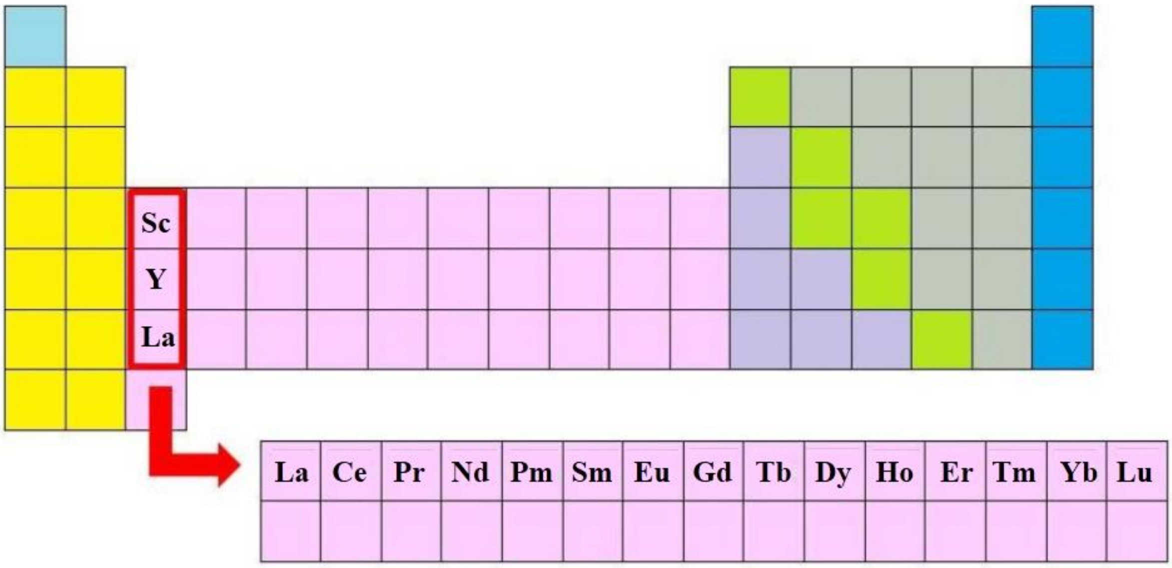

Figure 7. Periodic table showing the position and composition of the RE group.

The name ‘rare earths’ appeared at the end of the 18th century, in Sweden, together with the findings of the first elements of this group, with the term ‘earth’ referring to the fact that, at the time, these elements were found in the form of oxides, while that ‘rare’ is a mention to these having been found only in some regions of this country, close to Ytterby. Currently, it is known that this designation brings a false idea about this group of elements, which cannot be considered ‘earths’, as they are metallic in nature, and not ‘rare’, as they have a considerably high abundance. Thulium (Tm), for example, the least abundant Ln of the group, is more abundant than elements such as cadmium (Cd), mercury (Hg), silver (Ag), among others, while the most abundant lanthanide, cerium (Ce), is found in amounts similar to zinc (Zn) [48,49].

In nature, RE can be found in the composition of many minerals, monazite ($(TR, Th)PO_4$) being the most important of them, and together with xenothym ($TRPO_4$), gadolinite ($Be_2FeTR_2Si_2O_{10}$), alanite ($(Ca, TR)_2(Al, Fe, Mn, Mg)_3(SiO_4)_3(OH)$), bastnasite ($TRFCO_3$), euxenite ($(Ca, TR)(Nb, Ta, Ti)_2O_6$) and apatite ($(Ca, TR)_5(P, Si(O_4)_3(O, F)$) forms the group with the greatest commercial interest [48]. The world's largest reserve of RE (approximately 60 million tons) is located in China, a country that since the 1990s has been the leader in this market, selling around 95% of RE products. On the other hand, Brazil has a reserve half the size of the Chinese one, which still represents a considerable amount of these elements [49,50].

Despite having their names little known outside the academic environment, RE are widely present in our daily life in the composition of the most diverse types of materials, such as magnets, catalysts (mainly intended for oil cracking and pollutant reduction systems in automobiles), polishes, battery alloys, glass, phosphors ceramics, among others, as shown in Figure 8. Among the luminescent materials obtained based on RE, we can mention optical markers, LEDs (light-emitting diodes) and OLEDs (organic light-emitting diodes), fluorescent lamps, displays, cathode ray tubes, lasers, among others; which are widely used in various areas such as lighting, medicine, and security [48,51].

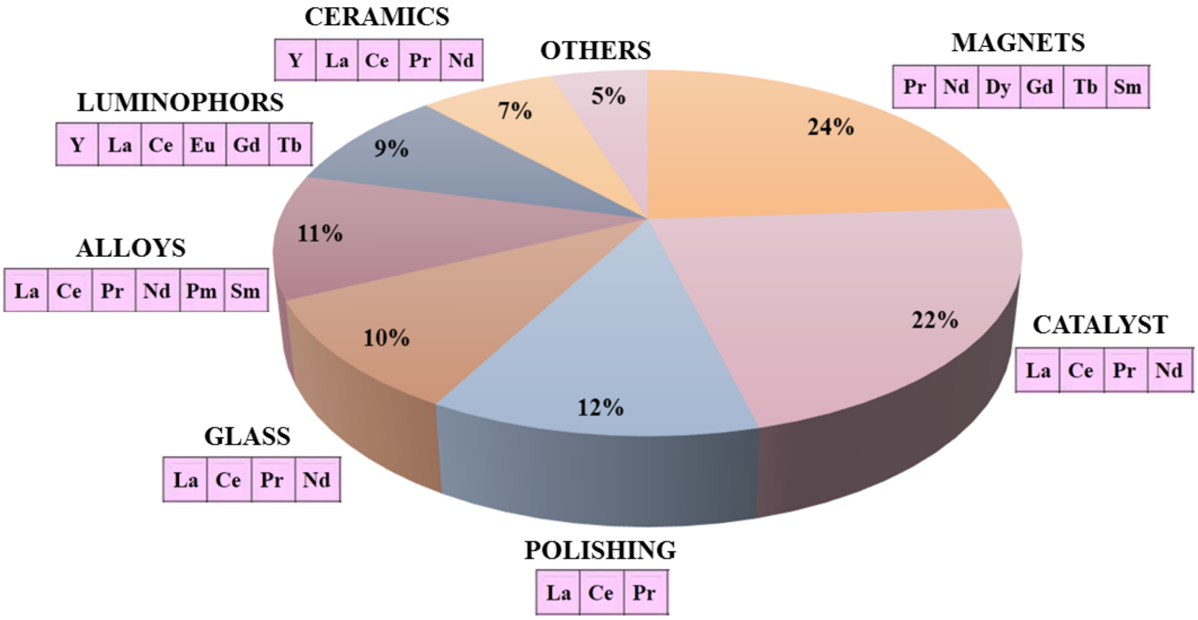

Figure 8. Graphic representing the main uses of RE, in percentage, and the main elements present in each one of them [49].

A difficulty encountered when working with RE, as the history of the discovery of these elements reports, is in the separation between them. This is due to the high chemical similarity existing between such elements and their subtle differences with regard, for example, to solubility and complex formation. RE elements are commonly classified between ‘light’ and ‘heavy’, the first group consisting of elements from lanthanum (La) to europium (Eu) (with the exception of promethium (Pm)), and the second by those located between gadolinium (Ga) and lutetium (Lu). However, despite this ‘classification’, all the constituent elements of this group are generally found in the 3+ oxidation state (forming RE^{3+} or Ln^{3+} species, in the case of lanthanides), and have very close ionic radius values, which leads to simultaneous occurrence of more than one RE element in its minerals. Thus, until the mid-twentieth century scientists worked exhaustively in an attempt to obtain these elements separately, but only the metals Ce and Eu were obtained with some ease and in significant quantities [12,48]. However, the Manhattan Project, started in 1939 during World War II, invested a great deal of attention to these elements and different separation methods such as ion exchange chromatography were employed in the separation of Ln, which made it possible to obtain them in a pure form, and in increasing amounts [52,53], thus enabling the development of the chemistry of these elements, until we reach what we know today.

1.2.1. Spectroscopic properties of lanthanide ions

The ground state electron configuration of the neutral Ln elements has the form [Xe] $6s^2$, $4f^n$, $5d^x$ (following the energetic order). The value of **n** can be comprised between 0 and 14 ($0 \leq \mathbf{n} \leq 14$), and that of **x** be equal to 1, for the elements La, Ce, Gd and Lu; or equal to 0 for the other metals in the series [48,54]. As already mentioned, all the constituent elements of the RE group are generally found in the 3+ oxidation state, and form oxides of the RE_2O_3 type [55]. However, some elements may have 2+ and 4+ oxidation states (less stable than 3+), such as Sm^{2+} ([Xe] $4f^6$), Eu^{2+} ([Xe] $4f^7$), Tm^{2+} ([Xe] $4f^{11}$), Yb^{2+} ([Xe] $4f^{14}$), Ce^{4+} ([Xe] $4f^0$), Pr^{4+} ([Xe] $4f^1$), and Tb^{4+} ([Xe] $4f^7$). The greater stability found in the 3+ form, for all Ln, is clear in the cases of La, Ce, Gd and Lu, since for these metals we have **x**=1, and, therefore, the removal of 3 electrons occurs in the 6s and 5d orbitals; the La^{3+} ion has an electronic configuration equal to that of the noble gas xenon, which is the most stable Ln^{3+} ion found, followed by Gd^{3+}, which has partially filled 4f orbitals, and Lu^{3+} with full filling of these orbitals. In the case of others, with a value of **x** equal to 0, the formation of the trivalent cation leads to a configuration of the type [Xe] $4f^{\mathbf{n-1}}$ after the loss of 2 electrons located in 6s and 1 electron in 4f. The loss of this 4f electron, in preference to the more external 5s or 5p orbitals, is explained by the fact that these, despite their external character, present greater penetrability to the nucleus, when compared to the f orbitals, as can be seen in Figure 9, where we observe that the radial distribution of probability for these orbitals, unlike the others represented, do not present maximums close to the nucleus. Thus, although 4f electrons are internal in nature, the low penetrability of orbitals makes them more ‘available’ when compared to electrons located in 5s or 5p [48,54,56].

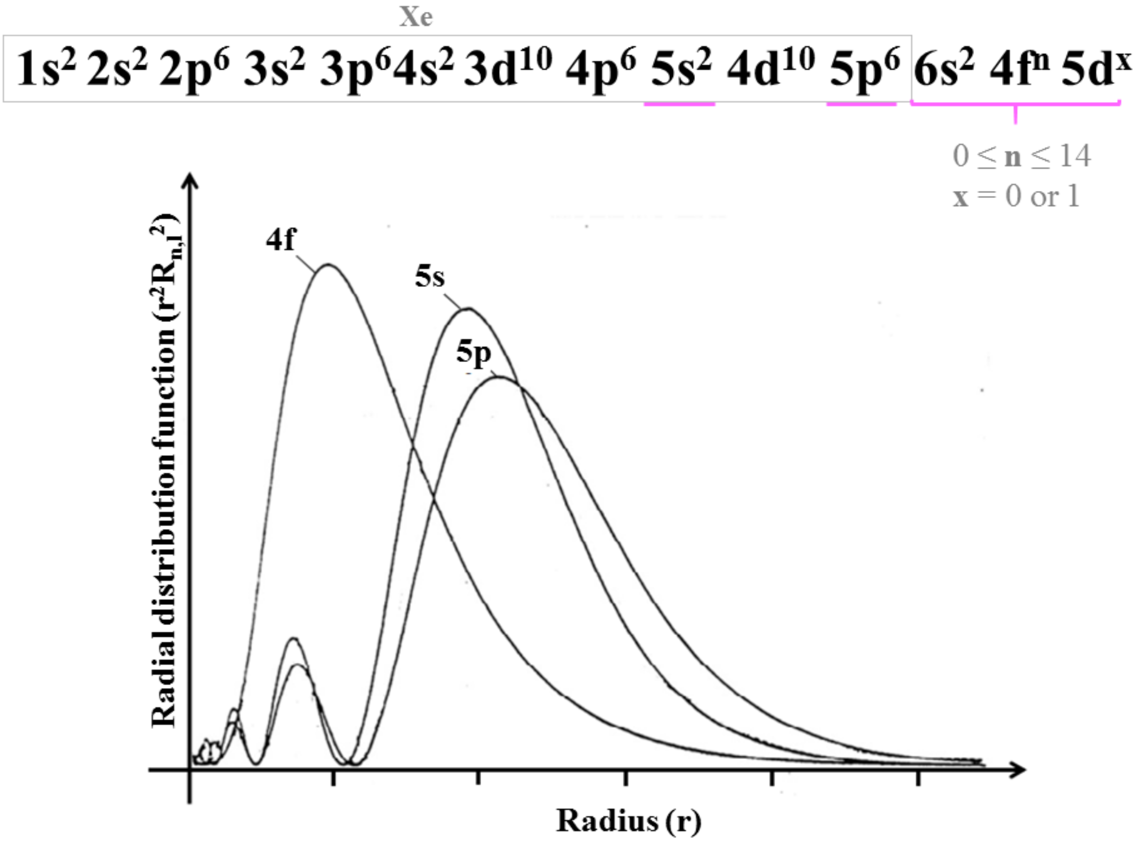

Figure 9. Generic electronic distribution of the Ln elements, and radial distribution function for the 4f, 5s and 5p orbitals of the Nd^{3+} ion [54].

Also, through the illustration represented in Figure 9, where we have the electronic distribution and radial distribution functions for the Ln, it is possible to explain the phenomenon known as ‘lanthanide contraction’, which deals with the progressive decrease of the atomic and ionic radius of these elements to as the atomic number increases. With this increase, there is a progressive filling of the f orbital, which is diffuse and, therefore, has less shielding effect to the nuclear charge. Consequently, on the electrons more external to those located in the 4f orbital, the effective nuclear charge is high, resulting in a more intense attraction on these electrons (5s and 5p) and a consequent decrease in the radius. This is one of the effects responsible for the high chemical similarity existing between the elements of the series, as already mentioned [48].

Due to the high charge/radius ratio observed in the formed RE cations, these are classified as hard acids, according to Person's theory, and therefore bind preferentially to hard ligands (bases), forming their complexes [57]. Regarding the small size of the ionic radius (which are around 80-100 pm), these complexes are commonly formed with high coordination numbers, going through 8-9 and reaching up to 12, and the character of the established bonds is predominantly ionic, due to the internal character of the f orbitals [12,48].

The internal location of these orbitals, despite their low penetrability, will still result in a shielding effect of them, in relation to the external environment, by the outermost 5s and 5p orbitals (in ionic form), making the 4f orbitals little affected by the ligand field and because of this, it presents narrow bands resulting from the f-f transitions in its electronic spectra, contrary to what was observed for the metals of the d block, and giving unique characteristics to the Ln elements. Another characteristic associated with these metals, and also contrary to what was observed for the d block elements, is the non-directional character of the 4f orbitals in relation to the assumed coordination geometries which are determined only by steric factors, in order to minimize the repulsion between the ligands, mainly due to the fact that, once again, these electrons are of an internal character and with a low orbital overlap in the bonds [58,59].

Due to the fact that the position of the 4f electronic levels of these Ln^{3+} ions are lightly affected by the ligand field, they can be represented in a way that applies to any chemical environment, in an almost universal way, through the partial energy level diagrams elaborated by Dieke and Carnall [60], and represented in Figure 10.

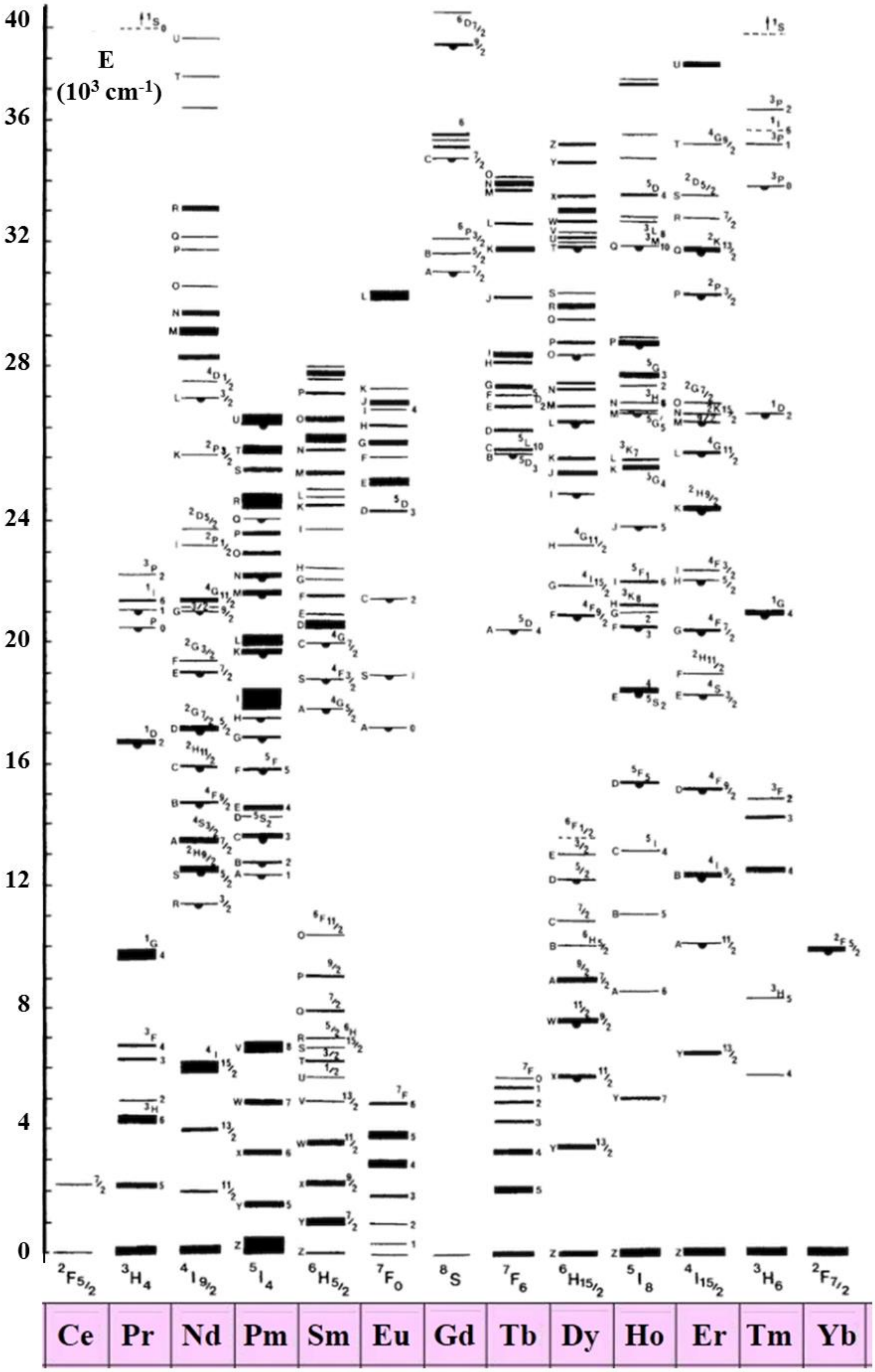

Figure 10. Partial diagram of energy levels for trivalent Ln ions (from Ce to Yb) [60].

An electron configuration of a multielectronic system can be represented through a spectroscopic term of form $^{(2S+1)}L_J$, which brings together in a unique way the quantum numbers of angular momentum involved in it. As noted in the representation term, these numbers are made up of the quantum numbers of total orbital angular momentum (**L**), total spin (**S**) and total angular momentum (**J**). The first one, quantum number of total orbital angular momentum, represented by L, is the result of the combination of the orbital angular momentum (*l*) of each electron, and can assume integer values of 0, 1, 2, 3... that are represented by the letters S, P, D, F... The total spin quantum number, **S**, consists of the sum of the spins (*s*) of the electrons, and has multiple values of ½. However, in the notation of the spectroscopic term it is represented by the multiplicity (**2S+1**) and, therefore, assumes entire values giving the systems the notations singlet (1), doublet (2), triplet (3), etc. Finally, the quantum number of total angular momentum, represented by **J**, is a combination of the others already mentioned, **L** and **S**, known as spin-orbit coupling (**LS**) and assuming values from (**L+S**) to (|**L-S**|). In the case of Ln, this coupling occurs intensely, and, regardless of the ligand field, the terms $^{(2S+1)}L$ are non-degenerate [58]. In Figure 11, we can see the different degrees of disturbances that can act in a $4f^n$ configuration.

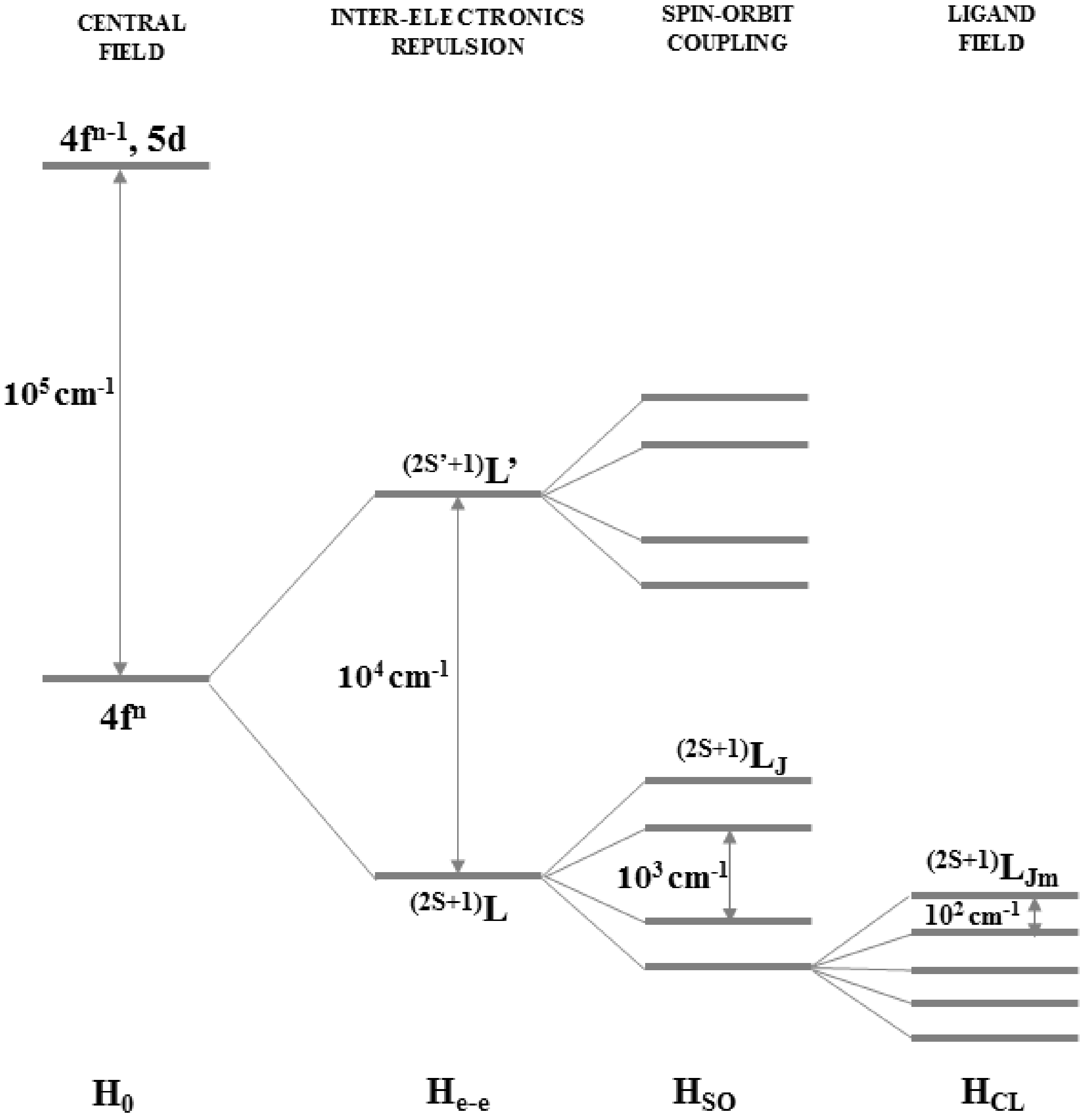

Figure 11. Schematic of the main perturbations under the $4f^n$ configuration and their magnitudes.

The energy levels of a Ln ion, or atom, can be described, in general, by the Schröedinger equation:

$$\mathbf{H\Psi = E\Psi} \qquad \textbf{Equation 2}$$

For the free ion, the energy levels can be used by a Hamiltonian (**H**), considering an interaction resulting from the central field ($\mathbf{H_0}$), the interelectronic repulsion ($\mathbf{H_{e\text{-}e}}$) and the spin-orbit interaction ($\mathbf{H_{SO}}$), which give to the form levels $\mathbf{^{(2S+1)}L_J}$, already mentioned, and that can be represented as follows:

$$\mathbf{H} = \mathbf{H_0} + \mathbf{H_{e-e}} + \mathbf{H_{SO}}$$ **Equation 3**

The first of them, central-field Hamiltonian, represented by $\mathbf{H_0}$, depends on the principal and azimuthal quantum numbers and is related to the electronic configuration of the system. This one separates the configurations into energies of approximately 10^5 cm^{-1}, but its perturbation does not remove the degeneracy of the 4f configuration, as it has spherical symmetry. Taking into account, for each ion, the energies of the possible electronic configurations, $\mathbf{H_0}$ can be described as:

$$\mathbf{H_0} = -\frac{\hbar^2}{2m}\sum_i \nabla_i^2 - \sum \frac{ze^2}{ri}$$ **Equation 4**

As the central field Hamiltonian is disturbed due to interelectronic repulsion ($\mathbf{H_{e-e}}$) and spin-orbit coupling ($\mathbf{H_{SO}}$), the free ion Hamiltonian ($\mathbf{H_{IL}}$), in turn, is given by:

$$\mathbf{H_{IL}} = \mathbf{H_0} + \mathbf{H_{e-e}} + \mathbf{H_{SO}}$$ **Equation 5**

The term that represents the system's interelectronic repulsion, $\mathbf{H_{e-e}}$, since it is a multielectronic case, is responsible for removing the degeneracy of the configuration, generating the terms $^{(2S+1)}\mathbf{L}$, which are separated by approximately 10^4 cm^{-1} in energy. $\mathbf{H_{e-e}}$ is described in terms of Racah's parameters and takes the form:

$$\mathbf{H_{e-e}} = \sum_{i>j=1} \frac{e^2}{r_{ij}} \sum_{i>j=1} \frac{e^2}{r_{ij}}$$ **Equation 6**

Finally, the spin-orbit coupling ($\mathbf{H_{SO}}$), which removes the degeneracy of the $^{(2S+1)}\mathbf{L}$ levels, generating the levels $^{(2S+1)}\mathbf{L_J}$, in relation to the (**2S+1**) **J** components and separated by energies of approximately 10^3 cm^{-1}, is described by:

$$\mathbf{H_{so}} = \sum_{i=1}^{n} \xi(r_i)(l_i . s_i)$$ **Equation 7**

After insertion into a ligand field, the symmetry adopted by the Ln ion is no longer spherical. The degeneracy of the levels $^{(2S+1)}\mathbf{L_J}$ is broken down into (**2J+1**) components, depending on the medium occupied, generating the levels $^{(2S+1)}\mathbf{L_{Jm}}$, and these generated levels are called Stark components and separated by energies of approximately 10^2 cm^{-1}. When the value of **J** is an integer (in which case the number of electrons located in the 4f orbital is an even number) the degeneracy is **2J+1**, in the case of semi-integer values of **J** (odd number of electrons) it is **2J+1/2**. Thus, adding the Hamiltonian that describes the free ion ($\mathbf{H_{IL}}$) to the term $\mathbf{H_{CL}}$ that describes the occupied ligand field, we have the description of the system through the Hamiltonian **H**, in the form [58]:

$$\mathbf{H = H_{IL} + H_{CL}} \qquad \textbf{Equation 8}$$

Based on the fundamental information to understand the $^{(2S+1)}\mathbf{L_j}$ notation, which describes an electronic state of a multielectronic system, as already mentioned, we will now deal with the luminescence phenomenon (or photoluminescence, more specifically) resulting from the transition between two of these states.

Luminescence could be defined as the photon emission resulted from electronic transition between excited levels and low energy states. This process can occur as a result of different kinds of excitation process that are reflected in the expressions photo-, chemo-, tribo-, fractoluminescence, among others. Photoluminescence, for example, occurs when the source of excitation is photons. And generally, luminescence processes are classified in books with respect to the nature of the electronic transitions involved, as fluorescence and phosphorescence [61].

Taking into account the $^{(2S+1)}\mathbf{L_j}$ notation, the first condition for a transition between two states to be allowed is the conservation of the total angular momentum, that is $\mathbf{\Delta J=0}$, +/-1. Furthermore, the total spin must be conserved, and then $\mathbf{\Delta S=0}$, while the total angular momentum must be $\mathbf{\Delta L=0}$, +/-1. Finally, with respect to the parity of the wavefunctions of their final and initial states, an electric dipole transition will be allowed if there is a change in these parities, a condition known as the Laporte rule [61].

Another important concept that should be mentioned when talking about luminescence is the so-called Stokes shift, which is nothing more than the observed difference between the absorption and emission maxima. The magnitude of this shift may be associated with the nature of the chemical environment and the structural characteristics of the species involved [61].

For Ln ions in centrosymmetric sites, transitions by an electric dipole mechanism between the different levels of the $4f^n$ configurations are prohibited by parity and, in some cases, by spin. However, there are several f-f transitions that have greater intensities than expected whereas they are prohibited. Thus, in the second half of the 20th century, Judd and Ofelt independently proposed that the f-f transitions must occur through a forced electric dipole mechanism. They proposed a theory where they consider the environment around the central ion to be a static disturbance to this free ion, while the interactions between electrons located in different configurations are negligible. With this, from the approximations and considerations suggested by the Judd-Ofelt theory, new selection rules emerge for the J↔J' transitions observed in Ln ions and are described as: **$\Delta S=0$**, **$\Delta l=+/-1$**, **$\Delta L\leq 2l$** and **$\Delta J\leq 2l$** (that is, for f-f transitions, **$\Delta L\leq 6$**), and, finally, if **$J=0$**, J' is pair, while if **$J'=0$**, J is pair [55,58,62].

The group of RE elements present a great versatility regarding possible applications. In Table 4, some relevant information for Ln^{3+} ions is summarized, and Figure 12 represents the emission profile for complexes formed by some of these ions.

Table 4. Atomic radius, electronic configuration, main excited states, end states, approximate wavelengths of the most intense emission lines, and their regions, for the main trivalent ions [56]

Ln^{3+}	**ATOMIC RADIUS**	**ELECTRONIC CONFIG.**	**EXCITED STATE**	**END STATE**	**λ (nm)**	**EMISSION**
Pr^{3+}	101 pm	[Xe] $4f^2$	$^1G_4$	^3H_J (J=4-6)	1300	NIR
			$^1D_2$	^3F_J (J=2-4)	890,1060	NIR
			$^3P_0$	^3H_J (J=4-6)	525-680	Orange
Nd^{3+}	100 pm	[Xe] $4f^3$	$^4F_{3/2}$	^4I_J (J=9/2-15/2)	1060	NIR
Sm^{3+}	96 pm	[Xe] $4f^5$	$^4G_{5/2}$	^6H_J (J=5/2-15/2)	590	Orange
Eu^{3+}	95 pm	[Xe] $4f^6$	$^5D_0$	^7F_J (J=0-6)	620	Red
Gd^{3+}	94 pm	[Xe] $4f^7$	$^6P_{7/2}$	$^8S_{7/2}$	312	UV
Tb^{3+}	93 pm	[Xe] $4f^8$	$^5D_4$	^7F_J (J=6-0)	550	Green
Dy^{3+}	91 pm	[Xe] $4f^9$	$^4F_{9/2}$	^6H_J (J=15/2-5/2)	570	Yellow

Ho^{3+}	89 pm	[Xe] $4f^{10}$	$^5F_5$	$^5I_{J\ (J=8-4)}$	970, 1450	NIR
			$^5S_2$	$^5I_{J\ (J=8-4)}$	540	Green
Er^{3+}	88 pm	[Xe] $4f^{11}$	$^4S_{3/2}$	$^4I_{J\ (J=15/2-9/2)}$	550	Green
			$^4I_{13/2}$	$^4I_{15/2}$	1530	NIR
Tm^{3+}	87 pm	[Xe] $4f^{12}$	$^1G_4$	$^3H_{j\ (J=6-4)}$	450	Blue
Yb^{3+}	86 pm	[Xe] $4f^{13}$	$^2F_{5/2}$	$^2F_{7/2}$	980	NIR

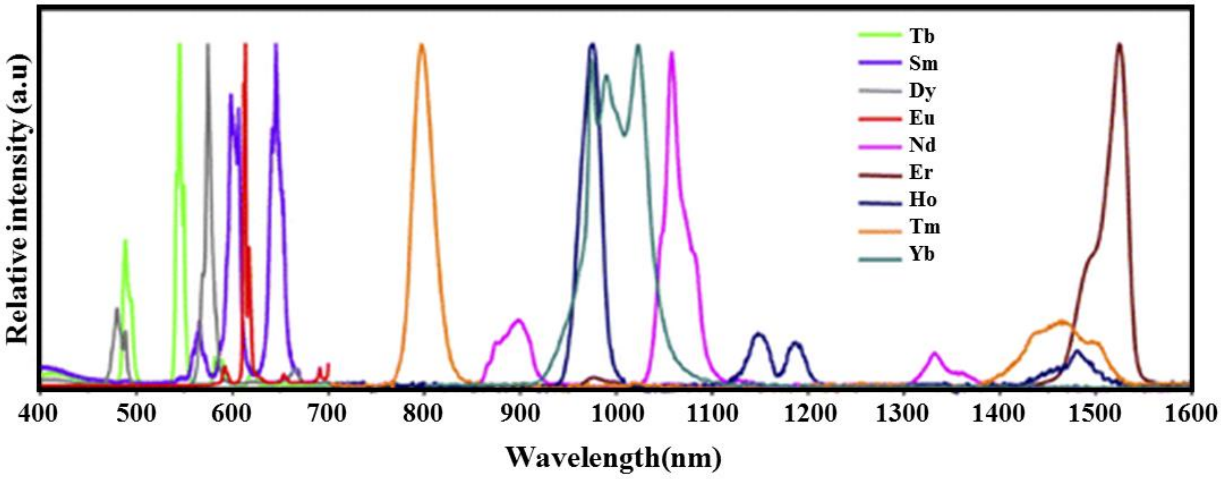

Figure 12. Representation of the emission profile and characteristic regions for some Ln ions [63].

Now, we will focus more specifically on the Ln^{3+} ions that were used in the development of materials during the execution of this work, in addition to the special case, the Eu^{3+} ion, widely used as a structural probe and in the development of phosphors.

1.2.1.1. The Eu^{3+} ion – a particular case

Europium is the seventh element in the Ln series, with an atomic number of 63 and a molar mass of 152 g/mol. The trivalent ion features electronic configuration [Xe] $4f^6$, and its emissions provide important commercial applications as they are widely applied in the production of phosphors[64].

The energy level diagram for the Eu^{3+} ion is represented in Figure 13, and it is a consequence of the central field interaction ($\mathbf{H_0}$), the interelectronic repulsion ($\mathbf{H_{RE}}$), and the spin-orbit interaction ($\mathbf{H_{SO}}$). The emissions commonly observed in the emission spectra of this ion consist of a set of lines in the red region, being assigned the transitions ${}^5D_0 \rightarrow {}^7F_J$ (**J=0-6**), represented by the arrows pointing downwards [59].

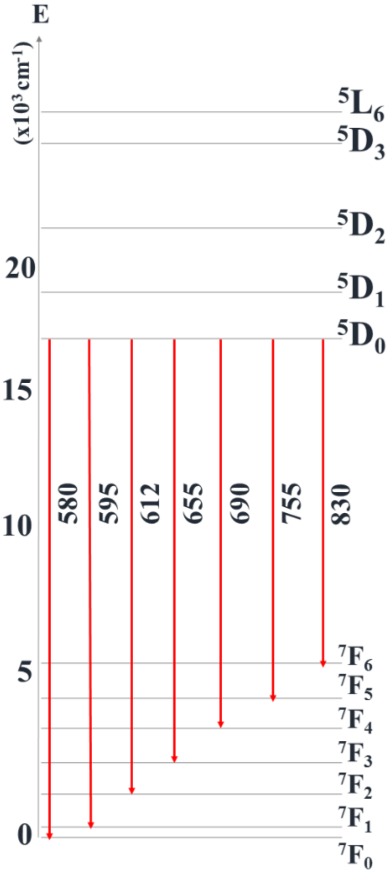

Figure 13. Partial diagram of energy levels for the Eu^{3+} ions and its ${}^5D_0 \rightarrow {}^7F_j$ transitions in visible region.

In addition to its technological importance, the characteristic transitions of the Eu^{3+} ions are also of great importance in the study of the spectroscopic characteristics of all the Ln ions, besides to being used in the study of the chemical environment in which the ion is inserted. This is possible because the emission level ${}^5D_0$ is not degenerated, and the band relative to the ${}^5D_0 \rightarrow {}^7F_1$ transition occurs by magnetic dipole (**MD**) mechanism and, therefore, its intensity does not depend on the crystalline field, so it could be used as a standard for intensity studies. The other bands occur by electric dipole (**ED**) mechanisms and are therefore dependent on the crystalline field. This fact exclusive to Eu^{3+} allows obtaining emission parameters for the studied systems, such as spontaneous emission coefficient and radiative lifetime, from the emission spectrum, taking the **MD**' transition as a reference; in addition to enabling the determination of the symmetry site of the ions, making the Eu^{3+} ion a structural probe [59]. In the emission spectrum represented in Figure 14, it is possible to observe the bands resulting from the transitions $^5D_0 \rightarrow {}^7F_J$ (**J=0-4**).

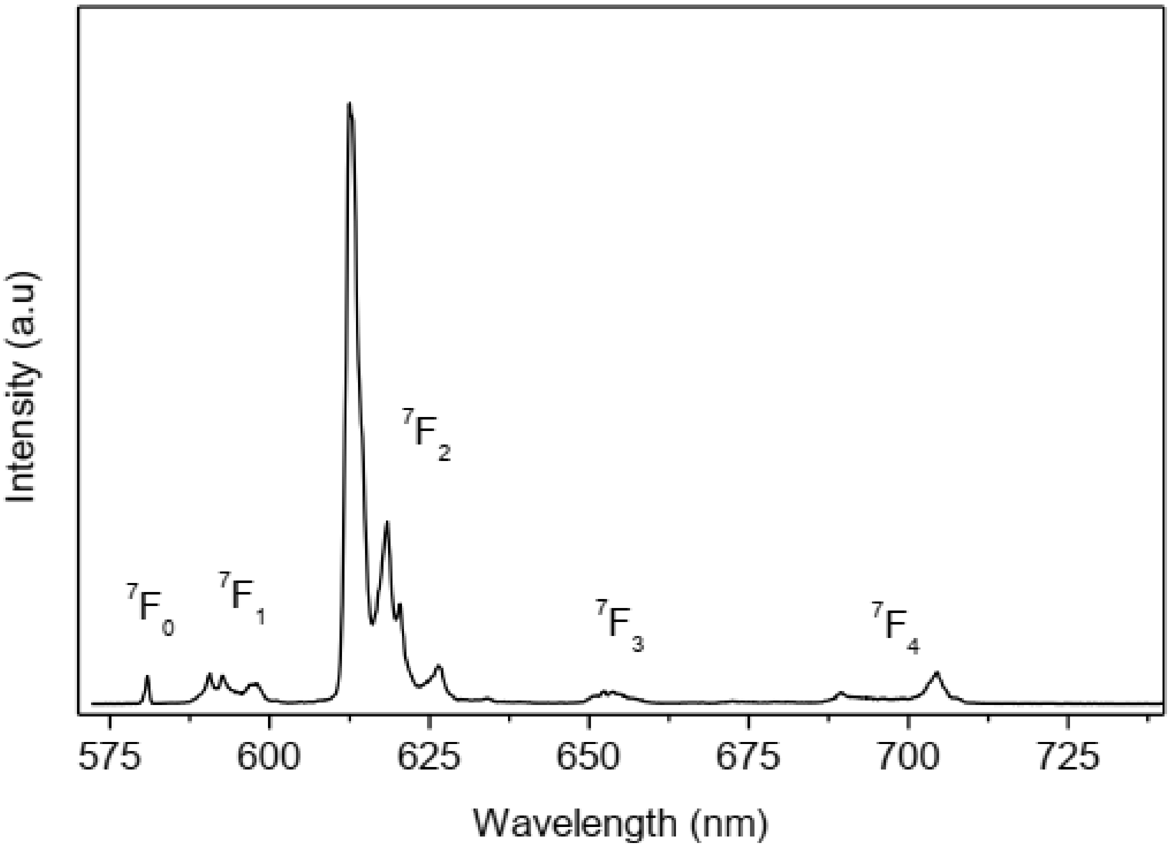

Figure 14. Luminescence spectrum [Eu(tta)$_3$(phen)] (λ_{ex}=396). All the transitions start from the $^5D_0$ state [59].

Table 5 presents an overview of the transitions observed in luminescence spectra of Eu^{3+} compounds, and its main information [59].

Table 5. Overview of the transitions (only starting from $^5D_0$ level), **ED**: induced magnetic dipole transition and **MD**: magnetic dipole transition, observed in luminescence spectra of Eu^{3+}compounds [59]

Transition	**Dipole Character**	**Wavelength Range (nm)**	**Relative Intensity**	**Remarks**
$^5D_0 \rightarrow {}^7F_0$	ED	570-585	very weak to strong	only observed in C_n, C_{nv} and C_s symmetry
$^5D_0 \rightarrow {}^7F_1$	MD	585-600	strong	intensity largely independent of environment
$^5D_0 \rightarrow {}^7F_2$	ED	610-630	strong to very strong	hypersensitive transition, intensity very strongly dependent on environment
$^5D_0 \rightarrow {}^7F_3$	ED	640-660	very weak to weak	forbidden transition
$^5D_0 \rightarrow {}^7F_4$	ED	680-710	medium to strong	intensity dependent on environment, but no hypersensitive

$^5D_0 \rightarrow {}^7F_5$	ED	740-770	very weak	forbidden transition
$^5D_0 \rightarrow {}^7F_6$	ED	810-840	very weak to medium	rarely measured and observed

Thus, the association of experimentally obtained spectra with theoretical data on each of the observed transitions can be a tool to determine the symmetry of the coordination environment in which the Eu^{3+} ion is inserted.

1.2.1.2. The Nd^{3+} ion – an important element for LASER studies

Neodymium is the element located in the fourth position of the Ln series, has an atomic number of 60 and a molar mass of 144 g/mol. The trivalent ion features an electronic configuration [Xe] 4f^3. This element is mainly used in the manufacture of magnets and solid-state lasers [10,65]. Its electronic states and main emissions, in Nd^{3+} form, are shown in the energy diagram in Figure 15.

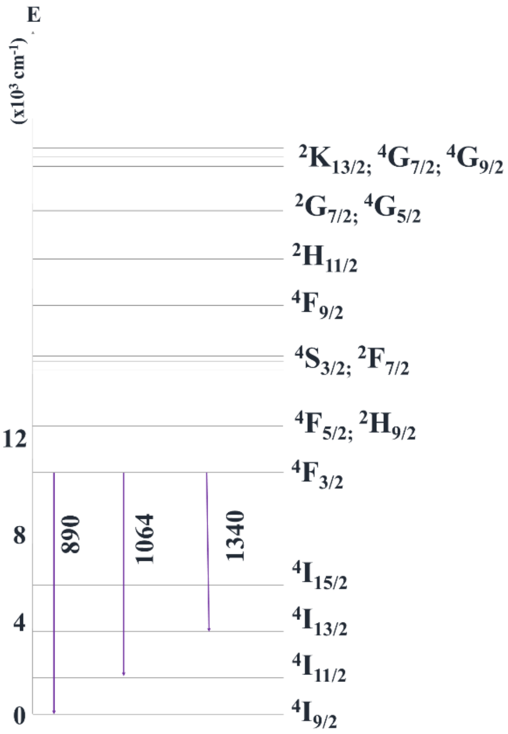

Figure 15. Partial diagram of energy levels for the Nd^{3+} ion.

The wide application in laser systems is due to the fact that Nd^{3+} has four energy levels, which facilitates the population inversion process because the lowest energy state of the laser transition is not the ground state of the ion, associated with absorption bands in the near infrared region ($^4I_{9/2} \rightarrow {}^4F_j$) and high emission efficiency for the $^4F_{3/2} \rightarrow {}^4I_{11/2}$ laser transition [12], shown more clearly in Figure 16.

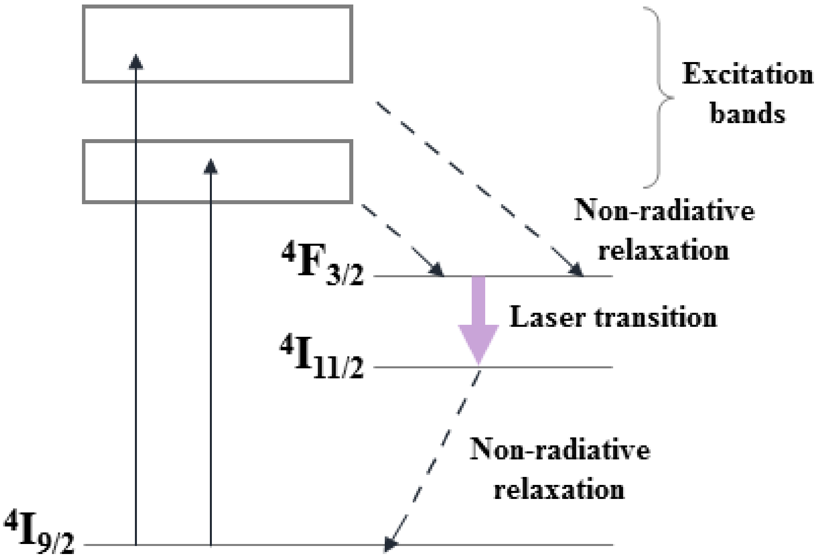

Figure 16. Partial diagram of energy levels for the Nd^{3+} ion. Focus on laser transition.

Besides being widely used for conventional lasers, Nd^{3+} ions in different matrices have been exploited as the gain medium for RLs, as reviewed in [39,66] and exploited in different matrices [67–69]. As already mentioned, the Nd^{3+}:YAG laser has over 50 years of history [10], it has been the most commonly used material in commercial solid-state lasers because it combines the advantageous properties of the YAG matrix and the inserted Nd^{3+}.

Moreover, $^4F_{5/2} \rightarrow {}^4I_{9/2}$ and $^4F_{3/2} \rightarrow {}^4I_{9/2}$ transitions (thermally coupled) have been widely studied in systems for measuring temperature [13,70–72]. This, together with the fact that this ion can be excited and emit within spectral regions called biological windows, makes it an important tool that provides information about the local temperature in tumor treatments [73], for example.

1.2.1.3. Yb^{3+}/Er^{3+} and Yb^{3+}/Tm^{3+} ions – important pairs for the up-conversion energy process

The element ytterbium is the penultimate element of the Ln series, has an atomic number of 70 and a molar mass equal to 173 g/mol. The Yb^{3+} ion has an electronic configuration [Xe]$4f^{13}$ and, therefore, it presents only one possible intra f-f transition, represented by $^2F_{7/2} \rightarrow {}^2F_{5/2}$, which occurs via excitation at 980 nm, as shown in Figure 17. The element erbium occupies the eleventh position in the Ln series and has an atomic number of 68 and a molar mass of 167 g/mol. Er^{3+} ion, in turn, with an electronic configuration [Xe]$4f^{11}$, presents intra f-f transitions in the visible and infrared regions. The latter, represented by $^4I_{13/2} \rightarrow {}^4I_{15/2}$, as shown in Figure 17 also, occurs at 1500 nm and is widely exploited in telecom [74] and also for systems aimed at biological applications [75].

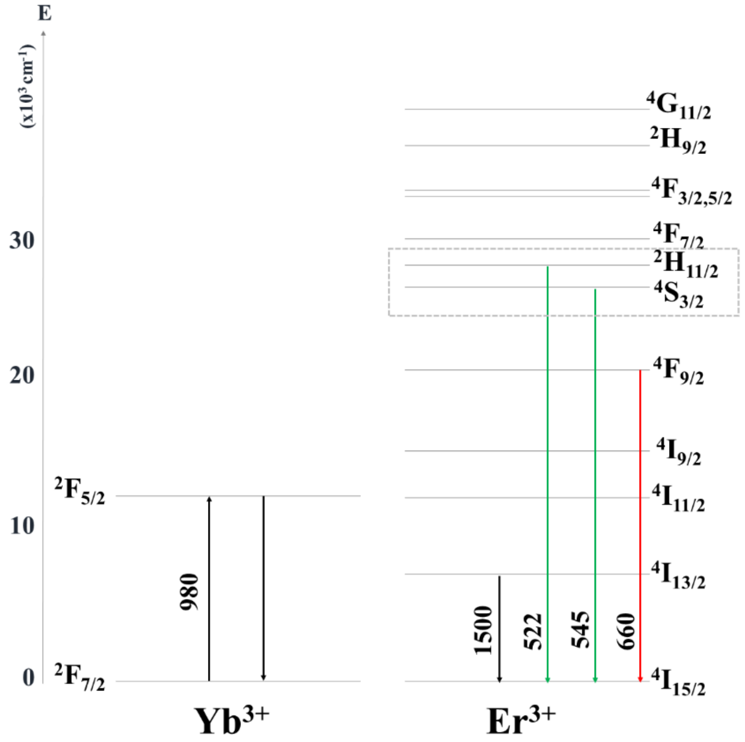

Figure 17. Partial diagram of energy levels for the Yb^{3+} and Er^{3+} ions, showing Er^{3+} ions emissions in the visible and infrared regions.

Due to the high absorption cross-section that the Yb^{3+} ion presents ($11.7x10^{-21}$ cm^2 about ten times greater than that of the Er^{3+} ion- $1.7x10^{-21}$ cm^2 [76]) for radiation in the 980 nm range, the Yb^{3+} is more effectively excited by these photons. Thus, in systems co-doped with the Yb^{3+}/Er^{3+} pair, under excitation at 980 nm, the Yb^{3+} ions are more effectively excited ($^2F_{7/2} \rightarrow {}^2F_{5/2}$), being able, in the sequence, to transfer energy to the Er^{3+} ions (which can also absorb energy under excitation at 980 nm) that will emit in the visible spectral region (by $^2H_{11/2} \rightarrow {}^4I_{15/2}$, $^4S_{3/2} \rightarrow {}^4I_{15/2}$ and $^4F_{9/2} \rightarrow {}^4I_{15/2}$ transitions) via **Up-Conversion (UC)** processes [77].

During UC, a higher-energy photon is emitted by conversion of two or more lower-energy photons. The emission mechanism involves sequential photon excitation, which can occur through two fundamental mechanisms: **ESA (Excited-State Absorption)** and **ETU (Energy Transfer Up-conversion)**. In the ESA mechanism, an ion is excited through the sequential absorption of two photons where, first, a photon is absorbed and promotes it to an excited metastable state. This state has a relatively long lifetime, allowing the absorption of one more photon and, as a consequence, the promotion of the ion to a higher energy state. Later, the return to the ground state occurs with the emission of a photon of higher energy than the absorbed one. In the case of Er^{3+} ions, the metastable excited state is $^4I_{13/2}$, and the highest energy states that can be populated in the sequence are $^2H_{11/2}$, $^4S_{3/2}$ and $^4F_{9/2}$. On the other hand, in the ETU mechanism, two distinct ions interact. A sensitizer ion that absorbs most of the photons, and an activator or emitter ion, which receives the energy from these absorbed photons in a non-radiative way [78].

ETU is the most efficient mechanism and is usually observed in systems co-doped with the Yb^{3+}/Er^{3+} pair, where Yb^{3+} ions sensitize Er^{3+} ions which are the activators. This is possible, as already mentioned, because Yb^{3+} ions have larger absorption cross-section, so they are more effectively excited with 980-nm radiation ($^2F_{7/2} \rightarrow {}^2F_{5/2}$), subsequently transferring energy to Er^{3+} ions, which will emit in the visible spectral region via $^2H_{11/2} \rightarrow {}^4I_{15/2}$, $^4S_{3/2} \rightarrow {}^4I_{15/2}$ and $^4F_{9/2} \rightarrow {}^4I_{15/2}$ transitions (Figure 18) [79].

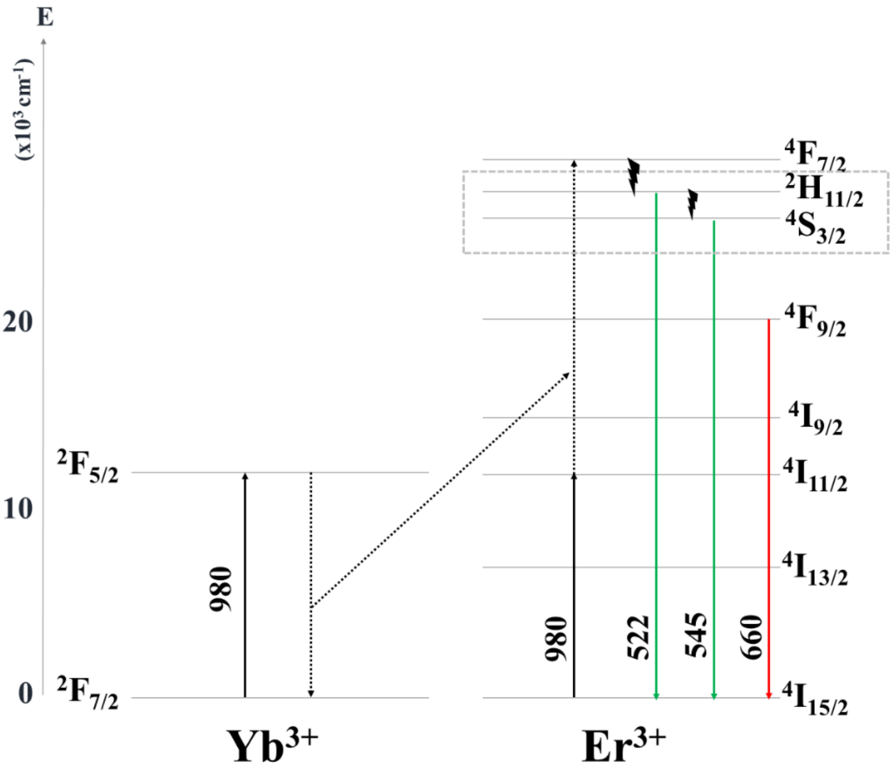

Figure 18. Partial diagram of energy levels for the Yb^{3+} and Er^{3+} ions, showing the UC mechanism and focus for thermally coupled levels $^2H_{11/2}$ and $^4S_{3/2}$.

Through this process, many applications are possible, for example, biomedical applications such as biosensory, imaging and theranostics [80]; in the development of displays and photonic devices [81] that can be used as sensors [82], in solar cells technology [83], in biosafety [84], among others. Furthermore, their excited levels $^2H_{11/2}$ and $^4S_{3/2}$ are energetically close (as also showed in Figure 18), so they can be classified as thermally coupled levels; that is, under 980-nm laser excitation, UC emissions sensitive to temperature changes can be achieved [13], as previously demonstrated [85–87] and will be better discussed next.

In turn, the element thulium is located between erbium and ytterbium elements, has an atomic number of 69 and a molar mass of 167 g/mol, and in Tm^{3+} present an electronic configuration $[Xe]4f^{12}$. The partial diagram of energy levels for the Tm^{3+} ions, showing emissions in the ultraviolet, visible, and NIR regions, is shown in Figure 19.

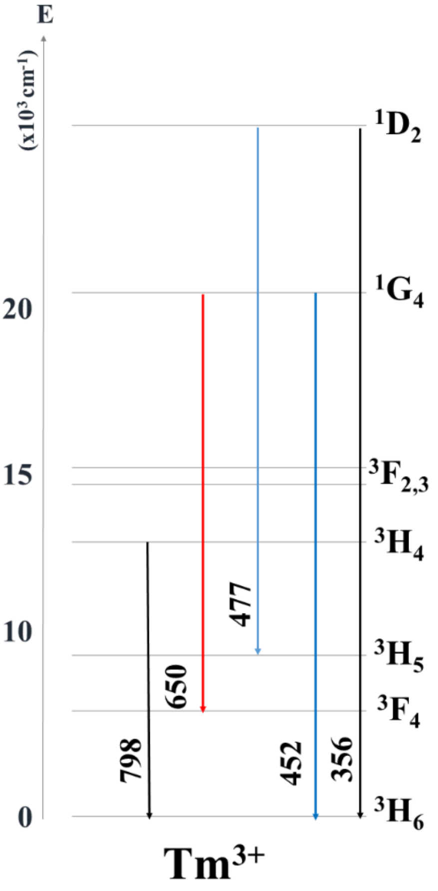

Figure 19. Partial diagram of energy levels for the Tm^{3+} ions, showing emissions in the ultraviolet, visible, and NIR regions.

Tm^{3+} ions present transitions in the visible and in the NIR regions by UC process (previously described) under excitation at 980 nm in the presence of another Ln ion, Yb^{3+} which has also been described. In this process, the electrons in ground state of the Tm^{3+} ions ($^3H_6$) can be excited to the highest energy state $^3H_5$ by ETU mechanism, described by $^3H_6$ (Tm^{3+}) + $^2F_{5/2}$ (Yb^{3+}) → $^3H_5$ (Tm^{3+}) + $^2F_{7/2}$ (Yb^{3+}) [78]. In sequence, the Tm^{3+} ions can non-radiatively decay to the $^3F_4$ level, and, the same ions in this same level can absorb another photon of excited Yb^{3+} ions, and then get to the $^3F_{2,3}$ level. From this level, the $^3F_{2,3} \rightarrow {}^3H_6$ transition (~ 706 nm) can occur, or else, the electrons can go to the level $^3H_4$, that in turn can be excited at the $^1G_4$ level by $^3H_4$ (Tm^{3+}) + $^2F_{5/2}$ (Yb^{3+}) → $^1G_4$ (Tm^{3+}) + $^2F_{7/2}$ (Yb^{3+}). In summary, by the union of the Yb^{3+}/Tm^{3+} pair under 980 nm excitation, it is possible to observe bands around 477, 650 and 800 nm, referent to $^1D_2 \rightarrow {}^3H_5$, $^1G_4 \rightarrow {}^3F_4$, and $^3H_4 \rightarrow {}^3H_6$ transitions, respectively (Figure 20). The last one is more intense due to the fact that the mechanism involved is only for 2 photons, whereas the transition situated in blue region occurs by a mechanism that involves 3 photons [88].

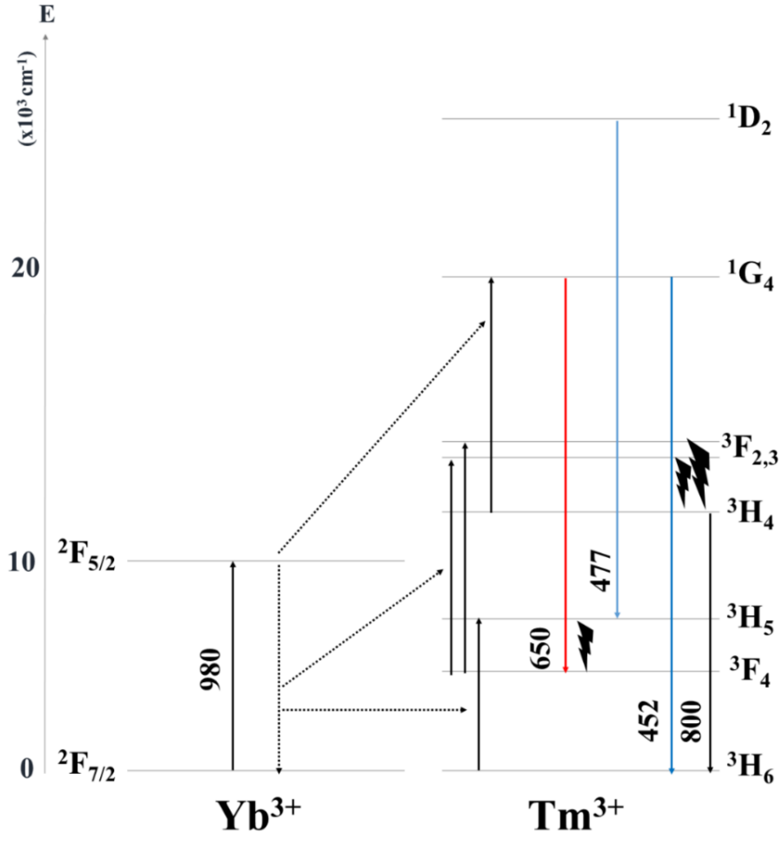

Figure 20. Partial diagram of energy levels for the Yb^{3+} and Tm^{3+} ions, showing the UC mechanism.

In this way, the observation of the blue color emitted in materials doped with Tm^{3+} ions under 980 nm excitation is less common, and this fact can be used as an anti-counterfeit device [88–91]. The needs and applications of anti-counterfeiting systems are many, once security has become indispensable, especially with regard to respect to official documents, as the falsification of documents violates copyright laws and causes huge losses [92]. As new technologies emerge, the need to develop systems able to stopping counterfeiting increases. In this way, devices that can help differentiate originals from counterfeit materials are an excellent alternative. In the development of these devices, the use of luminescent process has gained more attention, especially those prepared from Ln ions that can present the UC process [89,93]. Hereupon, a self-supported and flexible material was prepared in this work in the presence of Tm^{3+} ions, and has the potential to be applied as one of these devices, as will be presented in the results section.

1.3. Photonic and its Elements

Imagining our day-to-day life without light is practically impossible, since life on Earth is directly related to it and to the countless phenomena generated by its interaction with matter. In fact, the light has a central role in humanity development, and the science takes advantages of photon energy for developing new analysis, new sensor, so it becomes very important from medicine field to telecom. And it is not an overkill to say that the humanity is in the Photonic age. Specifically, the Photonic definition is "the science that makes it possible to generate, detect, transmit, modulate and amplify light". Another common definition is through an analogy with electronics, since, in general, photonics uses the photon quantum unit to play roles that, traditionally, were within the domain of electronics through electrons [94].

Photonics is present in several fields of our daily lives, such as lighting, light detection, information processing, telecommunications, spectroscopy, medicine (such as vision correction surgeries, endoscopies and other health monitoring), from supermarket barcode readers to military technologies, visual arts, robotics and agriculture. These applications are only possible thanks to the light's ability to interact with the matter. In 1917, Einstein proposed the explanation for the basic interaction between electromagnetic radiation and atoms [95]. In his work, three different mechanisms were proposed by which matter and photon can interact: absorption, spontaneous emission and stimulated emission, represented as I, II and III, respectively, in Figure 21.

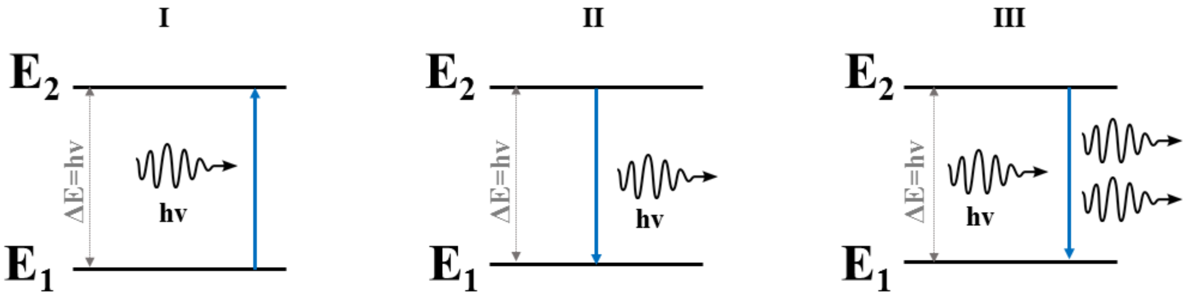

Figure 21. Representative diagrams of the processes of **(I)** absorption of a photon by an atom in the ground state, **(II)** spontaneous emission of a photon by an atom in the excited state, and **(III)** stimulated emission through a photon over atom in the excited state.

Let us consider $\mathbf{E_1}$ and $\mathbf{E_2}$ as two possible energy states for an atom, where **E** represents the energy value of these states, and $\mathbf{E_2>E_1}$. When this atom absorbs an amount of energy equal to **$\Delta E = E_2 - E_1$**, it is promoted from the **E_1** (ground) state to the **E_2** (excited) state, by the process we call **absorption** (Figure 21, I). After a certain time (called the excited state lifetime), this atom returns to its ground state, **E_1**, releasing the energy it had absorbed. This release can occur non-radiatively (ie, as heat), or radiatively through photon emission (of frequency hν). We call this process **spontaneous emission** (Figure 21, II), since the atom decays spontaneously. Finally, in the third process, if an atom like the one described is immersed in a radiation field, the change of states between **E_1** and **E_2** can occur by energy transfer from the electromagnetic field to the system, which is classified as a change of radiation-induced state. In this case, **stimulated emission** occurs, as a photon with energy equal to **ΔE** interacts with an atom that already has electrons occupying the **E_2** state and promotes the decay of this electron to **E_1** via the emission of a 'stimulated' photon, which has properties identical to of the incident photon (Figure 21, III). The operation of lasers, which will be discussed further below, is based on this principle [95,96].

In addition, light can still interact with matter by a process known as scattering. When, only its direction is changed while its amplitude is maintained, and also, the scattering process does not change the frequency (the energy was conserved), this process is called elastic scattering [97,98]. To characterize the scattering phenomena, we must first evaluate the scattering medium, which can be classified as homogeneous or heterogeneous, both on an atomic and macroscopic scale. In the case where the scattering medium is the atoms present in that medium, they act as microscopic electric dipoles, scattering the radiation and, due to their reduced dimensions and spacing compared to the wavelength (**λ**), the scattered field has the same characteristics of the incident field, except for the reduced speed (**v**) compared to the speed of light in a vacuum (**c**). In this case, the interaction is described by the refractive index (**n**):

$$\mathbf{n} = \frac{\mathbf{c}}{\mathbf{v}} \qquad \textbf{Equation 9}$$

and the medium is considered homogeneous. Conversely, in the case where the scattering properties of the medium are not uniform at distances of the order of **λ** or greater, the medium is considered heterogeneous [97].

Considering a medium composed of scattering particles, these interact in different ways with light, depending on their size, shape and composition. When considering their sizes, three different types of scattering can occur: **Rayleigh**, **Mie** and **geometric**. Before describing them, we must take into account two parameters that are of great relevance for the characterization of the scattering phenomenon: the size of the scattering particle (**x**), and the relative refractive index (**m**), described, respectively, by:

$$\mathbf{x} = \mathbf{k}\alpha = \frac{2\Pi\eta\alpha}{\lambda} \quad \textbf{Equation 10}$$

$$\mathbf{m} = \frac{\eta_1}{\eta} \quad \textbf{Equation 11}$$

where $\boldsymbol{\alpha}$: radius of the particle, and $\boldsymbol{\eta}$ and $\boldsymbol{\eta_1}$: refractive indices of medium and scatterer, respectively [97].

The scattering of light caused by the atoms that make up the system, as already mentioned, is a classic type of **Rayleigh scattering**, which describes the scattering of light by particles much smaller than the wavelength of incident radiation (**x, mx<<1**), which is the case for atoms and molecules [99]. This type of scattering is also observed in the atmosphere, being responsible for the predominance of the blue color in the sky and the appearance of the red color at sunset. When the scattering particle has a size comparable to the wavelength of the incident light (**x≈1**), we call the phenomenon **Mie scattering**. This type of scattering is handled by solving form of Maxwell's equations with appropriate boundary conditions, and can only be solved exactly for certain simple formats such as spheres and cylinders. Finally, for scatterers much larger than the wavelength of the radiation incident (**x, mx>>1**), **geometric** optics are used to determine the propagation intensity. Using appropriate corrections depending on the character of the radiation, geometry optics treats light as a beam, in a simplified way, and can be used, for example, to explain the appearance of the rainbow [97].

The intensity of scattering by particles can be expressed in terms of the scattering cross section ($\boldsymbol{\sigma_s}$) that is defined as the ratio of the power removed by scattering the incident beam intensity per unit of area:

$$\boldsymbol{\sigma_s} = \frac{\textbf{total energy scattered per second}}{\textbf{incident energy per m}^3\textbf{ per second}} \quad \textbf{Equation 12}$$

In simple light scattering, it is assumed that in a medium containing **N** scattering particles, the total scattered intensity is **N** times the intensity spread by a single particle [97].

Now, after discussing the phenomena arising from the interaction between light and matter, principles that enable multiple applications within the photonics field, we will discuss in more detail about conventional and random lasers. At the end of this topic, we will talk about temperature measurement via light-stimulated processes (thermometry via UC) as well as the possibility of developing anti-counterfeiting systems based on the same principles.

1.3.1. LASER

The word **LASER** is an acronym for **L**ight **A**mplification by **S**timulated **E**mission of **R**adiation, and refers to devices that produce intense, coherent, highly directional, monochromatic light beams, commonly used as a light source in photonic materials [100]. Since it was first demonstrated in 1960 for a ruby crystal-based system [101] the laser has developed rapidly and the number of applications is very broad. A common laser consists of an active medium and a set of mirrors for light feedback to the active medium, enabling a continuous beam amplification and the excitation power above the threshold, Figure 22.

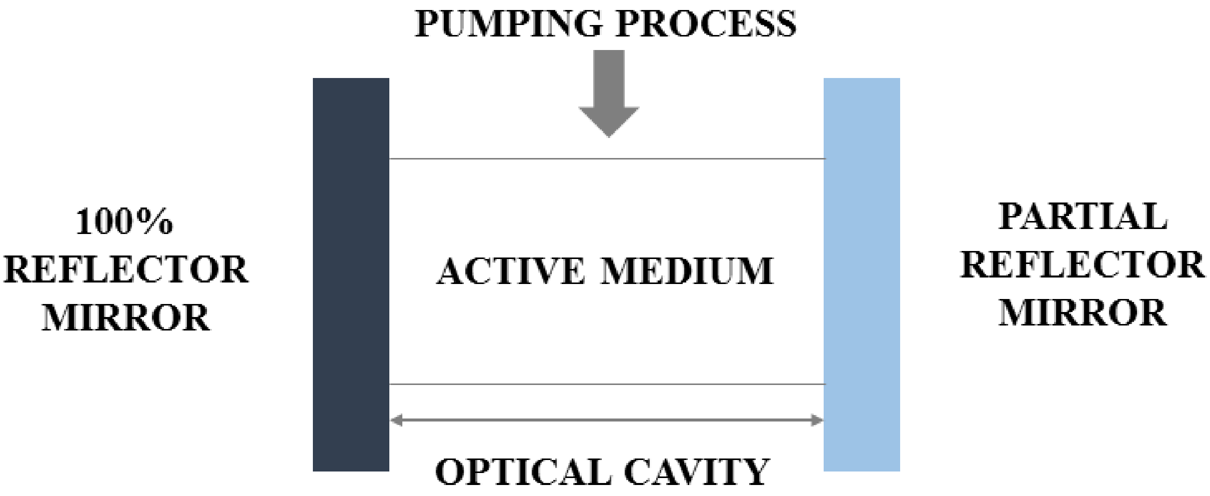

Figure 22. Schematic of the basic components of a conventional laser.

The **active medium** can consist of solids, liquids or gases, provided that its atoms, molecules or ions have electrons at metastable energy levels able of undergoing stimulated emission. The two parallel mirrors, one 100% reflector and the other partial reflector, constitute the known **optical cavity**, a system that reflects the photons allowing them to pass through the active medium several times, creating the necessary conditions for stimulated emission occurs predominantly in relation to spontaneous emission and thus resulting in beam amplification. Then, the intensity will increase a lot until the partially reflecting mirror allows the photon beam to escape from the cavity, so, the laser beam. This is the most common **feedback mechanism** used in conventional lasers. The **pumping** process can occur by different methods, such as optical pumping by another laser or a lamp, chemical reaction, electric current, among others. It must provide the necessary energy to populate the metastable levels of the active medium, thus creating the necessary conditions for light amplification [97,102,103].

Due to the phenomenon of stimulated emission that is the responsible for the amplification of light in lasers, an excited electron from the active medium generates a dipole moment that interacts resonantly with the field of electromagnetic radiation, intensifying the field while preserving its phase and wave vector. With this, the interaction of the excited species with the radiation induces a decay that generates an additional photon with the same properties as the incident field, that is, the incident photon is “copied” [97]. With this process occurring throughout the material, a high number of photons is generated in a short time, resulting in an avalanche of photons of the same frequency, phase, polarization and, mainly, the same propagation direction, characterizing a beam laser [98]. However, for this process and the gain to occur, excited electrons must be available which means that most of species must be in the excited state rather than in the ground state of the transition. This process is known as population inversion. Another important point, for the stimulated emission to occur, an initiator photon is required. The amplification of the radiation emitted in a cavity will occur, via stimulated emission, only if the gain at a certain frequency compensates for the losses. This condition is called laser threshold. In a simplified way, at low pumping rates, the population of the excited state is low and the radiation cannot be amplified because the intensity is lost faster than it is generated and then the spontaneous emission will be dominant. At high pump rates, the population inversion takes place, and that process compensates for cavity losses and, due to field strength, most species do not have time to spontaneously decay before being induced to decay by the incident field. The pump rate that limits these behaviors is known as the threshold pump rate [97,98].

The beginning of the exploration of photonics as a field of study is blended with the history of the laser, which as mentioned, was first demonstrated by Theodore Maiman [101], who built this laser using a ruby monocrystal as an active medium and a high-speed flash lamp power as a pump source. This device, illustrated in Figure 23, is a conventional three-level laser, where the ruby crystal acts as an active medium due to the chromium ions (Cr^{3+}) present in corundum structure.

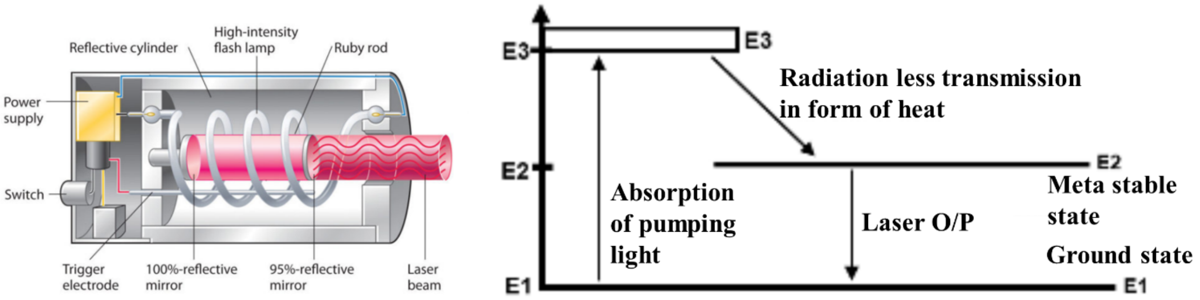

Figure 23. (left) Schematic illustration of the ruby laser with its components and (right) its three-level diagram (Cr^{3+} ions) [104].

In this three-level system, Figure 23, where **E1**, **E2** and **E3** are, respectively, the ground, intermediate excited (metastable), and higher energy excited states from Cr^{3+} ions, the pump source promotes electrons from **E1** ($^4A_2$) to **E3** ($^4T_1$ and $^4T_2$ levels). These excited states have relatively short lifetimes and, as a result, the excited electrons decay non-radiatively to the **E2** (^2E) level. Naturally, spontaneous emission $^2E \rightarrow {}^4A_2$ (**E2** → **E1**) occurs and as a result emitting a photon. However, as the **E2** level has a relatively long lifetime and the system is pumping, more species will be populated in the **E2** level, which is accompanied by a reduction in the population of the fundamental level, promoting the phenomenon of population inversion. As soon as an emitted photon moves across the crystal, this one interacts with the excited Cr^{3+} ions stimulating it to emit another photon, producing the cascade of photons that moves along the crystal. If this beam is perpendicular to the parallel mirrors, it will be reflected several times and stimulating further emissions rapidly, until the laser beam is strong enough to emerge through the partially reflective mirror [101,104].

A few years after the ruby laser demonstrations, the Nd^{3+}:YAG laser was discovered [10] and is currently the most commercially used solid-state laser. This device has a unique combination of laser-friendly properties because YAG is a colorless, optically isotropic crystal, and its refractive index does not depend on the direction of light or its polarization. Its cubic structure favors a narrow luminescence bandwidth from dopant ions, which results in high gain with low threshold in laser emission. In addition, YAG is a hard matrix, with good optical quality and with high thermal conductivity to dissipate the heat produced in the laser action. On the other hand, Nd^{3+} ions have received great attention due to the low threshold and high efficiency presented in a wide variety of matrices. These ions are widely used as active laser media, as they have four energy levels related to efficient absorption bands in the near-infrared region, and very high emission efficiency, especially for the laser transition $^4F_{3/2} \rightarrow {}^4I_{11/2}$ [10,39], as described earlier in this work (Figure 20). In addition, the $^4I_{11/2}$ level is not the ground one, so the population inversion is achieved at lower pumping fluency. This is why it is an advantage to use Nd^{3+} ions on laser studies in several kind of materials [12].

In the same decade of ruby and Nd^{3+}:YAG lasers development, a laser dye was presented by Sorokin and Lankard [105], through the observation of stimulated emission from the organic molecule chloroaluminium phthalocyanine. Since, laser dyes have gained importance in use as tunable sources of coherent radiation due to their operational flexibility. In addition, the high gain and wide emission bands allow these systems to work both in the pulsed and continuous regimes, their main characteristic being the wide range of frequencies they emit [98]. The use of these systems, which is generally an organic molecule with conjugated double bonds, is justified by the high gain and pumping efficiency that it presents as a function of the high absorption and emission shock section and high quantum fluorescence efficiency. These molecules still have the advantage of being a system composed of four levels, as shown in Figure 24.

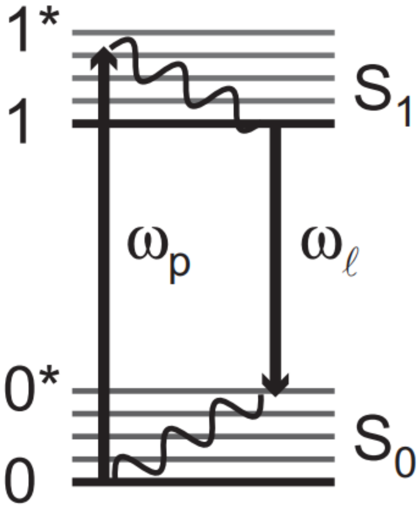

Figure 24. Energy scheme of a laser dye molecule [97].

Both ground states S_0 and the first excited state S_1 are composed of multiple vibrational states. The pump source (frequency ω_p) is absorbed and raises the molecule to a high vibrational level S_1. After relaxing, this electron decays to a lower S_1 level (with a short lifetime). Then, this electron decays to the highest energy S_0 level followed again by quick vibrational relaxation. This process allows population inversion and, consequently, the emission of a beam with laser characteristics. The active media most frequently employed have been those involving solutions of the dye in an organic solvent [97].

1.3.1.1. Random LASER

In a **Random LASER (RL)**, unlike what happens in conventional lasers, the feedback process is not generated by an optical cavity composed by two static mirrors. In fact, the cavity is replaced by multiple scatterings (Figure 25), produced by a disordered medium or by random refractive index variations in the medium, and this process provides the amplification of light.

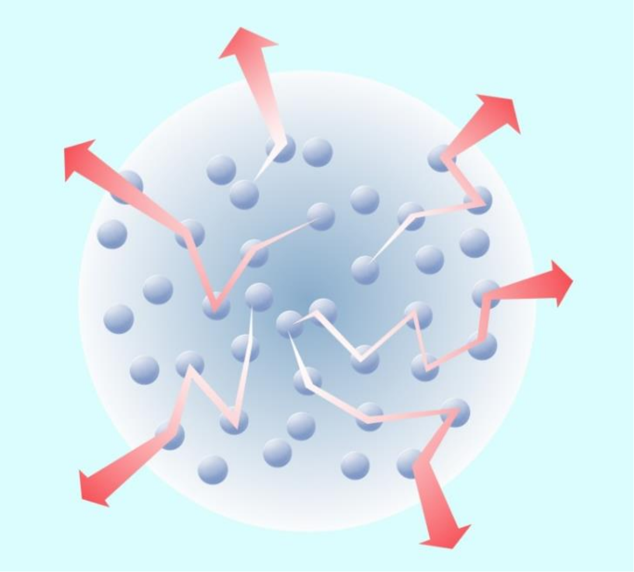

Figure 25. The feedback mechanism in a RL system [106].

In addition to the absence of the conventional optical cavity, RLs also do not present the same spatial coherence as conventional systems and the amplified emission leaves the material in all directions. However, the stimulated emission is responsible for the light amplification, which leads to the observation of narrow emission peaks and the characteristic laser threshold, and also, with a temporal behavior of the stimulated process. Furthermore, the emission present optical modes above threshold, which classify it as laser and the use of such nomenclature is justified [97,106,107].

In RL regime, the pump energy is absorbed by a gain medium and the excited species in this medium emit a photon by spontaneous emission, this could be amplified by stimulated emission as it moves across the length of the material. Multiple scattering increases the pathway that this photon travels and promotes the feedback of light. Consequently, this photon will be kept in the amplifying region of the material [95]. An important point is, to observe a laser emission, gain needs to overcome loss. Therefore, the gain depends on how long the light lies inside the amplifying medium, while the loss depends on how easily the light "escapes". For example, in a RL formed by spherical scattering particles (radius equal **a**), the gain is proportional to the particles volume ($\mathbf{4\,\pi\,a^3/3}$) and the loss will be proportional to particles surface area ($\mathbf{4\,\pi\,a^2}$). Then, when increasing the volume, the probability of the emitted photon to stay a longer time in the amplifying medium increases, and it is possible to reach a condition where the gain surpass loss and the system starts to lasing [106].

There are two different classes of the RL structure systems: (**I**) which the scattering particles constitute the active medium [108] and (**II**) another one in which the scattering particles are incorporated into the active medium [109]. In the particular case of Nd^{3+} doped materials or other active micro or nanoparticulated material, the gain and scatter can occur simultaneously, leading to multidirectional laser emission.

The history of RLs begins in mid-1968, when Letokhov stated that the combination of multiple scattering and light amplification would lead to a type of laser action [110], that proposal was at cutting-edge knowledge, because scattering was a problem in laser systems, as it removes photons in conventional ways from the cavity. However, only in 1986, that stimulated emission was observed for the first time in Markushev' work with sodium lanthanum molybdate powders [111]. Seven years later, Gouedard pumped hydrated neodymium chloride powders ($NdCl_3{\cdot}6H_2O$) under nanosecond laser pulses at room temperature, and observed a drastic decrease in the lifetime emission pulse and emission spectral line above the pumping threshold [112]. In this experiment, $NdCl_3{\cdot}6H_2O$ acted simultaneously as an emitter and a scattering medium. One year later, Lawandy clearly observed random laser emission from a solution of Rhodamine 640 (laser dye) in methanol with TiO_2 microparticles in suspension [113]. In this case the dye acted as an active medium excited by the pulses of a laser and the TiO_2 particles acted as scatters. In this work, it was observed that above a pump threshold, the full width at half maximum of the emission peak was decreased and the emitted pulse intensity increased as a function of pump power. Furthermore, an increase in the concentration of TiO_2 particles produced a reduction in the threshold, which indicated that scattering was responsible for the feedback that occurs in the system.

According to the feedback mechanism, RL can be divided into two categories, called **incoherent** and **coherent**. When the active medium's scattering length (**L**) is longer than the photon's free path (**ls**), and this pathway, in turn, is longer than the emission wavelength (**λ**), a situation described as: **λ < ls < L** and represented by the red arrows in Figure 26-(b), the propagation of light is diffused and, the interference contributes negligibly to a special resonance, which is called **incoherent**. In contrast, if the photon free path (**ls**) and the emission wavelength (**λ**) have the same order of magnitude (**ls ≈ λ**, green arrows in Figure 26-(b)) a photon localization occurs within the structure, and the feedback is **coherent**. In the first case (**incoherent**), the feedback promoted by scattering only returns part of the photons to the material and not to their original position, removing any spatial resonance. In the second case, the disordered nanostructures trap light in closed cycles, promoting **coherent** feedback and generating interference effects that result in fine peaks that appear in the emission band (spikes). The appearance of spikes is a fundamental feature to differentiate the incoherent from the coherent regime, since it is present only in the second case, due to the recurrent longitudinal modes of the system (Figure 26-(c)).

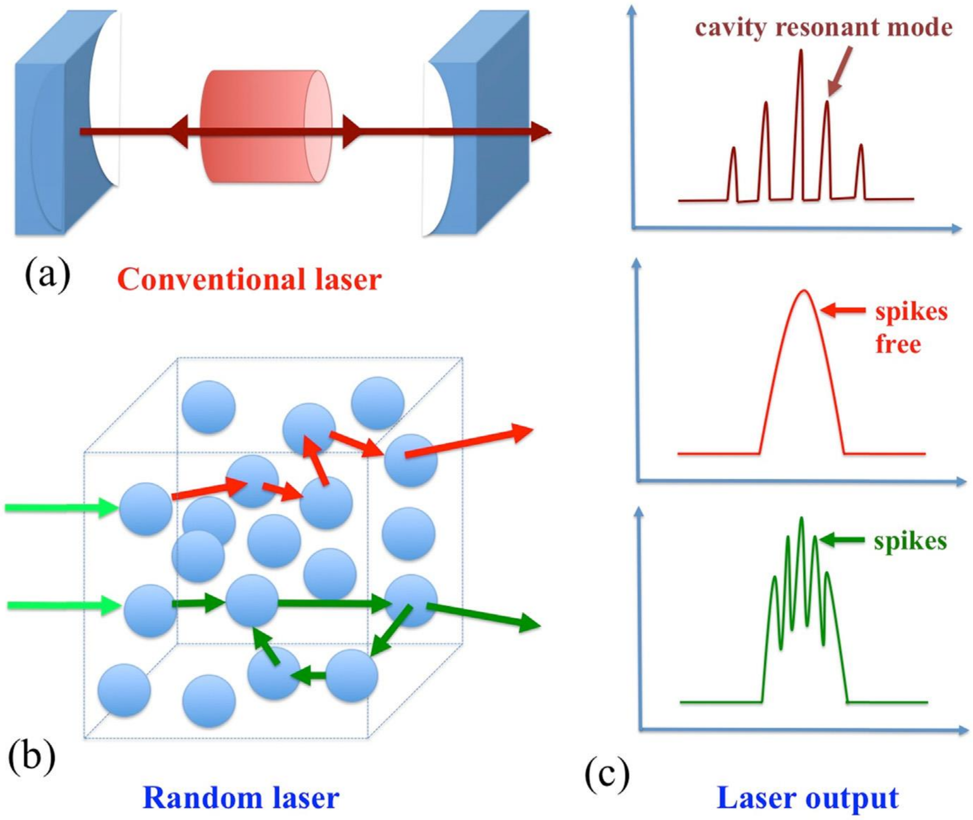

Figure 26. Operating principle of the laser in a (a) conventional cavity and in a (b) random medium with incoherent feedback (red arrows) and coherent feedback (green arrows); and (c) illustration of the emission spectra of a conventional and random lasers where the 'spikes free' corresponds to the laser with incoherent feedback while the spectrum with spikes corresponds to the coherent feedback [107].

As scattering increases the path traveled by light, generating amplification in a smaller system, the reduced size is one of the great advantages of RL. These devices can also have different shapes, to be optimized according to the application. Still as a consequence of their size, RLs can be integrated with other devices and applied in vivo, as biomarkers or in the treatment of certain diseases, for example. The random distribution of scatterers can generate a unique emission pattern for each system, such as a bar code, thus enabling its use as a security device. Furthermore, RLs are considered low-cost systems, as they do not need to have the same optical quality as a crystal and can be obtained from a wide range of materials, many of them with lower commercial values than those used in conventional lasers [106,107,114]. With this, a wide variety of RL systems has been developed, using semiconductor powders [115], in the form of fibers [116], through the use of SiO_2 particles and dyes [117], based on quantum dots [118], crystal liquids [119], biological materials [120], among others.

As mentioned, materials doped with Nd^{3+} ions can also be applied with laser devices. Similarly, RLs can also be obtained using this active medium, as demonstrated since the 1990s [67,69,121,122]. RLs based on Nd^{3+} are of great technological interest because they are not photodegradable, have relatively high efficiency and can act in a wide range of wavelengths [123]. Over the years, as in this work, RL emission has been demonstrated for different concentrations of this ion. This feature was investigated by Moura *et. al.* and it was reported that the RL onset time is shorter than the non-radiative relaxation time of the $^4F_{3/2}$ emitting state. The results presented motivate new studies of RL with high concentration of Ln^{3+} ions in glass, ceramic and crystalline matrices, which are normally avoided due to concentration quenching, which presents itself as a problem in several other applications, but not in the development of new RLs, thus enabling the development of a great diversity of materials [122].

1.3.2. Nanothermometry

Temperature is a fundamental concept of thermodynamics and a parameter of great influence for chemical and physical processes. Conventional techniques used for temperature measurement consist of heat exchange caused by contact between the system of interest and a thermometer. However, when it comes to micro or nanometric scales, traditional techniques have several limitations, such as the size of the thermometers, the difficult access to areas of interest, and the need for thermal balance between the thermometer and the environment in which the measurement is being performed. This type of limitation has driven the development of new measurement techniques that are accurate, that do not necessarily need to be in contact with the area to be measured, and that act with precision and high spatial resolution. In this sense, nanothermometry is an interesting proposal, as it is a non-invasive method that allows the measurement of temperatures even at the cellular level, with the objective of extracting the temperature of a given location, regardless of its spatial scale [13,124].

Optical nanothermometry is based on the analysis of changes in optical properties inherent to a given material caused by temperature change. Thus, optical sensors have been widely studied and developed, and exhibit several advantages over other devices, such as the possibility of remote sensing (non-contact), fast response time, little influence of the environment to be analyzed, among others. In this sense, among possible optical and non-invasive techniques, luminescent nanothermometry is of great interest. The properties of the photons involved in luminescence processes depend on the properties of their involved electronic states that, in turn, depend on the local temperature [13]. Since luminescence is affected by temperature, the resulting changes can be monitored measuring different parameters of the emitting center, such as the integrated emission intensity of a single transition or a pair of transitions, the spectral shift, band shape or bandwidth of a given transition, and lifetime measurements (Figure 27). Thus, this technique explores the relationship between the local temperature and the luminescent properties of the material, to obtain thermal sensing from spectroscopic analysis [73].

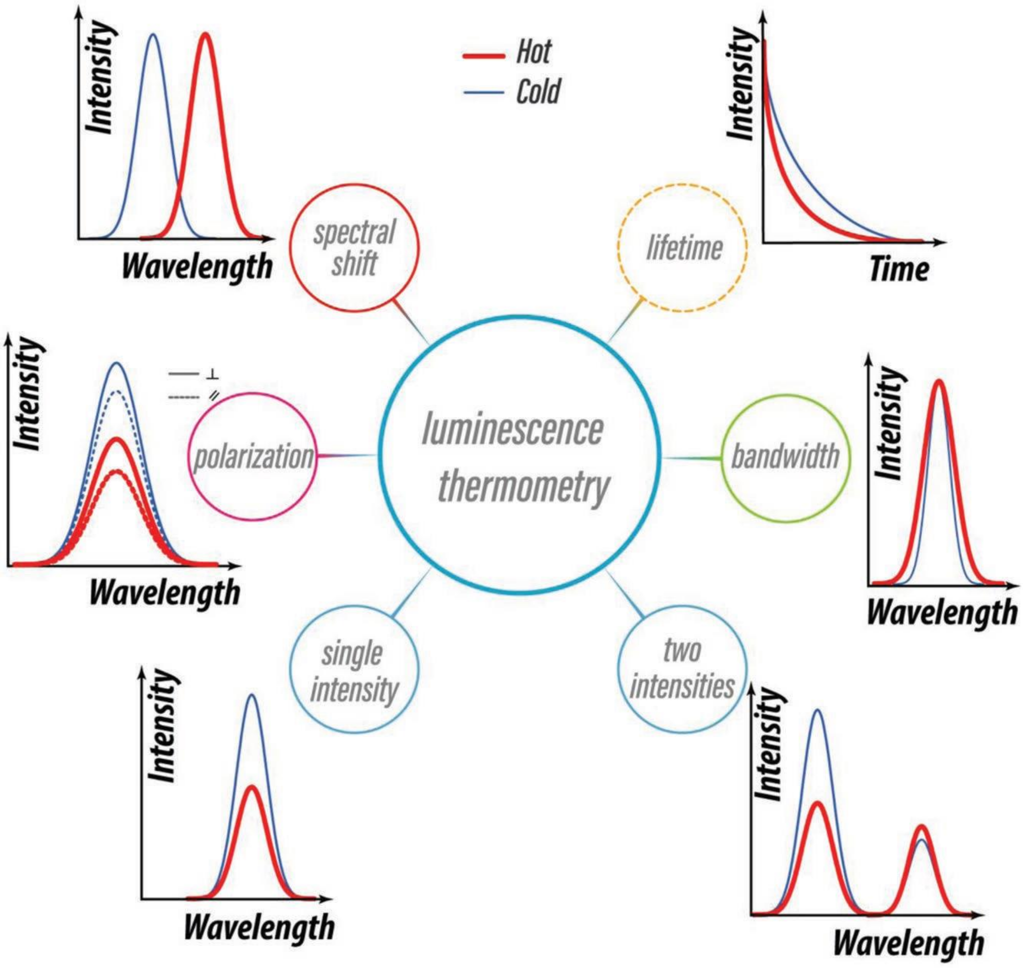

Figure 27. Schematic representation of possible effects on spectral characteristics caused by increasing temperature [73].

As described by Brites *et. al.* [13], these thermometry systems can be classified as **primary** and **secondary**. **Primary** systems are those that can be characterized by well-established equations, directly related to the values obtained with absolute temperatures, without the need for calibration. With this, they have the advantage of being able to be applied in different environments. The **secondary** ones, on the other hand, need to have a well-determined temperature in their calibration and, for this reason, are difficult to calibrate at nanoscales and why they are not usually applied as sensors [13].

In **primary** thermometers, it is possible to perform the analysis of the temperature variation based on the change in the emission intensity ratio between two transitions in a single emitting center, which proves to be an interesting strategy, given that the measurement is not compromised by experimental disadvantages. The ratio of the integrated intensity between two emissions, from energetically close transitions, can be analyzed based on the model of the

Boltzmann thermal equilibrium (Figure 28) between the two emitting levels, described as **|1>** and **|2>**. The absorption rate of the transition **|0>** → **|1>** is given by $\mathbf{W_{10}}$, and the intensities of the transitions as $\mathbf{I_{01}}$ and $\mathbf{I_{02}}$ [13].

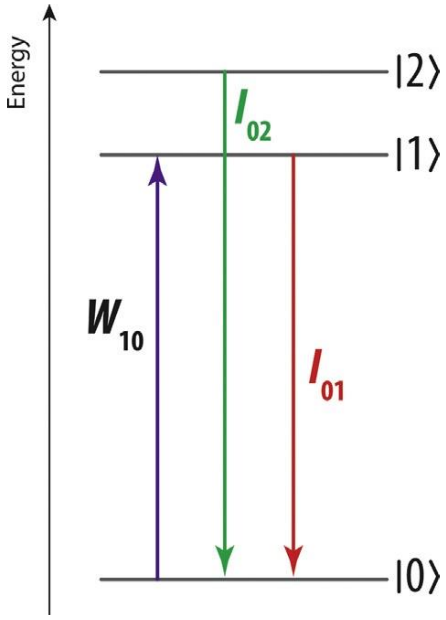

Figure 28. Schematic of a partial energy diagram of a generic ion [13].

If these two levels (**|1>** and **|2>**) are thermally in equilibrium, that is, thermally coupled, the population of these states, $\mathbf{N_1}$ and $\mathbf{N_2}$, can be related by:

$$\mathbf{N_2 = N_1 \left(\frac{g_2}{g_1}\right) exp\left(\frac{-\Delta E}{k_B T}\right)} \qquad \textbf{Equation 13}$$

where, $\mathbf{k_B}$: the Boltzmann constant, **T**: temperature, $\mathbf{g_1}$ and $\mathbf{g_2}$: the degeneracy of the levels 1 and 2, and **ΔE**: the energy difference between the barycenter of the emission bands **|2>** → **|0>** and **|1>** → **|0>**. The ratio between the integrated intensities of the two transitions is known as a thermometry parameter (**Δ**) and is given as:

$$\boldsymbol{\Delta = \frac{I_{02}}{I_{01}}} \qquad \textbf{Equation 14}$$

As $\mathbf{I_{0i}}$ can be written as:

$$\mathbf{I_{0i} \propto \hbar\, \omega_{0i}\, A_{0i}} \qquad \textbf{Equation 15}$$

where, $\mathbf{A_{0i}}$ is the spontaneous emission coefficient of the transition $\mathbf{0 \rightarrow i}$ and $\boldsymbol{\omega_{0i}}$: angular frequency. Since $\mathbf{N_i}$ is the population of state **i**, we can relate the thermometry parameter and the distribution of populations in the excited states:

$$\boldsymbol{\Delta = \frac{I_{02}}{I_{01}} = \frac{\hbar\, \omega_{02}\, A_{02} N_2}{\hbar\, \omega_{01}\, A_{01} N_1} = \frac{\omega_{02}\, A_{02} g_2}{\omega_{01}\, A_{01} g_1} \exp\left(\frac{-\Delta E}{k_B T}\right) = B \exp\left(\frac{-\Delta E}{k_B T}\right)} \qquad \textbf{Equation 16}$$

With this, the absolute temperature can be estimated by:

$$\boldsymbol{T = \frac{\Delta E}{k_B} \frac{1}{\ln(B/\Delta)}} \qquad \textbf{Equation 17}$$

where, **B** is a constant that can be obtained by the relation **Δ** as a function of the pump power, by extrapolating the curve to the zero-pump power limit. This constant depends on the degeneracy of the two excited states, on the rate of spontaneous emission total, the split ratio of the transitions relative to the ground state and the frequency angular.

An important parameter that must be evaluated when investigating the performance of a thermometer is the relative thermal sensitivity (**Sr**) of the fluorescence intensity ratio of an emitting site, which can be determined by the average parameter expressed:

$$\boldsymbol{S_r = \frac{1}{\Delta} \left|\frac{\delta\Delta}{\delta T}\right|} \qquad \textbf{Equation 18}$$

where, **δT**: temperature uncertainty, the smallest difference in temperature that can be detected in a given measurement. This quantity is also called temperature resolution, and can be given by:

$$\boldsymbol{\delta T = \frac{1}{S_r} \frac{\delta\Delta}{\Delta}} \qquad \textbf{Equation 19}$$

where **δΔ**: uncertainty in the determination of **Δ**.

In possession of the relative sensitivity and the value of the ratio between the integrated areas of the transitions of interest, it is possible to calculate the absolute sensitivity ($\mathbf{S_{abs}}$) by:

$$\boldsymbol{S_{abs} = \frac{I_{02}}{I_{01}} S_r} \qquad \textbf{Equation 20}$$

In addition to the parameters already demonstrated, the **reproducibility** and **repeatability** of a thermometer must be evaluated. **Reproducibility** indicates the variation in measurements performed under modified conditions, while **repeatability** refers to repeated measurements under identical conditions in the same equipment, which can be characterized as cycles. Thus, evaluating the variation in measurements, one can determine their ability to agree on measurements. Usually **repeatability** (**R**) is given in percentage and can be quantified by the following equation:

$$\mathbf{R = 1 - \frac{max\,(|\Delta_c - \Delta_i|)}{\Delta_c}} \qquad \textbf{Equation 21}$$

where, $\mathbf{\Delta_c}$**:** average of the values of $\mathbf{\Delta}$ obtained in each measurement, and $\mathbf{\Delta_i}$**:** parameter thermometry obtained in each temperature cycle [13,125].

Materials doped with Ln ions are being widely explored in the construction of thermally sensitive devices. In this sense, those containing Yb^{3+} and Er^{3+} ions are classic examples of primary thermometers, where the parameters are studied through the $^2H_{11/2} \rightarrow {}^4I_{15/2}$ and $^4S_{3/2} \rightarrow {}^4I_{15/2}$ transitions of Er^{3+} ions, since the $^2H_{11/2}$ and $^4S_{3/2}$ states are energetically close and thermally coupled, and better populated via UC process in the presence of Yb^{3+} ions, as already exposed in this work. In view of this, these ions were used in the preparation of YAG spheres and these were evaluated for their thermometry properties. The results obtained, as well as the equations used to calculate the parameters of interest, will be presented throughout this text.

1.4. The Silk

Legend says that silk was discovered while the Empress was drinking a cup of tea under a mulberry tree—a cocoon fell into her cup and, upon contact with the hot water, it broke apart, revealing the fiber produced by silkworm [126–128] Moved by curiosity, Hsi-Ling-Shi would have managed to transform that material into a piece of fabric and slowly started the weaving process, which is practically the same as the one used today. Although the textile industry was established at that time, it only peaked around 1500 BC, during the Shang dynasty. In the two following millennia, the Chinese were the exclusive manufacturers and exporters of silk: being aware of the commercial value of the fabric, the Chinese government banned mulberry seeds and silkworm eggs from being exported and threatened those who disrespected the ban with the death penalty. However, the ban was bypassed in 552 of the common era, when Justinian, the Roman Emperor, sent monks in disguise on a spy mission to China, to hide silkworm eggs in their luggage and take them to Constantinople inside bamboo sticks. The high commercial interest in it motivated the creation of the largest commercial route in the world, the so-called ‘Silk Road’, leading to the foundation of great civilizations. This path, which was the most important cultural and commercial link between the West and the East for hundreds of years, only received the name of ‘Silk Road’ in the 19th century. In Brazil, the history of silk fabric production began centuries later. Nevertheless, today Brazil is the fifth largest producer of silk fabric in the world. China still dominates the market, accounting for almost half of the silk fabric production on the planet. Even though Brazil remains behind China, India, Uzbekistan, and Thailand, the Brazilian silk fabric industry stands out for the quality of its yarns, produced mainly in the state of Paraná [126,129,130].

Obtaining silk on a large scale is only possible thanks to sericulture, the part of zootechnics that deals with the study and development of silkworm (Kingdom: Animalia, Phylum: Arthropoda, Clade: Pancrustacea, Order: Lepidoptera, Genus: Bombyx, Species: *Bombyx mori)* [131,132]. Sericulture is a thorough process that has been carried out pretty much the same way since silk was discovered approximately 4,500 years ago. It is the oldest known agroindustrial activity, and it is currently practiced by approximately 40 countries [128]. Silkworm uses silk to produce the cocoons, where it lives until it undergoes metamorphosis and becomes a moth [133,134].

The textile industry is interested in the cocoons. Starting from the egg, the estimated time for obtaining them is approximately 45 days. These cocoons consist mainly of two proteins: **Silk Fibroin-SF** (~70%), which belongs to the fibrous class and provides the cocoons with resistance, and **Silk Sericin-SS** (~30%), which belongs to the globular class and provides the cocoons with protection [8]. From a chemical standpoint, proteins are macromolecules built up from a set of 20 amino acids. The latter are smaller molecules bearing two functional groups – carboxyl and amino – in their structure. In the case of the proteins constituting the main core of the silk thread, there is high percentage of glycine and alanine in SF and of SS and threonine in sericin, as well as other subunits (in smaller proportions) [133]. Please see Table 6.

Table 6. Percentage of amino acids constituting the proteins present in the silk thread [133]

AMINO ACID	% in fibroin	% in sericin
Glycine (Gly)	42.8	8.8
Alanine (Ala)	32.4	4.0
Serine (Ser)	14.7	30.1
Tyrosine (Tyr)	11.8	4.9

Valine (Val)	3.0	3.1
Aspartic acid (Asp)	1.9	16.8
Glutamic acid (Glu)	1.7	10.1
Threonine (Thr)	1.2	8.5
Phenylalanine (Phe)	1.2	0.6
Isoleucine (Ile)	0.9	0.6
Arginine (Arg)	0.9	4.2
Leucine (Leu)	0.7	0.7
Proline (Pro)	0.6	0.5
Lysine (Lys)	0.5	5.5
Tryptophan (Trp)	0.5	0.5
Histidine (Hys)	0.3	1.4
Methionine (Met)	0.2	0.1
Cysteine (Cys)	0.1	0.3

SF, the major component in the silk thread, is a protein of the fibrous class. It plays a structural role and constitutes the nucleus of the silk filaments, providing the cocoons with resistance. On the other hand, SS is a protein of the globular class, which functions as a “glue” that unites two SF filaments, to form a silk thread that protects the cocoon [8,135].

1.4.1. Fibroin - the majority component: extraction, structure, and properties

Although the history regarding the use of silk as sutures is centuries old [135], it was in the mid-1940s that SF derived from cocoons aroused scientific interest. In 1947, the first academic article reporting the use of SF outside the textile industry was published [136]. Since then, the possibilities of using this protein have extended to several areas, such as tissue engineering [137,138]. SF has also been employed in the development of various types of biomaterials [139] and photonic devices [140]. Today, it is one of the most applied natural fibers.

Compared to SF, SS is still less often used due to biocompatibility and hypersensitivity issues [135,141]. However, many studies have investigated the application of sericin in other areas [142] including the development of compounds with antioxidant and bactericidal properties [134,143,144]. Sericin has also been employed in the prevention against UV rays [145], in the composition of cosmetics [146], and in the food industry [147]. This protein is commonly known as the "binding" protein. It involves and assembles the SF fibers, thereby providing the cocoon with a structure. Because it is a globular protein consisting predominantly of the amino acids serine (Ser) and aspartic acid (Asp) (Table 6), sericin is highly hydrophilic and is highly soluble in hot water [145], which allows it to be removed from silk during the ‘degumming’ process – the procedure through which SF is extracted from the silk threads, to give a solution of this fibrous protein [8].

While the textile industry disassembles the cocoon built from a single thread to produce fabrics, degumming is a ‘reverse engineering’ process that starts from the cocoon, to return to the original components, proteins and water, present in the silkworm sericigenic glands and which are spun to produce the cocoons [148]. This protein splitting process comprises four steps: (**I**) separation of proteins and extraction of SF from the silk threads; (**II**) fiber dissolution; (**III**) dialysis to remove excess salt from the medium; and (**IV**) centrifugation to remove impurities from the cocoons itself. At the end of these steps (shown in Figure 29), an aqueous, viscous, and yellowish solution (~5% mass/volume) is obtained. This solution must be kept at 4 ºC and remains stable for approximately 30 days [8].

In step (**I**), the cocoons are heated to 100 °C in an alkaline solution of sodium carbonate (Na_2CO_3). A salting-in effect takes place – the low concentration of salts increases the solubility of the proteins because the saline ions interact with the ionic charges of the proteins, increasing the effective charge and the amount of water molecules attached to the protein ionosphere. As already mentioned, the silk thread consists of two SF filaments linked together by a natural “glue”, SS. SS is a globular protein and is more soluble than SF. Thus, it is solubilized, becoming loose and remaining in solution, while the SF fibers remain rigid [8].

These now dried loose SF fibers undergo dissolution (**II**), which can be carried out in the presence of various organic solvents and/or aqueous solutions [8] such as $CaCl_2$-EtOH-H_2O

[149], $Ca(NO_3)_2$-MeOH-H_2O [150], LiBr-EtOH-H_2O [151] LiSCN-H_2O [152], NaSCN-H_2O [153], and LiBr-H_2O [8]. The latter is the most commonly used system. In this case, LiBr acts as a chaotropic agent. At high concentration in aqueous solution, LiBr “removes” the water molecules surrounding the SF molecules, thus affecting the stability of the native conformation of these macromolecules, weakening the hydrophobic effect [137].

After the SF fibers are completely dissolved, a yellow viscous gel is obtained. This gel is then dialyzed (**III**) against ultrapure water for 48 h. After this period, the solution is centrifuged (**IV**) at 3500 rpm, to remove impurities [8].

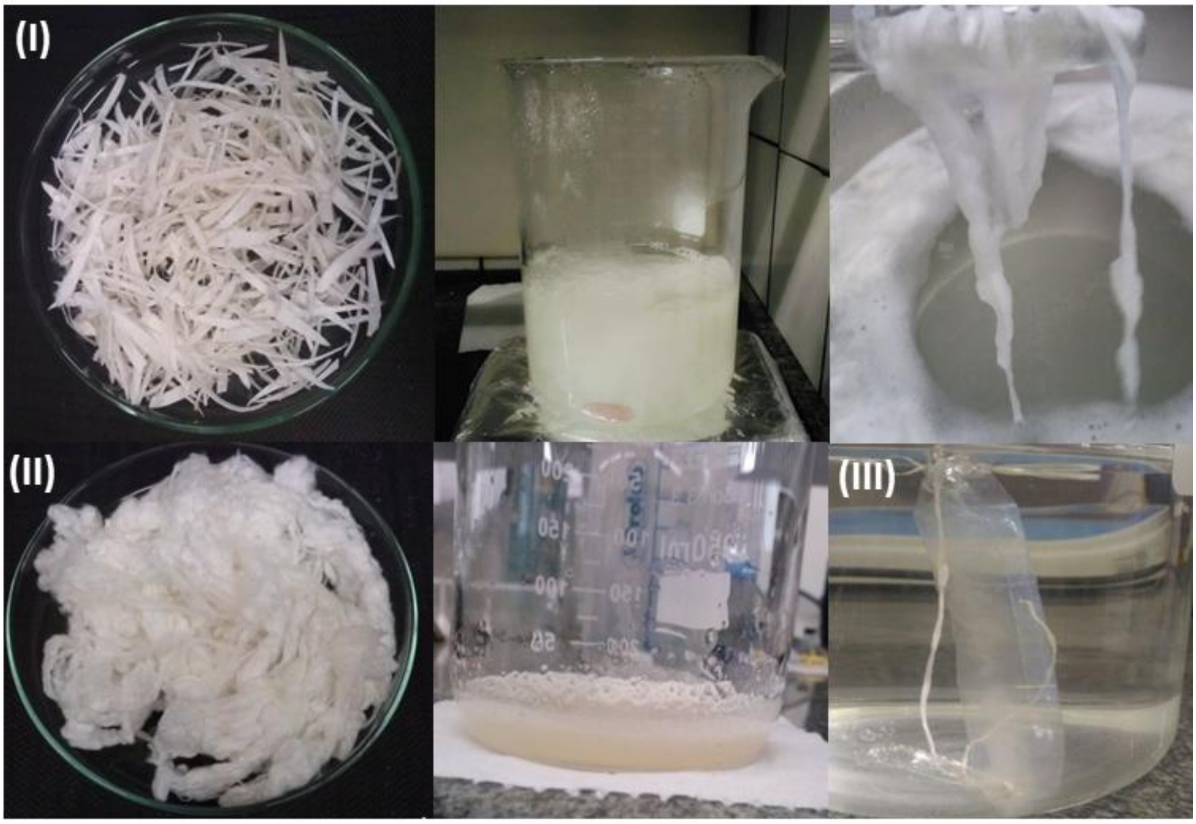

Figure 29. Photograph of the SF extraction process steps. **(I)** A sequence of three images showing cut cocoons, cocoons being heated in Na_2CO_3 solution, and loose SF fibers. **(II)** The first image shows dry SF fibers; the second image shows dissolved SF fibers after dissolution in LiBr solution. **(III)** Dialysis of the obtained solution.

Structurally, SF consists of two chains: a larger one, with ~325 kDa ((H) -chain), and a smaller one, with ~25 kDa ((L) -chain) [135]. These chains are linked by a disulfide bond formed between two cysteine residues [154], leading to an HL complex, which at the same time is also non-covalently linked to a P25 glycoprotein (~25 kDa). The whole structure of this protein [155–157] was first characterized by Marsh in collaboration with Corey and Pauling in 1955 [158]. The high-molar-mass region underlying the tension properties of SF is a crystalline structure composed by repetitions of the amino acids that build up its primary structure (in that order Gly - Ala - Gly - Ala - Gly - Ser) and which may have the so-called silk I and silk II. Silk I is a hydrophilic, less crystalline region consisting of alpha-helix structures or random coil; silk II is hydrophobic and is more crystalline due to the presence of antiparallel beta-leaves [159]. Silk I can be converted to silk II by specific treatment with methanol. In addition to these two regions, a small and unstable structure, known as silk III, may occur at the air/water interface of the SF in solution, but its structure has been less explored [160]. The low-molar-mass chain accounting for chemical resistance and moisture retention is an amorphous, hydrophilic structure that does not present the repetition of the amino acids that build up the primary structure [155,157,161]. SF comprises 5263 amino acid residues; Gly, Ser, and Ala are the main constituents of the primary structure, whereas other residual amino acids exist in smaller proportions [162,163], as shown in Table 6.

Because SF belongs to the fibrous class and presents many hydrophobic amino acid residues in its structure, it is a water-insoluble protein [133]. As mentioned previously, this protein has unique characteristics that allow it to be used in several areas. Among these characteristics, its biocompatibility [135,138,164], biodegradability [165], resorbability [166], high mechanical resistance [9,167], relative stability to the environment it occupies [135], flexibility [168], ability to self-crystallize [155] and to self-organize [8], structural functionality [169], possible coordinative environment for ions or molecules of interest [170], permeability to vapors of interest [171], transparency in all the visible spectrum, smooth surface, and variable refractive index [172] stand out.

After sericin is completely removed from the silk thread, the resulting SF solution can be used to prepare different materials, which is promising for several applications. Some designs are illustrated in Figure 30 and include gels, fibers, films, microspheres, tubes, and sponges. The time required to obtain these materials varies from one to five days [8], depending on the method.

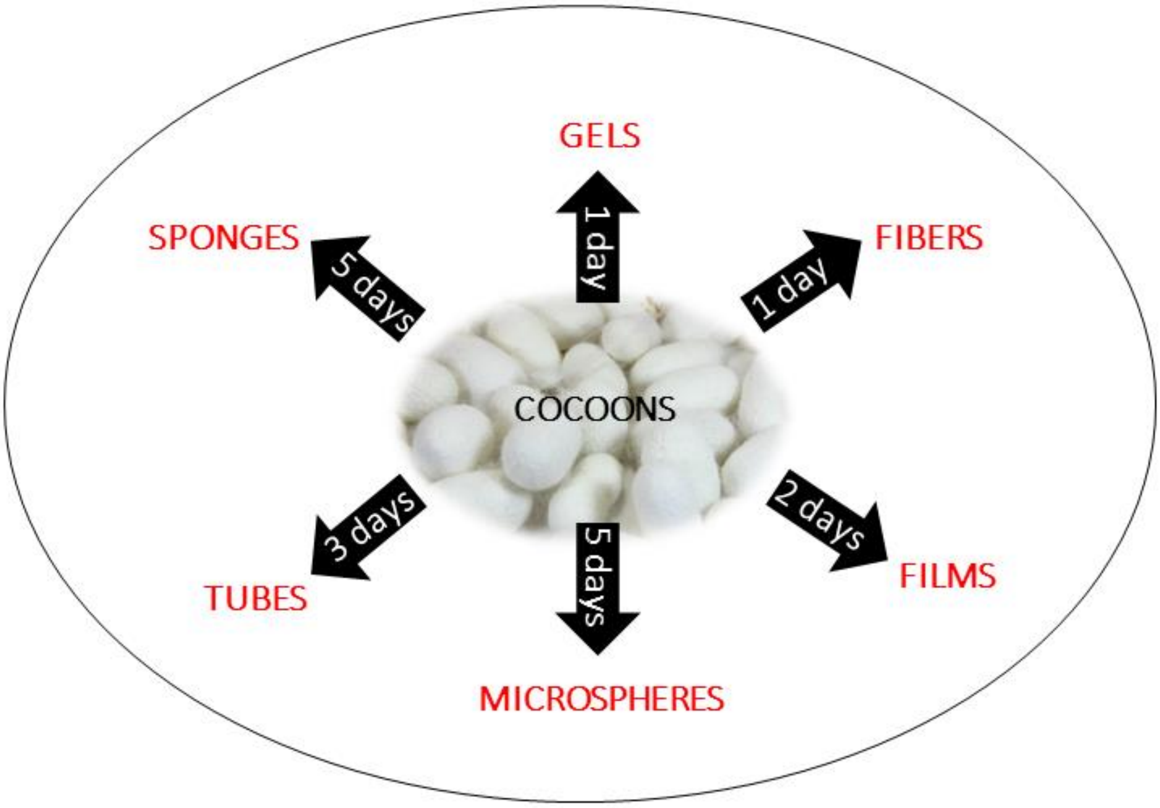

Figure 30. Scheme of the numerous shapes that can be obtained from the SF solution. The number of days that are necessary to obtain each shape is counted only after the SF solution is prepared.

The SF crystalline structure, and hence its mechanical properties, can be modified during the preparation of these materials, by altering the SF concentration in the solution, the solvent used during treatment (water or alcohols), and the treatment temperature [173] and by adding other components or creating/distributing pores [8,135,137,139]. The thickness and degradation time for materials such as films and tubes can be controlled by changing the SF concentration in the solution used during the preparation [8]. Through a simple drying process in ambient conditions, insoluble materials, like films, can be obtained – beta sheets (conversion of silk I to silk II) are formed as a result of water removal. However, the materials obtained by this method are brittle, but this can be improved through treatment with hot water or methanol [174,175]. Treatment with water vapor only affords more flexible materials that degrade within a shorter time than materials treated with methanol, a widely used method for preparing materials of different shapes, such as spheres and fibers. In addition to the previously mentioned films and tubes, because methanol can induce SF crystallization, a larger number of beta-sheet structures arise. In general, treatments with water vapor only give a smaller amount of beta sheets than treatment with alcohol, such as methanol. A small number of beta sheets results in less crystalline, more malleable, and softer materials, whilst an increase in the number of these structures affords more crystalline and rigid materials [8,176].

Besides these treatments, the mechanical properties of SF can be improved by adding other components [165,177]; for example, SF blends with acrylic polymers [153], polysaccharides [178], collagen [179], and sodium alginate [180], among others, can be obtained. Porous materials can also be achieved by using polyethylene oxide (PEO) [8], thus creating matrixes with defined porosity and modified surface properties [181]. Another factor that can influence the properties of the resulting materials is the age of the cocoons that are used to obtain the SF solution, as demonstrated by Ramirez and collaborators [182].

Film is one of the simplest forms into which SF can be molded. To prepare a film, the typical feature of proteins must be considered: these macromolecules tend to self-organize as they spread over a surface. Therefore, they acquire the shape of the surface after the solvent present in the protein solution, in this case water, is evaporated under ambient conditions (dry casting) [8,137]. In this way, non-patterned or patterned SF films can be achieved by changing only the substrate where the film is prepared. The choice of substrate will depend on the target application given that this film will “load” the characteristics of the substrate. Apart from this preparation method involving manual deposition, these materials can be obtained by other techniques, such as layer-by-layer (LbL) deposition [167,183,184], which produces ultrafine SF films, as well as spin coating [185], Langmuir-Blodgett (LB) process [160], and others.

SF tubes can also be obtained by a simple method like dip coating, by immersing a template in a solution with high SF concentration, as described by Rockwood and collaborators [8]. After immersion, the system must be homogenized and placed in contact with methanol, which can induce formation of beta-sheet structures and stiffen the material [137,176]. After treatment, the templates with the solution are dried at room temperature. This method enables tube thickness to be controlled through control of the SF concentration in the solution and the number of layers deposited on the template [8]; furthermore, porous tubes can be created [186]. Another methodology involves spinning gel (gel spinning) [187].

Wenk and collaborators [188] obtained SF microspheres by a method that uses mild conditions and a vibrating mouthpiece. In this system, the SF solution is added with a syringe and ejected in the form of drops by action of the mouthpiece with controlled vibration and frequency. The drops are poured into a reservoir containing liquid nitrogen and solidify upon contact with it.

Spherical SF materials can also be prepared by other methods. For instance, fatty acid lipids (DOPC: 1,2-Dioleyol-sn-glycerol-3-phosphocholine) can be employed to encapsulate the aqueous SF solution. The fatty acid lipids can be in the pure form or in the presence of a molecule of interest, which act as a template. After vesicles are generated, the lipid can be removed, and the resulting spheres are resuspended. In the case of DOPC, which is soluble in methanol and can stiffen SS, methanol is used to remove the lipid [8,189]. Phase separation between the aqueous SS solution and another polymer, such as PVA (polyvinyl alcohol), is another useful method that is simple and dismisses the use of other solvents [190].

SF fibers are generally obtained by electrospinning, a process that affords materials with large surface area and reduced diameter. This methodology is widely employed due to the simplicity of the experimental electrical force apparatus – it basically consists of three components, syringe, high voltage source, and collector – not to mention its high efficacy and low cost [191].

SF is also widely used to produce three-dimensional scaffolds with controlled morphology and porosity. These scaffolds can be obtained from gel, hydrogels, or sponges. Sponges can be achieved by adding and subsequently removing salts from the SF solution in aqueous medium; pore size can be controlled [8]. In addition to this aqueous method, sponges can also be prepared by using organic solvents, like the alcohol HFIP (1,1,1,3,3,3-hexafluoro-2-propanol) [192].

Finally, hydrogels can be prepared by a series of methods involving decreasing the pH value of the medium [193], sonication [194], or application of an electric current [195]. In all cases, the material is produced in a simple and fast way, and the choice of method will depend on the target application. Nogueira *et. al.* [196] demonstrated that these materials can be achieved by SF solution dialysis at different temperatures, without the need for further treatments, constituting another simple and effective route that affords promising structures for biological applications.

1.4.1.1. Its main applications - focus on electronic and photonic devices

Because SF provides positive responses due to its biocompatibility [8,139,164], among other properties, it has been widely explored for the development of diverse biomaterials in the medical field for decades; moreover, it has promising use in the development of photonic devices [140]. Among the possible applications of this natural polymer, we can mention its use in drug delivery systems [189], as scaffold in tissue engineering for repair of tissues (such as cornea, vascular and bone tissues), and as dressing for healing skin lesions [197]. Other application areas include cancer diagnosis and treatment, photodynamic therapy [198], enzyme immobilization [199], photonic devices [200], lasers [117,120], biosensors [184], waveguides [162], fuel cells [201], and materials with antithrombogenic properties [202].

In the field of electronics and photonics, biopolymer films have been used to obtain flexible devices [168]. This field requires materials that can be applied in unconventional interfaces, such as curvy and soft interfaces, to which traditional devices are unable to adhere. Indeed, electrodes that can intimately and non-invasively integrate with these surfaces offer important opportunities for disease treatment and diagnosis [166]. In this regard, SF has been extensively studied and stands out against other materials thanks to its unique properties, which include being mechanically robust [9] and transparent throughout the visible spectrum, presenting smooth surface and variable refractive index [172], and being susceptible to physical changes in its structure [176]. All these characteristics allow the preparation of passive or active devices [168] based on pure SF or SF in the presence of other components, to provide materials like supports for electrodes [166], lasers [117,203], biosensors [184], waveguide [162], and fuel cells [201], as mentioned.

Kim and collaborators built an electrode consisting of a chip supported on an ultrathin and resorbable SF substrate. To this end, they obtained a pure, smooth, and thin film in which the chip was placed. They observed that tissue adhesion improved with decreasing device thickness. The chip could be reabsorbed by the body within a programmed time because SF can be undone in days, months, or even years depending on the treatment to which it is submitted [166]. This work introduced a concept that could be extended to other areas: the preparation of electronic devices with biodegradable components as an alternative to replace some types of plastics.

Silva *et. al.* [117] took advantage of the ability of SF to copy the characteristics of the substrate to which it is added to prepare a laser system based on the DFB (distributed feedback grating) mechanism by using a commercial DVD as substrate. They poured the SF solution on the surface of the DVD and let it dry. The resulting film displayed the diffraction pattern of the DVD. This pattern is what causes amplification in this type of laser system, thus being an example of an active device based on SF in the presence of nanoparticles and dye incorporated into the protein structure.

A dielectric material with thickness (**l**) and refractive index ($\mathbf{n_1}$) and that can support wave propagation is known as a waveguide. Its refractive index ($\mathbf{n_1}$) must be different from the refractive index of the material on which the guide is supported ($\mathbf{n_2}$). In a study published in 2015, researchers obtained biocompatible waveguides from SF fiber ($\mathbf{n_1} = 1.54$) encapsulated with SF hydrogel ($\mathbf{n_2}$ = 1.34) and demonstrated that the materials can guide light in tissues by means of a robust system, thereby allowing great advances in the use of light in therapy or image acquisition [204].

The SF protein structure is also of great interest in the development of photonic devices. Among the amino acids that make up such a structure are the aromatic amino acids tryptophan (Trp), tyrosine (Tyr), and phenylalanine (Phe) (Table 6), which are commonly employed as fluorescent probes for interpretation of the protein structure (conformation, dynamics, and molecular interaction). In the case of SF, Trp stands out because its fluorescence is sensitive to the surrounding environment. This amino acid residue, with broadband emission between 300 and 400 nm, can sensitize Ln ions by energy transfer, populating the emitter levels more efficiently, as demonstrated in our study published in 2018 [170]. When the emitting levels are more efficiently populated, the emission of these ions intensify, a widely explored phenomenon in photonics.

Understanding how the physicochemical properties of SF affect the spectroscopic properties of Ln ions can be a strategy for the development of a new generation of photonic devices, such as biocompatible and biodegradable sensors with high transparency in the visible spectral region. In a recently published study, thin, highly transparent films consisting of SF and a europium ion (Eu^{3+}) complex, produced by immersion under controlled conditions, were presented. The study showed the highly intense emission typical of Eu^{3+} complexes and the dependence of the intensity of the $^5D_0 \rightarrow {}^7F_2$ transition on the concentration of ammonia vapor, thus demonstrating the possibility of using this system as a photonic vapor sensor [205]

2. Objectives

2.1. General objective

Our aim was synthesizing YAG (Yttrium Aluminum Garnet, $Y_3Al_5O_{12}$) spherical particles doped with lanthanide ions by Spray Pyrolysis, as well as inserting them in Fibroin matrix to develop new luminescent materials; and studying their spectroscopy behavior for photonic applications.

2.2. Specific objectives

- Structural and morphological study of the YAG phase obtained as dense spheres via Spray Pyrolysis;
- Luminescence spectroscopic study of the different lanthanide ions inserted into the YAG matrix for downshifting and up-conversion process;
- Laser emission studies in a random media composed of Nd^{3+}-doped YAG acting as an active and a scatter medium;
- Preparation of luminescent Silk Fibroin films for up-conversion emission by action of the Yb^{3+}/Er^{3+} pair, and also of the Yb^{3+} and Tm^{3+} ions;
- Investigation of the thermometry response, in different temperature ranges via up-conversion mechanism, of materials doped with the Yb^{3+}/Er^{3+} pair.

3. Materials and Methods

3.1. Chemicals

Yttrium, neodymium, ytterbium, erbium and thulium oxides (Y_2O_3, Nd_2O_3, Yb_2O_3, Er_2O_3 and Tm_2O_3, respectively, 99.9%, purchased from Sigma-Aldrich), nitric acid (HNO_3, 65%, supplied by Sigma-Aldrich), high-purity deionized water (18.2 MΩ/cm, obtained from Millipore Milli-Q water purification system), and aluminum tri-sec-butoxide ($C_{12}H_{27}AlO_3$, 97%, acquired from Sigma-Aldrich) were employed as purchased. All aqueous lanthanide nitrate solutions were titrated before used to confirm the absolute concentration of Ln^{3+} ions. *Bombyx mori* cocoons were provided by the silk spinning company BRATAC–Fiação de Seda, Brazil; sodium bicarbonate (Na_2CO_3, anhydrous, minimum 99.5%) was purchased from Merck; and lithium bromide (LiBr, purity ≥ 99%) and dialysis tubing cellulose membrane were acquired from Sigma-Aldrich.

3.2. Experimental procedure

3.2.1. Preparation of Boehmite – the precursor

3.2.1.1. Nd^{3+} ion doping

The required SP precursor to prepare Nd^{3+}:YAG particles was based on 100 mL of 0.2 M boehmite suspension [4,5,42] doped with 60% of Y^{3+} ion (mol/mol in relation to Al^{3+} from boehmite composition) and co-doped with 1.0, 2.0, 2.5, 3.0, 3.5, 4.0, 4.5 or 5.0% Nd^{3+} (mol/mol in relation to Y^{3+}). The Ln ion that was selected for phosphor production had to be added at the moment the precursor was being prepared. To this end, first the aqueous yttrium and neodymium nitrate solutions (0.5 M $Y(NO_3)_3.6H_2O$ and 0.1 M $Nd(NO_3)_3.6H_2O$) were obtained by acid digestion of the respective oxides (Y_2O_3 and Nd_2O_3). To prepare the suspension, aqueous yttrium nitrate solution (0.5 M $Y(NO_3)_3.6H_2O$) and aqueous neodymium nitrate solution (0.1 M $Nd(NO_3)_3.6H_2O$) (volumes according to the desired concentration) were added to 50 mL of ultrapure water previously heated to 83 ºC. Next, 4.93 g (0.02 mol) of the aluminum tri-sec-butoxide was added and hydrolyzed for 1 h under stirring. Then, 1 mL of nitric acid was added as peptizing agent. After the suspension was cooled, the final volume was adjusted to 100 mL with ultrapure water.

Table 7. Description of the amount of RE ions added to each YAG sample obtained after pyrolysis of suspensions

Samples (% mol/mol Y^{3+})	**mole of Y^{3+}**	**mole of Nd^{3+}**
Nd^{3+}:YAG (1.0%)	0.0118	0.0002
Nd^{3+}:YAG (2.0%)	0.0116	0.0004
Nd^{3+}:YAG (2.5%)	0.0115	0.0005
Nd^{3+}:YAG (3.0%)	0.0114	0.0006
Nd^{3+}:YAG (3.5%)	0.0113	0.0007
Nd^{3+}:YAG (4.0%)	0.0112	0.0008
Nd^{3+}:YAG (4.5%)	0.0111	0.0009
Nd^{3+}:YAG (5.0%)	0.011	0.001

3.2.1.2. $Yb^{3+}$and Er^{3+} ions doping

The Yb^{3+}/Er^{3+}:YAG particles were also prepared by SP. So, again a 50 mL of 0.2 M boehmite suspension, as detailed in the item 3.2.1.1, was used as precursor. To obtain the final Yb^{3+}/Er^{3+}:YAG particles, the Ln pair concentration was kept at 13.75% or 20%, in function of the Y^{3+} content on garnet structure, in addition, the specific Yb^{3+}/Er^{3+} % ratio was maintained at 12.5%/1.25% (for 13.75%), or 18.75%/1.25% (for 20%). Then, aqueous yttrium nitrate ($Y(NO_3)_3.6H_2O$), ytterbium nitrate ($Yb(NO_3)_3.6H_2O$), and erbium nitrate ($Er(NO_3)_3.6H_2O$) solutions (molar quantity according to the desired concentration) were added to 30 mL of ultrapure water previously heated to 83 ºC. Next, 2.45 g (0.01 mol) of aluminum tri-sec-butoxide was added and hydrolyzed for 1 h under stirring. After that, 0.5 mL of nitric acid was added as peptizing agent, and the suspension was cooled. The final volume was then adjusted to 50 mL with ultrapure water.

Table 8. Description of the amount of RE ions added to each YAG sample obtained after pyrolysis of suspensions

Samples (% mol/mol Y^{3+})	**mole of Y^{3+}**	**mole of Yb^{3+}**	**mole of Er^{3+}**
Yb^{3+}/Er^{3+}:YAG (13.75%)	0.004625	0.00125	0.000125
Yb^{3+}/Er^{3+}:YAG (20.0%)	0.004	0.001875	0.000125

3.2.1.3. $Yb^{3+}$and Tm^{3+} ions doping

In the same way, the Yb^{3+}/Tm^{3+}:YAG particles were prepared by SP as described for the YAG matrix doped with other Ln ions [4,5,42]. More specifically, YAG particles doped with two Yb^{3+} concentrations were prepared. In both cases, the Tm^{3+} concentration was kept at 0.5% (mol/mol in relation to Y^{3+}), whereas the Yb^{3+} concentration was 10 or 15% (mol/mol in relation to Y^{3+}). The resulting powders were labeled Yb^{3+}/Tm^{3+}:YAG (10%/0.5%) and Yb^{3+}/Tm^{3+}:YAG (15%/0.5%), respectively. Briefly, as described in the previous item, 50 mL of the precursor, 0.2 M Boehmite doped with the Ln, was prepared by addition of yttrium and thulium nitrates solutions to 30 mL of ultrapure water at 83 °C. Then, 2.45 g (0.01 mol) of aluminum tri-sec-butoxide was added to this solution and hydrolyzed for 1 h under stirring.

Table 9. Description of the amount of RE ions added to each YAG sample obtained after pyrolysis of suspensions

Samples (% mol/mol Y^{3+})	**mole of Y^{3+}**	**mole of Yb^{3+}**	**mole of Tm^{3+}**
Yb^{3+}/Tm^{3+}:YAG (10.5%)	0.00495	0.001	0.00005
Yb^{3+}/Tm^{3+}:YAG (15.5%)	0.00445	0.0015	0.00005

3.2.2. Preparation of the YAG particles by Spray Pyrolysis

To prepare the Ln^{3+}:YAG powders, Ln^{3+},Y^{3+}-doped boehmite suspensions (items 3.2.1.x) was pyrolyzed in an SP system, as shown in Figure 5 and described previously [4]. As already mentioned, on the equipment used in this work, the aerosol is originated in the ultrasound chamber. In this step, a 2.4-MHz frequency piezoelectric pellet was used to generate the aerosol. In sequence, the aerosol was carried through the two heat-treatment zones, the drying zone at 150 ºC and the pyrolysis zone at 700 ºC, by gas flow (0.1 m^3/h atmospheric air). After all the suspension had been pyrolyzed (around 20 mL/h), the product was collected in an electrostatic filter operating at 11 kV and 150 ºC to avoid water condensation. After, the collected powder was heat-treated at 1100 ºC for 12 h.

3.2.3. Obtaining composite films by Silk Fibroin and YAG particles

SF, used in the preparation of the films prepared below, was extracted by following the experimental procedure previously described by Rockwood [8] and shown in Figure 29.

3.2.3.1. SF + Nd^{3+}:YAG particles

To obtain the SF-Nd^{3+}:YAG composite films, the six Nd^{3+}:YAG particles, that present RL emission (2.5, 3.0, 3.5, 4.0, 4.5, and 5.0%, as will be shown in the sequence), were used. To this end, 30 mg of Nd^{3+}:YAG was dispersed in 2.5 mL of SF solution and dried on a plastic substrate with diameter of 2.0 cm at 45 °C for 4 h. All the prepared samples present the same appearance, since equal amounts of powders and SF solution were used.

3.2.3.2. SF + Yb^{3+}/Er^{3+}:YAG particles

To obtain the SF-Yb^{3+}/Er^{3+}:YAG composite films, the two Yb^{3+}/Er^{3+}:YAG particles were used. To this end, 50 mg of Yb^{3+}/Er^{3+}:YAG was also dispersed in 2.5 mL of SF solution and dried on a plastic substrate with diameter of 2.0 cm at 45 °C for 4 h. This procedure was carried out to four different amounts of Yb^{3+}/Er^{3+}:YAG particles (Yb^{3+}/Er^{3+} % ratio of 12.5/1.25 or 18.75/1.25)—50.0 mg, 5.0 mg, 2.5 mg, and 1.0 mg—and the resulting SF-Yb^{3+}/Er^{3+}:YAG composite films were numbered **I**, **II**, **III**, and **IV**, respectively, as shown in Figure 31.

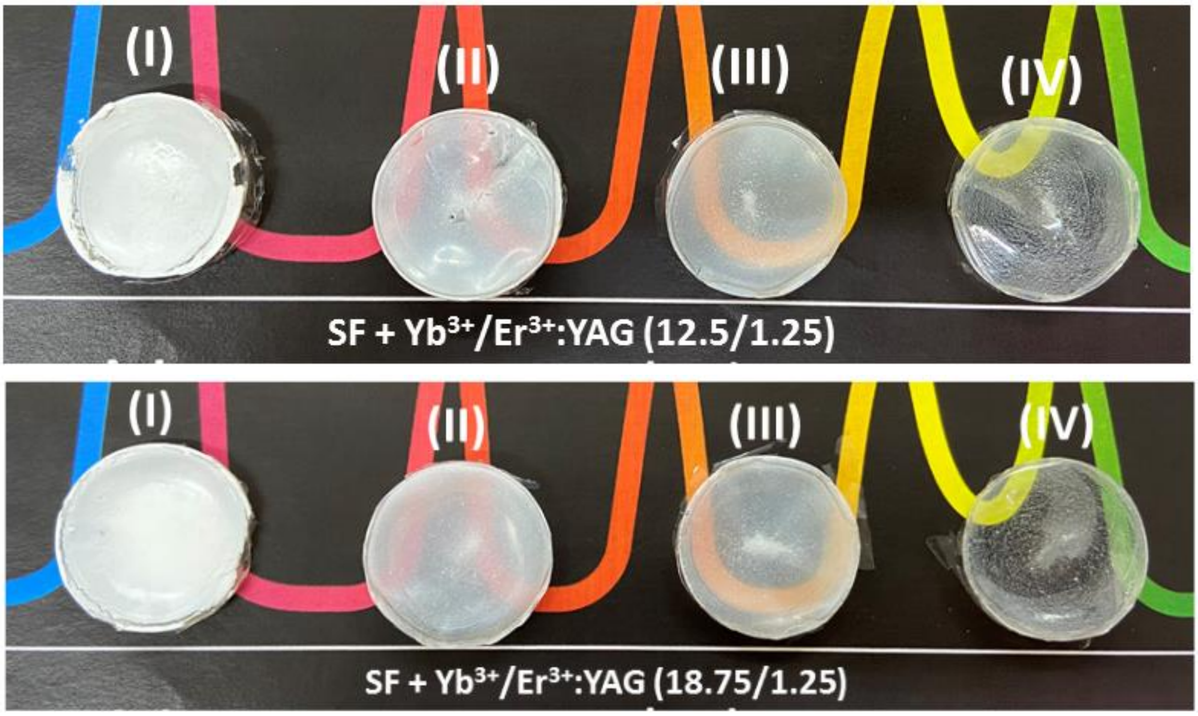

Figure 31. Photograph of the SF-Yb^{3+}/Er^{3+}:YAG composite films obtained with SF solution and **(I)** 50, **(II)** 5.0, **(III)** 2.5, and **(IV)** 1.0 mg of (above) Yb^{3+}/Er^{3+}:YAG (Yb^{3+}/Er^{3+} % ratio of 12.5/1.25) and (below) Yb^{3+}/Er^{3+}:YAG (Yb^{3+}/Er^{3+} % ratio of 18.75/1.25) particles.

3.2.3.3. SF + Yb^{3+}/Tm^{3+}:YAG particles

The composite films were also prepared by dispersing the Yb^{3+}/Tm^{3+}:YAG particles in the SF solution. To obtain films with different transmittance behaviors, different amounts of the particles were added to the SF solution. Briefly, to 2.5 mL of SF solution, 50, 5.0, or 2.5 mg of Yb^{3+}/Tm^{3+}:YAG (Yb^{3+}/Tm^{3+} % radio of 10/0.5) particles was added, and called **I**, **II** and **III**, respectively, as shown in Figure 32. The system was mixed, added to plastic petri dishes, and dried at 45 °C for 4 h, to obtain self-supported films with different transparency values.

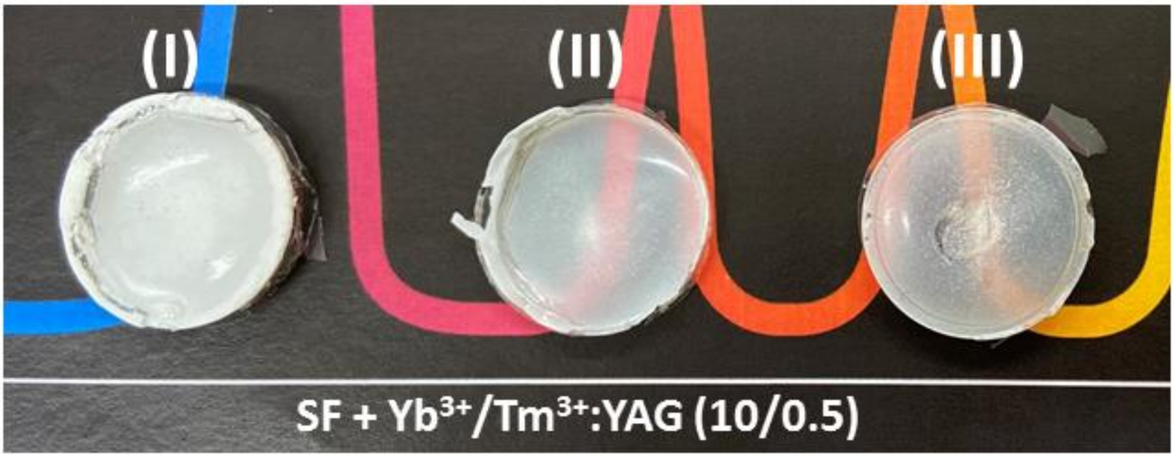

Figure 32. Photograph of the SF-Yb^{3+}/Tm^{3+}:YAG composite films obtained with SF solution and **(I)** 50, **(II)** 5.0, and **(III)** 2.5 mg of Yb^{3+}/Tm^{3+}:YAG (Yb^{3+}/Tm^{3+} % ratio of 10/0.5) particles.

3.2.4. Analysis techniques

3.2.4.1. Powders and films characterization

The Nd^{3+}:YAG powders were characterized by **X-ray diffraction (XRD)**, **infrared vibrational spectroscopy (FTIR)**, **scanning electron microscopy (SEM)**, and photoluminescence spectroscopy. The X-ray diffraction analyses (XRD) were conducted in the equipment D2 Phaser model from Bruker-AXS, operated at room temperature and with Kα radiation from the copper anode and scanning of θ/2θ, the equipment calibration was carried out with a standard from Bruker, Korundprobe A26-B26-S. The infrared vibrational spectroscopy (FTIR) analyses were carried out in an IRPrestige- 21- Shimadzu equipment in KBr pellet, with a proportion of sample/KBr as 1/100. The scanning electron microscopy (SEM) images were obtained on a Zeiss EVO 50 equipment, and all samples were previously covered with a thin layer of gold in a Bal-Tec SCD 050 Sputter coater. The particle diameter analysis was carried out by Image J software for a count of at least 200 particles observed in the electronic microscopy. The photoluminescence analyses were performed on a Fluorolog 3 Horiba Scientific (model FL3-22) equipment with dual excitation and emission monochromators and Hamamatsu R928 (visible) and H10330-75 (near infrared) photomultipliers; a pulsed Xe lamp of 450 W was used for the excitation spectra, and an 808-nm laser was employed for the emission spectra. The Yb^{3+}/Er^{3+}:YAG and Yb^{3+}/Tm^{3+}:YAG particles were characterized by XRD, SEM and photoluminescence spectroscopy, in the same equipment described above, but a pulsed 980-nm laser was employed for the emission and UC spectra. In the case of SF films formed by both particles, these were characterized by photoluminescence spectroscopy in the same way described.

3.2.4.2. Random Laser setup

The RL setup was typical of powder based RL, as can be seen in Figure 33.

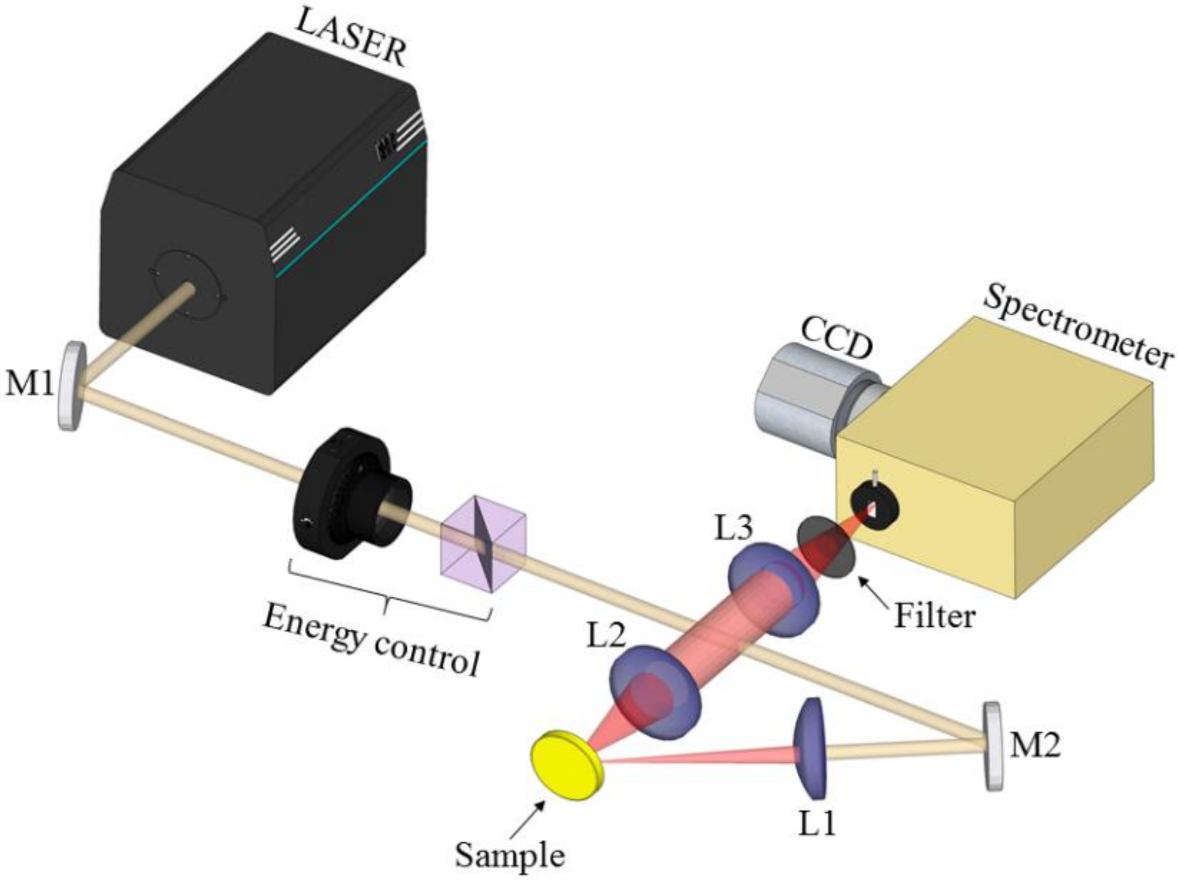

Figure 33. Experimental setup for RL emission detection, M1 and M2 are mirrors, and L1, L2, L3 are lens.

The pump source was an optical parametric oscillator (OPO, Opotek) pumped by the second harmonic of a Q-switched Nd^{3+}:YAG laser and tuned to the 810 nm emission wavelength. The OPO operated at 10 Hz, delivering pulses with energy up to 2.0 mJ and pulse duration ~5 ns. The illuminated area in the sample surface was 1.9 mm^2. The emission spectra were analyzed using a CCD coupled to a spectrometer (~0.01 nm resolution). Time resolved measurements were performed by using a fast photodetector (<10 ns risetime) also coupled to a second port of the spectrometer. The excitation pulse energy (EPE) was controlled by a pair of polarizers, and the direction of the incident beam was 45° with respect to the normal of the sample. The light emitted by the powder was collected in the direction normal to the sample surface and directed to the spectrometer with appropriated optics.

3.2.4.3. Thermometry study

Temperature-dependent UC spectra of the Yb^{3+}/Er^{3+}:YAG particles were acquired between 293 and 473 K, while the temperature-dependent UC spectra of the SF-Yb^{3+}/Er^{3+}:YAG composite films were registered between 293 and 333 K due to the lower thermal stability of the protein. In both cases, the samples were placed in a platinum crucible in a LINKAM Scientific temperature-controlled stage (T95-HT), show in Figure 34.

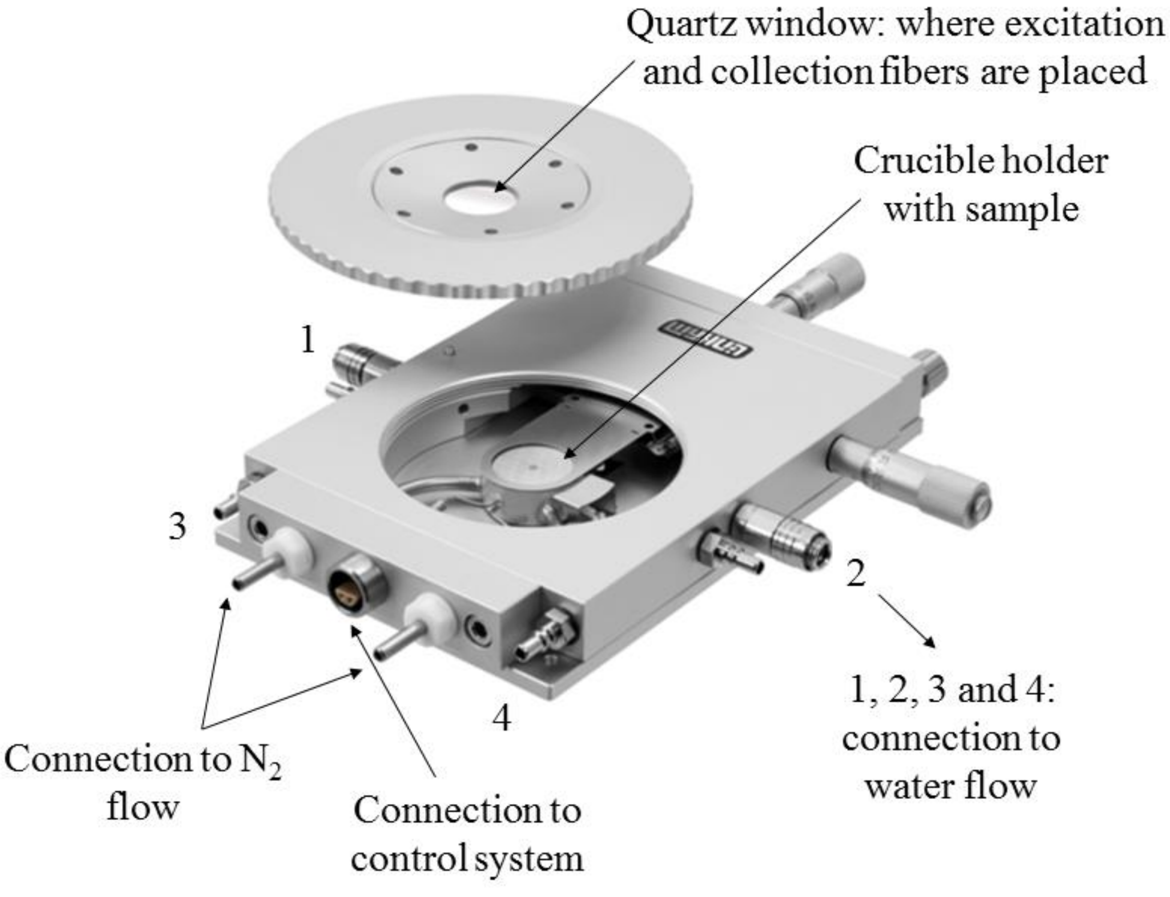

Figure 34. Temperature and environmental control from < -195 °C to 600 °C with XY sample manipulators [206]**.**

A stable temperature control of 0.1 °C was employed, and the temperature of the samples was stabilized before each analysis. The samples were excited with a continuous 980-

nm fiber laser (1000 mW for the Yb^{3+}/Er^{3+}:YAG particles and 700 mW for the SF-Yb^{3+}/Er^{3+}:YAG composite films) by using an optical fiber. The emission signals were collected by another optical fiber and guided from the sample to the detector, coupled to the equipment Fluorolog 3 Horiba Scientific previously described for photoluminescence analysis.

4. Results and Discussion

The results obtained during the development of this project will be presented in different sections. First, we will present the structural and morphology characterization of the YAG particles doped with all Ln ions studied. In the sequence, it will be shown, independently for each system (Nd^{3+}, Yb^{3+}/Er^{3+} and Yb^{3+}/Tm^{3+}), the luminescence spectroscopic studies of these materials. Finally, based in their potential applications, the thesis will present the results of the RL emission studied in materials doped with Nd^{3+} ions, and, followed by the studies of the thermometry properties of the systems containing Yb^{3+}/Er^{3+}.

4.1. Structural and morphological characterization of the YAG particles

The materials doped with Nd^{3+} (1.0, 2.0, 2.5, 3.0, 3.5, 4.0, 4.5 or 5.0%) were fully characterized by XRD and FTIR, after different thermal treatment of the powder obtained from pyrolysis, to determine the YAG phase. Initially, the Nd^{3+}:YAG particles without heat treatment were analyzed by powder XRD, herein, we are just showing the extreme concentrations (1.0 and 5.0%) and the intermediate one (3.5%), as all samples have a very similar profile. As observed in a previous work [4] and shown in the Figure 35, the powders had amorphous structure, which was corroborated by an enlarged and undefined halo in the diffractogram and was a consequence of the restricted time (few seconds) during which the precursor remained in the pyrolysis zone. Different temperature on SP setup was previously studied for the same precursor used herein [4]. In these previous studies, it was presented the structural evolution of powder obtained at different pyrolysis temperatures and at 200 °C and 500 °C boehmite particles were produced. It is known that boehmite structure is stable around 250 °C, but when the SP is performed at 500 °C, the boehmite structure is well defined. This is because the residence time in the hot zone of the SP process is very short (few seconds), so the reactions cannot be completed. The pyrolysis performed at 700 °C gives a very badly resolved diffraction, with some characteristic peaks of the γ-alumina. In addition, the difference between the covalent radius of Y^{3+} and Nd^{3+} ions could result in longer time for structural organization, as shown by López *et. al.* [207], which the increase of Nd^{3+} content may have been accounted for the low crystallization rate.

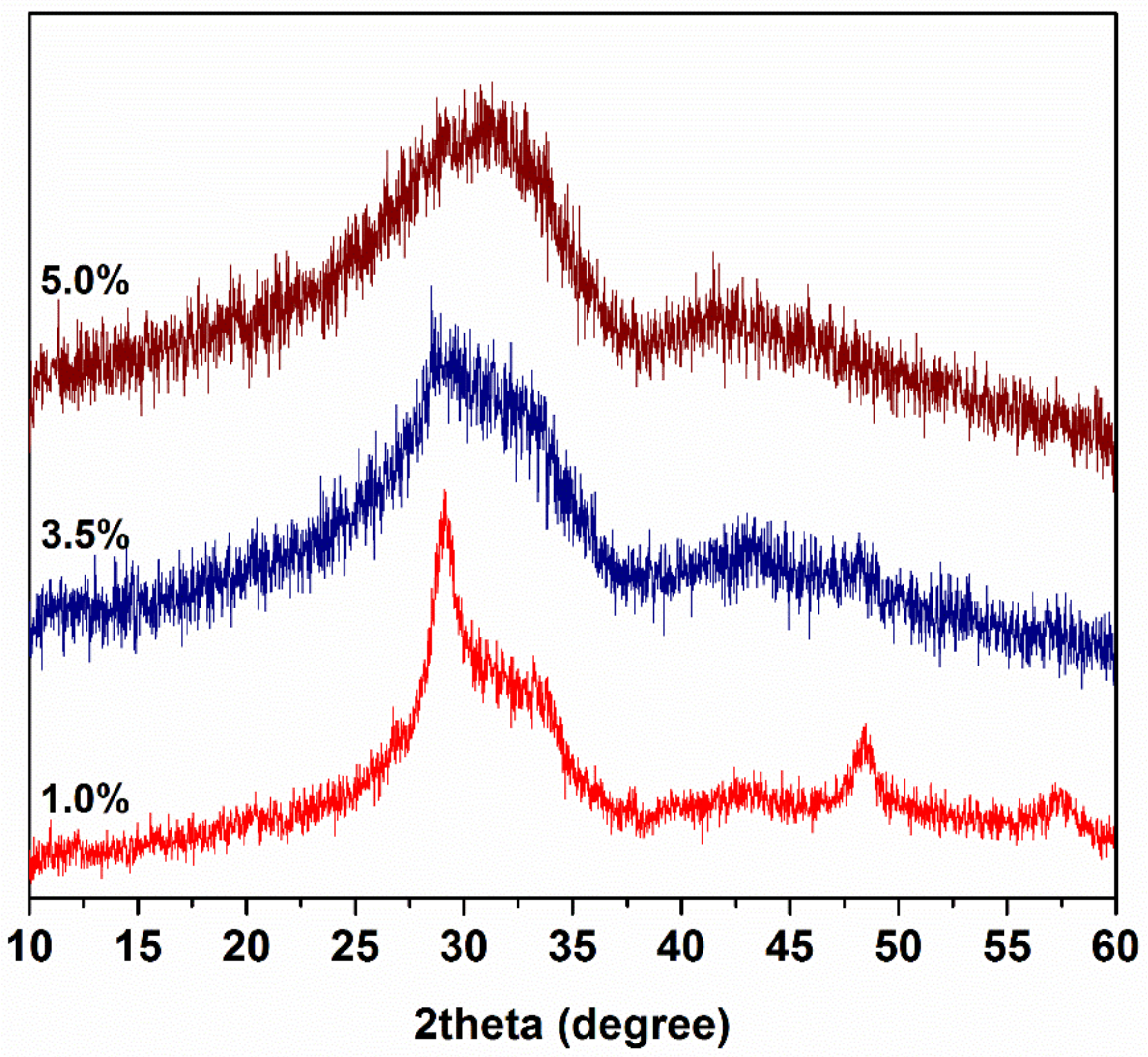

Figure 35. XRD patterns of the Nd^{3+}:YAG (1.0, 3.5 or 5.0%) powders obtained by SP without thermally treated. y axis: normalized intensity.

In the next step, the materials were heat treated at 900 °C for 3 h. The XRD results are showing in Figure 36, where is possible to observe that the YAG phase emerged but secondary structures as yttrium aluminum monoclinic (YAM) and yttrium aluminum perovskite (YAP) also be observed as spurious phases.

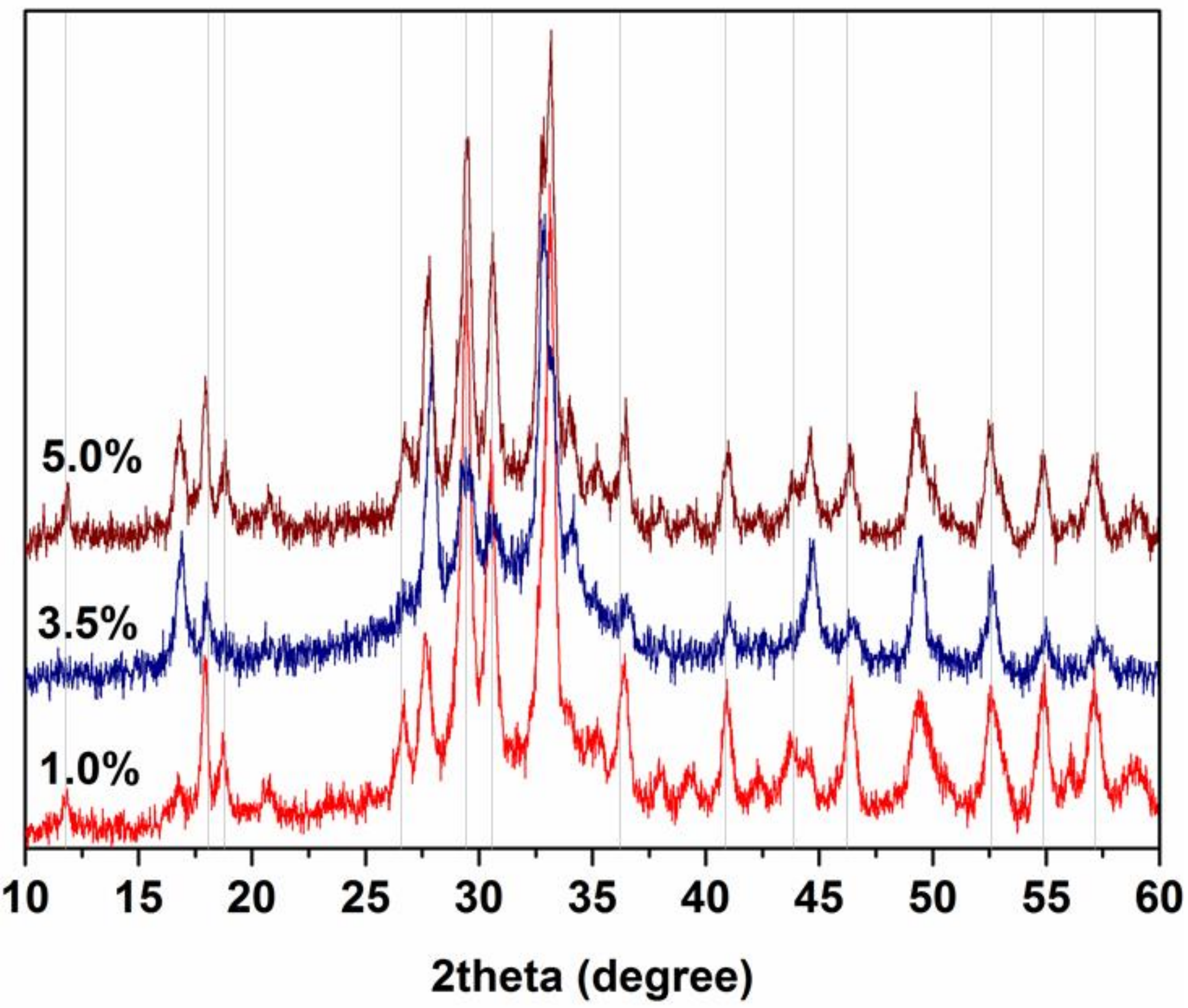

Figure 36. XRD patterns of the Nd^{3+}:YAG (1.0, 3.5 or 5.0%) powders obtained by SP and thermally treated at 900 ºC for 3 h. y axis: normalized intensity.

After a thermal treatment at 900 °C, several peaks referring to different planes were observed. Some of them can be attributed to intermediate phases of the Al_2O_3-Y_2O_3 binary system already described, for example, in 11.8, 17.9, 18.9, 26.7, 29.5, 30.6, 36.4, 41.0, 43.0, 46.4, 52.5, 54.9, and 57.1° 2theta positions, related to plans and the respective phases (011)-YAM, (211)-YAG, (012)-YAM, (111)-YAP, (400)-YAG, (023)-YAM, (422)-YAG, (521)-YAG, (232)-YAM, (532)-YAG, (444)-YAG, (640)-YAG, and (642)-YAG [7,25,208].

Thus, a new thermal treatment of the materials was carried out, just at 1100 °C for 30 minutes. Figure 37 shows the XRD results obtained.

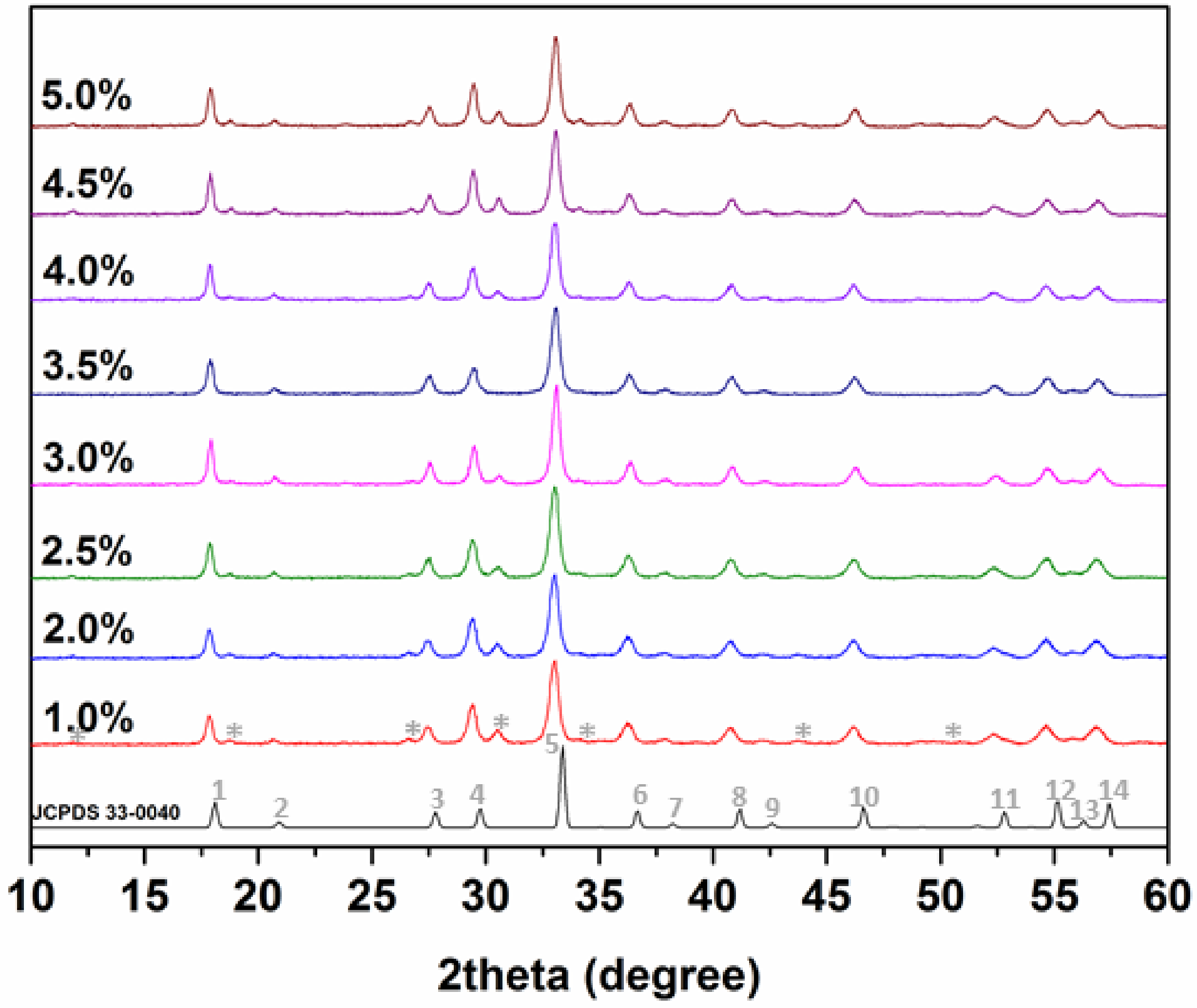

Figure 37. XRD patterns of the Nd^{3+}:YAG (1.0, 2.0, 2.5, 3.0, 3.5, 4.0, 4.5 or 5.0%) powders obtained by SP and thermally treated at 1100 °C for 30 minutes. y axis: normalized intensity.

Now, a preferential structure adopted from the material composition emerged, these diffractograms showed the peaks (noted from 1 to 14, respectively) related to the YAG structural planes (211), (220), (321), (400), (420), (422), (431), (521), (440), (532), (444), (640), (721), and (642) at 2θ close to 18.1, 20.9, 27.8, 29.7, 33.4, 36.7, 38.2, 41.2, 42.6, 46.6, 52.8, 55.1, 56.3, and 57.4° respectively [7]. This confirmed that the YAG structure was formed [209] after treatment at 1100 °C per 30 minutes and indicated that the 'garnet' phase (space group I_a3_d) [36] was obtained for all the studied concentrations.

However, in 2theta approximately equal to 12, 19, 26, 30, 34, 43 and 51° (noted with *****) there are also spurious peaks not indexed to the YAG structure. These peaks are attributed to the monoclinic (YAM) and perovskite (YAP) phases, which were formed and remained even after the heat treatment to which the material was submitted [7]. Due to the YAM phase, we have the occurrence of peaks at 2theta approximately equal to 12, 19, 30, and 43°, relative to the (011), (012), (023) and (232) planes [25], respectively; and to the YAP phase, we have, in 2theta equal to approximately 26, 34 and 51º, the peaks related to the planes (111), (121) and (230) [208].

Finally, to study the behavior of Nd^{3+} ion, *e.g.*, as lasing emission, a further thermal treatment was required to avoid spurious phases and confirm the pure YAG phase. Then, the next strategy adopted was the thermal treatment of the samples at 1100 °C for 12 h. The diffractograms obtained in the sequence are shown in Figure 38.

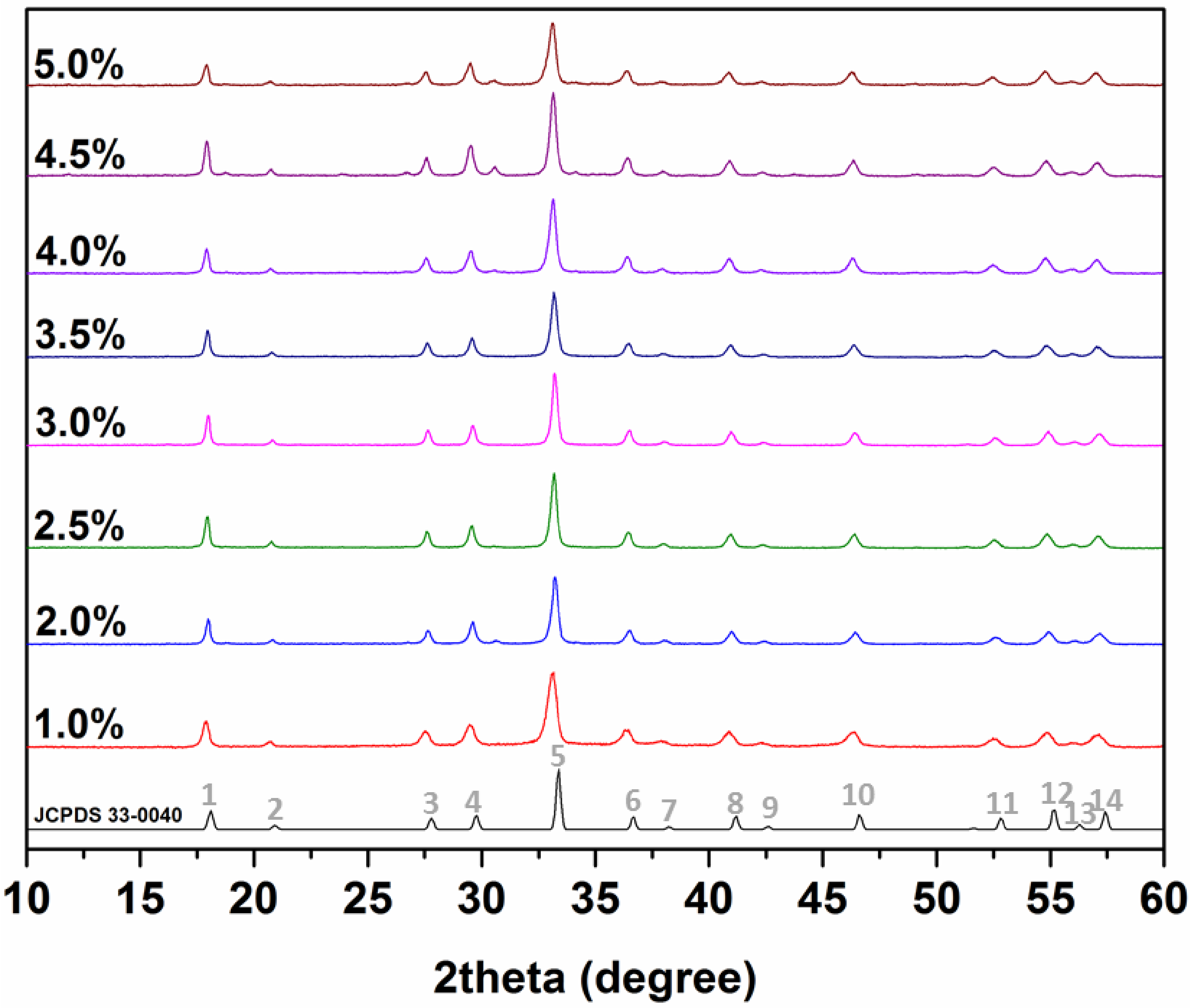

Figure 38. XRD patterns of the Nd^{3+}:YAG (1.0, 2.0, 2.5, 3.0, 3.5, 4.0, 4.5 or 5.0%) powders obtained by SP and thermally treated at 1100 ºC for 12 h.

Over again, these diffractograms contained the peaks (noted from 1 to 14) related to the YAG structural planes, confirming that the YAG structure was formed and it's pure after treatment at 1100 °C for 12 h in all the studied concentrations. As already mentioned, in the YAG structure, Nd^{3+} replaces Y^{3+} in D_2 symmetry sites. Whereas crystalline YAG has a body-centered cubic lattice, Y^{3+} (ionic radius = 1.159 Ǻ) replacement with the larger Nd^{3+} (ionic radius = 1.249 Ǻ) limits Ln ion insertion in this crystal lattice, and such insertion modifies the cell parameters [210]. Kostic *et. al.* [211] calculated the lattice parameter for pure YAG (a = 11.9538 Å) and Nd^{3+}:YAG (doped with 0.8 wt.% Nd^{3+}) single crystals (a = 11.9677 Å) and obtained a difference of 0.12% between these values. On the other hand, for materials consisting of nanoparticles, Li *et. al.* [212] calculated the lattice parameters for pure YAG (a = 12.0598 Å) and Nd^{3+}:YAG doped with 1.0% (a = 12.0619 Å) or 3.0% (a = 12.0703 Å) Nd^{3+} (% wt.) and achieved a difference of 0.017 and 0.087%, respectively. In the same way, Sakar *et. al.* [41] reported values for pure YAG (a = 12.042 Å), Nd^{3+}:YAG doped with 3.0% wt. Nd^{3+} (a = 12.044 Å), and Nd^{3+}:YAG doped with 5.0% wt. Nd^{3+} (a = 12.060 Å), to obtain a difference of 0.017 and 0.15% between pure YAG and Nd^{3+}:YAG doped with 3.0% or 5.0% wt. Nd^{3+}, respectively. In general, independent of the synthesis route and the characteristics of the resulting material, Nd^{3+} (whose ionic radius is 7.76% greater than the Y^{3+} ionic radius) will significantly increase the lattice parameters, which in turn will shift the diffraction peaks to the left (to lower 2theta values) [7,41,210,212]. This behavior is clear in the XRD patterns shown in Figure 39 below.

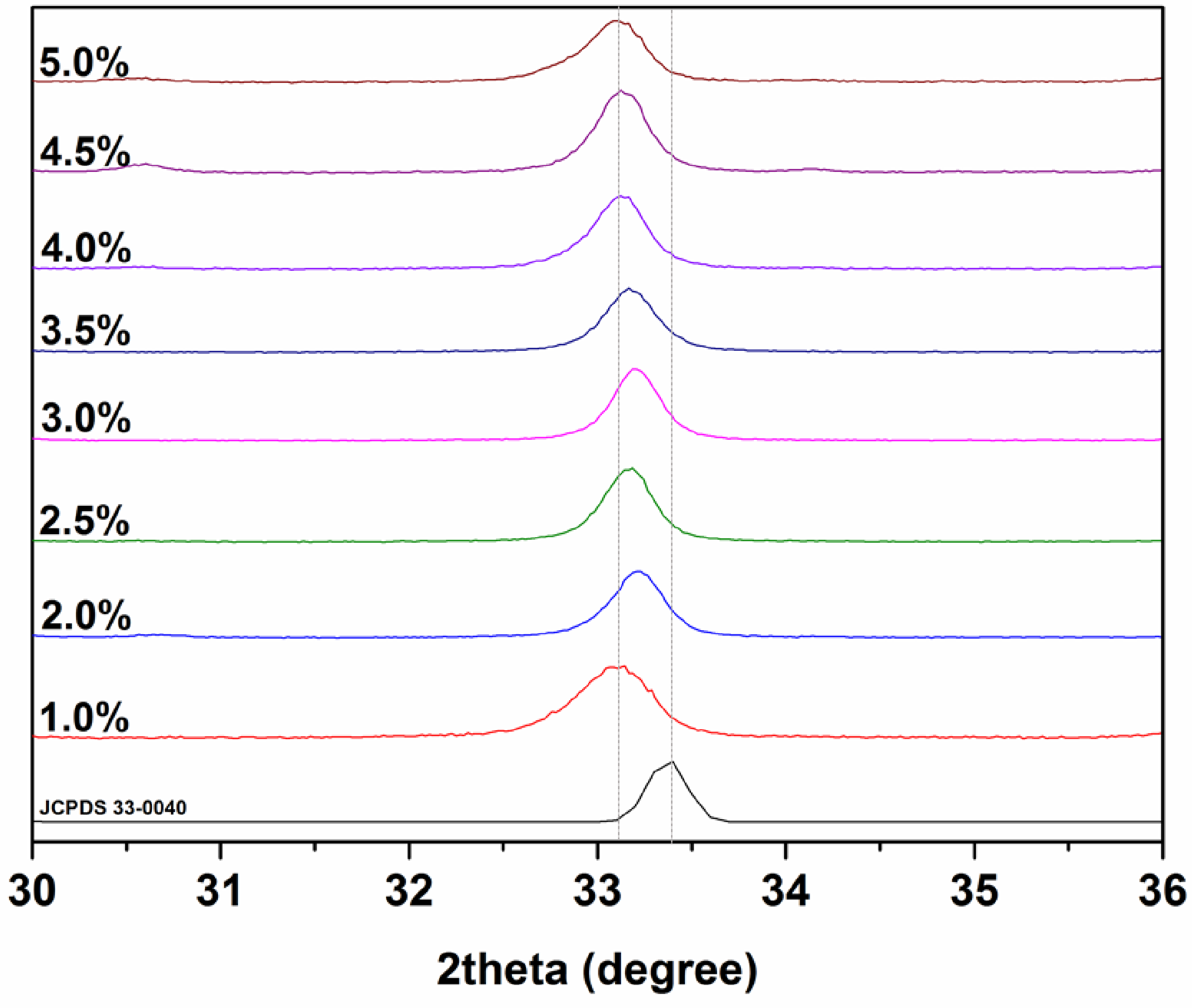

Figure 39. XRD patterns of the Nd^{3+}:YAG (1.0, 2.0, 2.5, 3.0, 3.5, 4.0, 4.5 or 5.0%) powders obtained by SP and thermally treated at 1100 °C for 12 h. Focus for the region between 30-36 degree.

As explained before, the higher Nd^{3+} content in the YAG structure significantly shifted the 2theta values as compared to other materials reported in the literature [209,213], *e.g.*, the peak at 2theta = 33.4° on diffraction patterns (JCPDS 33-0040) was shifted to 33.1° on YAG doped with 5.0% wt. Nd^{3+}, as a consequence of larger ionic radius of the Nd^{3+} ion, so the lattice parameters were enlarged, and that shift increases with Nd^{3+} content, from 2.0 to 5.0%. In Figure 39, it was possible to observe a similar shift for the sample doped only with 1.0% wt. Nd^{3+}, so the peak shift was not linear with the Nd^{3+} concentration. For that sample, a further consideration could be pointed at the lower crystallinity, as corroborated by the larger full width at half maximum (FWHM). Nevertheless, we confirmed that the YAG structure was formed, and that the methodology employed here could be useful to produce this phosphor on a large scale.

As described previously, the YAG crystalline structure could be depicted as a complex cube with three different types of polyhedron. In such structure, Y^{3+} occupies dodecahedral sites, and Al^{3+} occupies both octahedral and tetrahedral sites. A 2:3 Y^{3+}/Al^{3+} ratio is respected; the unit cell contains 8 $Y_3Al_5O_{12}$ units; and YAG presents 18 active modes in the infrared [6,36,210]. We recorded the FTIR spectra of all the YAG:Nd^{3+} samples and the spectra of 1.0, 3.5 and 5.0% Nd^{3+} samples (thermally treated at 1100 ºC for 30 minutes) are displayed in Figure 40, which shows the presence of the main bands between 900 and 400 cm^{-1}.

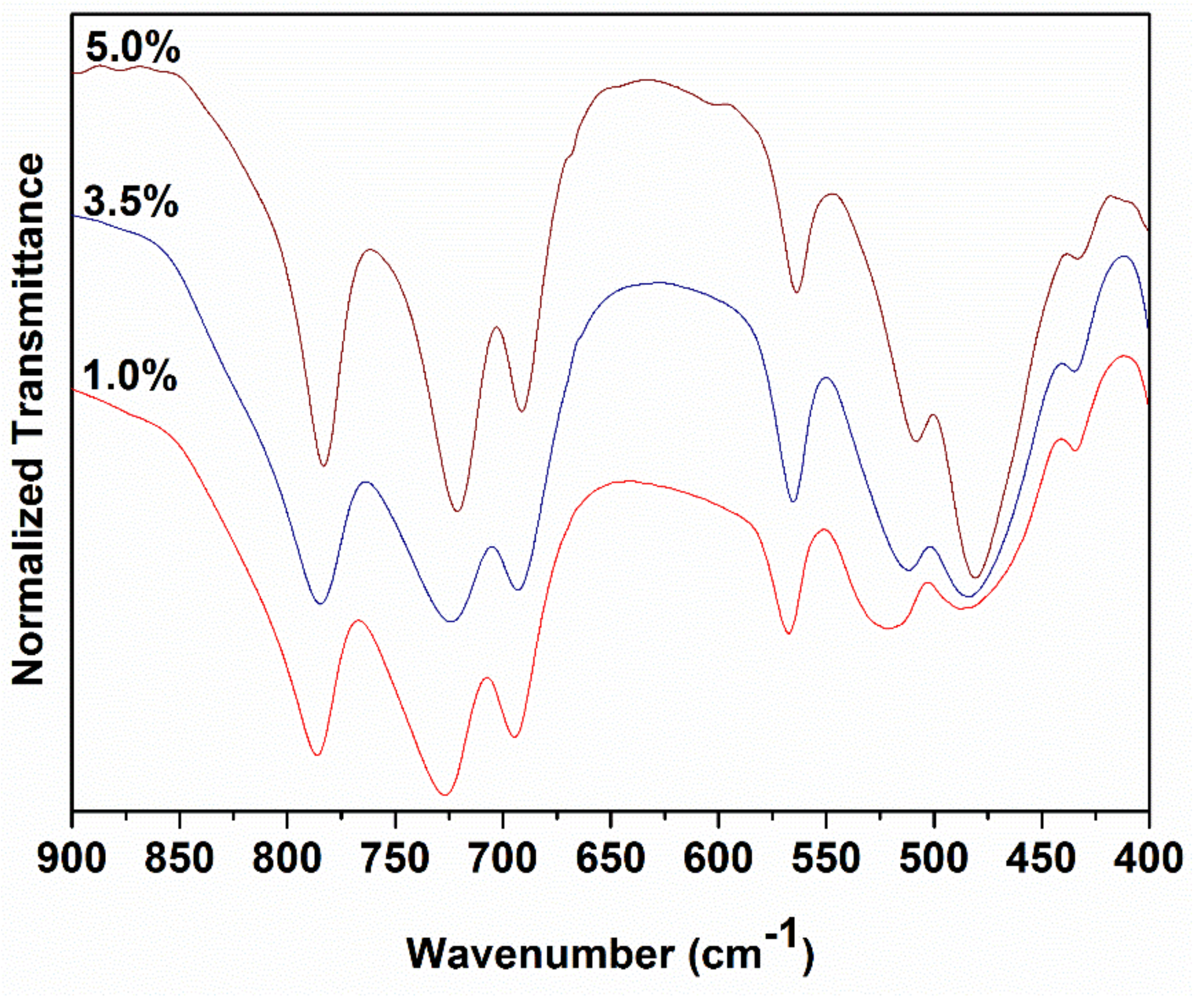

Figure 40. FTIR spectra (at KBr medium, cm^{-1}) of the Nd^{3+}:YAG (1.0, 3.5 e 5.0%) powders obtained via SP and thermally treated at 1100 ºC for 30 minutes.

On the other hand, the additional crystalline phase observed by XRD (YAM) presented a monoclinic crystal structure and $P_{21/c}$ space group, there are four different Y^{3+} sites in asymmetric units of $Y_4Al_2O_9$. As a consequence, the YAM has 45 active modes in the infrared, so, in the wavenumber range analyzed by FTIR spectra, there are bands from both structures resulting from vibrations of the bonds between oxygen atoms and metals (Y-O and Al-O), which are in positions 788, 728, 693, 568, 519 and 474 cm^{-1} [214]. These bands are assigned to the symmetric ν_3 (Al-O tetrahedral); ν_3 (Al-O); ν_3 (Y-O); ν_4 symmetric and asymmetric (A-O octahedral); ν_4 (Y-O) and ν_4 symmetric, respectively [209]. Most of the bands related to the YAM structure are overlapped by the YAG bands, except for the set of three bands between 900-850 cm^{-1}, related to the asymmetric stretching ν_1 (Al-O tetrahedral) and ν (Y-O) in the monoclinic structure [25] (better observed in the spectrum of the sample Nd^{3+}:YAG 5.0%).

After the thermal treatment at 1100 °C for 12 h, the FTIR spectra for the samples doped with 1.0, 3.5 and 5.0% of Nd^{3+} were obtained and are shown in Figure 41.

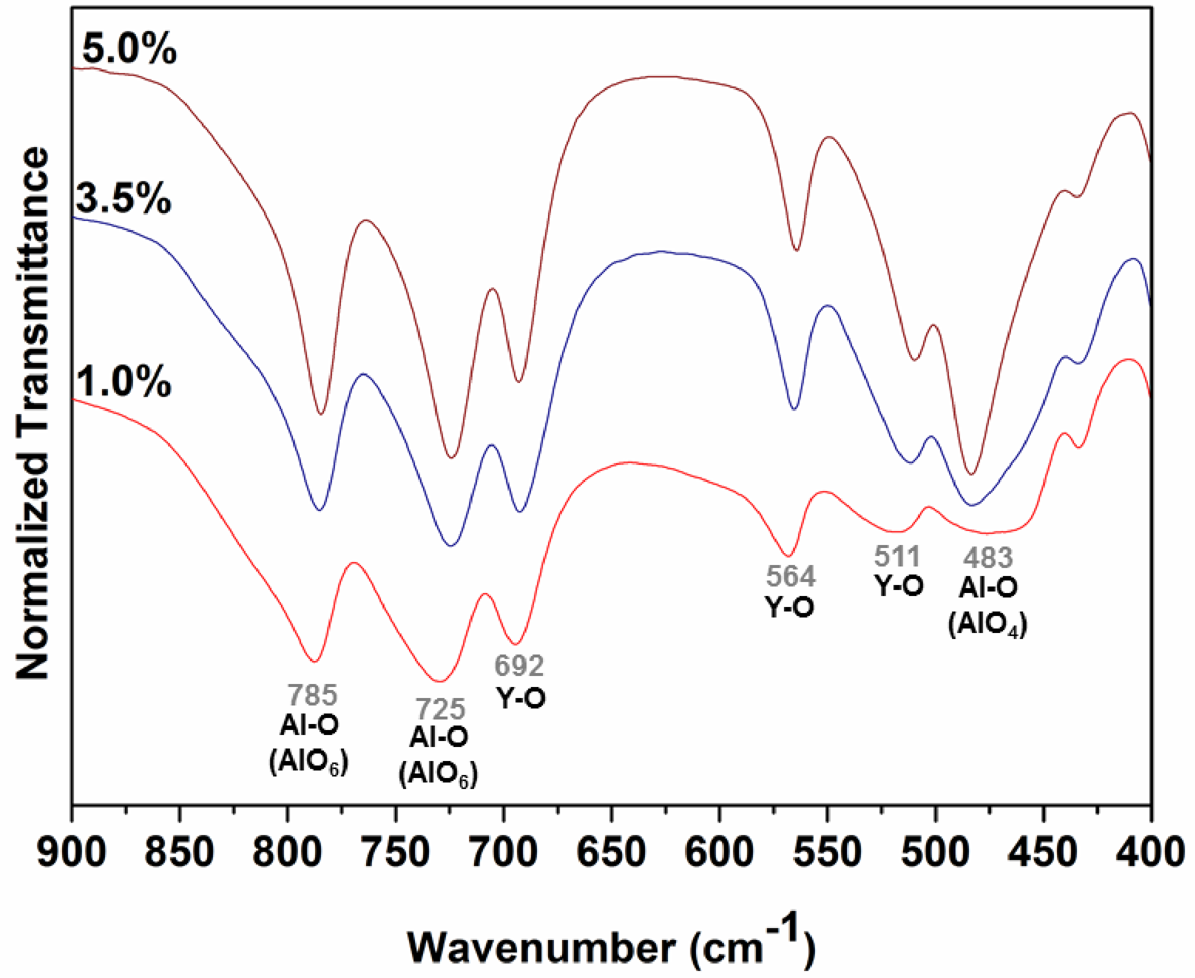

Figure 41. FTIR spectra (at KBr medium, cm^{-1}) of the Nd^{3+}:YAG (1.0, 3.5 e 5.0%) powders obtained via SP and thermally treated at 1100 ºC for 12 h.

On the basis of the FTIR analyses, all samples presented bands due to the metal-oxygen vibrations bonds (*e.g.*, Al-O and Y-O) at 788, 728, 693, 568, 519 and 474 cm^{-1}, as already described. The bands at 785 and 725 cm^{-1} were related to the stretching vibrations of AlO_6 in octahedral sites, whereas the bands at 483 and 434 cm^{-1} were attributed to AlO_4 in tetrahedral sites. Finally, the bands at 692, 564 and 511 cm^{-1}, associated with Y-O vibrations [41,209,214], confirmed that the YAG structure emerged, in agreement with the XRD data. It is also possible to observe that the 900-850 cm^{-1}, related to the asymmetric stretching ν_1 (Al-O tetrahedral) and ν (Y-O) in the monoclinic structure bands referring to the YAM structure are not present.

After this structural study with the YAG particles doped with Nd^{3+} ions, the other materials obtained in this work, Yb^{3+}/Er^{3+}:YAG and Yb^{3+}/Tm^{3+}:YAG particles, were prepared by the same methodology and treated directly at 1100 °C, for 12 h, in sequence. Figure 42 shows the diffractograms of the Yb^{3+}/Er^{3+}:YAG particles, which presented fourteen main peaks at 2theta close to 18.1, 21.0, 27.8, 29.7, 33.3, 36.6, 38.2, 41.0, 42.6, 46.5, 52.7, 55.1, 56.1, and 57.3°, related to the YAG structural (space group I_a3_d) planes (211), (220), (321), (400), (420), (422), (431), (521), (440), (532), (444), (640), (721), and (642), respectively. The diffractograms confirmed that SP and heat treatment afforded the target phase without spurious phases for the samples doped with this pair of ions also.

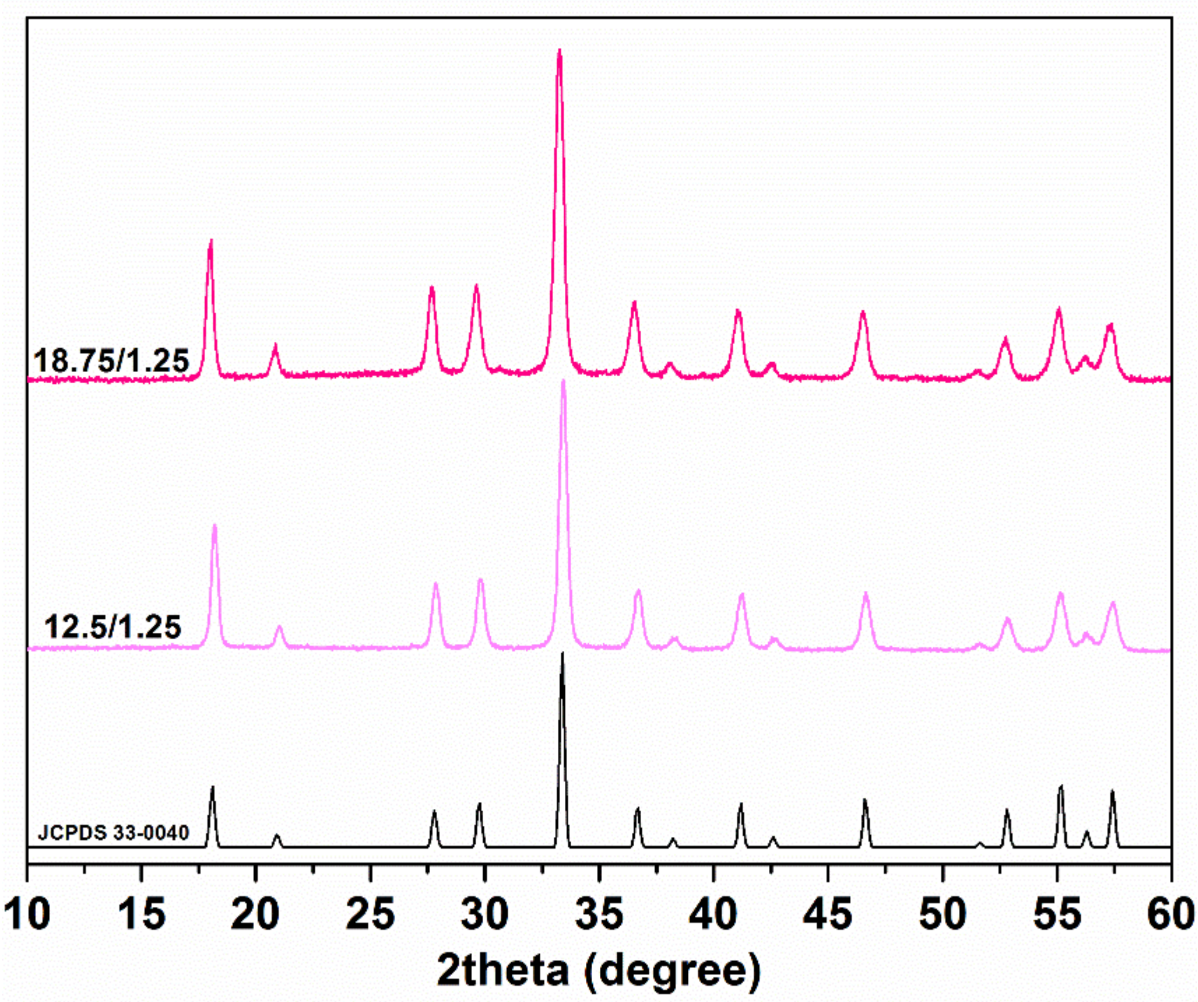

Figure 42. XRD patterns of Yb^{3+}/Er^{3+}:YAG (Yb^{3+}/Er^{3+} % ratio of 12.5/1.25 or 18.75/1.25) particles obtained by SP and heat treated at 1100 ºC for 12 h. y axis: normalized intensity.

In the same way, for samples doped with the Yb^{3+}/Tm^{3+} pair, the acquired patterns for all samples (Figure 43) confirmed the Yttrium Aluminum Garnet structure, as YAG phase, as corroborated by the JCPDS 33-0040 pattern.

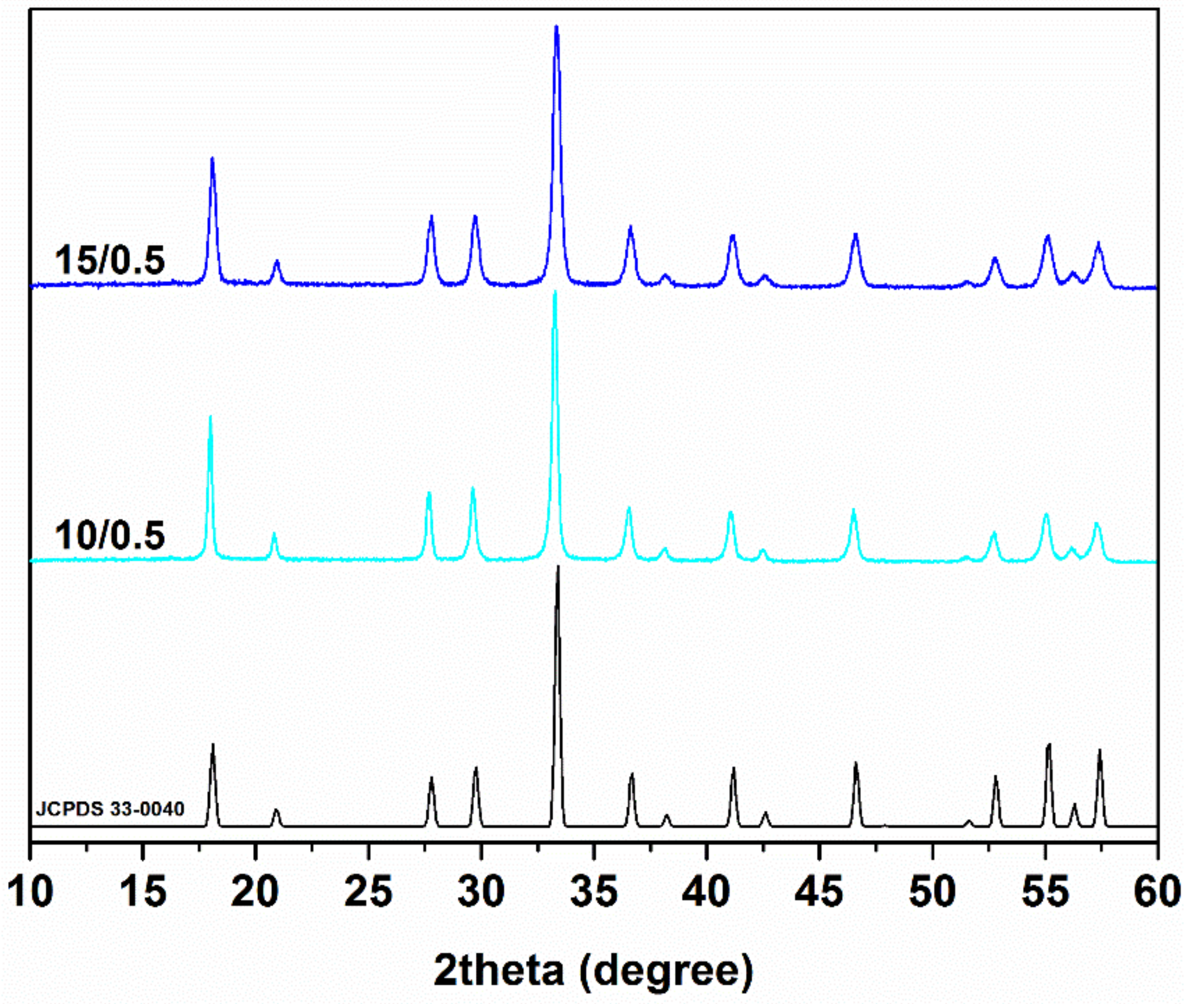

Figure 43. XRD patterns of Yb^{3+}/Tm^{3+}:YAG (Yb^{3+}/Tm^{3+} % ratio of 10/0.5 or 15/0.5) particles obtained by SP and heat treated at 1100 °C for 12 h. y axis: normalized intensity.

The used methodology to obtain the Ln^{3+}:YAG particles depends on aerosol generation. Each droplet acts as an individual reaction vessel, and particle morphology results from chemical and physical processes taking place inside the droplet. The particles that we obtained here were spherical with a broad size distribution, as illustrated in Figures 44 and 45 for the Nd^{3+}:YAG, Yb^{3+}/Er^{3+}:YAG and Yb^{3+}/Tm^{3+}:YAG samples, respectively. The SEM images revealed that dense spherical particles with sizes ranging between 100 and 2000 nm and average diameter of 600 nm were formed, see histogram in Figure 45-(e), resulting from droplet coalescence before the drying process due to spatial constraint into SP setup. The morphology of the materials obtained by this method depends on the synthesis conditions and precursor [4]. Herein, polymerization of the precursor boehmite and the solvent evaporation rate progressively moved the air/solution interface from the surface to the interior, which culminated in a dense and spherical particle. In fact, the evaporation process could produce a hollow particle if the solute diffusion is not efficient, but herein, the use of aluminum alkoxide allowed a continuous polymerization process to produce the gel phase, so the three-dimensional structure was formed in the precursor and that network will remain in the droplet at the drying section. The gel structure allows the solvent evaporation without the precipitation only on the surface and it avoids the precursor segregation. In addition, it is possible to observe that even after the heat treatment at 1100 °C for 12 h the particles coalescence was not noted.

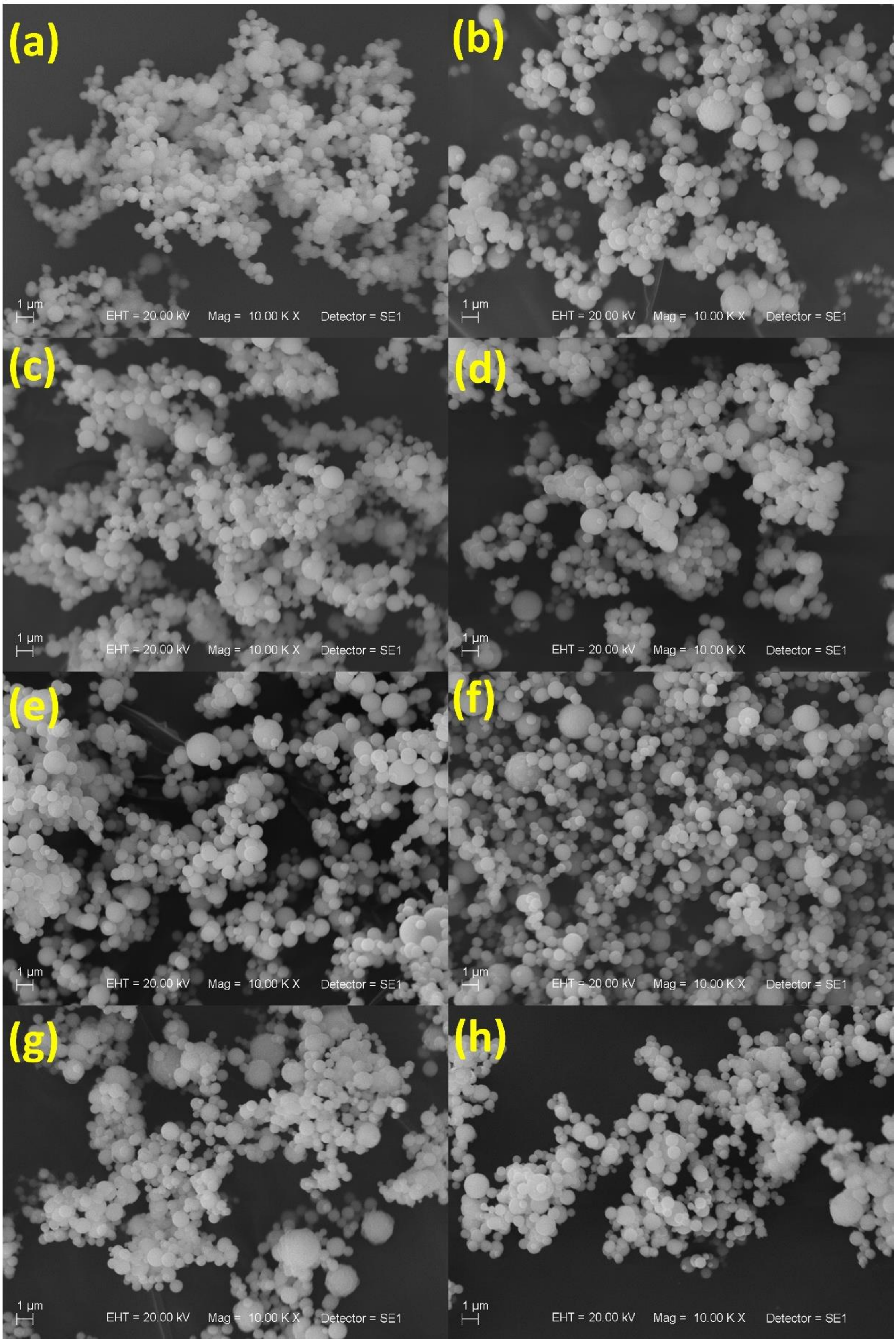

Figure 44. SEM images of the Nd^{3+}:YAG ((a) 1.0, (b) 2.0, (c) 2.5, (d) 3.0, (e) 3.5, (f) 4.0, (g) 4.5 and (h) 5.0%) powders obtained by SP and thermally treated at 1100 ºC for 12 h. Scale bar = 1 μm.

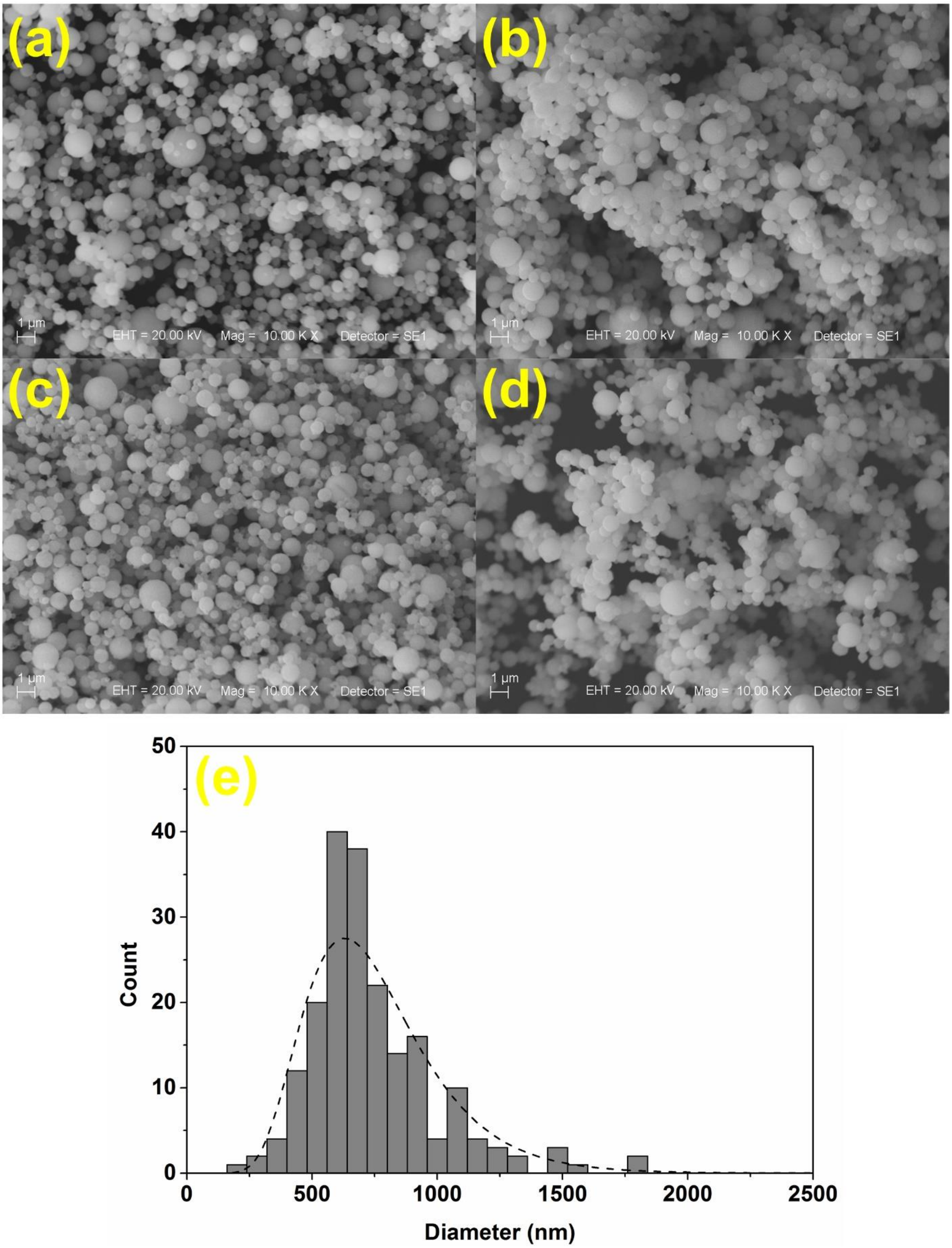

Figure 45. SEM images of the Yb^{3+}/Er^{3+}:YAG (Yb^{3+}/Er^{3+} % ratio of (a) 12.5/1.25 and (b) 18.75/1.25), and Yb^{3+}/Tm^{3+}:YAG (Yb^{3+}/Tm^{3+} % ratio of (c) 10/0.5 and (d) 15/0.5) powders obtained by SP and thermally treated at 1100 ºC for 12 h. Scale bar = 1 µm. (e) Typical diameter distribution from SP samples, that result was obtained from the Nd^{3+}:YAG (3.5%) sample.

After the structural and morphological characterization of the particles, the next paragraphs will show their luminescent properties studied via photoluminescence spectroscopy. And the results will be presented individually for each ion and/or ion pair doping.

4.2. Spectroscopic characterization

4.2.1. Nd^{3+}:YAG particles

Nd^{3+}-doped YAG is a well-known material for photonic applications, so we investigated the luminescent properties of the samples prepared by SP. In Figure 46 it was possible to corroborated the additional crystalline phase already discussed in the XRD analyses. The emission spectrum of the sample with 1.0% doping, treated at 1100 °C for 30 minutes showed two narrow bands between 937 and 945 nm attributed to the $^4F_{3/2} \rightarrow {}^4I_{9/2}$ transition. From 1040 to 1140 nm, there were eleven well-resolved bands concerning the $^4F_{3/2} \rightarrow {}^4I_{11/2}$ transition; the most intense band appeared at 1064 nm. Finally, the region from 1320 to 1360 nm contained bands of low intensity, assigned to the $^4F_{3/2} \rightarrow {}^4I_{13/2}$ transition [39,214,215].

In addition, the YAM phase contribution in that spherical particle was also confirmed. Indeed, Figure 46 shows the different profile for the $^4F_{3/2} \rightarrow {}^4I_{9/2}$ transition: Nd^{3+} insertion into the monoclinic structure led to three extra bands between 1080 as 1100 nm **(*)** as compared to the pure YAG spectral profile. These bands agreed with the characteristic emission of Nd^{3+} incorporated into a monoclinic structure, with C_1 symmetry [216].

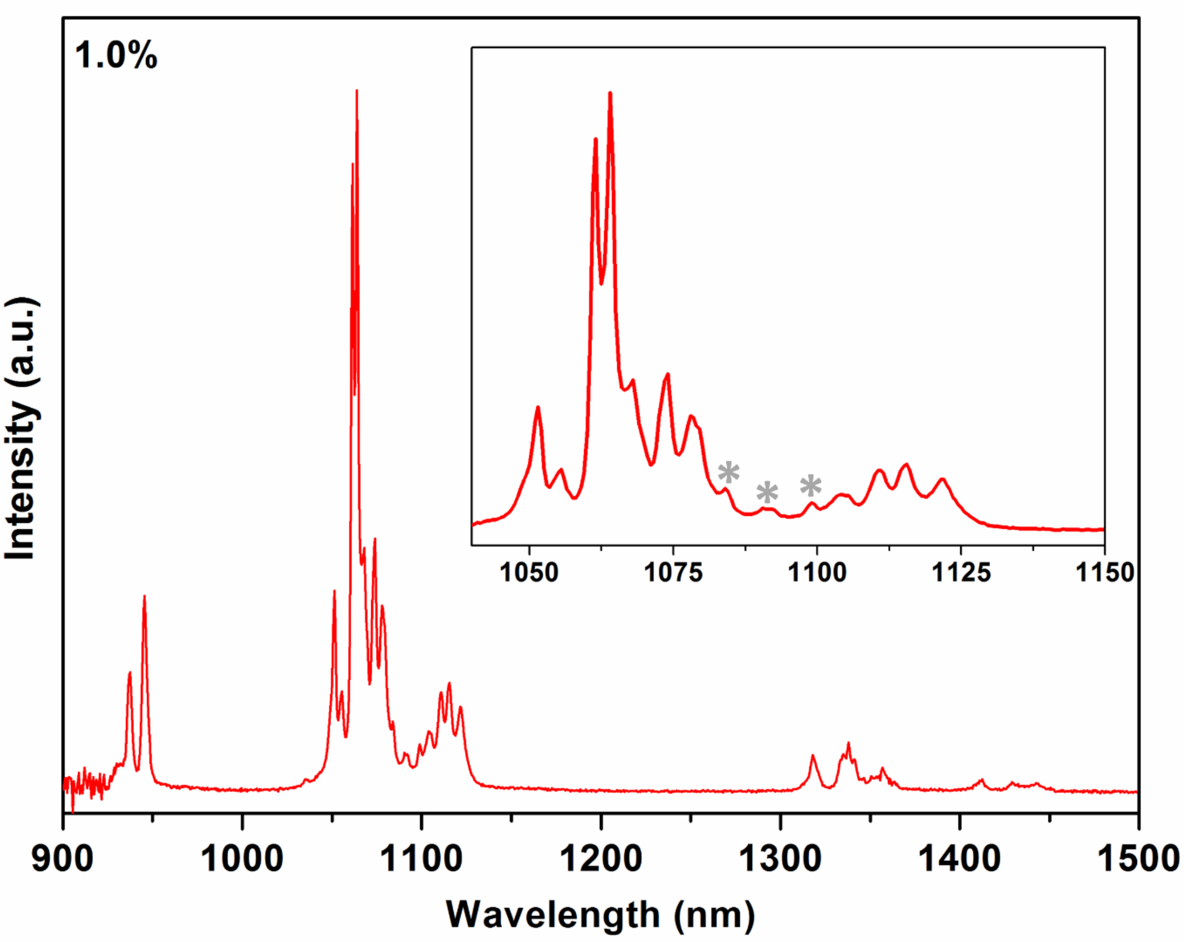

Figure 46. Emission (λ_{ex} = 808 nm) spectra of the Nd^{3+}:YAG (1.0%) powders obtained by SP and thermally treated at 1100 ºC for 30 minutes. Focus for 1050-1150 nm region.

After thermal treatment at 1100 °C for 12 h, the emission spectra of the samples were again obtained, as well as the excitation spectra, as shown in Figure 47.

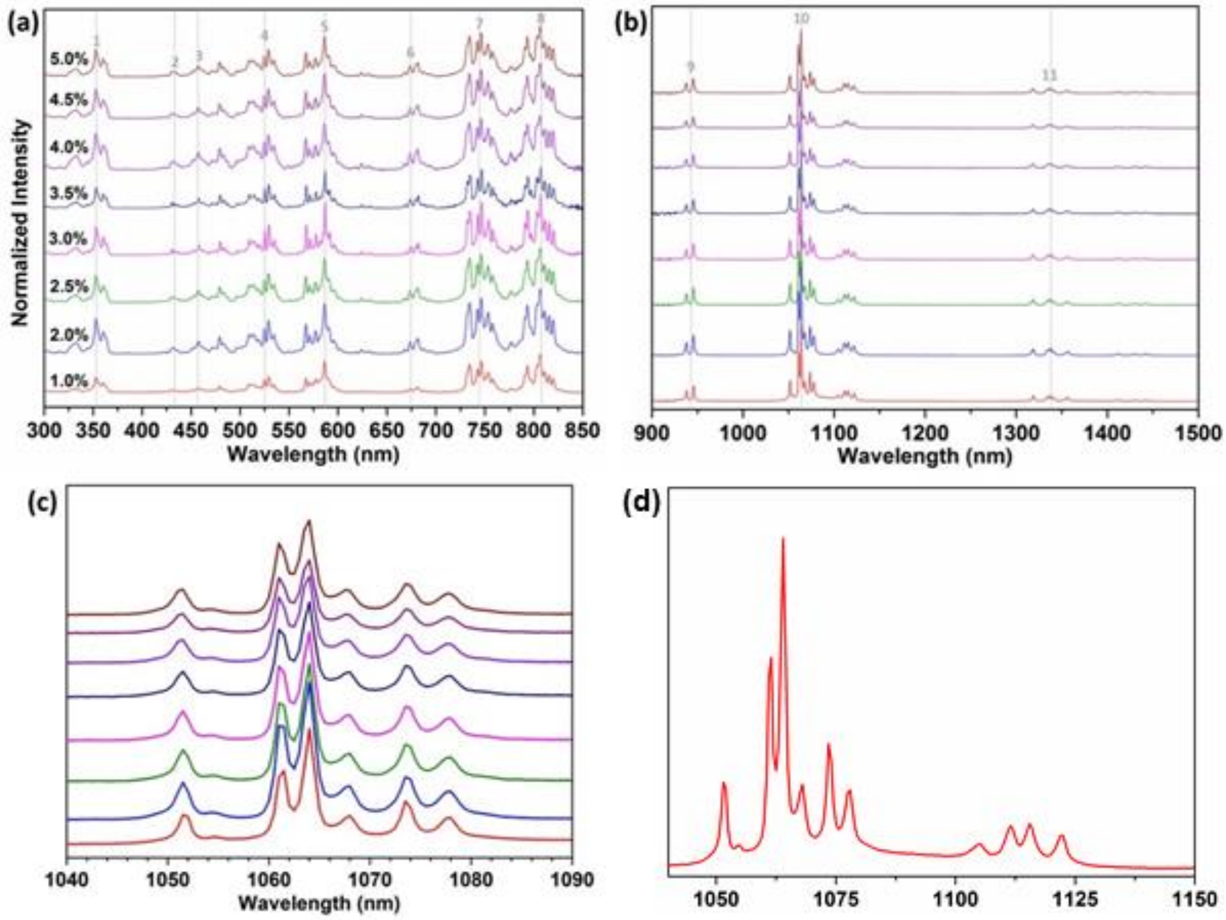

Figure 47. (a) Excitation (λ_{em} = 1064 nm) and (b) emission (λ_{ex} = 808 nm) spectra of the Nd^{3+}:YAG (X%) powders obtained by SP and thermally treated at 1100 ºC for 12 h, and (c) zoom at the spectral range from 1050-1080 nm, and (d) from 1040-1150 nm for Nd^{3+}:YAG (1.0%) sample.

The excitation spectra (Figure 47-(a)) were acquired by monitoring the $^4F_{3/2} \rightarrow {}^4I_{11/2}$ transition at λ_{em}= 1064 nm. The spectra were compatible with a highly crystalline sample that displayed narrow and well-resolved bands characteristic of the Nd^{3+} f-f transitions in the YAG structure. For the Nd^{3+}:YAG samples, the bands were attributed as follows: (1) 325–375 nm ($^4I_{9/2} \rightarrow {}^4D_{3/2}$, $^4D_{1/2}$), (2) 425–440 nm ($^4I_{9/2} \rightarrow {}^2D_{5/2}$), (3) 450–470 nm ($^4I_{9/2} \rightarrow {}^4G_{9/2}$, $^4G_{11/2}$, $^2K_{15/2}$), (4) 500–550 nm ($^4I_{9/2} \rightarrow {}^4G_{7/2}$, $^4G_{9/2}$, $^2K_{13/2}$), (5) 560–600 nm ($^4I_{9/2} \rightarrow {}^4G_{5/2}$, $^4G_{7/2}$, $^2H_{11/2}$), (6) 660–700 nm ($^4I_{9/2} \rightarrow {}^4F_{9/2}$), (7) 725–775 nm ($^4I_{9/2} \rightarrow {}^4F_{7/2}$, $^4S_{3/2}$), and (8) 780–825 nm ($^4I_{9/2} \rightarrow {}^4F_{5/2}$, $^5H_{9/2}$). The emission spectra of the Nd^{3+}:YAG samples (Figure 47-(b), λ_{ex}= 808 nm-laser) displayed the bands that are typical of the f-f transitions from Nd^{3+} replacing Y^{3+} at dodecahedral sites (D_2 symmetry) in the YAG cubic structure. The two narrow bands (9) between 937 and 945 nm were attributed to the $^4F_{3/2} \rightarrow {}^4I_{9/2}$ transition. From 1040 to 1140 nm (10), there were eleven well-resolved bands concerning the $^4F_{3/2} \rightarrow {}^4I_{11/2}$ transition; the most intense band appeared at 1064 nm. Finally, the region from 1320 to 1360 nm (11) contained bands of low intensity, assigned to the $^4F_{3/2} \rightarrow {}^4I_{13/2}$ transition, and the Figure 47-(c) shows the zoom of the spectral range from 1050-1080 nm [39,214,215]. Figure 47-(d) shows the zoom of the spectral range from 1040-1150 nm where it is possible to observe the absence of bands belonging to the YAM phase, when compared to the spectrum in the Figure 46. For all the samples, the same emission profile is observed under excitation with Xe lamp, in 526 nm, showed in Figure 48.

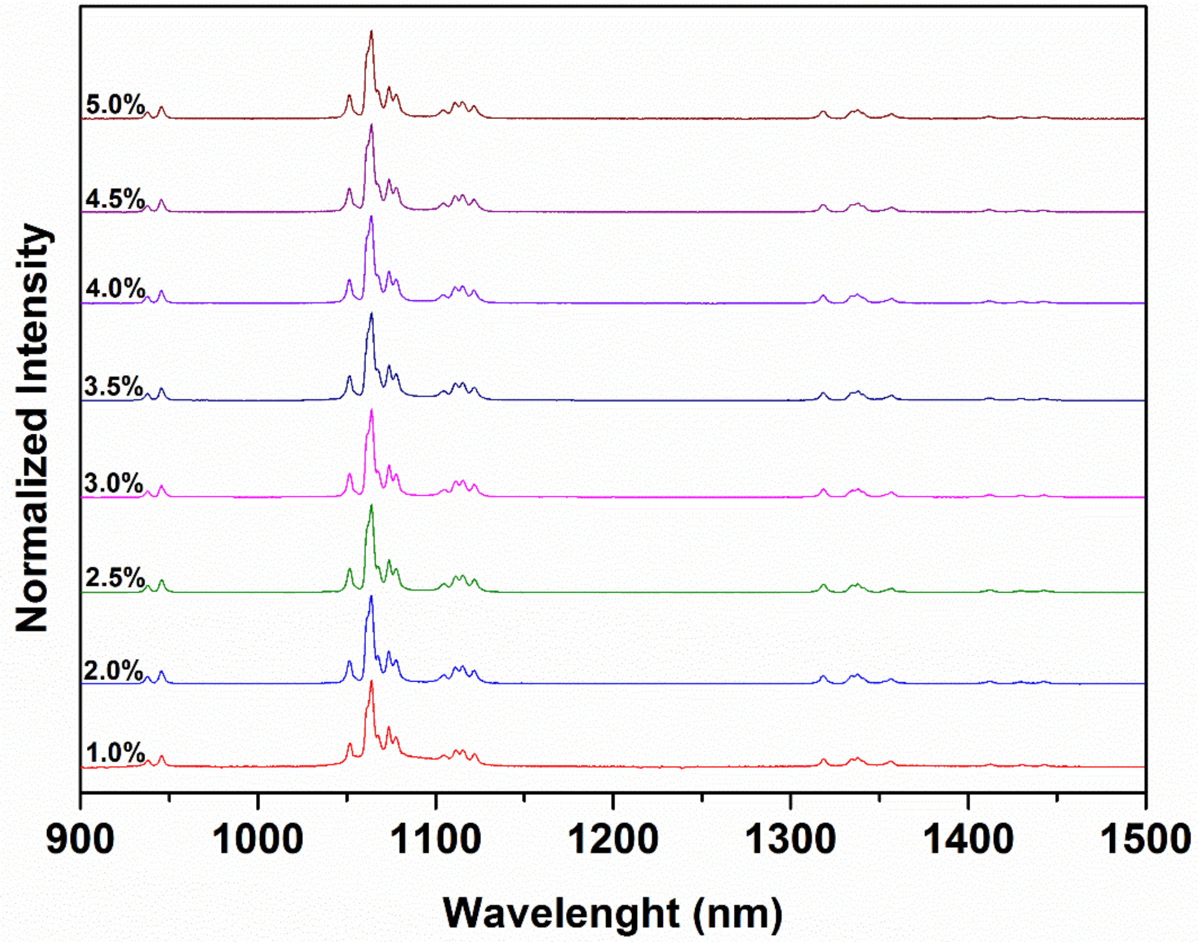

Figure 48. Emission (λ_{ex} = 526 nm) spectra of the Nd^{3+}:YAG (X%) powders obtained by SP and thermally treated at 1100 ºC, X =1.0, 2.0, 2.5, 3.0, 3.5, 4.0, 4.5 and 5.0% Nd^{3+} (mol/mol in relation to Y^{3+}).

We recorded the photoluminescence decay curves for the Nd^{3+} $^4F_{3/2}$ excited state in the YAG lattice for the eight samples (Figure 49). These values agreed with the data reported for similar materials doped with 1.0, 2.0, 3.0, and 4.0% Ln ion: 0.227, 0.184, 0.153, and 0.095 ms [41,217,218], respectively, as shown in the Table 10.

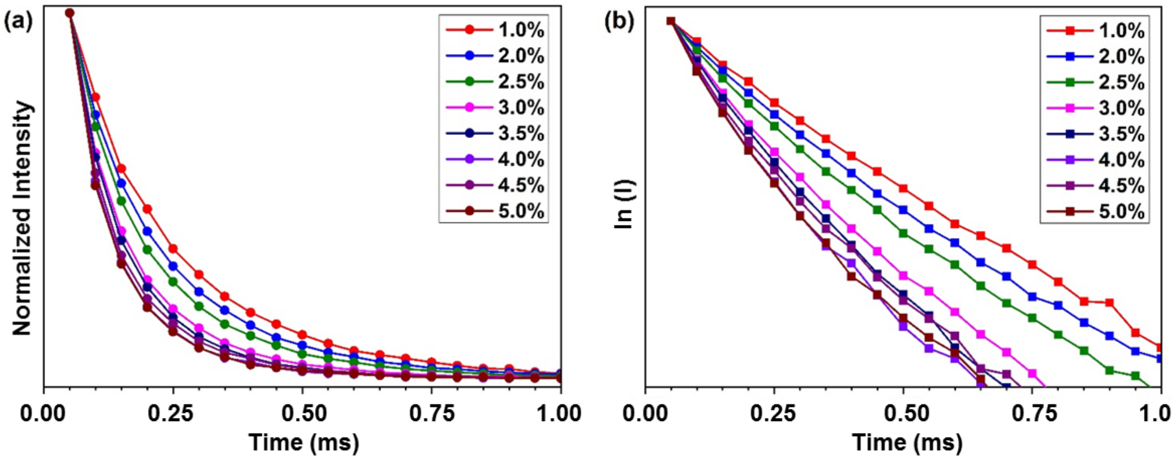

Figure 49. Photoluminescence decay curves of the Nd^{3+} $^4F_{3/2}$ state (λ_{ex} = 526 nm) in the Nd^{3+}:YAG (X%) particles obtained via SP and thermally treated at 1100 ºC. (a) Normalized Intensity *vs* time, and (b) Ln($I_{Normalized}$) *vs* time.

We calculated the lifetimes by the relation I_0/e for all obtained concentrations (1.0, 2.0, 2.5, 3.0, 3.5, 4.0, 4.5 or 5.0 %), and the experimental values were around 0.255, 0.221, 0.196, 0.166, 0,156, 0.141, 0.145 and 0.139 ms, respectively (Table 10). The lifetime decreased with increasing Nd^{3+} concentration, the smaller observed value was 0.139 ms (5.0%), which could result from a quenching effect due to the high concentration of the emitting ion. The higher Nd^{3+} content can reduce the average distance between the Ln centers, and as a consequence, there is an increasing in the probability of nonradiative energy transfer among them and the emitted level could be depopulated [122].

Table 10. Lifetime values for the Nd^{3+} $^4F_{3/2}$ excited state in the YAG matrices for samples obtained in this work (t.w.) compared to others reported in the literature

SAMPLE	LIFETIME (ms)	ref.
Nd^{3+}:YAG (1.0%)	0.255	t.w.
Nd^{3+}:YAG (1.0%)	0.227	41

Nd^{3+}:YAG (2.0%)	0.221	t.w.
Nd^{3+}:YAG (2.0%)	0.184	[218]
Nd^{3+}:YAG (2.5%)	0.196	t.w.
Nd^{3+}:YAG (3.0%)	0.166	t.w.
Nd^{3+}:YAG (3.0%)	0.153	[41]
Nd^{3+}:YAG (3.5%)	0.156	t.w.
Nd^{3+}:YAG (4.0%)	0.141	t.w.
Nd^{3+}:YAG (4.0%)	0.095	[217]
Nd^{3+}:YAG (4.5%)	0.145	t.w.
Nd^{3+}:YAG (5.0%)	0.139	t.w.

4.2.1.1. Composited films by SF + Nd^{3+}:YAG particles

The Nd^{3+}:YAG particles were used to produce new luminescent material based in the SF matrix, so composite films were obtained as self-supported films with six different Nd^{3+} concentration particles. Once the particles were immersed in aqueous SF solution and the films prepared at low temperature (45 ºC), luminescence quenching could occur. To check this, the films were also characterized by the photoluminescent spectroscopy and Nd^{3+} ions properties were evaluated into the matrix.

The excitation spectra (Figure 50, on the left) were acquired by monitoring the $^4F_{3/2} \rightarrow {}^4I_{11/2}$ transition at λ_{em}= 1064 nm. The spectra were compatible with the Nd^{3+}:YAG particles, and the bands were attributed as follows: 325–375 nm ($^4I_{9/2} \rightarrow {}^4D_{3/2}, {}^4D_{1/2}$), 425–440 nm ($^4I_{9/2} \rightarrow {}^2D_{5/2}$), 450–470 nm ($^4I_{9/2} \rightarrow {}^4G_{9/2}, {}^4G_{11/2}, {}^2K_{15/2}$), 500–550 nm ($^4I_{9/2} \rightarrow {}^4G_{7/2}, {}^4G_{9/2}, {}^2K_{13/2}$), 560–600 nm ($^4I_{9/2} \rightarrow {}^4G_{5/2}, {}^4G_{7/2}, {}^2H_{11/2}$), 660–700 nm ($^4I_{9/2} \rightarrow {}^4F_{9/2}$), 725–775 nm ($^4I_{9/2} \rightarrow {}^4F_{7/2}, {}^4S_{3/2}$), and 780–825 nm ($^4I_{9/2} \rightarrow {}^4F_{5/2}, {}^5H_{9/2}$). In emission spectra, Figure 50, on the right (λ_{ex}= 808 nm), is possible to observe that the Nd^{3+} ions' spectroscopic proprieties were held. In all spectra it was observed two narrow bands between 937 and 945 nm, attributed to the $^4F_{3/2} \rightarrow$

$^4I_{9/2}$ transition; from 1040 to 1140 nm, eleven well-resolved bands concerning the $^4F_{3/2} \rightarrow {}^4I_{11/2}$ transition; the most intense band appeared at 1064 nm; and finally, in the region from 1320 to 1360 nm bands of low intensity, assigned to the $^4F_{3/2} \rightarrow {}^4I_{13/2}$ transition.

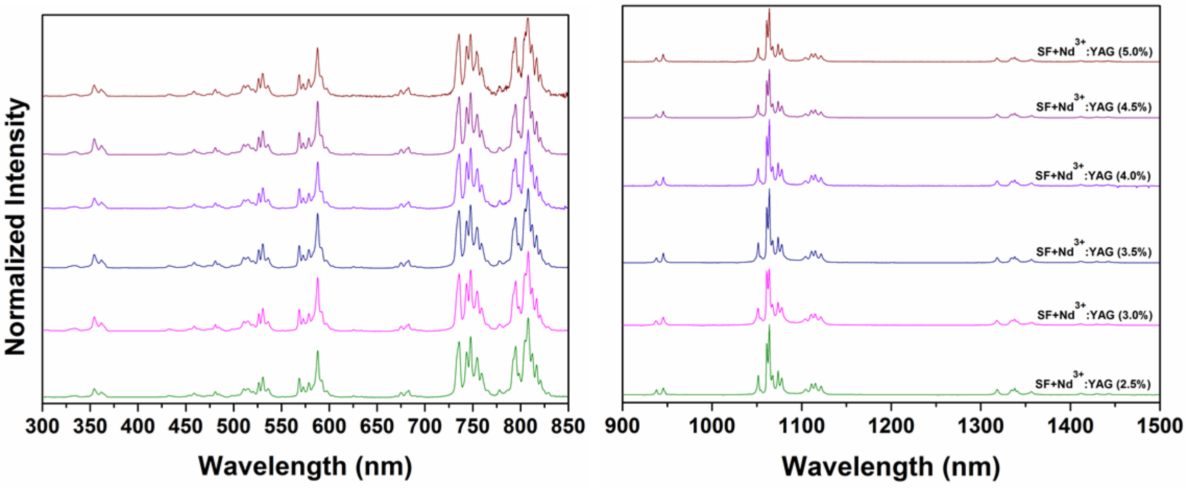

Figure 50. (left) Excitation (λ_{em}= 1064 nm) and (right) emission ($\lambda_{exc=}$ 808 nm) spectra of the SF-Nd^{3+}:YAG (2.5, 3.0, 3.5, 4.0, 4.5, and 5.0%) films.

Based on these results, these self-supporting materials based on Nd^{3+}:YAG particles will be tested for possible RL emission, in order to obtain a self-supported material able of acting as a laser from the combination of multiple scatterings.

4.2.2. Yb^{3+}/Er^{3+}:YAG particles

The Yb^{3+}/Er^{3+} pair is well-known for UC process, and herein, the luminescence properties of the particles by photoluminescence spectroscopy were studied. The excitation spectra of the Yb^{3+}/Er^{3+}:YAG particles (Figure 51, obtained by monitoring the $^2F_{7/2} \rightarrow {}^2F_{5/2}$ transition at 980 nm) displayed narrow bands attributed to the f-f transitions at 380 ($^4I_{15/2} \rightarrow {}^4G_{11/2}$), 407 ($^4I_{15/2} \rightarrow {}^2H_{9/2}$), 448 ($^4I_{15/2} \rightarrow {}^4F_{5/2}$), 486 ($^4I_{15/2} \rightarrow {}^4F_{7/2}$), 522 ($^4I_{15/2} \rightarrow {}^2H_{11/2}$), 541 ($^4I_{15/2} \rightarrow {}^4S_{3/2}$) ,and 644 nm ($^4I_{15/2} \rightarrow {}^4F_{9/2}$). In addition, monitoring the emission at 1550 from Er^{3+}, the excitation spectra showed the transitions $^4I_{15/2} \rightarrow {}^4I_{9/2}$ at 793 nm and $^4I_{15/2} \rightarrow {}^4I_{11/2}$ at 969 nm from Er^{3+} ion, and the transition $^2F_{7/2} \rightarrow {}^2F_{5/2}$ centered at 940 nm resulting from the absorption from Yb^{3+} into the matrix [12]. The YAG bandgap values depend on the synthesis methodology: experimental bandgap values of 6.4 – 7.2 eV (193 – 174 nm) for YAG structures have been reported [219]. Here, we recorded the excitation spectra at lower energy than expected to observe the bandgap of the YAG matrix. Thus, the broad band below 300 nm could be related to the O-Ln^{3+} charge-transfer band [220]. The emission spectra showed the characteristic transitions of Er^{3+} ion from 1450 to 1600 nm ($^4I_{13/2} \rightarrow {}^4I_{15/2}$) with several level Stark resulting from the presence of that ion replacing the Y^{3+} at dodecahedral sites (D_2 symmetry) in the YAG cubic structure. The emission from Yb^{3+} ions (transition $^2F_{5/2} \rightarrow {}^2F_{7/2}$) was also observed at 1030 nm [221,222].

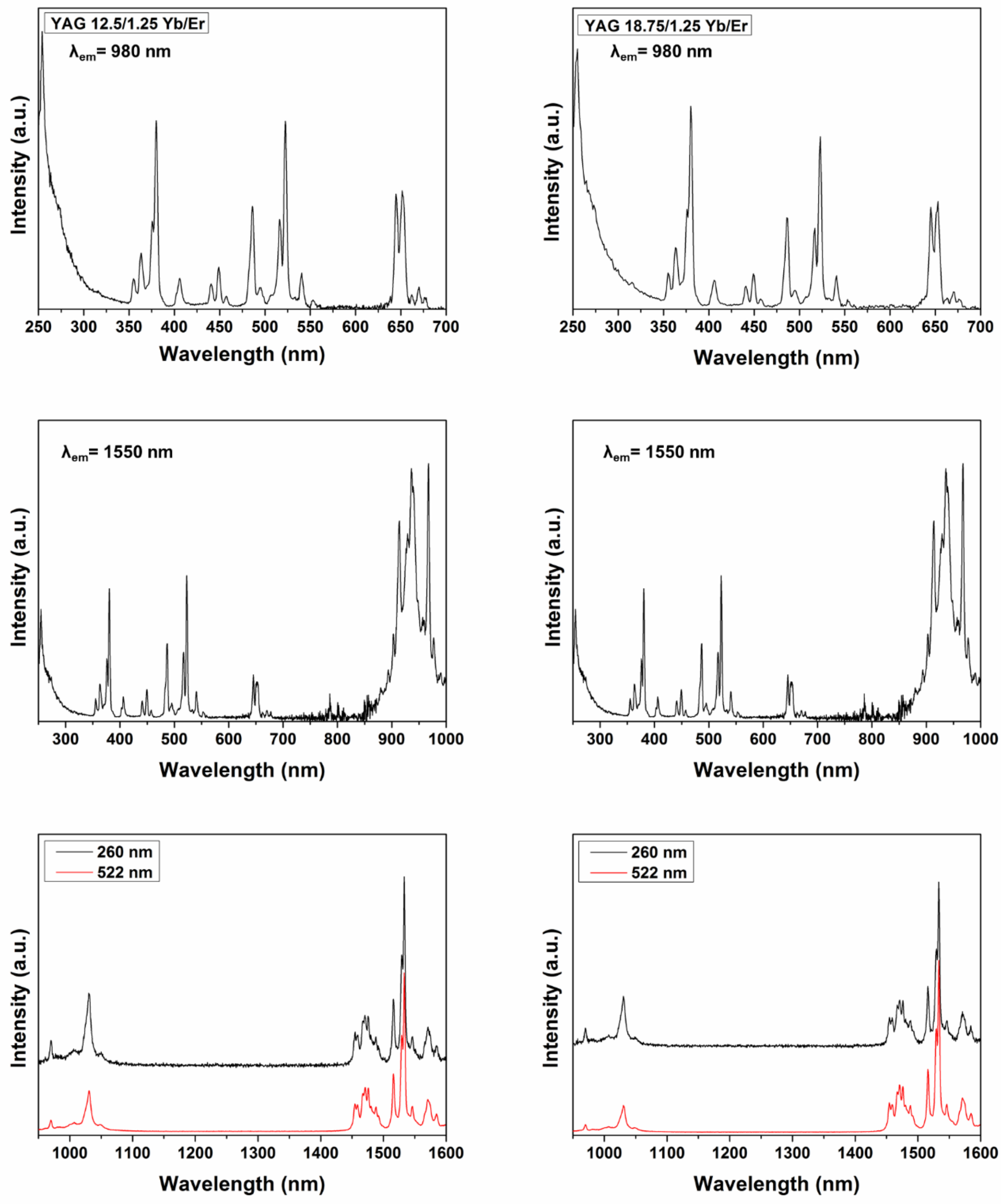

Figure 51. (first and second lines) Excitation (λ_{em} = 980 nm and 1550 nm) and (third line) emission spectra (λ_{ex} = 260 and 522 nm) from Yb^{3+}/Er^{3+}:YAG (Yb^{3+}/Er^{3+} % radio of 12.5/1.25 on the left and 18.75/1.25 on the right) powders after heat treatment at 1100 ºC for 12 h.

The UC emissions from YAG particles were visible to the naked eye, under 980-nm laser excitation. Both Yb^{3+} and Er^{3+} ions could be excited at 980 nm by means of f-f transition like ${}^{2}F_{7/2} \rightarrow {}^{2}F_{5/2}$ for Yb^{3+} and ${}^{4}I_{15/2} \rightarrow {}^{4}I_{11/2}$ for Er^{3+} [79]. Figure 52 illustrates the UC emission spectra, acquired under laser excitation at 980 nm for several pump power values. Regardless of the laser power, we verified the green and red emissions, related to the ${}^{2}H_{11/2}$, ${}^{4}S_{3/2} \rightarrow {}^{4}I_{15/2}$ and ${}^{7}F_{9/2} \rightarrow {}^{4}I_{15/2}$ transitions [79], respectively.

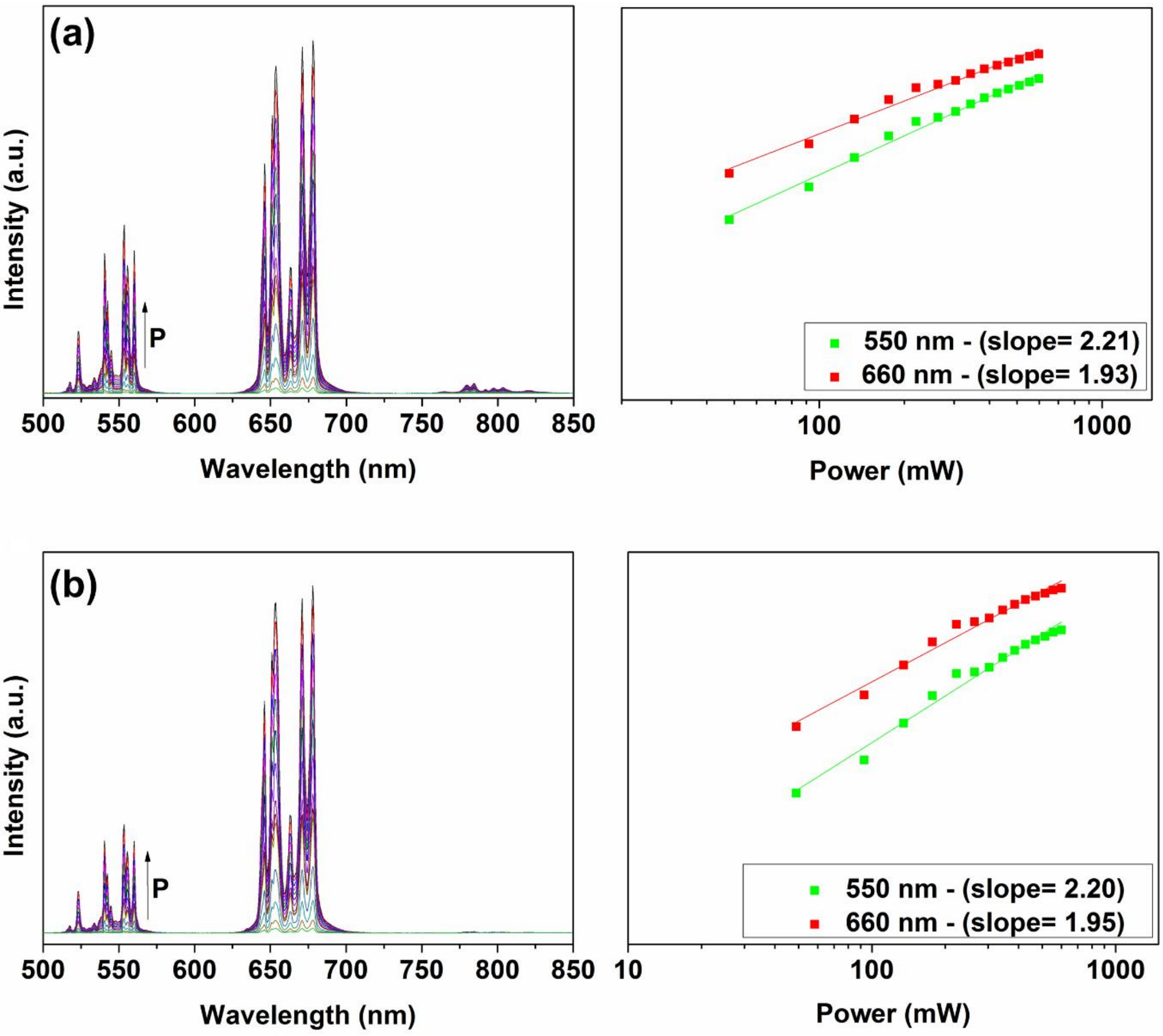

Figure 52. UC emission ($\lambda_{ex} = 980$ nm) spectra, on the left, of the Yb^{3+}/Er^{3+}:YAG (Yb^{3+}/Er^{3+} % radio of (a) 12.5/1.25 and (b) 18.75/1.25) samples, after heat treatment at 1100 ºC for 12 h. On the right shows the relationship $I \propto P^{n}$ at a log vs log graph for UC emission in the green and red regions.

Determining the number of photons involved in UC could help us to understand the UC mechanism and to determine whether a secondary process, such as cross-relaxation, took place [223,224]. Therefore, we analyzed the emission intensity (I) as a function of the pump power (P) under 980-nm excitation (Figure 52) for all the particles. We calculated the number of photons *n* required to populate each Er^{3+}excited emitting level (like $^2H_{11/2}$, $^4S_{3/2}$, or $^7F_{9/2}$) from the relationship $I \propto P^n$ [225]: this relationship has linear slope for each UC band, so *n* can be obtained from the calculated angular coefficient. For all the UC bands, we found $n = 2$, within the experimental error. Specifically for the Yb^{3+}/Er^{3+}:YAG (Yb^{3+}/Er^{3+} % ratio of 12.5/1.25) and Yb^{3+}/Er^{3+}:YAG (Yb^{3+}/Er^{3+} % ratio of 18.75/1.25) particles, the angular coefficient values in the green and red region were 2.21 and 1.93, and 2.20 and 1.95, respectively.

These results agreed with the ETU mechanism for UC emission. In this mechanism, two distinct ions interact. A sensitizer ion that absorbs most of the photons, and an activator or emitter ion, which receives the energy from these absorbed photons in a non-radiative way [78]. ETU is the most efficient mechanism and is usually observed in systems co-doped with the Yb^{3+}/Er^{3+} pair, where Yb^{3+} ions sensitize Er^{3+} ions which are the activators. This is possible because Yb^{3+} ions have larger absorption cross-section, so they are more effectively excited with 980-nm radiation ($^2F_{7/2} \rightarrow {}^2F_{5/2}$), subsequently transferring energy to Er^{3+} ions metastable excited state is $^4I_{13/2}$ **(1)**. The highest energy states that can be populated in the sequence are $^2H_{11/2}$ **(2)**, $^4S_{3/2}$ **(3)** and $^4F_{9/2}$ **(4)**, which will emit in the visible spectral region via $^2H_{11/2} \rightarrow {}^4I_{15/2}$, $^4S_{3/2} \rightarrow {}^4I_{15/2}$ and $^4F_{9/2} \rightarrow {}^4I_{15/2}$ transitions [79], as shown in Figure 53.

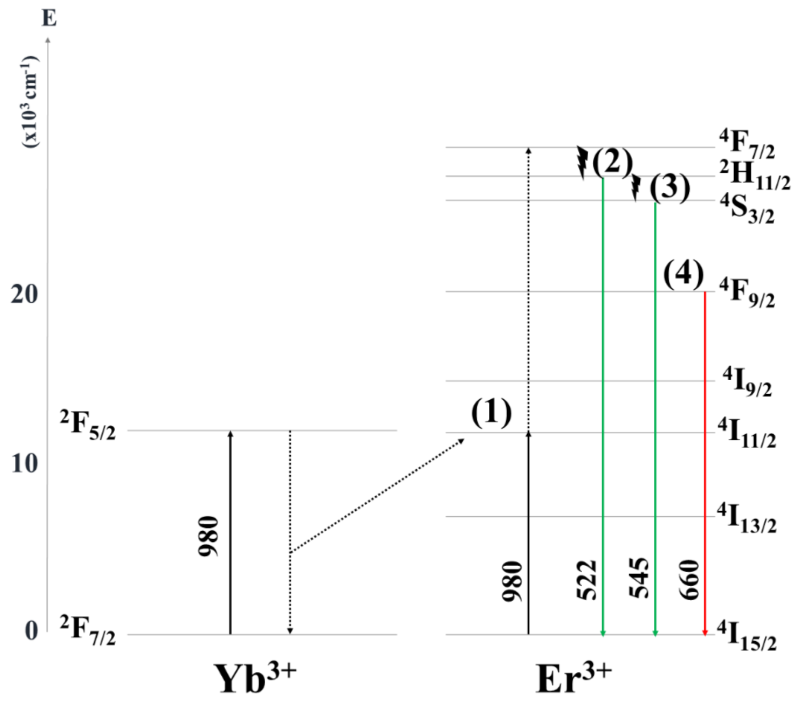

Figure 53. Partial diagram of energy levels for the Yb^{3+} and Er^{3+} ions, showing the UC mechanism by steps from **(1)** to **(4)**.

We did not observe any predominant cross-relaxation process for the studied Ln concentrations. Furthermore, the luminescent performance of the particles was suitable for the studies at different temperatures, which will determine their thermometry behavior.

4.2.2.1. Composited films by SF + Yb^{3+}/Er^{3+}:YAG particles

In the same way, because the Yb^{3+}/Er^{3+}:YAG particles become dispersed in the SF matrix, we decided to prepare SF-Yb^{3+}/Er^{3+}:YAG composite films from particles we obtained self-supported films with different concentrations of the particles, and we wanted to ensure that the Yb^{3+} ion concentration would guarantee efficient excitation even in the SF-Yb^{3+}/Er^{3+}:YAG composite film with small amount of Yb^{3+}/Er^{3+}:YAG particles. Thus, we used four particle concentrations to produce different systems, as described in section 3.2.3.2. We designated these one as **I**, **II**, **III**, and **IV** for each Yb^{3+}/Er^{3+}:YAG particle (Yb^{3+}/Er^{3+} % ratio of 12.5/1.25 or 18.75/1.25), and the amounts of particles we used were 50, 5.0, 2.5 and 1.0 mg, respectively, for a constant proportion of SF solution.

We also evaluated UC emission of the SF-Yb^{3+}/Er^{3+}:YAG composite films by photoluminescence spectroscopy, at 980-nm excitation. The emission spectra of films **I** to **IV** for both Yb^{3+}/Er^{3+}:YAG particles (Yb^{3+}/Er^{3+} % ratio of 12.5/1.25 or 18.75/1.25) are shown in Figure 54. We also plotted the log-log relation of the emission intensity (I) as a function of P under 980-nm excitation (Figure 54) for all the SF-Yb^{3+}/Er^{3+}:YAG composite films. As expected, the relationship gave a linear slope for each UC band, and n was 2.

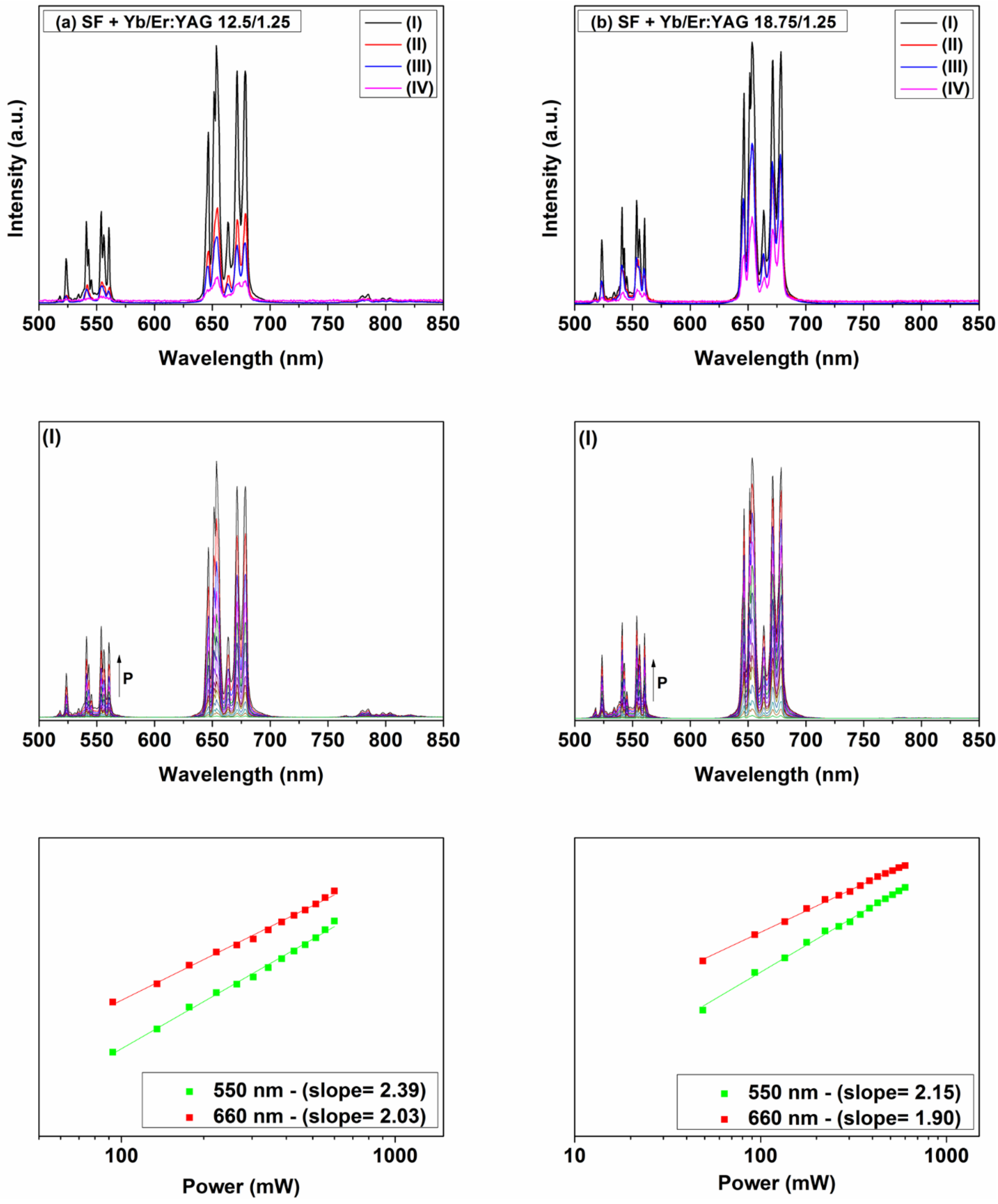

Figure 54. (first line) UC emission spectra ($\lambda_{ex} = 980$ nm) of the SF-Yb^{3+}/Er^{3+}:YAG (Yb^{3+}/Er^{3+} % radio of (a) 12.5/1.25 and (b) 18.75/1.25) composite films. (second line) UC emission spectra of film **I** (higher amount of Yb^{3+}/Er^{3+}:YAG particles) for several *P* values. The third line shows the relationship $I \propto P^{n}$ at a log *vs* log graph for UC emission in the green and red regions.

Therefore, we confirmed that UC emission was related to the Yb^{3+}/Er^{3+}couple in the YAG matrix for all the SF-Yb^{3+}/Er^{3+}:YAG composite films, and that the UC process also occurred in the composite films with smaller amount of Yb^{3+}/Er^{3+}:YAG particles, which was also more transparent, see picture in Figure 31. In conclusion, the UC emission has been detected in SF-based materials, and the ratio of particles allowed us to control the transparence of the self-supported films, which should allow their use as sensor or smart ink, for example, in security applications such as anti-counterfeiting [93]. As well as the particles, these systems were analyzed for their thermometry properties.

4.2.3. Yb^{3+}/Tm^{3+}:YAG particles

As observed to Er^{3+} ions, the Tm^{3+} ions show emission in visible and near-infrared spectrum by UC process, and the luminescence properties of the particles by photoluminescence spectroscopy were also studied. The excitation spectra were obtained (λ_{em}= 800 nm, Figure 55, at $^3H_4 \rightarrow {}^3H_6$ transition) and the three main bands observed are related to the following transitions and wavelengths: $^3H_6 \rightarrow {}^1I_6$ (265 nm), $^3H_6 \rightarrow {}^1D_2$ (356 nm), $^1G_4$ (457 nm) and $^3F_{2,3}$ (679 nm) [226,227]. The excitation spectra monitoring the emission from Yb^{3+} ions (transition $^2F_{5/2} \rightarrow {}^2F_{7/2}$) at 980 nm showed a broad band below of 350 nm related to the O-Yb^{3+} charge-transfer band [220]. At higher concentration of Yb^{3+} in the sample, a low band attributed to Tm^{3+} transition ($^3H_6 \rightarrow {}^3F_{2,3}$ (679 nm)) was noted. But, the $Yb^{3+} \rightarrow Tm^{3+}$ energy transfer could be confirmed by the excitation spectra monitoring the Tm^{3+} emission at 1600 nm ($^3F_4 \rightarrow {}^3H_6$), beyond the characteristic excitation bands from Tm^{3+} as $^3H_6 \rightarrow {}^1D_2$ (356 nm), $^1G_4$ (457 nm), $^3F_{2,3}$ (679 nm) and $^3H_4$ (789 nm) [226,227], the transition $^2F_{7/2} \rightarrow {}^2F_{5/2}$ centered at 940 nm resulted from the absorption from Yb^{3+} into the matrix was noted.

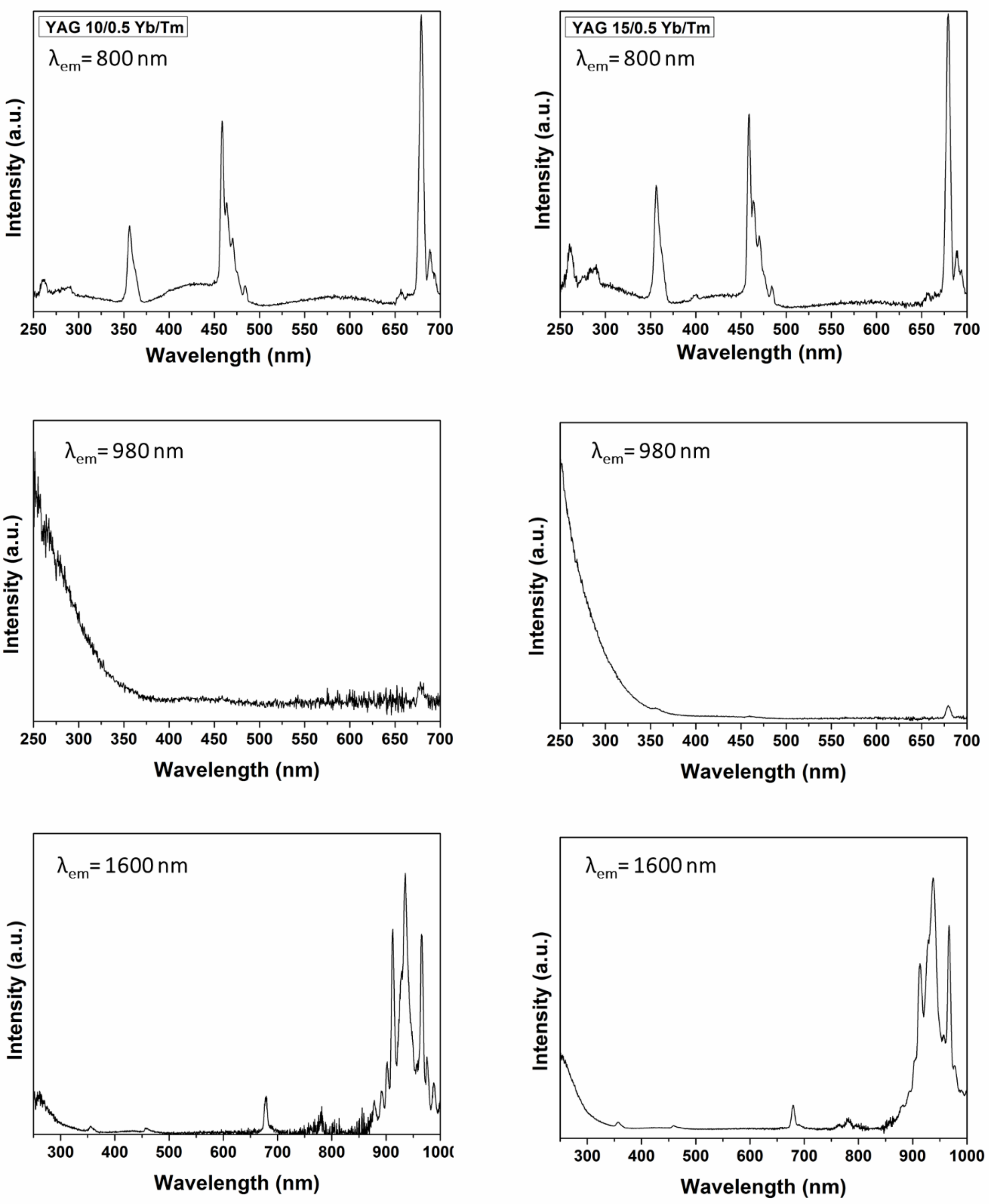

Figure 55. Excitation spectra (λ_{em} = 800, 980 and 1600 nm) from Yb^{3+}/Tm^{3+}:YAG (Yb^{3+}/Tm^{3+} % radio of 10/0.5 on the left and 15/0.5 on the right) powders after heat treatment at 1100 ºC for 12 h.

The UC emission spectra were acquired under several laser power, Figure 56. It was possible to observe, in both samples, a low intense band in 625-700 nm (red spectra) due to $^1G_4 \rightarrow {}^3F_4$ and $^3F_{2,3} \rightarrow {}^3H_6$ transitions, a medium intense band around 477 nm (blue) attributed to

$^1D_2 \rightarrow {}^3H_5$ transition, and a high intense band nearly 800 nm (NIR) due to $^3H_4 \rightarrow {}^3H_6$ transition from Tm^{3+} ions [228]. The number of photons involved in UC process were determined as described by Pollnau et.al. [225]. For Yb^{3+}/Tm^{3+}:YAG (10/0.5) and Yb^{3+}/Tm^{3+}:YAG (15/0.5) samples, the coefficient angular values for blue and NIR region were 2.9 and 1.9, and 2.8 and 1.8, respectively.

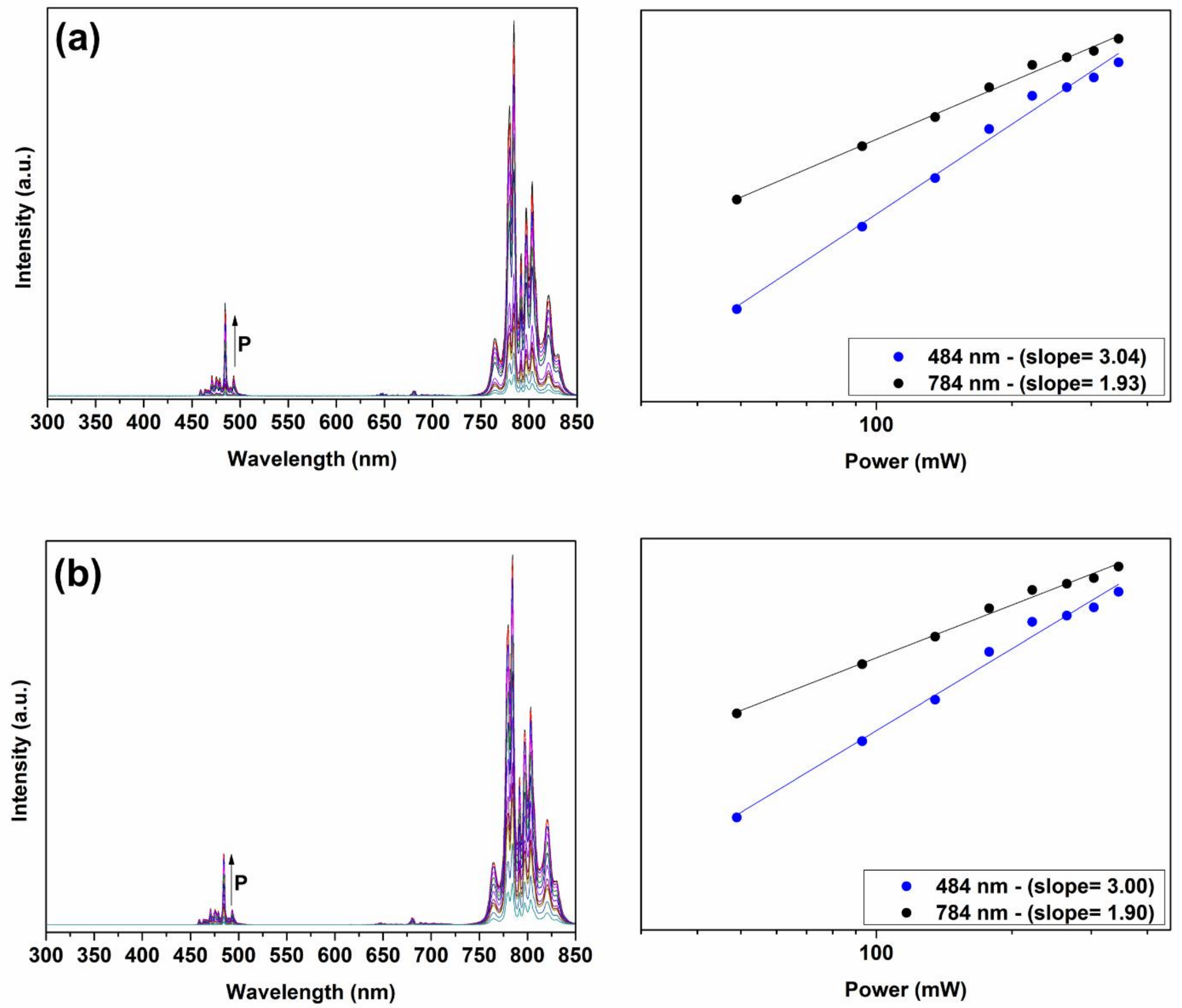

Figure 56. (left) UC emission (λ_{ex} = 980 nm) spectra of the Yb^{3+}/Tm^{3+}:YAG (Yb^{3+}/Tm^{3+} % radio of (a)-10/0.5 and (b)-15/0.5) samples, after heat treatment at 1100 ºC for 12 h. The right shows the relationship $I \propto P^n$ at a log *vs* log graph for UC emission in the blue and NIR regions.

These results suggested an ETU mechanism depending of 3 photons for the blue emission. In this mechanism, the electrons in ground state of the Tm^{3+} ions ($^3H_6$) can be excited to the highest energy state $^3H_5$, described by $^3H_6$ (Tm^{3+}) + $^2F_{5/2}$ (Yb^{3+}) → $^3H_5$ (Tm^{3+}) + $^2F_{7/2}$ (Yb^{3+}) [78] **(1)**. In sequence, the Tm^{3+} ions can non-radiatively decay to the $^3F_4$ level **(2)**, and, the same ions in this same level can be excited by energy transfers from another excited Yb^{3+} ions, and then get to the $^3F_{2,3}$ level **(3)**. From this level, the $^3F_{2,3} \rightarrow {}^3H_6$ transition (~ 706 nm) can occur, or else, the electrons can go to the level $^3H_4$ **(4)**, that in turn can be excited at the $^1G_4$ level by $^3H_4$ (Tm^{3+}) + $^2F_{5/2}$ (Yb^{3+}) → $^1G_4$ (Tm^{3+}) + $^2F_{7/2}$ (Yb^{3+}) **(5)**. In summary, by the union of the Yb^{3+}/Tm^{3+} pair under 980 nm excitation, it is possible to observe bands around 477, 650 and 800 nm, referent to $^1D_2 \rightarrow {}^3H_5$, $^1G_4 \rightarrow {}^3F_4$, and $^3H_4 \rightarrow {}^3H_6$ transitions, respectively, as shown in Figure 57.

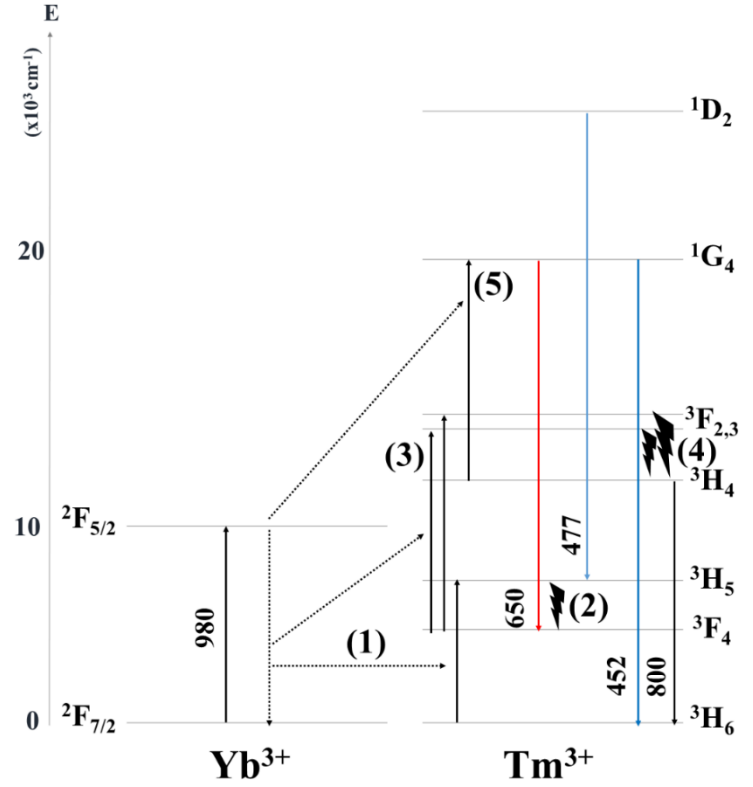

Figure 57. Partial diagram of energy levels for the Yb^{3+} and Tm^{3+} ions, showing the UC mechanism by steps from **(1)** to **(5)**.

The last one ($^3H_4 \rightarrow {}^3H_6$) is more intense due to the fact that the mechanism involved is only for 2 photons, whereas the transition situated in blue region ($^1D_2 \rightarrow {}^3H_5$ and $^1G_4 \rightarrow {}^3H_6$) occurs by a mechanism that involves 3 photons [88].

4.2.3.1. Composited films by SF + Yb^{3+}/Tm^{3+}:YAG particles

Aiming to obtain an UC luminescent self-supported film, composited films from SF and the YAG particles doped with Yb^{3+} and Tm^{3+} ions (section 3.2.3.3) were characterized also by the photoluminescent spectroscopy, and Tm^{3+} ions properties were evaluated into the matrix. In Figure 58 was possible to observe that UC behavior were kept, and the UC emission bands in blue and NIR regions were observed, as also a naked eye.

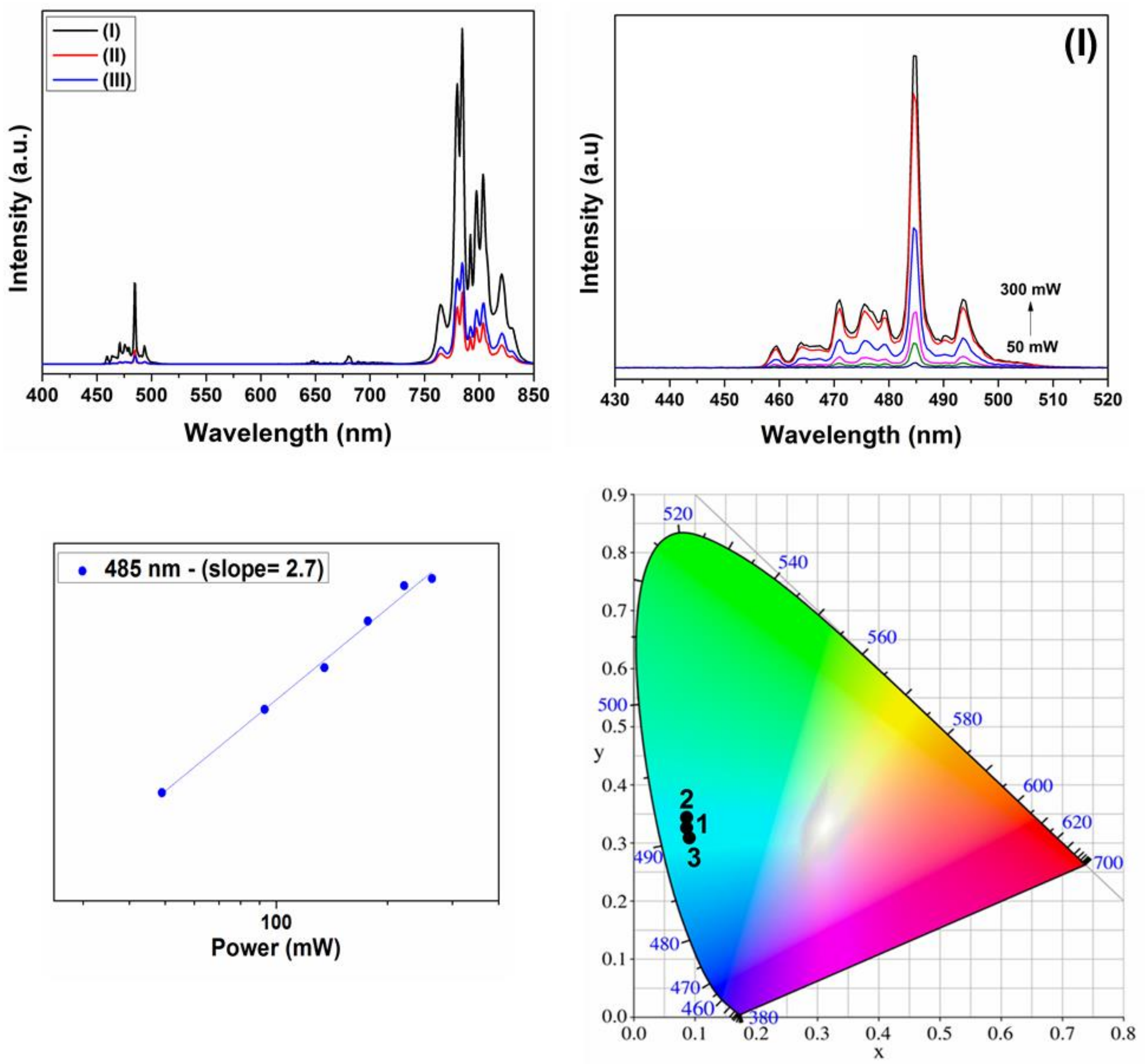

Figure 58. Emission (λ_{ex} = 980 nm) spectra of the SF-Yb^{3+}/Tm^{3+}:YAG (10/0.5) composite films obtained with (**I**-black line) 50, (**II**-blue line) 5.0, and (**III**-red line) 2.5 mg of the particles. Emission spectra of **(I)** composite film in the blue region, and log–log plots of the laser power dependence of the UC emission intensity under 980-nm excitation in the blue region. Chromaticity diagrams of **1**. Yb^{3+}/Tm^{3+}:YAG (10/0.5), **2**. Yb^{3+}/Tm^{3+}:YAG (15/0.5), and **3**. SF-Yb^{3+}/Tm^{3+}:YAG (10/0.5) samples obtained in the visible region.

The number of photons involved in UC process were also determined, Figure 58, on the right, the UC emission spectra for the SF-Yb^{3+}/Tm^{3+}:YAG (10/0.5) composited film were acquired under several laser power (P), and the coefficient angular values obtained for blue region was equal to 2.7.

Figure 58 also show the chromaticity diagram, that presents the coordinates of color emission for two powders and the film samples: points **(1)** Yb^{3+}/Tm^{3+}:YAG (10/0.5), **(2)** Yb^{3+}/Tm^{3+}:YAG (15/0.5), and **(3)** SF-Yb^{3+}/Tm^{3+}:YAG (10/0.5). For all samples, it was possible to observe that the materials emit in the blue region, confirming our initial aims, so the self-supported film composited by SF and Yb^{3+}/Tm^{3+}:YAG (10/0.5) particles is a potential material to be use as blue-emitting markers or 3D-ink applied in anti-counterfeit technology.

In conclusion of this part, we present an efficient way to obtain blue emission by UC process in SF composites. The strategy was protecting the Ln ion from quenching process *e.g.* phonon deexcitation from protein structure, and for that YAG particles doped with Yb^{3+} and Tm^{3+} ions were obtained via SP and used to prepare a self-supported film with SF. All materials (powders and films) were fully characterized, and the blue color emission due to $^1D_2 \rightarrow {}^3H_5$ transition from Tm^{3+} ion, under 980 nm excitation in the Yb^{3+} ion was observed, also a naked eye. These films, in turn, kept the SF properties as self-supporting and biodegradable, and had the emission properties of Ln ions present. In the end, this new material, flexible, self-supporting, and prepared from a low-cost substrate, can be considered as a potential material for the applying as an anti-counterfeiting device, since its emission spectrum is well resolved, with fine lines, and with bands located in the blue spectral region, which appears from selective excitation at 980 nm and UC process involving 3 photons, which makes it more difficult to play under any conditions. In addition, this material could also be applied as a surface coating or used as an ink for 3D printers.

4.3. Photonic applications

4.3.1. Random LASER emission in Nd^{3+}:YAG particles

Nd^{3+}-based RL have been demonstrated using different crystals and glasses as hosts, and different pump wavelengths. An optical thermometer based on a two-color Nd RL has also been demonstrated [121]. As a proof of concept for an application the material developed here, we show in this section that the SP synthesized Nd^{3+}:YAG can operate as a RL, with characteristics similar to those found in the literature. The spectra obtained at three different excitation energies for all the samples are showed in Figure 59.

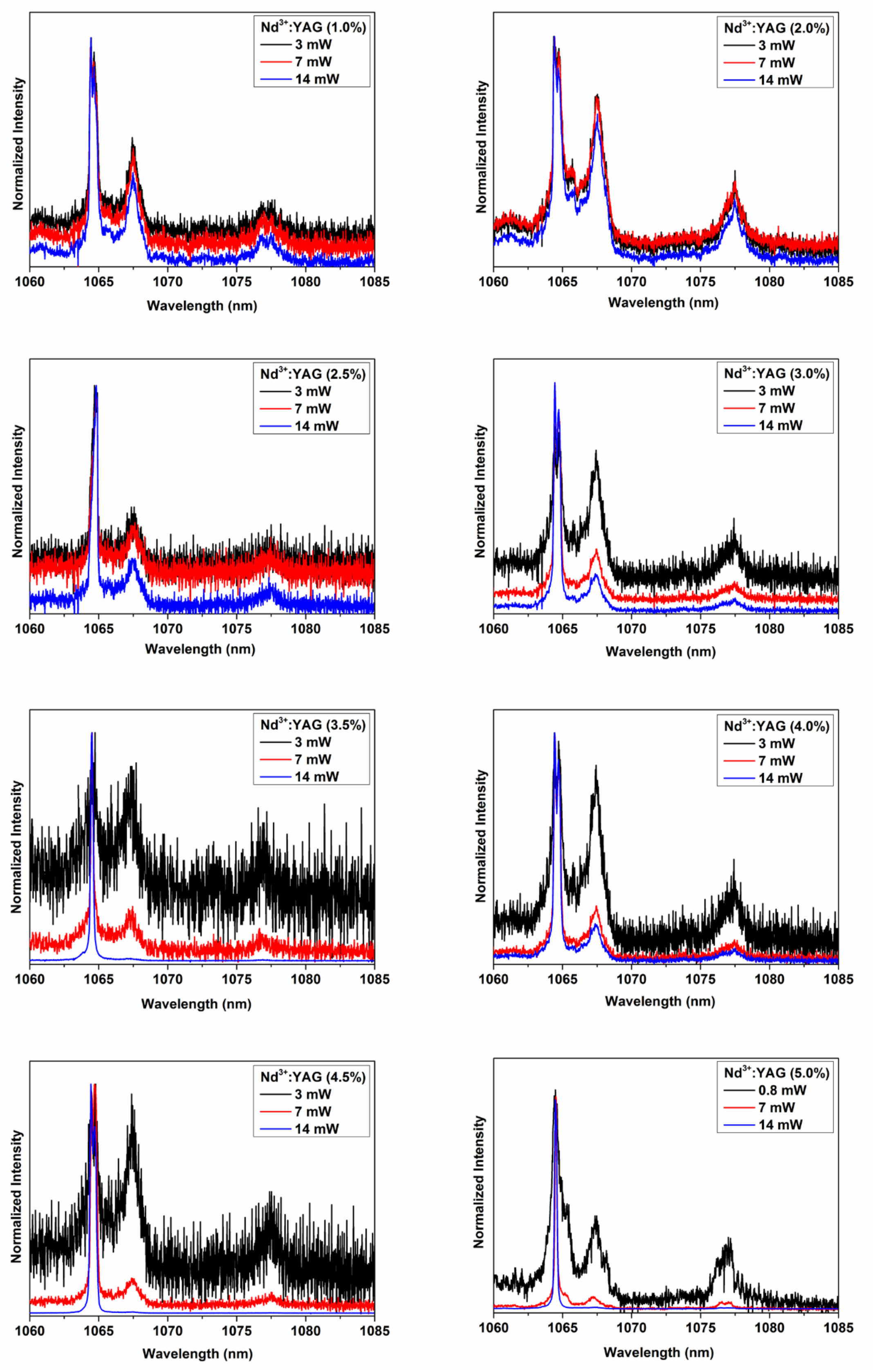

Figure 59. Emission spectra at three different excitation energies (transition $^4F_{3/2} \rightarrow {}^4I_{11/2}$) in the Nd^{3+} doped samples 1.0, 2.0, 2.5, 3.0, 3.5, 4.0, 4.5 and 5.0%.

RL emission was readily obtained for samples with the available concentrations of 2.5, 3.0, 3.5, 4.0, 4.5 and 5.0%, where is possible to observe the spectral narrowing of the Nd^{3+} photoluminescence band. The emitted intensity versus excitation energy for three concentrations (2.5, 3.5 and 5.0%, for the sake of clarity) is shown in Figure 60, on the left. As can be seen, as the concentration increases, the threshold decreases, a behavior already seen in other Nd-based RLs [122]. At 5.0% concentration, a threshold of 0.2 mJ (0.1 mJ/mm^2) is inferred, which is almost five times smaller than for the 2.5% concentration sample. The full width at half maximum (FWHM) linewidth narrowing for the same concentration are shown in the same figure, on the right.

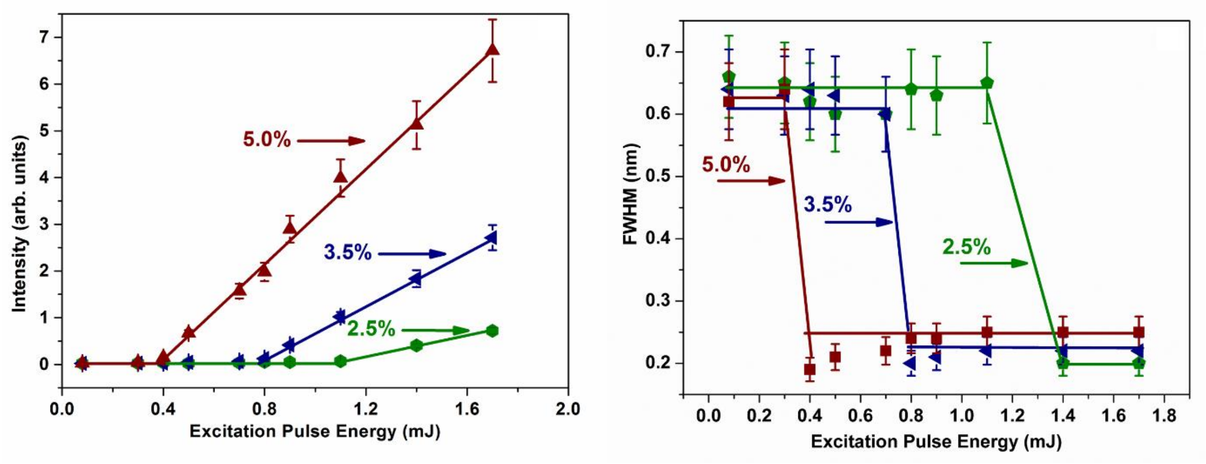

Figure 60. (left) Corresponding output peak intensity *vs* the EPE for powders and (right) FWHM of the Nd^{3+} emission with peak at 1064 nm for 2.5%, 3.5% and 5.0%.

A very steep narrowing, characteristic of Ln based RL was observed. Plotted in Figure 61 are the thresholds and bandwidth reduction versus concentration, for all 5 samples with indicated concentrations, showing that the final linewidth varies by 20% upward as the Nd^{3+} concentration increases from 2.5% to 5.0%, whereas the threshold reduces a factor of 5.

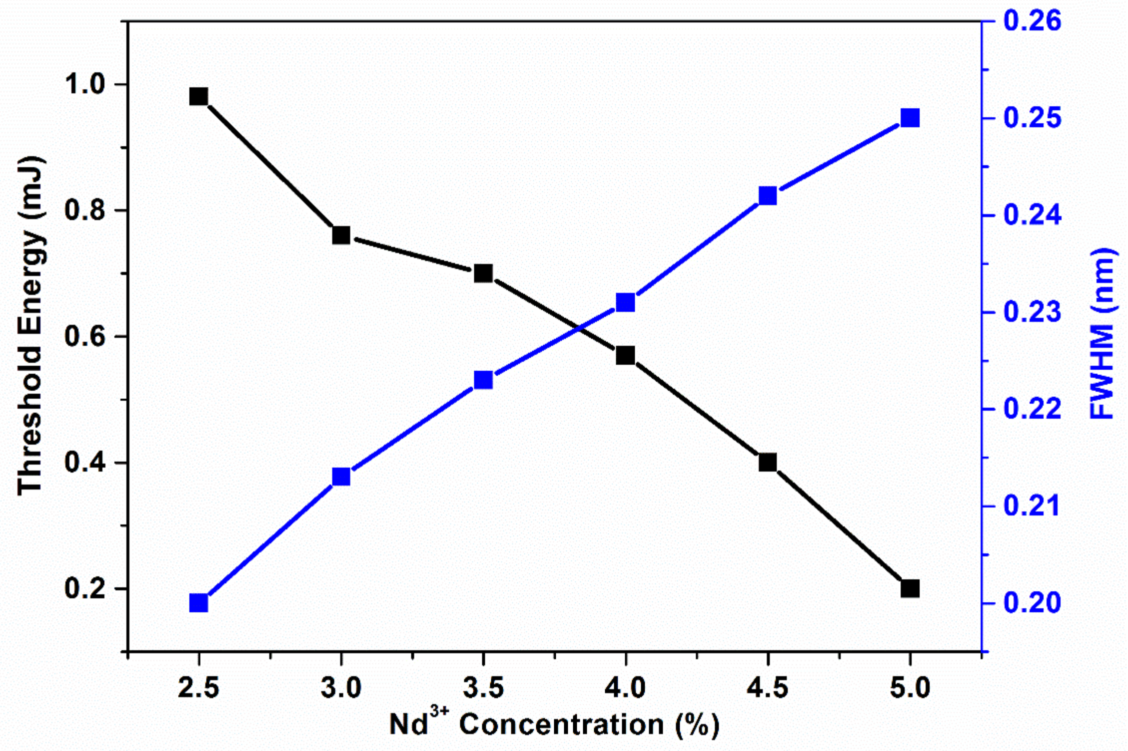

Figure 61. RL EPE threshold and FWHM in function of the Nd^{3+} concentration.

This work presented an efficient synthesis methodology to obtain Nd^{3+}:YAG particles. The light scattering resulted from the broad size distribution of particles, initially would be a trouble for photonic application, but not for RL since the resulted emission light scattering is important to trapping light in random walks inside the material until the gain overcomes the loss. Herein, the obtained materials were produced with different Ln contents, and the RL emission gain was affected, with threshold values lower than that observed for other Nd^{3+} ion based RL studies (Table 11). For example, Azkargorta *et. al.* prepared a YAG crystal doped with 1.0% of Nd^{3+} ions (YAG1%Nd) and the threshold observed was 8 mJ/mm^2 [39]. In 2015, Moura *et. al.* prepared $KGd(WO_4)_2$:Nd^{3+} crystal powder with 4.0% of Nd^{3+} and the threshold was 6.5 mJ/mm^2 [67]. In the next year, Moura *et. al.* demonstrated a RL emission in $Nd_{0.10}Y_{0.90}Al_3(BO_3)$ with threshold value equal to 0.40 mJ/mm^2 [69]. Carreño *et. al.*, in its turn, prepared $Nd_xY_{1.00-x}Al_3(BO_3)_4$ nanocrystals powders, and with 4.0, 40.0 and 80.0%, the threshold values were 0.40, 0.31 and 0.27 mJ/mm^2, respectively [229]. In our group, were prepared $Y_{1-x}Nd_xAl_3(BO_3)_4$ powders doped with 20.0, 40.0, 60.0 and 80.0%-Nd^{3+} and the threshold values were 0.38, 0.34, 0.31 and 0.25 mJ/mm^2, respectively [230].

Table 11. Values of the threshold for different Nd^{3+}-doped materials reported in the literature and obtained in this work (t.w.)

MATERIAL	**THRESHOLD (mJ/mm^2)**	**ref.**
Nd^{3+}:YAG (2.5%)	0.57	t.w.
Nd^{3+}:YAG (3.0%)	0.40	t.w.
Nd^{3+}:YAG (3.5%)	0.36	t.w.
Nd^{3+}:YAG (4.0%)	0.30	t.w.
Nd^{3+}:YAG (4.5%)	0.21	t.w.
Nd^{3+}:YAG (5.0%)	0.10	t.w.
YAG1%Nd	8	39
$KGd(WO_4)_2$: Nd^{3+}	6.5	67
$Nd_{0.10}Y_{0.90}Al_3(BO_3)$	0.4	69
$Nd_{0.04}Y_{0.96}Al_3(BO_3)_4$	0.40	229
$Nd_{0.4}Y_{0.6}Al_3(BO_3)_4$	0.31	229
$Nd_{0.8}Y_{0.2}Al_3(BO_3)_4$	0.27	229
$Y_{0.8}Nd_{0.2}Al_3(BO_3)_4$	0.38	230
$Y_{0.6}Nd_{0.4}Al_3(BO_3)_4$	0.34	230
$Y_{0.4}Nd_{0.6}Al_3(BO_3)_4$	0.31	230
$Y_{0.2}Nd_{0.8}Al_3(BO_3)_4$	0.25	230

In Figure 62 the temporal behavior of the emission well below (first column) and well above (second column) threshold clearly proofs that RL emission is occurring. As the RL emission occurs through stimulated emission, the high number of atoms in the excited state during this process results in a decrease in the lifetime. It should be emphasized that the focus position of the input beam was optimized for the best beam diameter on the sample. The value of the energy density at threshold is as low as reported before [39,67,122] making the Nd^{3+}:YAG RL very competitive for potential applications.

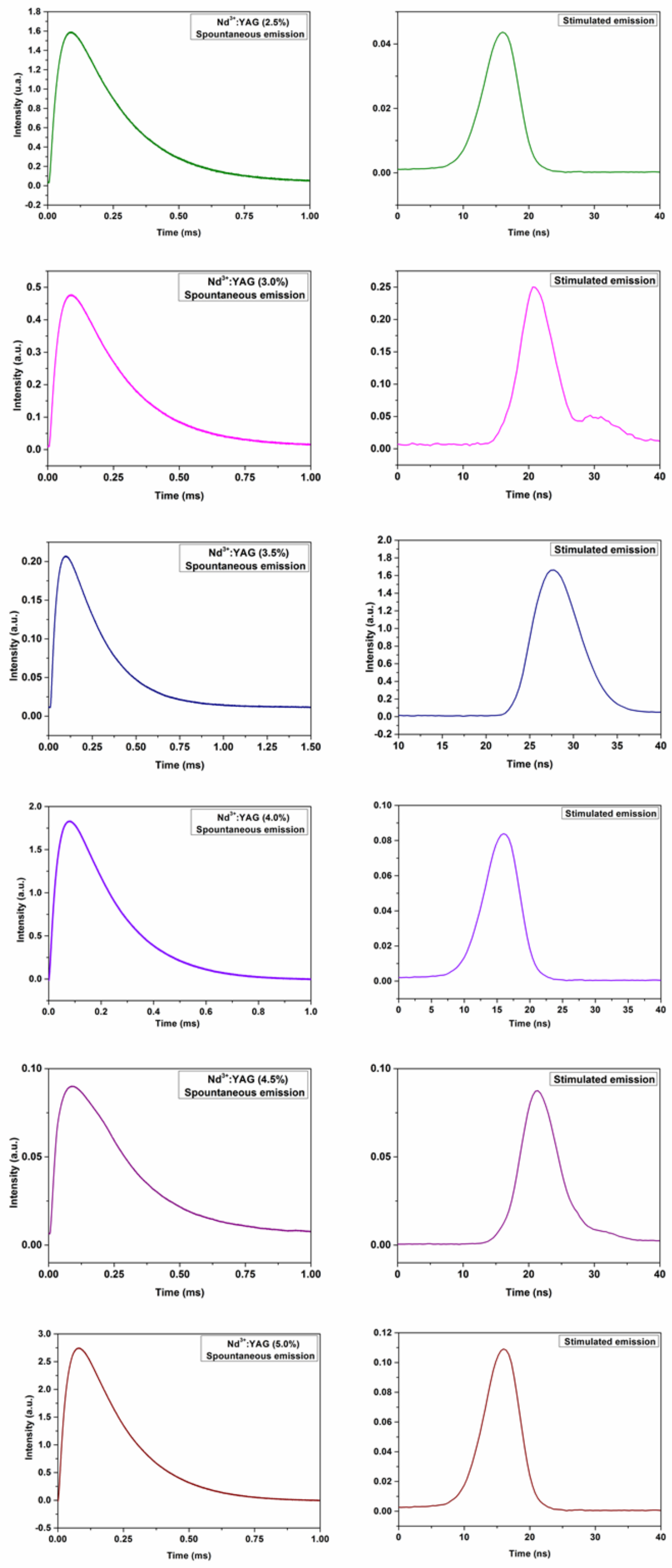

Figure 62. Temporal behavior for Spontaneous emission and Lasing emission for Nd^{3+} doped sample 2.5, 3.0, 3.5, 4.0, 4.5 and 5.0%.

In conclusion of this part, we have successfully synthesized YAG microparticles with Nd^{3+} ions by SP, which is a highly flexible methodology, since different precursors as suspensions or solutions could be nebulized, just by control the surface tension. In addition, pyrolysis may be conducted at high temperatures and only depends on the furnace temperature and gas flow, so different phases may be achieved in one step. Apart from affording high yield, this methodology can be scaled up from a lab setup to industrial production without byproducts being generated. Herein, the pyrolysis procedure adopted was fast, then the powder obtained by SP did not form a crystalline YAG lattice in one step. However, further heat treatment at 1100 °C for 12 h produced highly crystalline, spherical, dense, non-coalesced particles, as confirmed by electron microscopy and XRD analysis. The expected Nd^{3+} spectroscopic profile emerges, and the narrow emission bands corroborate the assumption that the Ln ions replace Y^{3+} ions at dodecahedral sites (D_2 symmetry) in the YAG cubic structure. The radius difference between Y^{3+} and Nd^{3+} ion was responsible by a little change on the lattice parameters, but no spurious phases were formed, and pure YAG structure was obtained. The increase of Nd^{3+} concentration was followed by the lifetime decrease, as expected, due to a quenching of the excited level by the concentration effect. Moreover, the intense emission at 1064 nm, concerning the $^4F_{3/2} \rightarrow {}^4I_{11/2}$ transition, was studied on RL emission as a result of different Nd^{3+} contents, and as the concentration of Nd^{3+} ion increases, the threshold energy decreases, *e.g.*, the sample doped with 5.0% of neodymium, the threshold was 0.2 mJ, almost five times lower than for the 2.5% concentration sample. In conclusion, a Nd^{3+}:YAG micropowder RL was demonstrated as a proof of concept for a future application, with characteristics similar to other Nd^{3+} based RL reported in the literature.

4.3.2. Temperature measurement by up-conversion process in Yb^{3+}/Er^{3+}:YAG particles and its composite films

We evaluated the thermal dependence of the green UC emission of the Yb^{3+}/Er^{3+}:YAG particles. Figure 63 shows the green UC emission for both particles under excitation at 980 nm, at different temperatures (from 293 to 473 K). We normalized the spectra with respect to the $^2H_{11/2} \rightarrow {}^4I_{15/2}$ transition (523.5 nm) to show the relative emissions intensities. The populated excited levels ($^2H_{11/2}$ and $^4S_{3/2}$) behave distinctly with temperature, and the intensity of the $^4S_{3/2} \rightarrow {}^4I_{15/2}$ transition decreased slightly in relation to the intensity of the $^2H_{11/2} \rightarrow {}^4I_{15/2}$ transition, indicating potential sensitivity for thermometry.

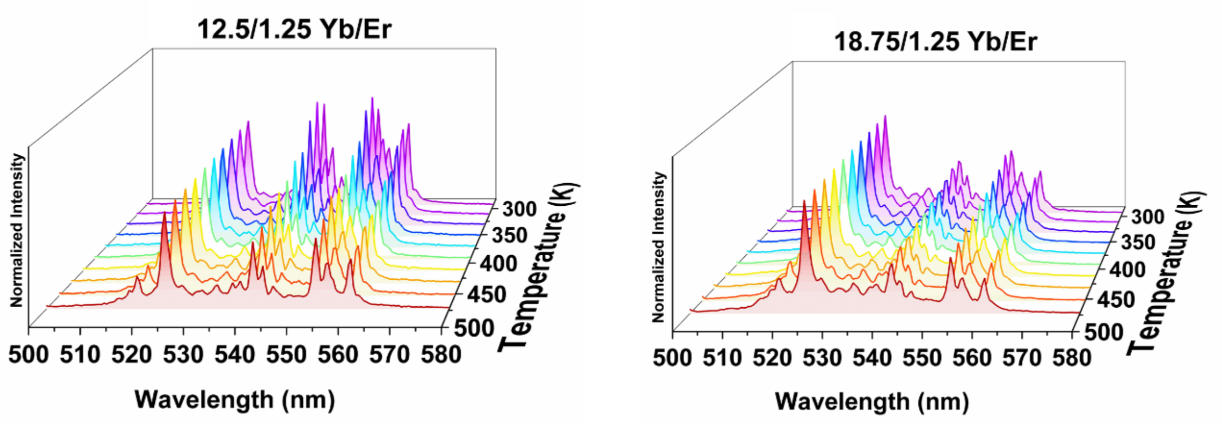

Figure 63. Temperature dependent UC 3D emission spectra (λ_{exc} = 980 nm, from 293 K to 473 K) of the Yb^{3+}/Er^{3+}:YAG (Yb^{3+}/Er^{3+} % radio of 12.5/1.25 and 18.75/1.25) particles in the green range (500-580 nm) normalized as a function of the band at 523.5 nm.

Figure 64 illustrates the dependence of the green UC intensity for transitions from both the $^2H_{11/2}$ and $^4S_{3/2}$ levels separately as a function of the temperature. The $^2H_{11/2}$ and $^4S_{3/2}$ levels had a difference of energy (**ΔE**) of about 1035 cm^{-1} for both particles. To calculate **ΔE**, we plotted one representative spectrum for each particle, so we were able to determine the barycenter of each transition and to obtain **ΔE**. The **ΔE** values confirmed that the $^2H_{11/2}$ and $^4S_{3/2}$ levels were thermally coupled; that is, when the temperature was increased, the electron in the $^4S_{3/2}$ level was thermally excited to the $^2H_{11/2}$ level, consequently increasing the relative intensity of the $^2H_{11/2} \rightarrow {}^4I_{15/2}$ transition. Hence, the population of electrons in these levels could respect the Boltzmann distribution, and the Fluorescence Intensity Ratio (**FIR**) as a function of temperature (**T**) could be described by [231]:

$$\mathbf{FIR} = \frac{IH}{IS} = \mathbf{A}\ \mathbf{exp}\left(-\frac{\Delta E}{kT}\right) \qquad \textbf{Equation 22}$$

where **IH** and **IS**, respectively, are the integrated intensities of the $^2H_{11/2} \rightarrow {}^4I_{15/2}$ and $^4S_{3/2} \rightarrow {}^4I_{15/2}$ transitions; **A** is a constant that contains their spontaneous emission rates; **ΔE** is the energy gap between the coupled excited $^2H_{11/2}$ and $^4S_{3/2}$ energy levels; **k** is the Boltzmann constant; and **T** is the absolute temperature.

Equation 22 can be rewritten as a linear equation:

$$\mathbf{ln(FIR) = ln(A)} - \frac{\Delta E}{kT} \qquad \textbf{Equation 23}$$

According to Equation 23, we verified the best linearity for the plot of ln(**FIR**) *versus* **1/T** [86] for the Yb^{3+}/Er^{3+}:YAG particles. As we increased the amount of Yb^{3+}, the linear slope became far from 1. Tian *et. al.* [232] observed a similar effect—they found that the Yb^{3+} ion can reduce the radiative transition rate between the $^2H_{11/2}$ and $^4S_{3/2}$ levels by an energy back-transfer mechanism, so that high Yb^{3+} concentration could decrease thermal sensitivity [232–234].

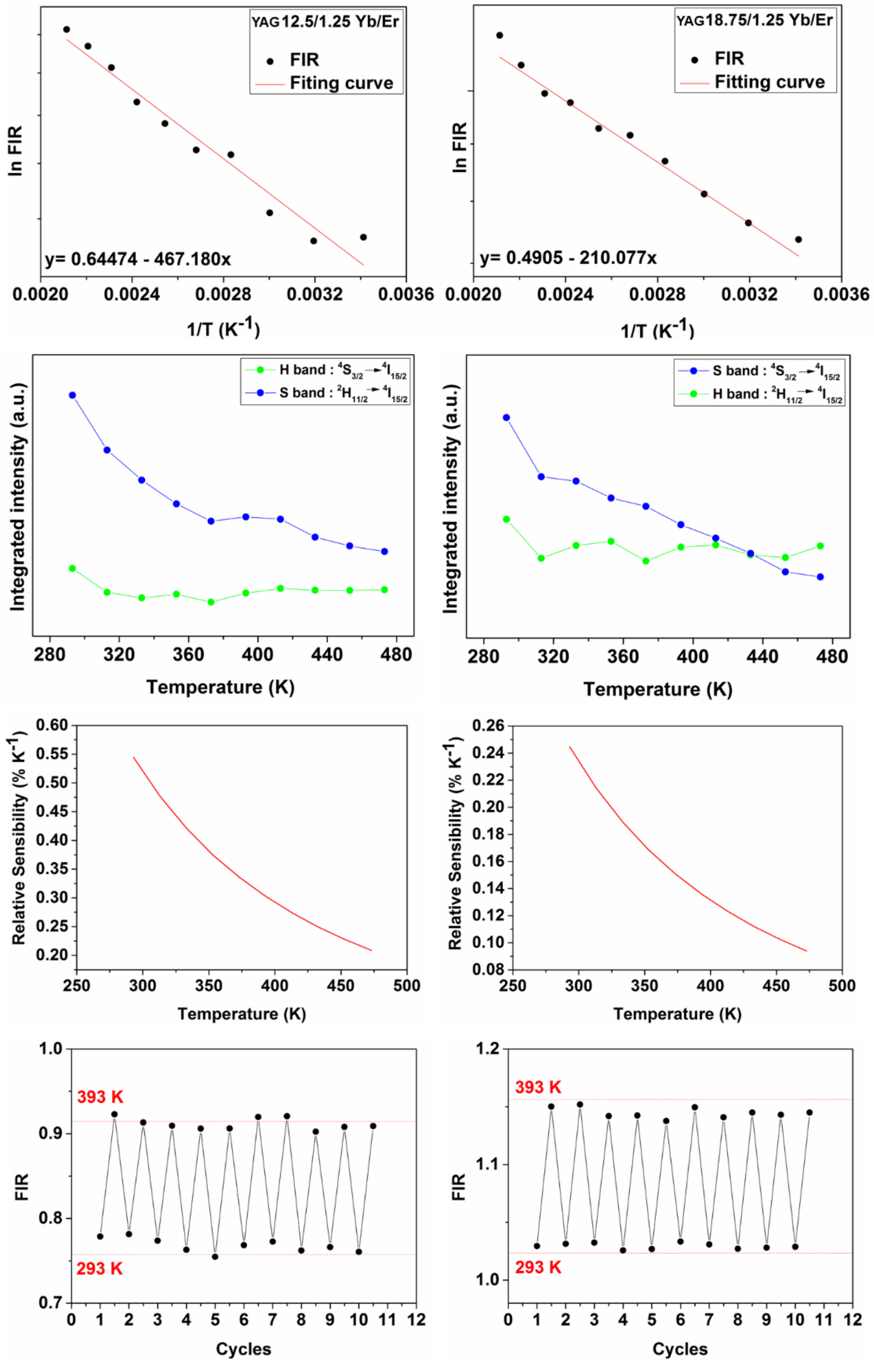

Figure 64. (first line) Fluorescence intensity ratio (**FIR** for $^2H_{11/2}/^4S_{3/2}$) as a function of temperature (**1/T**), (second line) integrated intensity of the S and H bands as a function of temperature (**T**), and (third line) relative sensitivity as a function of temperature. (fourth line) Temperature measurement repeatability of **FIR** for $^2H_{11/2}/^4S_{3/2}$ for ten cycles between 293 and 393 K. Columns are related to Yb^{3+}/Er^{3+}:YAG particles with Yb^{3+}/Er^{3+} % radio of 12.5/1.25 and 18.75/1.25, respectively.

The relative sensitivity (**S_r**) is an important parameter to evaluate the thermometry performance and potential application of materials [235] and allows us to compare the materials obtained herein with other materials reported in the literature [86].

$$\mathbf{S_r = \frac{\Delta E}{kT^2} \times 100\%} \qquad \textbf{Equation 24}$$

The third line of Figure 64 shows **S_r** as a function of temperature for all the particles. We verified maximum **S_r** at the lower temperature, 293 K, and obtained **S_r** values of 0.54 % K^{-1} and 0.24 % K^{-1} for the Yb^{3+}/Er^{3+}:YAG particles with Yb^{3+}/Er^{3+} % ratio of 12.5/1.25 and 18.75/1.25, respectively. As discussed above, the particles with low Yb^{3+} concentration presented the highest **S_r** due to the role that Yb^{3+} ions play in energy transfer mechanisms. Moreover, these S_r values agreed with the S_r values of other materials found in the literature, as showed in Table 12.

Table 12. Values of the absolute and relative sensitivities (**S_{abs}** and **S_r**) at a certain temperature (**T_{max}**) for different Yb^{3+}/Er^{3+}-doped materials reported in the literature and obtained in this work (t.w.)

MATERIAL	**T_{max} (K)**	**S_{abs} ($x10^{-3}$ K^{-1})**	**S_r (% K^{-1})**	**ref.**
Yb^{3+}/Er^{3+}:YAG (12.5/1.25)	293	2.25	0.54	t.w.
Yb^{3+}/Er^{3+}:YAG (18.75/1.25)	293	1.95	0.24	t.w.
Yb^{3+}/Er^{3+}:YAG	-----	4.8 (577 K)	1.3 (298 K)	87
Yb^{3+}/Er^{3+}:TeO_2–WO_3 glass	690	2.6	0.20	85
Yb^{3+}/Er^{3+}:tellurite glass	473	8.9	0.53	235
Yb^{+3}/Er^{3+}:$La_2Ti_2O_7$	333	5.7	0.63	236
Yb^{3+}/Er^{3+}:silicate glass	296	3.3	0.63	237
Yb^{3+}/Er^{3+}:$BaMoO_4$	-----	1.15 (430 K)	1.07 (293 K)	238

$Yb^{3+}/Er^{3+}:GdVO_4$	307	-----	1	239
$Yb^{3+}/Er^{3+}:Ba_5Y_8Zn_4O_{21}$	-----	3.9 (563 K)	1.36 (293 K)	240

The slight difference between our results and the results reported in the literature was satisfactory if we consider that the material described in the literature was a single crystal. Finally, the temperature response repeatability of the particles upon ten heating-cooling cycles (293 to 393 K, Figure 64) allowed us to conclude that these materials presented rapid and sensitive response to abrupt changes in temperature and confirmed their stability, good repeatability, and reproducibility.

Aiming at application as sensors or other biological uses and given that variable dispersion of particles is a way to control film transparency, we prepared SF-Yb^{3+}/Er^{3+}:YAG composite films doped with higher concentration of Yb^{3+} ions, as described in section 3.2.3.2 because they presented better emission intensity in response to excitation at 980 nm, even for the smallest observed relative sensitivity. We evaluated the temperature sensing behavior between 293 and 333 K to avoid thermal SF degradation. Figure 65 shows the UC emission spectra at several temperatures. We normalized the intensity with respect to the $^2H_{11/2} \rightarrow {}^4I_{15/2}$ transition (523.5 nm).

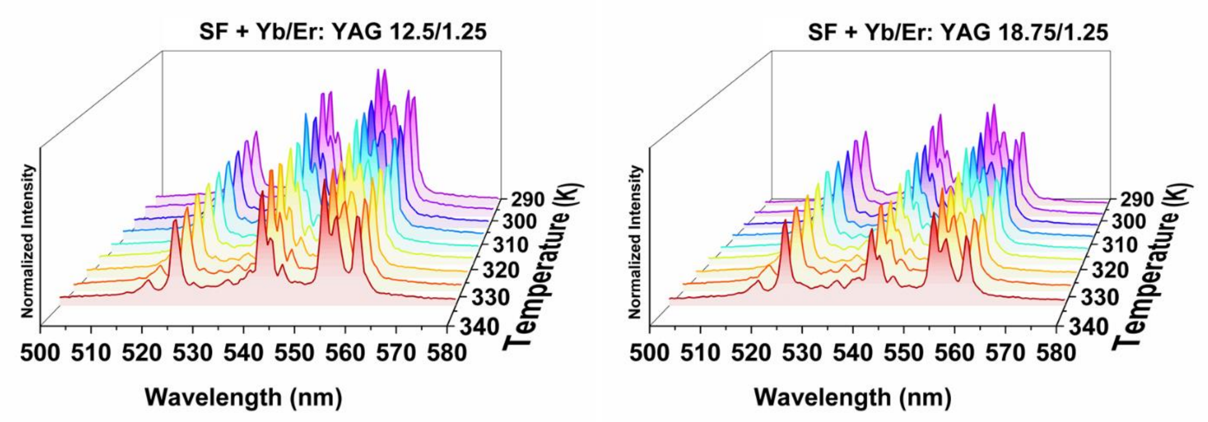

Figure 65. Temperature-dependent UC 3D emission spectra (λ_{exc} = 980 nm, from 293 K to 333 K) for SF-Yb^{3+}/Er^{3+}:YAG (Yb^{3+}/Er^{3+} % radio of 12.5/1.25 and 18.75/1.25) composite films normalized as a function of the band at 523.5 nm.

Compared to the Yb^{3+}/Er^{3+}:YAG particles, Figure 66 showed a similar behavior for the **FIR** for $^2H_{11/2}/^4S_{3/2}$, and the protein matrix did not damage the aimed thermometry answer. In fact, the relative sensitivity increase was noted for the SF-Yb^{3+}/Er^{3+}:YAG composite films, which gave maximum $\mathbf{S_r}$ values of 0.80% K^{-1} and 0.96% K^{-1} for SF- Yb^{3+}/Er^{3+}:YAG with Yb^{3+}/Er^{3+} % ratio of 12.5/1.25 and 18.75/1.25, respectively; and $\mathbf{S_{abs}}$ values of 2.32×10^{-3} K^{-1} and 3.69×10^{-3} K^{-1} for these same samples.

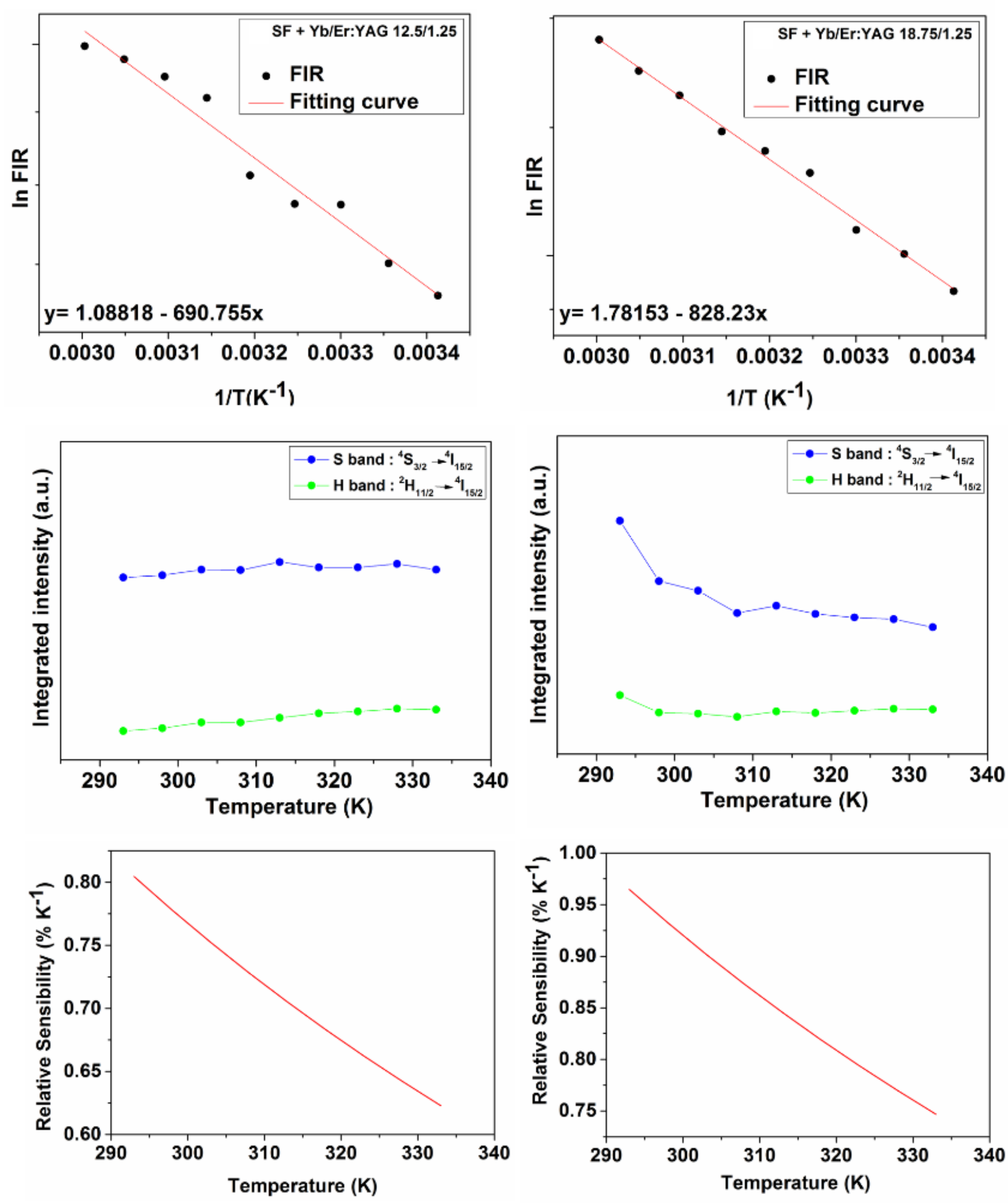

Figure 66. (first line) Fluorescence intensity ratio (**FIR** for $^2H_{11/2}/^4S_{3/2}$) as a function of temperature (**1/T**); (second line) integrated intensity of the S and H bands as a function of temperature (**T**); and (third line) relative sensitivity as a function of temperature. Columns are related to SF- Yb^{3+}/Er^{3+}:YAG composite films with Yb^{3+}/Er^{3+} % ratio of 12.5/1.25 and 18.75/1.25, respectively.

To confirm the temperature response repeatability in the SF-Yb^{3+}/Er^{3+}:YAG (SF-Yb^{3+}/Er^{3+}:YAG composite film with Yb^{3+}/Er^{3+} % ratio of 18.75/1.25, we carried out ten heating-cooling cycles (293 to 333 K, Figure 67). The results attested that the rapid and sensitive response observed for the Yb^{3+}/Er^{3+}:YAG particles also emerged for the composite film, which remained stable despite the fast change in temperature.

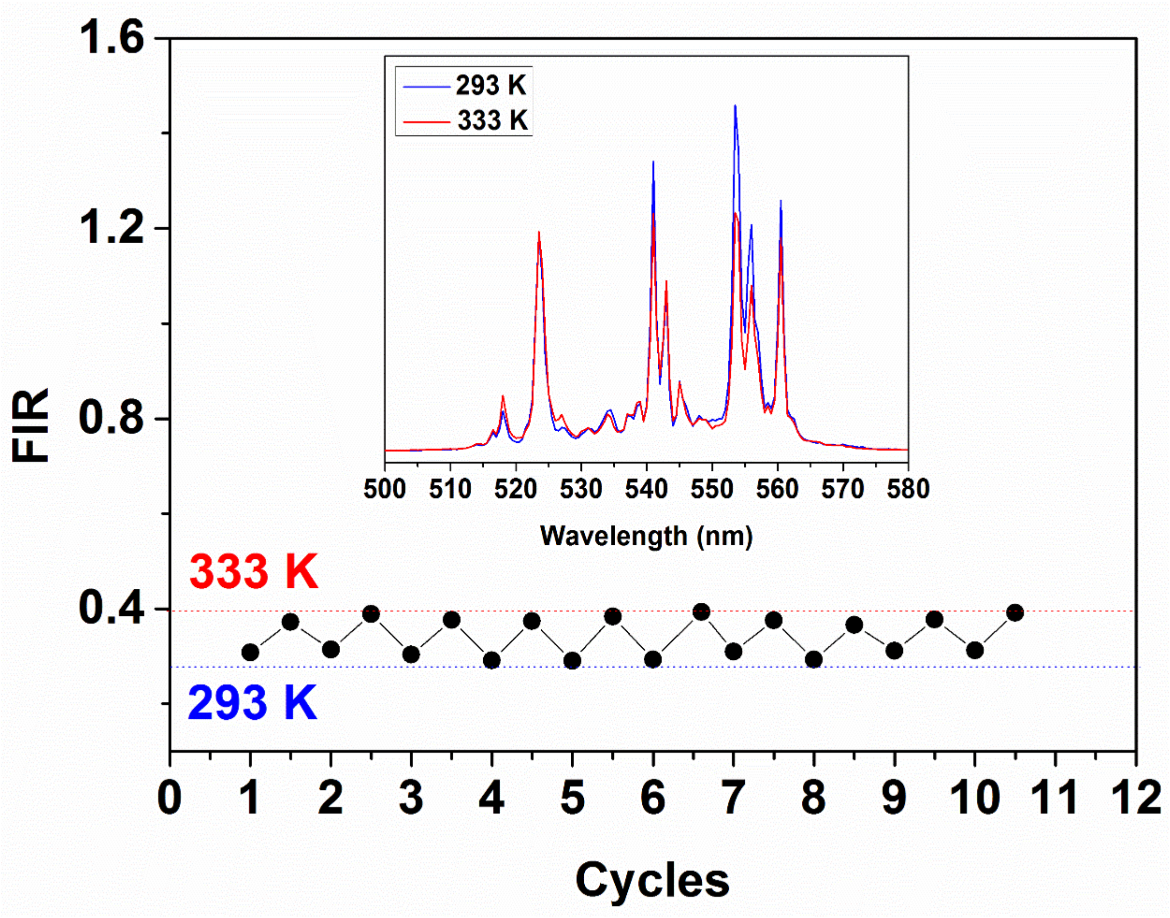

Figure 67. Emission spectra (λ_{exc} = 980 nm) obtained at 293 and 333 K and temperature measurement repeatability of **FIR** for $^2H_{11/2}/^4S_{3/2}$ for ten cycles between 293 and 333 K for SF-Yb^{3+}/Er^{3+}:YAG composite film with Yb^{3+}/Er^{3+} % ratio of 18.75/1.25.

In conclusion of this part, for the first time, the set of UC emission in SF-based materials and their photoluminescent properties were used as thermometer sensor. The strategy herein proposed ensured the UC emission of Er^{3+} ion even immersed in a protein matrix. We have synthesized YAG microparticles doped Yb^{3+} and Er^{3+} ions by SP, followed by a further heat treatment at 1100 °C for 12 h. These particles showed as highly crystalline, spherical, and non-coalesced particles, as confirmed by characterization analysis. The composite films were obtained with different concentrations of the particles disperse in the SF matrix, and the ratio of particles allowed us to control the transparence of the self-supported films. The UC emission was studied and were also visible to the naked eye, for the particles and also for the composite films. Moreover, that intense UC emission at the green spectrum, related to the $^2H_{11/2} \rightarrow {}^4I_{15/2}$ and $^4S_{3/2} \rightarrow {}^4I_{15/2}$ transitions, was studied on different temperature of sample, and the thermometry behavior as a result of different Yb^{3+} and Er^{3+} contents was carried out. The population of electrons in these thermally coupled levels was analyzed based on the Boltzmann distribution, and the Fluorescence Intensity Ratio (**FIR**) as a function of temperature (**T**) showed a linear slope. And the samples with low Yb^{3+} ion content presented higher thermal relative sensitivity. For the SF composite films, the particles with great Yb^{3+} concentration was used to guarantee an efficient excitation even in the SF-Yb^{3+}/Er^{3+}:YAG composite film with small amount of Yb^{3+}/Er^{3+}:YAG particles. The thermometry behavior observed for the UC emission from the Er^{3+} ion was kept on the silk composite, so in addition of the first time that UC emission has been detected in SF-based materials, the obtained material could be used as thermal sensor or smart ink, based on the UC emission for anti-counterfeiting applications, as mentioned.

5. Final Considerations

The project titled “Structural and spectroscopic study of luminescent composites based on fibroin and rare earth ions for photonic applications” proposed to obtain particles doped with Nd^{3+} ions and their SF-based compounds for studies of laser emission in a random environment. In the NanoLum group, YAG spheres had already been prepared via SP with boehmite suspension as a precursor, by changing the Y^{3+} ion content to control the crystalline network, and, also using lower concentrations of dopant ions. During the development of this project, YAG spheres doped with different concentrations of these ions were obtained by the SP technique. Although, obtaining the pure YAG phase was not immediately achieved due to the presence of the secondary phases YAP and YAM in the materials, that was identified after studies with XRD and photoluminescence spectroscopy. This is why we decided to carry out different heat treatments, where it was possible to obtain the pure YAG phase in spheres without coalescence after 12 h at 1100 °C. However, as a consequence of larger ionic radius of the Nd^{3+} ion, the lattice parameters were enlarged, and that shift increased with Nd^{3+} content, from 2.0 to 5.0%. The emission spectra of the Nd^{3+}:YAG samples confirmed the f-f transitions from Nd^{3+} replacing Y^{3+} at dodecahedral sites (D_2 symmetry) in the YAG cubic structure. The high solubility of Nd^{3+} into matrix avoided the clusters formation. However, the higher Nd^{3+} content reduced the average distance between the Ln centers, as a consequence, a quenching effect in their lifetime was noted. These materials were tested for their laser emissions in a random environment, and the spheres doped with 2.5, 3.0, 3.5, 4.0, 4.5 and 5.0% of Nd^{3+} ions showed this type of characteristic emission. The increase of Nd^{3+} concentration was followed by the lifetime decrease, as expected, due to a quenching of the excited level by the concentration effect. Moreover, the intense emission at 1064 nm, concerning the $^4F_{3/2} \rightarrow {}^4I_{11/2}$ transition, was studied on RL emission as a result of different Nd^{3+} contents, and as the concentration of Nd^{3+} ion increases, the threshold energy decreases, *e.g.*, the sample doped with 5.0% of neodymium, the threshold was 0.2 mJ, almost five times lower than for the 2.5% concentration sample.

After that, it was decided to obtain systems doped with Yb^{3+}/Er^{3+} ions, in order to study the energy conversion process and, based on this, the possible applications of this material as an optical thermometer. Obtaining Yb^{3+}/Er^{3+}:YAG was successfully achieved at different concentrations of doped ions (Yb^{3+}/Er^{3+} % radio of 12.5/1.25 and 18.75/1.25). In DRX diffractograms the peak related to plane (420) was shifted in different samples, *e.g.*, it was at 2theta equal to 33.4° (pattern), 33.4° (sample 12.5/1.25), and 33.2° (sample 18.75/1.25). In fact, the replacement of Y^{3+} ion (1.019Å) by the smaller ions as Yb^{3+} (0.985 Å) and Er^{3+} (1.004 Å) could induce a lattice parameter smaller than the standard value of cubic YAG but, herein, the shifted was not linear by the doping concentration, so secondary aspects could be pointed, as for example, the determination of reflection positions is very sensitive towards the sample position, in XDR equipment, then, that slightly shift could be only a pitfalls in the characterization. The UC process proved to be effective (the green color can be easily seen with the naked eye), as well as its thermometry properties. The population of electrons in these thermally coupled levels was analyzed based on the Boltzmann distribution, and the Fluorescence Intensity Ratio (FIR) as a function of temperature (T) showed a linear slope. And the samples with low Yb^{3+} ion content presented higher thermal relative sensitivity. Finally, it was decided to obtain self-supporting films based on SF. By inserting the particles in the SF matrix, flexible and self-supporting systems were obtained, where it was possible to observe, with the naked eye, the green emission within this matrix. For the SF composite films, the particles with great Yb^{3+} concentration was used to guarantee an efficient excitation even in the SF-Yb^{3+}/Er^{3+}:YAG composite film with small amount of Yb^{3+}/Er^{3+}:YAG particles. The thermometry behavior observed for the UC emission from the Er^{3+} ion was kept on the silk composite.

Still in order to study the UC processes, however, looking for blue-emissions, spheres doped with Yb^{3+}/Tm^{3+} ions were obtained. In the same way as for the Yb^{3+}/Er^{3+} doped system, the blue color was observed with the naked eye, both in the spheres and in the SF films prepared with this material. Because the protein matrix consists of amino acids with hydrophobic and hydrophilic chains, UC may be quenched. To solve this problem, Ln ions can be incorporated into an inorganic crystalline matrix, which will protect them from the quenching phonon effect of the protein structure, preventing their emissions from being suppressed. With this, it is believed that these self-supporting systems have the potential to be applied with an anti-counterfeiting device, as already reported in the literature for other systems doped with Tm^{3+} ions. Obtaining this type of device is based on the fact that UC processes involving 3 photons are less common than the mechanism involving only 2 photons, which was observed in the materials prepared in this work.

In summary, Ln^{3+}:YAG particles doped at different concentrations were successfully obtained by the SP technique, showing the possibility of obtaining sphere particles, without coalescence and with a large amount of dopant ions through a methodology that presents high yield, does not generate byproducts, and can be used on a large scale, which can be used as an important tool for the production of photonic materials. In the same way, systems based on inorganic particles and protein matrix were also successfully obtained, and presented important characteristics that can be explored by the field of photonics. Based on these results, it is believed that other materials aimed at photonic applications can be successfully obtained via SP, as well as devices based on protein matrices. Given this, new precursors must be tested in the pyrolysis system, to obtain other matrices in particulate materials. In addition, the globular portion of the silk threads, sericin, will begin to be studied as a possible photonic material, aiming at the full use of the thread.

6. References

1. Kang, Y. C., Lenggoro, I. W., Park, S. Bin & Okuyama, K. YAG:Ce phosphor particles prepared by ultrasonic spray pyrolysis. *Mater. Res. Bull.* **35**, 789–798 (2000).
2. Gurav, A., Kodas, T., Pluym, T. & Xiong, Y. Aerosol processing of materials. *Aerosol Sci. Technol.* **19**, 411–452 (1993).
3. Reuge, N. *et al.* Modeling of spray pyrolysis—why are the synthesized Y2O3 microparticles hollow? *AIChE J.* **54**, 394–405 (2008).
4. Caiut, J. M. A. *et al.* Elaboration of boehmite nano-powders by spray-pyrolysis. *Powder Technol.* **190**, 95–98 (2009).
5. Riul, A., da Fonseca, F. A. A., Pugina, R. S. & Caiut, J. M. A. Tuned structure of europium-doped Al2O3-ytrium luminescent composites and their spectroscopic behavior. *J. Lumin.* **233**, 3–10 (2021).
6. Wang, J. *et al.* Mechanism of Intrinsic Point Defects and Oxygen Diffusion in Yttrium Aluminum Garnet: First-Principles Investigation. *J. Am. Ceram. Soc.* **95**, 3628–3633 (2012).
7. Mancic, L., Marinkovic, K., Marinkovic, B. A., Dramicanin, M. & Milosevic, O. YAG:Ce3+ nanostructured particles obtained via spray pyrolysis of polymeric precursor solution. *J. Eur. Ceram. Soc.* **30**, 577–582 (2010).
8. Rockwood, D. N. *et al.* Materials fabrication from Bombyx mori silk fibroin. *Nat. Protoc.* **6**, 1612–1631 (2011).
9. Omenetto, F. G. & Kaplan, D. L. New opportunities for an ancient material. *Science (80-.).* **329**, 528–531 (2010).
10. Lupei, V. & Lupei, A. Nd:YAG at its 50th anniversary: Still to learn. *J. Lumin.* **169**, 426–439 (2016).
11. Pugina, R. S. *et al.* Nd3+:YAG microspheres powders prepared by spray pyrolysis: Synthesis, characterization and random laser application. *Mater. Chem. Phys.* **269**, (2021).
12. Cotton, S. Lanthanide and Actinide Chemistry. 1-280 (2006).
13. Brites, C. D. S., Millán, A. & Carlos, L. D. Lanthanides in Luminescent Thermometry. *Handb. Phys. Chem. Rare Earths* **49**, 339–427 (2016).
14. web site. https://abal.org.br/aluminio/historia-do-aluminio/.
15. Constantino, V. R. L., Araki, K., Oliveira, D. De & Oliveira, W. De. Preparação de

Compostos de Alumínio a partir da Bauxita: Considerações Sobre Alguns Aspectos Envolvidos em um Experimento Didático. *Quim. Nova* **25**, 490–498 (2002).

16. web site. http://www.gruporeciclabr.com.br/pt/o-que-reciclamos/aluminio/aplicacoes.
17. web site. https://www.preparaenem.com/quimica/aluminio.htm.
18. web site. https://abal.org.br/sustentabilidade/reciclagem/reciclagem-no-brasil/.
19. Carvalho, A. As bauxitas no Brasil - síntese de um programa de pesquisa. 1–130 (1989).
20. web site . https://www.statista.com/statistics/271671/countries-with-largest-bauxite-reserves/.
21. Cockayne, B. The uses and enigmas of the Al2O3-Y2O3 phase system. *J. Less-Common Met.* **114**, 199–206 (1985).
22. web site. https://icsd.products.fiz-karlsruhe.de/.
23. Zhou, X. *et al.* Y4Al2O9 ceramics as a novel thermal barrier coating material for high-temperature applications. *Mater. Lett.* **134**, 146–148 (2014).
24. Medraj, M., Hammond, R., Parvez, M. A., Drew, R. A. L. & Thompson, W. T. High temperature neutron diffraction study of the Al2O3-Y2O3 system. *J. Eur. Ceram. Soc.* **26**, 3515–3524 (2006).
25. Lemański, K., Michalska, M., Ptak, M., Małecka, M. & Szysiak, A. Surface modification using silver nanoparticles for Y4Al2O9:Nd – Synthesis and their selected studies. *J. Mol. Struct.* **1202**, 1–6 (2020).
26. Hernández-Rodríguez, M. A., Lozano-Gorrín, A. D., Martín, I. R., Rodríguez-Mendoza, U. R. & Lavín, V. Spectroscopic properties of Nd3+ ions in YAP nano-perovskites. *J. Lumin.* **188**, 204–208 (2017).
27. Harada, M. & Goto, M. Synthesis of Y–Al–O compounds by a polymer complex method. *J. Alloys Compd.* **408–412**, 1193–1195 (2006).
28. Liu, S. & Su, Q. Sol-gel synthesis and luminescence of Y4Al2O9:RE3+ (RE=Eu, Tb). *J. Alloys Compd.* **255**, 102–105 (1997).
29. Basavalingu, B., Girish, H. N., Byrappa, K. & Soga, K. Hydrothermal synthesis and characterization of orthorhombic yttrium aluminum perovskites (YAP). *Mater. Chem. Phys.* **112**, 723–725 (2008).
30. Lo, J.-R. & Tseng, T.-Y. Phase development and activation energy of the Y2O3-Al2O3 system by a modified sol-gel process. *Mater. Chem. Phys.* **56**, 56–62 (1998).
31. Kenyon, A. Recent developments in rare-earth doped materials for optoelectronics.

Prog. Quantum Electron. **26**, 225–284 (2002).

32. Kniec, K. & Marciniak, L. The influence of grain size and vanadium concentration on the spectroscopic properties of YAG:V3+,V5+ and YAG: V, Ln3+ (Ln3+ = Eu3+, Dy3+, Nd3+) nanocrystalline luminescent thermometers. *Sensors Actuators, B Chem.* **264**, 382–390 (2018).
33. Cantarano, A., Ibanez, A. & Dantelle, G. Garnet-Type Nanophosphors for White LED Lighting. *Front. Mater.* **7**, 1–9 (2020).
34. Liang, J. *et al.* Full-visible-spectrum lighting enabled by an excellent cyan-emitting garnet phosphor. *J. Mater. Chem. C* **8**, 4934–4943 (2020).
35. Wu, L. *et al.* Synthesis and optical properties of a Y3(Al/Ga)5O12:Ce3+,Cr3+,Nd3+persistent luminescence nanophosphor: A promising near-infrared-II nanoprobe for biological applications. *Nanoscale* **12**, 14180–14187 (2020).
36. Geller, S. Crystal Chemistry of the Garnets. *Z. Krist. Cryst. Mater* **125**, 1–47 (1967).
37. Ikesue, A., Kamata, K. & Yoshida, K. Effects of neodymium concentration on optical characteristics of polycrystalline Nd:YaG laser materials. *J. Amer. Ceram. Soc.* **79** 1921–1926 (1996).
38. Bi, F., Dong, X., Wang, J. & Liu, G. Electrospinning Preparation and Photoluminescence Properties of Y3Al5O12:Eu3+ Nanobelts. *Mater. Res.* **18**, 411–416 (2015).
39. Azkargorta, J. *et al.* Random laser action in Nd:YAG crystal powder. *Materials (Basel).* **9**, 1–8 (2016).
40. Veith, M. New synthetic routes to nano-composites with ceramic particles, using lanthanide compounds. *J. Sol-Gel Sci. Technol.* **46**, 291–298 (2008).
41. Sakar, N., Gergeroglu, H., Akalin, S. A., Oguzlar, S. & Yildirim, S. Synthesis, Structural and Optical Characterization of Nd: YAG Powders via Flame Spray Pyrolysis. *Opt. Mater. (Amst).* **103**, 109819 (2020).
42. Caiut, J. M. A. *et al.* Synthesis and luminescence properties of water dispersible Eu 3+-doped boehmite nanoparticles. *Nanotechnology* **18**, (2007).
43. Rajabi, L. & Derakhshan, A. A. Room Temperature Synthesis of Boehmite and Crystallization of Nanoparticles : Effect of Concentration and Ultrasound. **2**, 163–172 (2010).
44. Souza Santos, P., Vieira Coelho, A. C., Souza Santos, H. & Kunihiko Kiyohara, P.

Hydrothermal synthesis of well-crystallised boehmite crystals of various shapes. *Mater. Res.* **12**, 437–445 (2009).

45. Kang, H. S., Kang, Y. C., Park, H. D. & Shul, Y. G. Morphology of particles prepared by spray pyrolysis from organic precursor solution. *Mater. Lett.* **57**, 1288–1294 (2003).
46. Falcony, C., Aguilar-Frutis, M. A. & García-Hipólito, M. Spray pyrolysis technique; High-K dielectric films and luminescent materials: A review. *Micromachines* **9**, 1–33 (2018).
47. Dexpert-Ghys, J., Dexpert-ghys, J., Verelst, M. Synthese par pyrolyse d'aerosol et caracterisation de luminophores : Y2O3:Eu3+ et An2SiO4:Mn2+ pour application dans les panneaux a plasma. (2004).
48. Abrão, A. *Química e Tecnologia das Terras-Raras*. *CETEM/CNPq*, 1-115 (1994).
49. Sousa Filho, P. C. de & Serra, O. A. Terras Raras no Brasil: histórico, produção e perspectivas. *Quim. Nova* **37**, 753–760 (2014).
50. De Sousa Filho, P. C., Galaço, A. R. B. S. & Serra, O. A. Rare earths: Periodic table, discovery, exploration in brazil and applications. *Quim. Nova* **42**, 1208–1224 (2019).
51. Lucas, J., Lucas, P., Le Mercier, T., Rollat, A. & Davenport, W. Overview. *Rare Earths* **8**, 1–14 (2015).
52. Spedding, F. H. *et al.* The Separation of Rare Earths by Ion Exchange. II. Neodymium and Praseodymium. *J. Am. Chem. Soc.* **69**, 2786–2792 (1947).
53. Spedding, F. H., Voigt, A. F., Gladrow, E. M. & Sleight, N. R. The Separation of Rare Earths by Ion Exchange. 1,2 I. Cerium and Yttrium. *J. Am. Chem. Soc.* **69**, 2777–2781 (1947).
54. Bunzli, J. C. G. & Choppin, G. R. Lanthanide Probes in Life , Chemical a Earth Sciences : Theory and Practice. (2014).
55. Judd, B. R. Optical absorption intensities of rare-earth ions. *Phys. Rev.* **127**, 750–761 (1962).
56. Bünzli, J. C. G. & Piguet, C. Taking advantage of luminescent lanthanide ions. *Chem. Soc. Rev.* **34**, 1048–1077 (2005).
57. Martins, T. S. & Isolani, P. C. Terras raras: Aplicações industriais e biológicas. *Quim. Nova* **28**, 111–117 (2005).
58. Malta, O. L. & Carlos, L. D. Intensities of 4f-4f transitions in glass materials. *Quim. Nova* **26**, 889–895 (2003).
59. Binnemans, K. Interpretation of europium(III) spectra. *Coord. Chem. Rev.* **295**, 1–45

(2015).

60. Ma, C. G. *et al.* Energy level schemes of fN electronic configurations for the di-, tri-, and tetravalent lanthanides and actinides in a free state. *J. Lumin.* **170**, 369–374 (2016).
61. Edgar, A. *Luminescent Materials*. (2007).
62. Ofelt, G. S. Intensities of crystal spectra of rare-earth ions. *J. Chem. Phys.* **37**, 511–520 (1962).
63. Zhang, F. Near-infrared Nanomaterials: Preparation, Bioimaging and Therapy Applications (2016).
64. Ivanov, M. G., Kynast, U. & Leznina, M. Eu3+ doped yttrium oxide nano-luminophores from laser synthesis. *J. Lumin.* **169**, 744–748 (2016).
65. Sagawa, M., Fujimura, S., Togawa, N., Yamamoto, H. & Matsuura, Y. New material for permanent magnets on a base of Nd and Fe (invited). *J. Appl. Phys.* **55**, 2083–2087 (1984).
66. Moura, A. L. *et al.* Nonlinear effects and photonic phase transitions in Nd3+ -doped nanocrystal-based random lasers . *Appl. Opt.* **59**, D155 (2020).
67. Moura, A. L. *et al.* Random lasing in Nd3+ doped potassium gadolinium tungstate crystal powder. *J. Appl. Phys.* **117**, 10–13 (2015).
68. Câmara, J. G., da Silva, D. M., Kassab, L. R. P., de Araújo, C. B. & Gomes, A. S. L. Random laser emission from neodymium doped zinc tellurite glass-powder presenting luminescence concentration quenching. *J. Lumin.* **233**, (2021).
69. Moura, A. L. *et al.* Tunable ultraviolet and blue light generation from Nd:YAB random laser bolstered by second-order nonlinear processes. *Sci. Rep.* **6**, 2–7 (2016).
70. Marciniak, L., Bednarkiewicz, A. & Strek, W. The impact of nanocrystals size on luminescent properties and thermometry capabilities of Cr, Nd doped nanophosphors. *Sensors Actuators B Chem.* **238**, 381–386 (2017).
71. Balabhadra, S. *et al.* Boosting the sensitivity of Nd3+-based luminescent nanothermometers. *Nanoscale* **7**, 17261–17267 (2015).
72. Marciniak, L., Bednarkiewicz, A. & Elzbieciak, K. NIR-NIR photon avalanche based luminescent thermometry with Nd3+ doped nanoparticles. *J. Mater. Chem. C* **6**, 7568–7575 (2018).
73. Brites, C. D. S., Balabhadra, S. & Carlos, L. D. Lanthanide-Based Thermometers: At the Cutting-Edge of Luminescence Thermometry. *Adv. Opt. Mater.* **7**, 1–30 (2019).
74. Saleh, B. E. A. & Teich, M. C. *Fundamentals of photonics* (2019).

75. Venkatachalam, N. *et al.* Er 3+-doped y 2 O 3 nanophosphors for near-infrared fluorescence bioimaging applications. *J. Am. Ceram. Soc.* **96**, 2759–2765 (2013).
76. Reis, D. H. S. *et al.* Multifunctional possible application of the Er3+/Yb3+-coped Al2O3 prepared by recyclable precursor (aluminum can) and also by sol-gel process. *Opt. Mater. (Amst).* **84**, 504–513 (2018).
77. Hehlen, M. P., Cockroft, N. J., Gosnell, T. R. & Bruce, A. J. Spectroscopic properties of Er3+-and Yb3+-doped soda-lime silicate and aluminosilicate glasses. *Phys. Rev. B* **56**, 9302–9318 (1997).
78. Auzel, F. Upconversion processes in coupled ion systems. *J. Lumin.* **45**, 341–345 (1990).
79. Dubey, A., Soni, A. K., Kumari, A., Dey, R. & Rai, V. K. Enhanced green upconversion emission in NaYF4:Er3+/Yb3+/Li+phosphors for optical thermometry. *J. Alloys Compd.* **693**, 194–200 (2017).
80. Duan, C., Liang, L., Li, L., Zhang, R. & Xu, Z. P. Recent progress in upconversion luminescence nanomaterials for biomedical applications. *J. Mater. Chem. B* **6**, 192–209 (2018).
81. Zhou, B., Shi, B., Jin, D. & Liu, X. Controlling upconversion nanocrystals for emerging applications. *Nat. Nanotechnol.* **10**, 924–936 (2015).
82. Chen, J. & Zhao, J. X. Upconversion nanomaterials: Synthesis, mechanism, and applications in sensing. *Sensors* **12**, 2414–2435 (2012).
83. Ramasamy, P., Manivasakan, P. & Kim, J. Upconversion nanophosphors for solar cell applications. *RSC Adv.* **4**, 34873–34895 (2014).
84. Gulzar, A., Xu, J., Yang, P., He, F. & Xu, L. Upconversion processes: Versatile biological applications and biosafety. *Nanoscale* **9**, 12248–12282 (2017).
85. Pandey, A. *et al.* Enhanced upconversion and temperature sensing study of Er 3+-Yb3+ codoped tungsten-tellurite glass. *Sensors Actuators, B Chem.* **202**, 1305–1312 (2014).
86. Li, X. *et al.* Enhancing upconversion emission and temperature sensing modulation of the La2(MoO4)3: Er3+, Yb3+ phosphor by adding alkali metal ions. *Ceram. Int.* **46**, 20664–20671 (2020).
87. Bao, R., Yu, L., Ye, L., Zhang, X. & Wang, L. G. Compact and sensitive Er3+/Yb3+ co-doped YAG single crystal optical fiber thermometry based on up-conversion luminescence. *Sensors Actuators, A Phys.* **269**, 182–187 (2018).
88. Ma, M. *et al.* Intense ultraviolet and blue upconversion emissions in Yb3+–Tm3+

codoped stoichiometric Y7O6F9 powder. *Phys. B Condens. Matter* **406**, 3256–3260 (2011).

89. You, M. *et al.* Inkjet printing of upconversion nanoparticles for anti-counterfeit applications. *Nanoscale* **7**, 4423–4431 (2015).
90. Liu, Y., Ai, K. & Lu, L. Designing lanthanide-doped nanocrystals with both up- and down-conversion luminescence for anti-counterfeiting. *Nanoscale* **3**, 4804–4810 (2011).
91. da Luz, L. L. *et al.* Inkjet Printing of Lanthanide–Organic Frameworks for Anti-Counterfeiting Applications. *ACS Appl. Mater. Interfaces* **7**, 27115–27123 (2015).
92. Nogueira, M. *et al.* Método Manual Para Deposição De Tintas Fotoluminescentes Baseadas Em Lofs Mistas Aplicado a Codificação De Documentos. *Quim. Nova* **43**, 1393–1396 (2020).
93. Zhang, Y. *et al.* Multicolor barcoding in a single upconversion crystal. *J. Am. Chem. Soc.* **136**, 4893–4896 (2014).
94. Nalin, M. *et al.* Glassy materials and light: Part 1. *Quim. Nova* **39**, 328–339 (2016).
95. Einstein, A. The Quantum Theory of Radiation. *Phys. Zeitschrift* **35**, 317–322 (1926).
96. Nikjoo, H., Uehara, S. & Emfietzoglou, D. *Interaction of radiation with matter*. (CRC press, 2012).
97. Wiersma, D. S. Experiments on random lasers. (2001).
98. Wiersma, D. Light in strongly scattering and amplifying random media. *Thesis* (1995).
99. Strutt, J. W. XV. On the light from the sky, its polarization and colour . *London, Edinburgh, Dublin Philos. Mag. J. Sci.* **41**, 107–120 (1871).
100. Balachandran, R. M. & Lawandy, N. M. Laser action in strongly scattering media. *Proc. Int. Quantum Electron. Conf.* **368**, 239–240 (1994).
101. Maiman, T. H. Stimulated Optical Radiation in Ruby. *Nature* **187**, 493–494 (1960).
102. Holzrichter, J. F. & Emmett, J. L. Design and Analysis of a High Brightness Axial Flash lamp. *Appl. Opt.* **8**, 1459–1465 (1969).
103. Camacho-Aguilera, R. E. *et al.* An electrically pumped germanium laser. *Opt. Express* **20**, 11316–11320 (2012).
104. web site. https://semesters.in/construction-and-working-of-ruby/.
105. Sorokin, P. P. & Lankard, J. R. Stimulated Emission Observed from an Organic Dye, Chloro-aluminum Phthalocyanine. *IBM J. Res. Dev.* **10**, 162–163 (2010).
106. Wiersma, D. The smallest random laser. *Nature* **406**, 133–135 (2000).

107. Luan, F. *et al.* Lasing in nanocomposite random media. *Nano Today* **10**, 168–192 (2015).
108. Stassinopoulos, A. *et al.* Random laser action in ZnO nanohybrids. *Opt. InfoBase Conf. Pap.* **184**, 181–184 (2007).
109. Sha, W. L., Liu, C.-H. & Alfano, R. R. Spectral and temporal measurements of laser action of Rhodamine 640 dye in strongly scattering media. *Opt. Lett.* **19**, 1922–1924 (1994).
110. Letokhov, V. Generation of Light by a Scattering Medium with Negative Resonance Absorption. *Sov. J. Exp. Theor. Phys.* **26**, 835 (1968).
111. Markushev, V. M., Zolin, V. F. & Briskina, C. M. Luminescence and stimulated emission of neodymium in sodium lanthanum molybdate powders. *Sov. J. Quantum Electron.* **16**, 281–283 (1986).
112. Gouedard, C., Husson, D., Sauteret, C., Auzel, F. & Migus, A. Generation of spatially incoherent short pulses in laser-pumped neodymium stoichiometric crystals and powders. *J. Opt. Soc. Am. B* **10**, 2358–2363 (1993).
113. Lawandy, N. M., Balachandran, R. M., Gomes, A. S. L. & Sauvain, E. Laser action in strongly scattering media. *Nature* **368**, 436–438 (1994).
114. Polson, R. C. & Vardeny, Z. V. Random lasing in human tissues. *Appl. Phys. Lett.* **85**, 1289–1291 (2004).
115. Cao, H. *et al.* Random laser action in semiconductor powder. *Phys. Rev. Lett.* **82**, 2278–2281 (1999).
116. de Matos, C. J. S. *et al.* Random Fiber Laser. *Phys. Rev. Lett.* **99**, 153903 (2007).
117. Da Silva, R. R. *et al.* Silk fibroin biopolymer films as efficient hosts for DFB laser operation. *J. Mater. Chem. C* **1**, 7181–7190 (2013).
118. Chen, Y. *et al.* Colloidal quantum dot random laser. *Opt. Express* **19**, 2996–3003 (2011).
119. Sznitko, L., Kaliciak, K., Adamow, A. & Mysliwiec, J. A random laser made of nematic liquid crystal doped with a laser dye. *Opt. Mater. (Amst).* **56**, 121–128 (2016).
120. Santos, M. V. *et al.* Silk fibroin as a biotemplate for hierarchical porous silica monoliths for random laser applications. *J. Mater. Chem. C* **6**, 2712–2723 (2018).
121. Moura, A. L., Pincheira, P. I. R., Maia, L. J. Q., Gomes, A. S. L. & de Araújo, C. B. Two-color random laser based on a Nd3+ doped crystalline powder. *J. Lumin.* **181**, 44–48 (2017).

122. Moura, A. L., Maia, L. J. Q., Jerez, V., Gomes, A. S. L. & de Araújo, C. B. Random laser in Nd:YBO3 nanocrystalline powders presenting luminescence concentration quenching. *J. Lumin.* **214**, 116543 (2019).
123. Moura, A. L., Maia, L. J. Q., Gomes, A. S. L. & de Araújo, C. B. Optimal performance of NdAl3(BO3)4 nanocrystals random lasers. *Opt. Mater. (Amst).* **62**, 593–596 (2016).
124. Quintanilla, M. & Liz-Marzán, L. M. Guiding Rules for Selecting a Nanothermometer. *Nano Today* **19**, 126–145 (2018).
125. Balabhadra, S., Debasu, M. L., Brites, C. D. S., Ferreira, R. A. S. & Carlos, L. D. Upconverting Nanoparticles Working As Primary Thermometers in Different Media. *J. Phys. Chem. C* **121**, 13962–13968 (2017).
126. Pezzolo, D. Tecidos: histórias, tramas, tipos e usos (2007).
127. Strathern, P. Confúcio em 90 minutos. (1998).
128. Santos, V. C. *et al.* Sericicultura : colhendo os frutos da criação do bicho-da-seda Sericulture : reaping the fruits of silkworm rearing. *INTESA – Inf. Técnico do Semiárido* **10**, 62–68 (2016).
129. Lucia, M. & Gnerre, A. Rota da seda: trânsitos culturais e sagrados nos caminhos da China. *Rev. Reli.* **12**, 244–259 (2015).
130. Barbosa, M. P., Costa Lima, M., Fonseca, P. A. & Gomes, R. A. M. Nova Rota da Seda e a Ascensão Pacífica Chinesa. *NEARI em Rev.* **2**, 21–31 (2016).
131. web site. https://www.dicionarioinformal.com.br/.
132. Regier, J. C. *et al.* A Large-Scale, Higher-Level, Molecular Phylogenetic Study of the Insect Order Lepidoptera (Moths and Butterflies). *PLoS One* **8**, (2013).
133. Ude, A. U. *et al.* Bombyx mori silk fibre and its composite: A review of contemporary developments. *Mater. Des.* **57**, 298–305 (2014).
134. Kundu, S. C., Dash, B. C., Dash, R. & Kaplan, D. L. Natural protective glue protein, sericin bioengineered by silkworms: Potential for biomedical and biotechnological applications. *Prog. Polym. Sci.* **33**, 998–1012 (2008).
135. Altman, G. H. *et al.* Silk-based biomaterials. *Biomaterials* **24**, 401–416 (2003).
136. Coleman, D. & Howitt, F. Studies on silk proteins I. The properties and constitution of fibroin. The conversion of fibroin into a water-soluble form and its bearing on the phenomenon of denaturation. *Proc. R. Soc. London. Ser. B - Biol. Sci.* **134**, 544–545 (1947).
137. Kundu, B., Rajkhowa, R., Kundu, S. C. & Wang, X. Silk fibroin biomaterials for tissue

regenerations. *Adv. Drug Deliv. Rev.* **65**, 457–470 (2013).

138. Kon'kov, A. S., Pustovalova, O. L. & Agapov, I. I. Biocompatible materials from regenerated silk for tissue engineering and medicinal therapy. *Appl. Biochem. Microbiol.* **46**, 739–744 (2010).
139. Vepari, C. & Kaplan, D. L. Silk as a biomaterial. *Prog. Polym. Sci.* **32**, 991–1007 (2007).
140. Omenetto, F. G. & Kaplan, D. L. A new route for silk. *Nat. Photonics* **2**, 641–643 (2008).
141. Zhang, Y. Q. Applications of natural silk protein sericin in biomaterials. *Biotechnol. Adv.* **20**, 91–100 (2002).
142. Kunz, R. I., Brancalhão, R. M. C., Ribeiro, L. D. F. C. & Natali, M. R. M. Silkworm Sericin: Properties and Biomedical Applications. *Biomed Res. Int.* **2016**, (2016).
143. Takechi, T., Wada, R., Fukuda, T., Harada, K. & Takamura, H. Antioxidant activities of two sericin proteins extracted from cocoon of silkworm (Bombyx mori) measured by DPPH, chemiluminescence, ORAC and ESR methods. *Biomed. Reports* **2**, 364–369 (2014).
144. Kato, N. *et al.* Silk Protein, Sericin, Inhibits Lipid Peroxidation and Tyrosinase Activity. *Biosci. Biotechnol. Biochem.* **62**, 145–147 (1998).
145. Barajas-Gamboa, J. A., Serpa-Guerra, A. M., Restrepo-Osorio, A. & Álvarez-López, C. Aplicaciones de la sericina: una proteina globular proveniente de la seda. *Ing. y Compet.* **18**, 193 (2016).
146. Padamwar, M. N., Pawar, A. P., Daithankar, A. V & Mahadik, K. R. Silk sericin as a moisturizer: an in vivo study. *J. Cosmet. Dermatol.* **4**, 250–257 (2005).
147. Fan, J. B., Wu, L. P., Chen, L. S., Mao, X. Y. & Ren, F. Z. Antioxidant activities of silk sericin from silkworm bombyx mori. *J. Food Biochem.* **33**, 74–88 (2009).
148. Wurm, F. M. Human therapeutic proteins from silkworms. *Nat. Biotechnol.* **21**, 34–35 (2003).
149. Li, M. *et al.* Study on porous silk fibroin materials. II. Preparation and characteristics of spongy porous silk fibroin materials. *J. Appl. Polym. Sci.* **79**, 2192–2199 (2001).
150. Mathur, A. B., Tonelli, A., Rathke, T. & Hudson, S. The dissolution and characterization of bombyx mori silk fibroin in calcium nitrate-methanol solution and the regeneration of films. *Biopolym. - Nucleic Acid Sci. Sect.* **42**, 61–74 (1997).
151. Chen, X., Knight, D. P., Shao, Z. & Vollrath, F. Regenerated Bombyx silk solutions

studied with rheometry and FTIR. *Polymer (Guildf).* **42**, 09969–09974 (2001).

152. Kamhaengpol, A. Fibroin protein extract from red ant nests for a production of electrospun nanofibers. *Asia-Pacific J. Sci. Technol.* **15**, 919–929 (2010).

153. Sun, Y. *et al.* Acrylic polymer-silk fibroin blend fibers. *J. Appl. Polym. Sci.* **65**, 959–966 (1997).

154. Tanaka, K. *et al.* Determination of the site of disulfide linkage between heavy and light chains of silk fibroin produced by Bombyx mori. *Biochim. Biophys. Acta* **1432**, 92–103 (1999).

155. Qi, Y. *et al.* A Review of Structure Construction of Silk Fibroin Biomaterials from Single Structures to Multi-Level Structures. *Int. J. Mol. Sci.* **18**, (2017).

156. Tanaka, K., Inoue, S. & Mizuno, S. Hydrophobic interaction of P25, containing Asn-linked oligosaccharide chains, with the H-L complex of silk fibroin produced by Bombyx mori. *Insect Biochem. Mol. Biol.* **29**, 269–276 (1999).

157. Inoue, S. *et al.* Silk fibroin of Bombyx mori is secreted, assembling a high molecular mass elementary unit consisting of H-chain, L-chain, and P25, with a 6:6:1 molar ratio. *J. Biol. Chem.* **275**, 40517–40528 (2000).

158. Marsh, R. E., Corey, R. B. & Pauling, L. An investigation of the structure of silk fibroin. *Biochim. Biophys. Acta* **16**, 1–34 (1955).

159. Motta, A., Fambri, L. & Migliaresi, C. Regenerated silk fibroin films: Thermal and dynamic mechanical analysis. *Macromol. Chem. Phys.* **203**, 1658–1665 (2002).

160. Valluzzi, R., Gido, S. P., Muller, W. & Kaplan, D. L. Orientation of silk III at the air-water interface. *Int. J. Biol. Macromol.* **24**, 237–242 (1999).

161. Tanaka, K. *et al.* Determination of the site of disulfide linkage between heavy and light chains of silk fibroin produced by Bombyx mori. *Biochim. Biophys. Acta - Protein Struct. Mol. Enzymol.* **1432**, 92–103 (1999).

162. Yang, Y., Shao, Z., Chen, X. & Zhou, P. Optical spectroscopy to investigate the structure of regenerated Bombyx mori silk fibroin in solution. *Biomacromolecules* **5**, 773–779 (2004).

163. Meng, Z., Zheng, X., Tang, K., Liu, J. & Qin, S. Dissolution of natural polymers in ionic liquids: A review. *E-Polymers* **28**, 1–29 (2012).

164. Kundu, B. *et al.* Silk proteins for biomedical applications: Bioengineering perspectives. *Prog. Polym. Sci.* **39**, 251–267 (2014).

165. Arai, T., Freddi, G., Innocenti, R. & Tsukada, M. Biodegradation of bombyx mori silk

fibroin fibers and films. *J. Appl. Polym. Sci.* **91**, 2383–2390 (2004).

166. Kim, D. H. *et al.* Dissolvable films of silk fibroin for ultrathin conformal bio-integrated electronics. *Nat. Mater.* **9**, 511–517 (2010).
167. Jiang, C. *et al.* Mechanical properties of robust ultrathin silk fibroin films. *Adv. Funct. Mater.* **17**, 2229–2237 (2007).
168. Zhu, B. *et al.* Silk Fibroin for Flexible Electronic Devices. *Adv. Mater.* **28**, 4250–4265 (2016).
169. Tansil, N. C., Koh, L. D. & Han, M. Y. Functional silk: Colored and luminescent. *Adv. Mater.* **24**, 1388–1397 (2012).
170. Pugina, R. S., da Rocha, E. G., Ribeiro, S. J. L. & Caiut, J. M. A. Study of the energy transfer process in rare earth-doped silk fibroin for future application in luminescent compounds. *J. Lumin.* **205**, 423–428 (2019).
171. Minoura, N., Tsukada, M. & Nagura, M. Physico-chemical properties of silk fibroin membrane as a biomaterial. *Biomaterials* **11**, 430–434 (1990).
172. Lawrence, B. D., Cronin-Golomb, M., Georgakoudi, I., Kaplan, D. L. & Omenetto, F. G. Bioactive silk protein biomaterial systems for optical devices. *Biomacromolecules* **9**, 1214–1220 (2008).
173. Sacco, B. L. & De Santana, H. Impact of temperature on the stability of silkworm cocoon fibers. *Quim. Nova* **42**, 1014–1019 (2019).
174. Jin, H. J. *et al.* Water-stable silk films with reduced β-sheet content. *Adv. Funct. Mater.* **15**, 1241–1247 (2005).
175. Hu, X. *et al.* Regulation of silk material structure by temperature-controlled water vapor annealing. *Biomacromolecules* **12**, 1686–1696 (2011).
176. Koh, L.-D. *et al.* Structures, mechanical properties and applications of silk fibroin materials. *Prog. Polym. Sci.* **46**, 86–110 (2015).
177. De Moraes, M. A. & Beppu, M. M. Biocomposite membranes of sodium alginate and silk fibroin fibers for biomedical applications. *J. Appl. Polym. Sci.* **130**, 3451–3457 (2013).
178. França, C. G. *et al.* Synthesis and Properties of Silk Fibroin/Konjac Glucomannan Blend Beads. *Polymers (Basel).* **10**, (2018).
179. Ghaeli, I. *et al.* Phase Behaviour and Miscibility Studies of Collagen/Silk Fibroin Macromolecular System in Dilute Solutions and Solid State. *Molecules* **22**, (2017).
180. de Moraes, M. A., Silva, M. F., Weska, R. F. & Beppu, M. M. Silk fibroin and sodium

alginate blend: miscibility and physical characteristics. *Mater. Sci. Eng. C. Mater. Biol. Appl.* **40**, 85–91 (2014).

181. Weska, R. F., Vieira, W. C., Nogueira, G. M. & Beppu, M. M. Effect of freezing methods on the properties of lyophilized porous silk fibroin membranes. *Mater. Res.* **12**, 233–237 (2009).
182. Ramirez, S. M. V., De Moraes, M. A. & Beppu, M. M. Assessing the influence of silkworm cocoon's age on the physicochemical properties of silk fibroin-based materials. *J. Mater. Res.* **34**, 1944–1949 (2019).
183. Nogueira, G. M., Swiston, A. J., Beppu, M. M. & Rubner, M. F. Layer-by-layer deposited chitosan/silk fibroin thin films with anisotropic nanofiber alignment. *Langmuir* **26**, 8953–8958 (2010).
184. Moraes, M. L., Lima, L. R., Silva, R. R., Cavicchioli, M. & Ribeiro, S. J. L. Immunosensor based on immobilization of antigenic peptide NS5A-1 from HCV and silk fibroin in nanostructured films. *Langmuir* **29**, 3829–3834 (2013).
185. Perry, H., Gopinath, A., Kaplan, D. L., Negro, L. D. & Omenetto, F. G. Nano- and micropatterning of optically transparent, mechanically robust, biocompatible silk fibroin films. *Adv. Mater.* **20**, 3070–3072 (2008).
186. Lovett, M. *et al.* Silk fibroin microtubes for blood vessel engineering. *Biomaterials* **28**, 5271–5279 (2007).
187. Lovett, M. L., Cannizzaro, C. M., Vunjak-Novakovic, G. & Kaplan, D. L. Gel spinning of silk tubes for tissue engineering. *Biomaterials* **29**, 4650–4657 (2008).
188. Wenk, E., Wandrey, A. J., Merkle, H. P. & Meinel, L. Silk fibroin spheres as a platform for controlled drug delivery. *J. Control. Release* **132**, 26–34 (2008).
189. Wang, X. *et al.* Silk microspheres for encapsulation and controlled release. *J. Control. Release* **117**, 360–370 (2007).
190. Wang, X., Yucel, T., Lu, Q., Hu, X. & Kaplan, D. L. Silk nanospheres and microspheres from silk/pva blend films for drug delivery. *Biomaterials* **31**, 1025–1035 (2010).
191. Kim, S. H., Nam, Y. S., Lee, T. S. & Park, W. H. Silk fibroin nanofiber. Electrospinning, properties, and structure. *Polym. J.* **35**, 185–190 (2003).
192. Nazarov, R., Jin, H.-J. & Kaplan, D. L. Porous 3-D scaffolds from regenerated silk fibroin. *Biomacromolecules* **5**, 718–726 (2004).
193. Yucel, T., Kojic, N., Leisk, G. G., Lo, T. J. & Kaplan, D. L. Non-equilibrium silk

fibroin adhesives. *J. Struct. Biol.* **170**, 406–412 (2010).

194. Wang, X., Kluge, J. A., Leisk, G. G. & Kaplan, D. L. Sonication-induced gelation of silk fibroin for cell encapsulation. *Biomaterials* **29**, 1054–1064 (2008).

195. Leisk, G. G., Lo, T. J., Yucel, T., Lu, Q. & Kaplan, D. L. Electrogelation for protein adhesives. *Adv. Mater.* **22**, 711–715 (2010).

196. Nogueira, G. M., De Moraes, M. A., Rodas, A. C. D., Higa, O. Z. & Beppu, M. M. Hydrogels from silk fibroin metastable solution: Formation and characterization from a biomaterial perspective. *Mater. Sci. Eng. C* **31**, 997–1001 (2011).

197. Kasoju, N. & Bora, U. Silk fibroin in tissue engineering. *Adv. Healthc. Mater.* **1**, 393–412 (2012).

198. Rojas, J. E. U. *et al.* Silk fibroin hydrogels for potential applications in photodynamic therapy. *Biopolymers* (2018).

199. Zhang, Y.-Q. Natural silk fibroin as a support for enzyme immobilization. *Biotechnol. Adv.* **16**, 961–971 (1998).

200. Da Silva, R. R. *et al.* Fabrication of Biocompatible, Functional, and Transparent Hybrid Films Based on Silk Fibroin and Epoxy Silane for Biophotonics. *ACS Appl. Mater. Interfaces* **9**, 27905–27917 (2017).

201. Pasternak, G. *et al.* Regenerated silk fibroin membranes as separators for transparent microbial fuel cells. *Bioelectrochemistry* **126**, 146–155 (2019).

202. Park, W. H. *et al.* Relationships between antithrombogenicity and surface free energy of regenerated silk fibroin films. *Fibers Polym.* **2**, 58–63 (2001).

203. Toffanin, S. *et al.* Low-threshold blue lasing from silk fibroin thin films. *Appl. Phys. Lett.* **101**, (2012).

204. Applegate, M. B., Perotto, G., Kaplan, D. L. & Omenetto, F. G. Biocompatible silk step-index optical waveguides. *Biomed. Opt. Express* **6**, 4221 (2015).

205. da Rocha, E. G., Pugina, R. S. & Caiut, J. M. A. Luminescent sensor based on the lanthanide-fibroin composite. *Opt. Mater. (Amst).* **109**, 110236 (2020).

206. web site. https://www.linkam.co.uk/thms600.

207. López, R., Aguilar, E. A., Zárate-Medina, J., Muñoz-Saldaña, J. & Lozano-Mandujano, D. Nanoindentation of melt-extracted amorphous YAG and YAG:Eu, Nd micrometric fibers synthesized by the citrate precursor method. *J. Eur. Ceram. Soc.* **30**, 73–79 (2010).

208. Ju, M. *et al.* Structural Evolutions and Crystal Field Characterizations of Tm-Doped

YAlO3: New Theoretical Insights. *ACS Appl. Mater. Interfaces* **8**, 30422–30429 (2016).

209. Kostić, S. *et al.* Study of structural and optical properties of YAG and Nd:YAG single crystals. *Mater. Res. Bull.* **63**, 80–87 (2015).
210. Kanchanavaleerat, E. *et al.* Crystal growth of high doped Nd:YAG. *Opt. Mater. (Amst).* **26**, 337–341 (2004).
211. Kostić, S. *et al.* Spectroscopic characterization of YAG and Nd:YAG single crystals. *Phys. Scr.* **162**, (2014).
212. Li, J. *et al.* Synthesis of nanosized Nd:YAG powders via gel combustion. *Ceram. Int.* **33**, 1047–1052 (2007).
213. Lamber, R., Wetjen, S. & Jaeger, N. I. Size dependence of the lattice parameter of small palladium particles. *Phys. Rev. B* **51**, 10968–10971 (1995).
214. Lukowiak, A., Wiglusz, R. J., MacZka, M., Gluchowski, P. & Strek, W. IR and Raman spectroscopy study of YAG nanoceramics. *Chem. Phys. Lett.* **494**, 279–283 (2010).
215. Kumar, G. A. *et al.* Spectroscopic and stimulated emission characteristics of Nd3+ in transparent Y2O3 ceramics. *IEEE J. Quantum Electron.* **42**, 643–650 (2006).
216. Ryba-Romanowski, W., Lisiecki, R., Rzepka, A., Lipińska, L. & Pajaczkowska, A. Luminescence and excitation energy transfer in rare earth-doped Y4Al2O9 nanocrystals. *Opt. Mater. (Amst).* **31**, 1155–1162 (2009).
217. Lu, J. *et al.* Potential of ceramic YAG lasers. *Laser Phys.* **11**, 1053–1057 (2001).
218. Lu, J. *et al.* Optical properties and highly efficient laser oscillation of Nd:YAG ceramics. *Appl. Phys. B* **71**, 469–473 (2000).
219. Vrubel, I. I. *et al.* Bandgap Engineering in Yttrium-Aluminum Garnet with Ga Doping. *Cryst. Growth Des.* **17**, 1863–1869 (2017).
220. Kamenskikh, I. *et al.* Temperature dependence of the charge transfer and f-f luminescence of Yb3+ in garnets and YAP. *J. Phys. Condens. Matter* **17**, 5587–5594 (2005).
221. Chen, X. *et al.* Fabrication and spectroscopic properties of Yb/Er:YAG and Yb, Er:YAG transparent ceramics by co-precipitation synthesis route. *J. Lumin.* **188**, 533–540 (2017).
222. Zhou, J. *et al.* Optical properties of Er,Yb co-doped YAG transparent ceramics. *Ceram. Int.* **37**, 513–519 (2011).
223. Yan, S. A., Wang, J. W., Chang, Y. S., Hwang, W. S. & Chang, Y. H. Synthesis and

luminescence properties of Ln3+ (Ln3+ = Er3+, Sm3+)-doped barium lanthanum tungstate BaLa 2WO7 phosphors. *Opt. Mater. (Amst).* **34**, 147–151 (2011).

224. Martín-Rodríguez, R., Rabouw, F. T., Trevisani, M., Bettinelli, M. & Meijerink, A. Upconversion Dynamics in Er3+-Doped Gd2O2S: Influence of Excitation Power, Er3+ Concentration, and Defects. *Adv. Opt. Mater.* **3**, 558–567 (2015).

225. Pollnau, M., Gamelin, D., Lüthi, S., Güdel, H. & Hehlen, M. Power dependence of upconversion luminescence in lanthanide and transition-metal-ion systems. *Phys. Rev. B - Condens. Matter Mater. Phys.* **61**, 3337–3346 (2000).

226. Li, Y., Chen, B., Zhao, X., Wang, Z. & Lin, H. Upconversion emissions in YAG glass ceramics doped with Tm 3+/Yb 3+ ions. *J. Alloys Compd.* **536**, 198–203 (2012).

227. Thomas, J. T. *et al.* Optical spectroscopy of Tm3+ : YAG transparent ceramics. *J. Phys. D. Appl. Phys.* **46**, (2013).

228. Zhang, M. *et al.* Study on upconversion and thermal properties of Tm3+/Yb3+ co-doped La2O3-Nb2O5-Ta2O5 glasses. *Materials (Basel).* **11**, 1–8 (2018).

229. Carreño, S. J. M. *et al.* Interplay between random laser performance and self-frequency conversions in NdxY1.00−xAl3(BO3)4 nanocrystals powders. *Opt. Mater. (Amst).* **54**, 262–268 (2016).

230. Hilário, E. G. *et al.* Structural and morphological characterization of Y1-xNdxAl3(BO3)4 micron-sized crystals powders obtained by the urea precipitation method and its random laser properties. *J. Lumin.* **243**, (2022).

231. Gonçalves, I. M. *et al.* Phonon-assisted NIR-to-visible upconversion in single β -NaYF 4 microcrystals codoped with Er 3 + and Yb 3 + for microthermometry applications : Experiment and theory. *J. Lumin.* **231**, 117801 (2021).

232. Tian, Y. *et al.* Effect of Yb3+ concentration on upconversion luminescence and temperature sensing behavior in Yb3+/Er3+ co-doped YNbO4 nanoparticles prepared via molten salt route. *Chem. Eng. J.* **297**, 26–34 (2016).

233. Vetrone, F., Boyer, J. C., Capobianco, J. A., Speghini, A. & Bettinelli, M. Significance of Yb3+ concentration on the upconversion mechanisms in codoped Y2O3:Er3+, Yb 3+ nanocrystals. *J. Appl. Phys.* **96**, 661–667 (2004).

234. Dey, R. & Rai, V. K. Yb3+ sensitized Er3+ doped La2O 3 phosphor in temperature sensors and display devices. *Dalt. Trans.* **43**, 111–118 (2014).

235. Manzani, D., Petruci, J. F. D. S., Nigoghossian, K., Cardoso, A. A. & Ribeiro, S. J. L. A portable luminescent thermometer based on green up-conversion emission of

Er3+/Yb3+ co-doped tellurite glass. *Sci. Rep.* **7**, 1–11 (2017).

236. Liu, Y. *et al.* Upconversion fluorescence property of Er3+/Yb3+ codoped lanthanum titanate microcrystals for optical thermometry. *J. Alloys Compd.* **822**, 153449 (2020).

237. Li, C., Dong, B., Li, S. & Song, C. Er3+-Yb3+ co-doped silicate glass for optical temperature sensor. *Chem. Phys. Lett.* **443**, 426–429 (2007).

238. Lei, R. *et al.* Optical thermometry based on anomalous temperature-dependent 1.53 µm infrared luminescence of Er3+ in BaMoO4: Er3+/Yb3+ phosphor. *Opt. Mater. (Amst).* **86**, 278–285 (2018).

239. Gavrilović, T. V., Jovanović, D. J., Lojpur, V. & Dramićanin, M. D. Multifunctional Eu3+- and Er3+/Yb3+-doped GdVO4 nanoparticles synthesized by reverse micelle method. *Sci. Rep.* **4**, 1–9 (2014).

240. Chen, J. *et al.* Up-conversion luminescence properties and temperature sensing performances of Ba5Y8Zn4O21:Yb3+, Er3+ phosphors. *J. Alloys Compd.* **875**, 159922 (2021).

Appendix

Curriculum Vitae

Roberta Silva Pugina

Born on 2th October 1990 at Monte Azul Paulista, São Paulo, Brazil

Academic Formation

2010-2015: Graduation in Chemistry at University of São Paulo (FFCLRP-USP), Ribeirão Preto, São Paulo, Brazil.

2012-2013: Exchange student at University of Évora (UE), Évora, Portugal.

2016-2018: Master degree in Science at University of São Paulo (FFCLRP-USP), Ribeirão Preto, São Paulo, Brazil.

2018-current: PhD student in Science at University of São Paulo (FFCLRP-USP), Ribeirão Preto, São Paulo, Brazil.

Teaching experience

Graduate monitor at University of São Paulo (FFCLRP-USP), Chemistry Department-

2016: General Chemistry

2017: Experimental Inorganic Chemistry I

2018: Inorganic Chemistry I

2021: Inorganic Chemistry II

Award

2018: One of the top 10 posters presented at the 8th International Conference on Optical, Optoelectronic and Photonic Materials and Applications (ICOOPMA).

Jury Member

2019: 27th SIICUSP at University of São Paulo.

2019: Vitor dos Santos de Souza’ graduation work entitled “Materiais a base de óxido de germânio e óxido de nióbio tridopados com íons terras raras: da emissão do infravermelho a luz branca” at University of São Paulo. Supervision: Prof. Rogéria Rocha Gonçalves.

Languages

Portuguese (native language)

English

Publications

[1] PUGINA, ROBERTA S.; DA ROCHA, EUZANE G.; RIBEIRO, SIDNEY J.L.; CAIUT, JOSÉ MAURÍCIO A. Study of the Energy Transfer Process in Rare Earth-Doped Silk Fibroin for Future Application in Luminescent Compounds. JOURNAL OF LUMINESCENCE, v. 205, p. 423, 2019.

[2] PUGINA, ROBERTA S.; DA ROCHA, EUZANE G.; CAIUT, JOSÉ MAURÍCIO A. Beta-diketones in the Intensification of the Luminescence of the Silk Fibroin Films Doped Rare Earth Ions. JOURNAL OF MATERIALS SCIENCE-MATERIALS IN ELECTRONICS, v. 30, p. 16732-16739, 2019.

[3] DA ROCHA, EUZANE G.; PUGINA, ROBERTA S.; CAIUT, JOSÉ MAURÍCIO A. Luminescent Sensor Based on the Lanthanide-Fibroin Composite. OPTICAL MATERIALS, v. 109, p. 110236, 2020.

[4] RIUL, ANDRÉ; DA FONSECA, FERNANDO A.A.; PUGINA, ROBERTA S.; CAIUT, JOSÉ MAURÍCIO A. Tuned Structure of Europium-doped Al_2O_3-Ytrium luminescent composites and their spectroscopic behavior. JOURNAL OF LUMINESCENCE, v. 233, p. 117925, 2021.

[5] PUGINA, ROBERTA S.; CAIUT, JOSÉ MAURÍCIO A. Silk: History, Obtaining, Structure and Properties of an old Material in the Development of New Technologies. INTERNATIONAL JOURNAL OF ADVANCES IN MEDICAL BIOTECHNOLOGY, v. 4, p. 27-45, 2021.

[6] PUGINA, ROBERTA S.; HILÁRIO, ELOÍSA G.; DA ROCHA, EUZANE G.; DA SILVA-NETO, MANOEL L.; DAS, AVISHEK; CAIUT, JOSÉ MAURÍCIO A.; GOMES, ANDERSON S.L. Nd^{3+}:YAG Microspheres Powders Prepared by Spray Pyrolysis: Synthesis, Characterization and Random Laser Application. MATERIALS CHEMISTRY AND PHYSICS, v. 269, p. 124764, 2021.

[7] HILÁRIO, ELOÍSA G.; PUGINA, ROBERTA S.; DA SILVA-NETO, MANOEL L.; MAIA, LAURO J. Q.; CAIUT, JOSÉ MAURÍCIO A.; GOMES, ANDERSON S.L. Structural and Morphological Characterization of $Y_{1-x}Nd_xAl_3(BO_3)_4$ Micron-sized Crystals Powders Obtained

by the Urea Precipitation Method and its Random Laser Properties. JOURNAL OF LUMINESCENCE, v. 243, p. 118624, 2022.

[8] SILVA, DOUGLAS L.; PUGINA, ROBERTA S.; CAIUT, JOSÉ MAURÍCIO A. Green, Red, and Near-infrared Up-conversion Emission of $NaY(MoO_4)_2:Er^{3+}$ Submicrometric Particles Obtained by One-step Synthesis, and its Thermometric Application. JOURNAL OF LUMINESCENCE, v. 243, p. 118639, 2022.

[9] PUGINA, ROBERTA S.; SILVA, DOUGLAS L.; RIUL, ANDRÉ; DA SILVA-NETO, MANOEL L.; GOMES, ANDERSON S.L.; CAIUT, JOSÉ MAURÍCIO A. Silk Fibroin-Yb^{3+}/Er^{3+}:YAG Composite Films and Their Thermometric Applications based on Up-conversion Luminescence. POLYMER, v. 241, p. 124541, 2022.

[10] CORONEL, EDWIN D.; DA SILVA-NETO, MANOEL L.; MOURA, ANDRÉ L.; GONZÁLEZ, IVÁN R. R.; PUGINA, ROBERTA S.; HILÁRIO, ELOÍSA G.; DA ROCHA, EUZANE G.; CAIUT, JOSÉ MAURÍCIO A.; GOMES, ANDERSON S. L.; RAPOSO, ERNESTO P. Simultaneous Evaluation of Intermittency Efects, Replica Symmetry Breaking and Modes Dynamics Correlations in a Nd:YAG Random Laser. SCIENTIFC REPORTS, v. 12, p. 1050, 2022.

[11] PUGINA, ROBERTA S.; CAIUT, JOSÉ MAURÍCIO A. Blue Emission From Silk Fibroin-Yb^{3+}/Tm^{3+}:YAG Films by Up-conversion. MATERIALS LETTERS, v. 314, p. 131866, 2022.

REVIEW ARTICLE

I|J|A|M|B

INTERNATIONAL JOURNAL OF ADVANCES IN MEDICAL BIOTECHNOLOGY

Silk: history, obtaining, structure and properties of an old material in the development of new technologies

Roberta S. Pugina[1]; **José Maurício A. Caiut**[2];

*Corresponding author: E-mail address: caiut@ffclrp.usp.br

Abstract: For thousands of years, the silk produced in the Bombyx mori glands and used in the preparation of cocoons has been employed in the textile industry to produce fabric. These cocoons consist mainly of fibroin (SF – silk fibroin), a fibrous protein with unique mechanical properties and which is biocompatible, biodegradable, and inexpensive. SF can be extracted from the cocoons by processing in aqueous medium, and it can be employed to obtain materials for different applications, including biomaterials for body implants, scaffolds for tissue engineering, and materials for photonic devices such as sensors, waveguides, and lasers.

Keywords: Silk.Fibroin. Applications.

Introduction

Silk is a natural and semicrystalline polymer with high malleability, unique mechanical properties, and superior tenacity as compared to any currently employed synthetic fiber.[1,2] For thousands of years, since silk was discovered in China in the middle of 2600 BC, the textile industry has explored this material in its natural form.[3] Silk is produced in specific glands called sericigenic glands. Some invertebrates spin it into the fiber form during metamorphosis, but silk composition will depend on source.[4,5] The silk from silkworm (Bombyx mori) is the most produced and commercialized. It consists chiefly of fibroin and sericin proteins, and Bombyx mori uses it to manufacture the cocoons, to which fibroin and sericin acids provide resistance and protection, respectively.[2,6] Sericulture refers to the cultivation of silkworm. This culture was spread in Brazil in the beginning of the last century. It occurs mainly in the state of Paraná, in the so-called Vale da Seda paranaense, where silk threads are produced and exported to several countries.[7-9] However, in the 1940s, fibroin, a fibrous protein and a major component of the silk thread, started to arouse scientific interest. Structurally, this protein consists of two chains, one ~25-kDa chain and one ~325-kDa chain.[6] The largest chain comprises distinct regions known as silk I and silk II, which present different degrees of crystallinity.[10] Fibroin can be extracted from silk threads by degumming, a low-cost process that requires water.[2] The solution obtained after this process can be used to develop numerous materials such as films, fibers, and spheres, among others. Additionally, the solution can be submitted to several treatments, to give a series of products;[2] e.g., silk sutures,[6,11] which have been employed for decades. Moreover, the solution can be used to obtain biomaterials, including implants and scaffolds for tissue engineering[12,13] as well as photonic devices like sensors, waveguides, and lasers.[14] Silk-based materials have the advantage of being biocompatible,[2,12,13] biodegradable,[15] resorbable,[16] and mechanically robust[1], among other characteristics, which allows them to be widely applied and opens various possibilities for their use in countless areas. In addition, the cocoons can be obtained as waste from the textile industry, which reduces the cost of producing new materials.

History

The story that describes the discovery of silk by humanity is full of legends and divergences.[3] According to the account of the Chinese thinker and philosopher Confucius (571–479 BC), the most accepted to date, in 2640 BC silk was accidentally discovered by the Chinese Empress Hsi-Ling-Shi, wife of Emperor Huang Di (or Huang-Ti), also known as the “Yellow Emperor”, who is thought to have ruled China from 2697 to 2597 BC, before the Xia dynasty. Legend has it that silk was discovered while the Empress was drinking a cup of tea under a mulberry tree—a cocoon fell into her cup and, upon contact with the hot water, it broke apart, revealing the fiber produced by silkworm.[3,17-19] Moved by curiosity, Hsi-Ling-Shi would have managed to transform that material into a piece of fabric and slowly started the weaving process, which is practically the same as the one used today. Although the textile industry was established at that time, it only peaked around 1500 BC, during the Shang dynasty. In the two following millennia, the Chinese were the exclusive

---

[1] Departamento de Química, Faculdade de Filosofia, Ciências e Letras de Ribeirão Preto, Universidade de São Paulo,Ribeirão Preto – SP, Brazil

Received 10 january 2021; Accepted 02 Februaryt 2021; Available online 1 March 2021.

DOI: https://doi.org/ 10.52466/ijamb.v4i1.88

Materials Chemistry and Physics 269 (2021) 124764

Contents lists available at ScienceDirect

Materials Chemistry and Physics

journal homepage: www.elsevier.com/locate/matchemphys

Nd^{3+}:YAG microspheres powders prepared by spray pyrolysis: Synthesis, characterization and random laser application

Roberta Silva Pugina [a], Eloísa Garibalde Hilário [a], Euzane Gomes da Rocha [a], Manoel L. da Silva-Neto [b], Avishek Das [c], José Maurício Almeida Caiut [a],*, Anderson S.L. Gomes [c]

[a] Departamento de Química, Faculdade de Filosofia, Ciências e Letras de Ribeirão Preto, Universidade de São Paulo, 14040-901, Ribeirão Preto, São Paulo, Brazil
[b] Graduate Program in Materials Science, Universidade Federal de Pernambuco, 50670-901, Recife, PE, Brazil
[c] Departamento de Física, Universidade Federal de Pernambuco, Av. Prof. Moraes Rego, 1235, Cidade Universitária, Recife, PE, 50670 -901, Brazil

HIGHLIGHTS

- Nd^{3+}:YAG particles without spurious phases have been prepared by spray pyrolysis.
- The YAG spheres obtained herein enable it to be used as Random Laser source.
- The particles act as gain and scatter medium, leading to multidirectional laser emission.

GRAPHICAL ABSTRACT

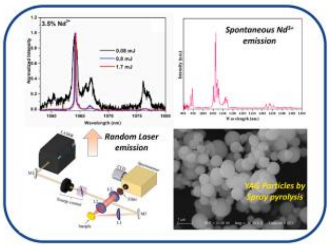

ARTICLE INFO

Keywords:
Spray pyrolysis
Rare earth materials
$Y_3Al_5O_{12}$
Lanthanides
Random lasers

ABSTRACT

Nd^{3+}:YAG crystals have been used to develop photonic devices since the 1960s. Its unique properties, which stem from the combination of the YAG structure with lanthanide ions, have made it the most widely employed material in commercial solid-state lasers. This work reports the synthesis of dense Nd^{3+}:YAG particles prepared by spray pyrolysis. During the synthesis, no clusters emerged, and the particles did not coalesce even after thermal treatment at 1100 °C. All characterization confirmed that the YAG phase was obtained as a spherical micro- and sub-micrometric material. In addition, the photoluminescence spectra showed the expected spectroscopic profile of Nd^{3+} replacing Y^{3+} at the dodecahedral sites. The presence of high Nd^{3+} concentration was exploited as a simultaneous gain and scatter medium for random laser application. The spray pyrolysis methodology described could be easily scaled up for a pilot setup or industrial production. Further applications as sensors or superluminescent sources can be envisaged.

1. Introduction

Since the 1960s, luminescent rare earth doped materials based on the binary aluminum and yttrium oxide system (Al_2O_3–Y_2O_3) have been one of the most important materials for the development of opto-electronic devices [1], as luminescent temperature sensor based on $Y_3Al_5O_{12}$ doped V^{3+}/V^{4+} and Ln^{3+} [2], Ce^{3+}-doped $Y_3Al_5O_{12}$ as nanophosphors in LED lighting technology [3], warm-light and cyan emitting garnet

---

* Corresponding author.
E-mail address: caiut@ffclrp.usp.br (J.M.A. Caiut).

https://doi.org/10.1016/j.matchemphys.2021.124764
Received 1 April 2021; Received in revised form 17 May 2021; Accepted 20 May 2021
Available online 25 May 2021

Polymer 241 (2022) 124541

Contents lists available at ScienceDirect

Polymer

journal homepage: www.elsevier.com/locate/polymer

Silk fibroin-Yb^{3+}/Er^{3+}:YAG composite films and their thermometric applications based on up-conversion luminescence

Roberta S. Pugina [a], Douglas L. da Silva [a], André Riul [a], Manoel L. da Silva-Neto [b], Anderson S. L. Gomes [b], José Maurício A. Caiut [a,*]

[a] Departamento de Química, Faculdade de Filosofia, Ciências e Letras de Ribeirão Preto, Universidade de São Paulo, 14040-901, Ribeirão Preto, São Paulo, Brazil
[b] Departamento de Física, Universidade Federal de Pernambuco, Av. Prof. Moraes Rego, 1235, Cidade Universitária, Recife, PE, 50670 -901, Brazil

ARTICLE INFO

Keywords:
Spray pyrolysis
Rare earth materials
Luminescent thermometer

ABSTRACT

Silk Fibroin (SF) is a well-known protein, and has been employed in the development of diverse advanced materials for applications on medical and biological field, drug delivery systems and, also, in the electronic and photonic area. In addition, the up-conversion emission process could be proposed in fibroin-based materials and becomes a challenge for the photonic field based on biocompatible devices obtained from fibroin. To avoid the unwanted upconversion (UC) quenching process, herein, lanthanide ions were used as sensitizer and emitters ions, and them was incorporated into an inorganic particle obtained from spray pyrolysis synthesis. Specifically, we have obtained Yb^{3+} and Er^{3+} ions doped YAG (Yttrium Aluminum Garnet, $Y_3Al_5O_{12}$) spherical submicrometric particles, without spurious phases. All samples were characterized by X-Ray Diffraction, Scanning Electron Microscopy, and photoluminescence. The spectroscopic studies showed an intense UC emission from Er^{3+} ions. Furthermore, looking for the development of a new fibroin composite which should be used as sensor or smart ink, we inserted the YAG particles in SF, and a new flexible composite film with controlled amounts of particles and tuned transmittance behavior was obtained. Finally, it was confirmed the characteristic luminescent behavior (as UC emission) of the particles in the composite films. As the emitters levels ($^2H_{11/2}$ and $^4S_{3/2}$) from Er^{3+} ions are thermally coupled, all materials (particles and films) were exploited as luminescent thermometer, and data confirmed the thermal sensibility comparable to other systems based on Yb^{3+}/Er^{3+} ions.

1. Introduction

Bombyx mori silkworms produce silk, a fibrous material that they use to fabricate their cocoons. This ancient and unique material is historically known for its luster and strength; for millennia, it has been employed to prepare fabrics [1,2]. The major component in silk is the fibrous protein known as Silk Fibroin (SF), a natural, resistant, and biocompatible polymer that has been studied for several applications over the last 70 years [1,3,4]. SF can be used in the development of diverse systems with applications in various areas, including tissue engineering [5], bone regeneration [6], drug delivery [7], and electronic and photonic devices [4,8].

Fluorescent proteins have been employed for many decades. In this context, SF has gained attention because the fluorescence gene can be inserted in silk cocoons, giving rise to possible biotechnological and medical applications [9]. To obtain this fluorescent SF system, organic dyes or even quantum dots are commonly used [10,11]. Another strategy would be taking advantage of the widely known and applied luminescent properties of lanthanide elements, which have not been completely explored in the SF matrix [12,13]. Combining the properties of lanthanide elements with the structure of SF and its ability to incorporate ions and molecules can result in interesting systems for the development of new photonic devices, such as biosensors [14,15] and lasers [16,17]. Energy conversion (UC) is an attractive property of lanthanide ions and can be studied in fibroin-based materials [18–20]. During UC, a higher-energy photon is emitted by conversion of two or more lower-energy photons. The emission mechanism involves sequential photon excitation, which can occur through two fundamental mechanisms: ESA (Excited-State Absorption) and ETU (Energy Transfer Up-conversion). ETU is the most efficient mechanism and is usually observed in systems co-doped with the Yb^{3+}/Er^{3+} pair, where Yb^{3+} ions sensitize Er^{3+} ions, the activators. This is possible because Yb^{3+} ions have larger absorption cross-section, so they are more effectively excited with 980-nm radiation ($^2F_{7/2} \rightarrow {}^2F_{5/2}$), subsequently transferring energy

---

* Corresponding author.
E-mail address: caiut@ffclrp.usp.br (J.M.A. Caiut).

https://doi.org/10.1016/j.polymer.2022.124541
Received 10 October 2021; Received in revised form 7 January 2022; Accepted 10 January 2022

Materials Letters 314 (2022) 131866

Contents lists available at ScienceDirect

Materials Letters

journal homepage: www.elsevier.com/locate/matlet

Blue emission from silk fibroin-Yb^{3+}/Tm^{3+}:YAG films by up-conversion

Roberta S. Pugina, José Maurício A. Caiut [*]

Departamento de Química, Faculdade de Filosofia, Ciências e Letras de Ribeirão Preto, Universidade de São Paulo, 14040-901 Ribeirão Preto, São Paulo, Brazil

ARTICLE INFO

Keywords:
Lanthanide ions
Spray pyrolysis
Anti-counterfeiting
$Y_3Al_5O_{12}$

ABSTRACT

Developing systems that can stop counterfeiting is crucial. In this sense, luminescent markers are a good strategy because the label is only visible under special conditions. In this scenario, the up-conversion emission mechanism is an example of cutting-edge knowledge, especially the blue emission, which requires at least three photons to occur. Here, we have prepared a new material based on silk fibroin and inorganic particles doped with Yb^{3+}/Tm^{3+} ions and investigated the blue up-conversion process in it. This association of particles and silk fibroin allowed us to explore the exceptional properties of this protein allied with the multifunctionality of lanthanides: the resulting biodegradable, self-supported film emits in the blue region and can be applied as an anti-counterfeiting device, surface coating, or even an ink for 3D printers.

1. Introduction

Up-conversion (UC) materials are a fascinating luminescent technology for several applications. In particular, lanthanide (Ln^{3+})-doped materials, which exhibit luminescence by UC from the near-infrared (NIR) to the visible region, have attracted attention for promising applications [1,2]. Under excitation at 980 nm and sensitization by Yb^{3+}, Tm^{3+} undergoes a UC process, to present efficient emission in the visible and NIR range. In this nonlinear process, Tm^{3+} electrons in the ground state ($^3H_6$) can be excited to the highest energy levels by the *Energy Transfer Up-conversion* (ETU) mechanism [3]. This mechanism causes Tm^{3+}-doped materials to emit around 477 ($^1D_2 \rightarrow {}^3H_5$), 650 ($^1G_4 \rightarrow {}^3F_4$), and 800 nm ($^3H_4 \rightarrow {}^3H_6$). The blue color emitted by Tm^{3+}-doped materials excited at 980 nm involves three photons and can be useful in an anti-counterfeiting device [4,5]. The nature of Tm^{3+}-doped material can affect the blue UC emission efficiency, whereas energy migration through Yb^{3+} to lattice defects or phonon de-excitation from high Tm^{3+} excited levels can lead to quenching. For instance, the biomaterial can be combined with inorganic particles that prevent de-excitation and allow the development of devices displaying the most important characteristics of each of their components. In this context, Silk Fibroin (SF), a protein extracted from silkworm cocoons, is a great candidate: it is biocompatible, biodegradable, mechanically robust, and moldable, and ions, molecules, or particles can be incorporated into its structure [6]. In fact, red UC emission from Er^{3+} incorporated into SF has already been observed [7,8], but the amino acids of the SF structure may quench the three-photon-dependent UC process. To circumvent this problem, we propose inserting lanthanide ions in an inorganic crystalline matrix, obtained by Spray Pyrolysis (SP), to protect them from the quenching phonon effect. To this end, we have prepared YAG (*Yttrium Aluminum Garnet*) spherical particles doped with different Yb^{3+}/Tm^{3+} concentrations and used cocoons, a waste from the textile industry, to obtain a blue UC SF material that can be considered as proof of concept that a biodegradable self-supported system can be employed as a blue-emitting marker for application in anti-counterfeit technology. We structurally and spectroscopically analyzed the YAG particles and inserted them into the SF matrix, to obtain self-supported films. Spectroscopic analyses of the films confirmed blue emission from Tm^{3+} by a UC process.

2. Experimental procedure

2.1. Yb^{3+}/Tm^{3+}:YAG powders

The Yb^{3+}/Tm^{3+}:YAG particles were prepared by SP, as described for the YAG matrix ($Y_3Al_5O_{12}$) doped with other lanthanide ions [9,10]. More specifically, YAG particles doped with two Yb^{3+} concentrations were prepared. In both cases, the Tm^{3+} concentration was kept at 0.5% (mol/mol in relation to Y^{3+}), whereas the Yb^{3+} concentration was 10 or 15% (mol/mol in relation to Y^{3+}). The resulting powders were labeled Yb^{3+}/Tm^{3+}:YAG (10%/0.5%) and Yb^{3+}/Tm^{3+}:YAG (15%/0.5%), respectively.

---

[*] Corresponding author.
E-mail address: caiut@ffclrp.usp.br (J.M.A. Caiut).

https://doi.org/10.1016/j.matlet.2022.131866
Received 10 November 2021; Received in revised form 15 January 2022; Accepted 1 February 2022
Available online 5 February 2022


03/01/2022 13:05 Rightslink® by Copyright Clearance Center

Nd3+:YAG microspheres powders prepared by spray pyrolysis: Synthesis, characterization and random laser application

Author:
Roberta Silva Pugina,Eloísa Garibalde Hilário,Euzane Gomes da Rocha,Manoel L. da Silva-Neto,Avishek Das,José Maurício Almeida Caiut,Anderson S.L. Gomes

Publication: Materials Chemistry and Physics

Publisher: Elsevier

Date: 1 September 2021

© 2021 Elsevier B.V. All rights reserved.

Journal Author Rights

Please note that, as the author of this Elsevier article, you retain the right to include it in a thesis or dissertation, provided it is not published commercially. Permission is not required, but please ensure that you reference the journal as the original source. For more information on this and on your other retained rights, please visit: https://www.elsevier.com/about/our-business/policies/copyright#Author-rights

© 2022 Copyright - All Rights Reserved | Copyright Clearance Center, Inc. | Privacy statement | Terms and Conditions
Comments? We would like to hear from you. E-mail us at customercare@copyright.com

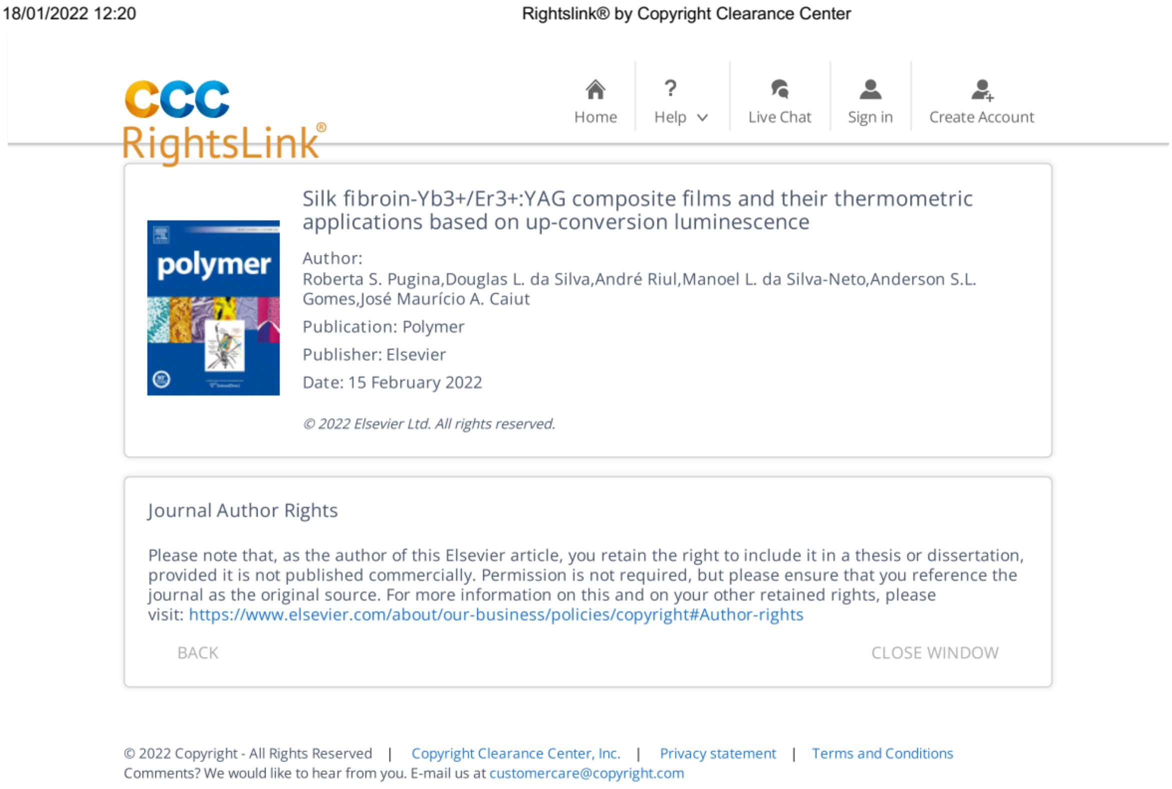
18/01/2022 12:20 Rightslink® by Copyright Clearance Center

Silk fibroin-Yb3+/Er3+:YAG composite films and their thermometric applications based on up-conversion luminescence

Author:
Roberta S. Pugina,Douglas L. da Silva,André Riul,Manoel L. da Silva-Neto,Anderson S.L. Gomes,José Maurício A. Caiut

Publication: Polymer

Publisher: Elsevier

Date: 15 February 2022

© 2022 Elsevier Ltd. All rights reserved.

Journal Author Rights

Please note that, as the author of this Elsevier article, you retain the right to include it in a thesis or dissertation, provided it is not published commercially. Permission is not required, but please ensure that you reference the journal as the original source. For more information on this and on your other retained rights, please visit: https://www.elsevier.com/about/our-business/policies/copyright#Author-rights

© 2022 Copyright - All Rights Reserved | Copyright Clearance Center, Inc. | Privacy statement | Terms and Conditions
Comments? We would like to hear from you. E-mail us at customercare@copyright.com

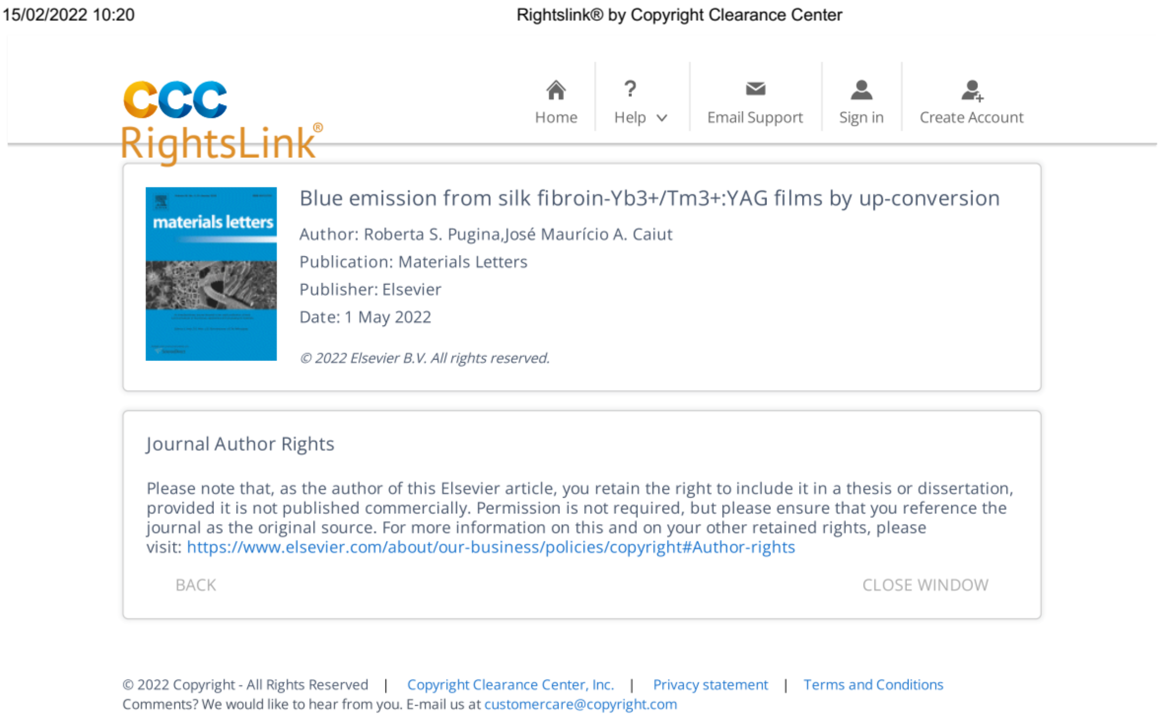

15/02/2022 10:20 Rightslink® by Copyright Clearance Center

Blue emission from silk fibroin-Yb3+/Tm3+:YAG films by up-conversion

Author: Roberta S. Pugina,José Maurício A. Caiut

Publication: Materials Letters

Publisher: Elsevier

Date: 1 May 2022

© 2022 Elsevier B.V. All rights reserved.

Journal Author Rights

Please note that, as the author of this Elsevier article, you retain the right to include it in a thesis or dissertation, provided it is not published commercially. Permission is not required, but please ensure that you reference the journal as the original source. For more information on this and on your other retained rights, please visit: https://www.elsevier.com/about/our-business/policies/copyright#Author-rights

© 2022 Copyright - All Rights Reserved | Copyright Clearance Center, Inc. | Privacy statement | Terms and Conditions

Comments? We would like to hear from you. E-mail us at customercare@copyright.com